UNIVERSITÉ DE STRASBOURG

ÉCOLE DOCTORALE ED182

UMR 7504

THÈSE présentée par :

Rémi Goerlich

soutenue le : **29 septembre 2022**

pour obtenir le grade de : **Docteur de l'université de Strasbourg**

Discipline/ Spécialité : Physique

Optical control of Brownian diffusion: from bath engineering to quantum analogues

Contrôle optique de la diffusion brownienne : de l'ingénierie de bain aux analogues quantiques

THÈSE dirigée par :

M. MANFREDI Giovanni	Dr., IPCMS, Université de Strasbourg, CNRS
M. GENET Cyriaque	Dr., ISIS-CESQ, Université de Strasbourg, CNRS

RAPPORTEURS :

M. AMAROUCHÈNE Yacine	Dr., LOMA, Université de Bordeaux
M. GUÉRY-ODELIN David	Prof., LCAR, Université Paul Sabatier, Toulouse

AUTRES MEMBRES DU JURY :

M. THALMANN Fabrice	Prof., ICS, Université de Strasbourg
Mme ROICHMAN Yael	Prof., School of Chemistry, Tel Aviv University

Acknowledgements

I acknowledge my reviewers Yacine Amarouchène and David Guéry-Odelin, for the time and energy they spent reading the manuscrit. Having such a careful and dedicated feedback on my PhD work has been very valuable. I also would like to acknowledge their interest on the day of the defense, allowing such a good discussion. I would like to thank Yael Roichman for joining this jury, crossing miles from Tel Aviv to Strasbourg. I also thank Fabrice Thalmann, accepting to be the president of this jury. Finally, I would like to thank Thierry Charitat for being here.

Of course, I would like to deeply thank my supervisors Giovanni Manfredi and Cyriaque Genet. These three years of PhD have been a time of constant enthousiasme and this was due to their energy, support and understanding, but also to their large scientific horizon, allowing us to progress from a project to another with continuity and excitement. I'm convinced that these years working together where the best possible way for me to enter into this world. I'm also very grateful to Paul-Antoine Hervieux, third voice in this dedicated team of supervisors, his knowledge and curiosity, scientific and beyond helped me to find my way in this work. I would like to thank Thomas Ebbesen for welcoming me in his nanostructure lab, and for always keeping a warm interest to our work. Thanks to Éloïse Devaux, for teaching us so many things needed to build samples and engineered material, but also for her kind attention.

I am naturally very grateful to Yoseline Rosales-Cabara, Minghao Li and Samuel Albert, the three first guides in the maze of an optics room. They thought me many things in physics and mathematics, but also electronics, data analysis, coding, all these daily tasks of lab-life. Thanks also for bringing so much laughter in dark optics lab. I also deeply thank Luis Barbosa-Pires for all the time spent together, in the lab but also from the small peaks of Vosges by bike to the high peaks of Alpes in Les Houches. Not only did I learned a lot, but I also found again an understanding friend in the lab. I thank a lot Antoine Tartare who spent six months with us with an unlimited enthousiasme, it has been a very good time to learn and work together, thanks to Baptiste Weyrich with whom we rebuilt the interfacing of the experiment, thanks to Edgar

Bingler and Simon Ricon, thanks also to Arthur Fonseca, bringing new energy this fall.

Since the beginning of my PhD, Jérôme Gauthier and Bianca Patrahau became my companions of journey in the nanostructure lab. Their kindness, attention and presence everyday, from a morning coffee to a late beer, built a joyful atmosphere in our office. We went together through the many steps of PhD life, reading and writing, ideas and trials, excitement and despair. Thank you for your friendship, we'll meet again, in Strasbourg or elsewhere.

The lab atmosphere was also shared with many other talented scientists, Kripa Joseph, Soh Kushida, Kalaivanan Nagarajan, Shahana Nizar, Gian-Lorenzo Paravicini, Sudipta Saha, Yoichi Sasaki, Weijian Tao Anoop Thomas, Robrecht Vergauwe, Kuidong Wang, I'm thankful to all of them.

The QDyNO group in Cronenbourg was a second scientific family, where I met many gifted students for sharing a theoretical life. Of course, I thank Vincent Hardel, with whom I was very happy to work on numerics and quantum-classical parallels. Thanks also to all the young team, Adrien Andoche, Louise Desplat, Jean-Gabriel Hartmann, Denis Jankovic, Rémi Muller, it was always a pleasure to spend time in your dyno-office.

I would like to thank QMat for financial support, but also Alena Gradt for all the help. I also thank Marie-Claude Jouaiti and the administrative team from ISIS for the constant energy spent to keep this place special. I would also like to thank the people from IPCMS, Catherine Bonnin for the help and advice, Beatrice Masson, for keeping alive the best librairie I know.

Pour finir, je veux remercier mes amis et ma famille, pour leur soutien et leur affection depuis longtemps, je réalise à quel point vous m'entourez. Merci Antoine d'avoir su créer, avec Volta, un projet commun ; merci à Mathilde, Marie et aux autres *voltistes* ; merci Camille et Pierre, pour un quart de siècle d'amitié fidèle ; merci Quentin et Enrique pour votre attention et votre affection ; merci Florence pour ces années partagées et pour ton soutien. Merci Jean pour ton amitié, on a mis huit ans à trouver notre vraie cantine mais ça valait le coup. Merci Manon d'avoir continué à faire des détours par Strasbourg entre tes voyages. Merci aux amis des bancs de la fac, Emma, Andrea, Anaïs, Loïc et tous les autres. Merci Anne, Ewald, et Caroline, pour votre soutien, votre confiance et tout ce que vous m'avez donné, merci Juliette pour tant et tant de choses.

Contents

List of publications and communications

Publications

- R. Goerlich, M. Li, S. Albert, G. Manfredi, P.-A. Hervieux, C. Genet, *Noise and ergodic properties of Brownian motion in optical tweezers: looking at regime crossovers in an Ornstein-Uhlenbeck process*; Phys. Rev. E. **103** 032132 (2021)

- R. Goerlich, G. Manfredi, P.-A. Hervieux, C. Genet, *Probing quantum effect with classical stochastic analogues*; Phys. Rev. Research **3** 033203 (2021)

- R. Goerlich, L. B. Pires, G. Manfredi, P.-A. Hervieux, C. Genet, *Harvesting information to control non-equilibrium states of active matter* ; Preprint ArXiv 2112.10842

Conferences

- Summer school *The New Mechanics* in Les Houches (France), about the latest development on ultra-sensitive optomechanical systems, 2022, August 1^{st}-26^{th}; student talk: *Harvesting information to control non-equilibrium states of active matter*

- Soft matter meeting Strasbourg (France), 2022, June 2^{nd}; talk: *Harvesting information to control non-equilibrium states of active matter*

- Journées scientifiques ITI QMat, Strasbourg (France), 2022, June 1^{st}; poster: *Harvesting information to control non-equilibrium states of active matter*

- Journées de la physique statistique, Paris (France), 2022, January 27^{th}-28^{th}; talk: *Harvesting information to control non-equilibrium states of active matter*

- Qrevolution, from the first to the second quantum revolution Peyresq (France), 2021, October 24^{th}-29^{th}; poster: *Probing quantum effect with classical stochastic analogues*

- Optique Dijon (France), 2021, July 5^{th}-9^{th}; poster: *Probing quantum effect with classical stochastic analogues*

- Soft matter meeting Strasbourg (France), 2021 July 3^{rd}-4^{th}; talk: *Probing quantum effect with classical stochastic analogues*

- Nanolights2020 Benasque (Spain), 2020, March 8^{th}-14^{th}; poster: *Noise and ergodic properties of Brownian motion in optical tweezers: looking at regime crossovers in an Ornstein-Uhlenbeck process*

Chapter 1

Introduction

1.1 Brownian trajectories in an optical trap

When a micron-sized object is suspended in a fluid, it undergoes a perpetual erratic motion. Such an object, a thousand times smaller than a millimetre, can seem minute with respect to everyday life meter-scale, but still is ten thousand times larger than an atom. Light enough to be sensitive to the molecular agitation of the fluid in which it lies, it is large enough to be observed with a simple microscope. This very simple fact of having a size in between our macroscopic world and the nanoscopic world of atomic and molecular physics is the cornerstone of the interest in so-called *Brownian motion*.

The measurement of its random trajectories can be made quantitative [1] and it is through the probing of the stochastic position of microspheres suspended in water, that Jean Perrin measured Avogadro's number in 1909 (see Fig. 1.1 (left)). Similarly, the angle fluctuations of a small suspended mirror where used in 1931 by Eugene Kappler to measure the equilibrium probability distribution in a potential (Fig. 1.1 (middle)). An important development in the experimental investigation of Brownian motion was provided by optical trapping (Fig. 1.1 (right)). This technique developed in the eighties by Arthur Ashkin [2, 3] has provided a very large number of applications in many fields of physics [4, 5]. Its coupling with Brownian motion is probably among the most fruitful. It relies on possibility to use a focused laser beam to build a mechanical potential in which a Brownian object is confined while still being influenced by the surrounding medium, allowing very precise and controllable experiments. In the following paragraphs, we review three examples from recent literature of application

of optically trapped Brownian motion as transducer mechanically displaying physical phenomena of various nature.

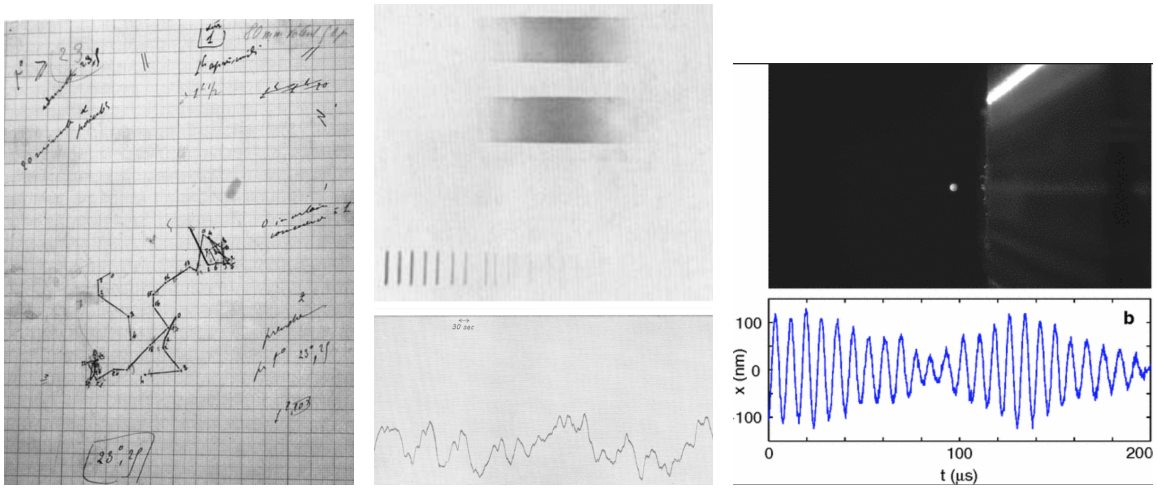

Figure 1.1: (left) **1909**: Jean Perrin notebook, ca. 1909 from [6]. This seminal experimental investigation of free diffusion, in agreement with Einstein theory of Brownian motion [1, 7], led to the first physical measurement of Avogadro's, number, key step in the acceptance of atomic theory. (center) **1931**: Eugene Kappler's experiment [8] on the motion of a small mirror suspended on a quartz wire under thermal fluctuation. The shaded area corresponds to the reflected light, imprinted on a sensitive paper. Its gradient is connected to the fluctuations of angle of the mirror, direct visualization of its probability distribution. This experimental probing of Brownian diffusion with a restoring force is central since it connects it to equilibrium statistical mechanics and to the equipartition of energy. (right) **2012**: on top is a photograph of a nanoparticle diffusing in a rarefied gas, optically trapped by a focused laser beam in Lukas Novotny's lab [9]. The low viscosity of the gas allow a ballistic motion to the nanoparticle, as in Langevin's equation [10]. On the bottom is a recorded trajectory, where one can see both a deterministic oscillation and a random fluctuation.

As a first example, optically trapped Brownian motion allowed to visualize the effect of non-conservative optical force fields. In an experimental work from the team of Ernst-Ludwig Florin in 2009 [11] the trajectory of a Brownian object allows to build a quantitative map of the optical forces inside a focused laser beam. The force field is

measured with a spatial resolution of 10 nanometers and with a femtonewton precision in force, demonstrating the high level of accuracy obtained with optical traps. Ten years later, by performing similar experiments in a dilute gas [12], where the motion becomes inertial, Yacine Amarouchène and Yann Louyer unveiled the mechanical effects of non-conservative forces, with toroidal currents both on position and velocity of the trapped object.

Optically trapped Brownian motion also allows to visualize the mechanical effect of complex environment, as found in biology. If we think of a human cell, the cytoplasm forming most of its volume is far from a simple fluid as pure water, as from a dilute gas as mentioned above. It is crowded by many object, such as actin, intermediate filaments or microtubules that form its architecture, but also numerous floating molecules of various sizes. An explicit description of such a fluid is a hard task, both because of its intrinsic complexity and because of the difficulty to perform non-destructive study giving biologically relevant results. However, many fundamental properties of the cytoplasm can be retrieved by looking at its effect on a micrometric object diffusing in it. The Brownian motion reveals here its crucial mesoscopic nature: it does not show the detailed dynamics of its environment, but only a mechanically filtered simplified version of it. It can therefore be analyzed with reasonable cost, but still reveals much informations on its environment, as we will detail in the next paragraph.

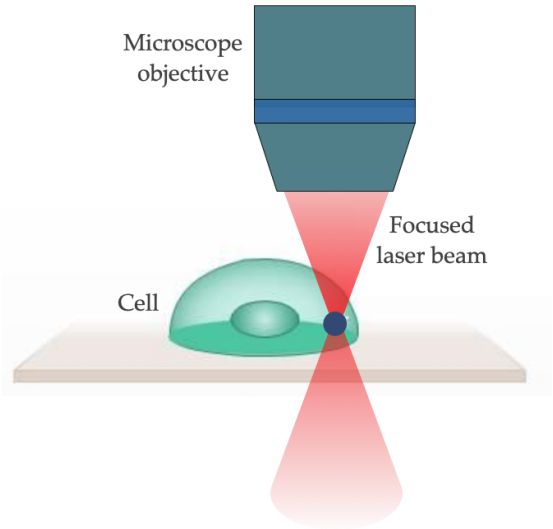

Figure 1.2: Schematic view of in-cell rheology: a micrometric particle is injected inside a living cell and optically trapped from the outside. It allow to probe the mechanical properties of the cytoplasm and cytoskeleton, as explained in the main text.

By injecting a micrometric sphere inside a living cell and trapping it with an optical tweezer, as schematized on Fig. 1.2, the group of Lene B. Oddershede was able to access diffusive process inside the complexe cytoplasmic fluid [13]. By furthermore applying on the microsphere a time-dependant perturbation, it becomes possible to implement an in-cell rheometer, which provides a measure of the viscoelastic properties of the cytoskeleton. This technique unveils rheological changes in the cytoplasm during the different phases of mitosis [14] connected to dramatic

changes in the architecture of the cytoskeleton
during this dynamical process [15, 16]. The statistical nature of the diffusion of a tracer inside an actin network was also extensively studied by the group of Yael Roichman [17, 18] revealing non-trivial dynamics.

Another important development of optically trapped Brownian motion during the last decade, is its coupling with optomechanical techniques [19] inherited from atomic manipulation, as cavity cooling (implemented independently by the team of René Reimann [20] and Markus Aspelmeyer [21]) and feedback and cavity cooling [22, 23], as schematized in Fig. 1.3.

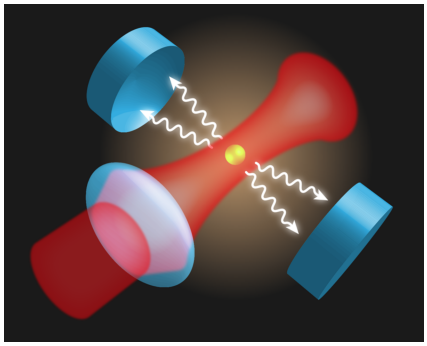

Figure 1.3: Cavity cooling of a trapped nanoparticle (from [23]): the tuning of the cavity will preferentially allow well defined modes for the photons scattered by the nanoparticle from the trapping beam. The slight detuning is chosen so that only the modes that takes out energy from the mechanical degrees of freedom of the particle can propagate. This coherent scattering cools down the motion of the nanoparticle.

With those methods, more recently it became possible to reach the quantum ground state for the motional degree of freedom [24], paving the way to the exploration of quantum thermodynamics. In a recent work by the team of Nikolai Kiesel [25] a trapped nanoparticle undergoes a transition between two potentials in quantum regime.

In the following paragraphs, we will focus on the application of optically trapped Brownian motion to statistical mechanics experiments. We will review important examples from the recent experimental and theoretical literature, that contextualize the work of this thesis.

1.2 Optically trapped Brownian motion for statistical mechanics experiments

At microscopic scales, thermal fluctuations cannot be neglected, and every physical, chemical or biological process takes place whithin these fluctuations. This is the case of biological phenomena happening inside every cell of our body, as gene transcription or material transport, that are complex processes, involving mechanical and chemical agents. These different

functions take place in this microscopic fluctuating environment, which modifies their relative efficiencies. For example, the group of Daisuke Mizuno studied in details the fluctuating energetic rules governing the axonal transport of kinesin molecular motor [26], finally demonstrating that the fluctuations of the environment are increasing the velocity of the motor [27]. In a different field, nanoscopic electronic devices, because of their small scales are also affected by fluctuations and similar rules apply on their energetic exchanges. This aspect was extensively studied by Jukka Pekola on single electron devices [28, 29, 30].

Brownian motion appears as a paradigmatic example of microscopic objects dominated by fluctuations and it therefore shares many features with the aforementioned examples. This applicability stems from the universal character of fluctuations at small scales combined with the formal simplicity of Brownian trajectories. Yet to be able to quantitatively answer questions relevant for the physics of small natural system, two important points must be addressed. The first is the precision of the experiments: the Brownian trajectories must be recorded with a sufficiently high resolution and a good control on the parameters governing their dynamics. The second point is the flexibility of the experimental platform to induce non-trivial effects. For example, one emulates with a Brownian motion experiment the behaviour of a micrometric biological object evolving inside the cytoplasm of a living cell by applying on the Brownian objects forces that mimic those felt inside a living cell.

Those two aspects can be directly combined in optical trapping experiments. The role of optically trapped Brownian motion in the study of statistical mechanics and small scale thermodynamics stems on the one side from the universal character of fluctuations, well captured by Brownian dynamics as well as the simple and intuitive nature of Brownian motion, and on the other side, on the control, flexibility and resolution of optical trapping platforms. With these elements, it is possible to use a simple optically trapped microsphere to build genuine statistical mechanics experiments to probe fundamental questions, as fluctuation-dissipation theorem [31], thermodynamic laws and fluctuation theorems [32], accelerated and engineered thermalisation [33, 34], Landauer bound [35, 36], information engines [37] to cite only some striking examples taken from the recent literature.

The case of Kramers description of a thermal barrier crossing [38] is an example of theoretical and experimental research based on the ability of Brownian motion to simulate statistical mechanics. Indeed, many physical, chemical and biological processes [39] are well described by a system lying in a metastable state with a non-zero

probability of decaying into another energy minimum of lower energy. Among the best known examples of reaction-rate theory are chemical kinetics [40] and protein folding [41]. The striking power of Kramers theory is to unify these various phenomena under a single model : a Brownian object diffusing across a potential barrier, either in a metastable or a bistable potential. For a bistable potential, it predicts that, for a barrier potential of the same order as thermal energy, the Brownian object jumps from one well to another with an exponential distribution of residency times. The results of Kramers theory can be applied to many other systems, as the aforementioned protein folding [42], with successful quantitative description.

The exponential distribution of residency times of Brownian object has been experimentally tested at the end of twentieth century [43] in an overdamped experiment, in water at ambiant temperature. Another major result of Kramers theory is that for a certain combination of barrier curvature and strength of the thermal force, a maximal crossing rate can be achieved. This cannot be tested in an overdamped case, where the high pressure prevents reaching the right regime. It is only in 2017 that it became possible to test the so-called Kramers turnover in an optically trapped Brownian motion experiment by the team of Lukas Novotny [44].

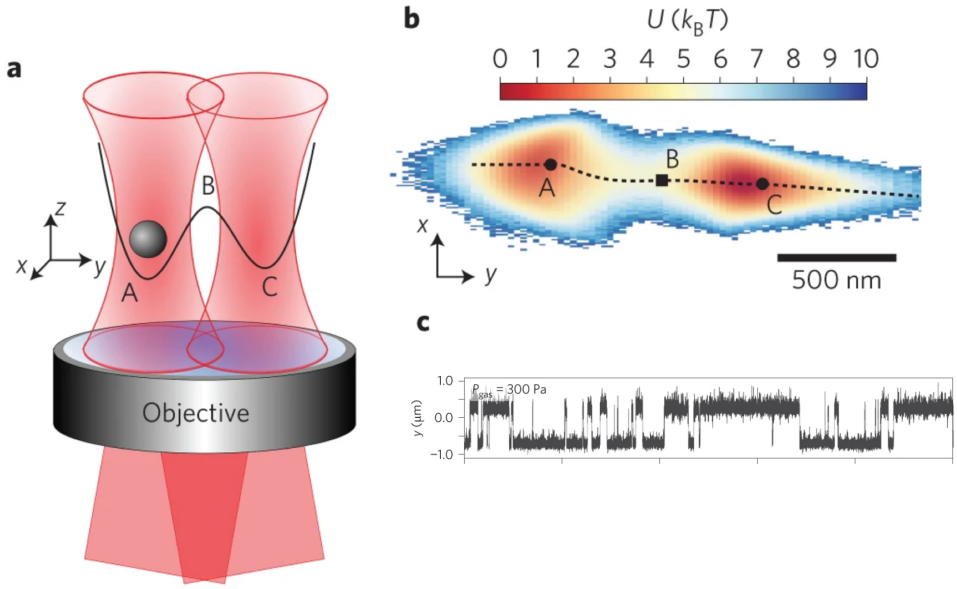

Figure 1.4: Adapted from [44]. (a) two high-intensity laser beams are sent into a microscope objective, creating a genuine double well optical potential. (b) Potential energy along a plan orthogonal to the optical axis, the two minima are clearly visible. (c) a typical bistable trajectory along the y axis.

On Fig. 1.4 we reproduce the main results of [44]. Using two tightly focused laser beam, a double-well potential is created in a high vacuum environment and the diffusion of a nanoparticle inside this energy landscape is recorded. The resulting trajectories (Fig. 1.4 c.) exhibit typical bistable dynamics with a hopping statistics depending, as expected by the theory, on the curvature and height of the energy barrier, the temperature and the pressure of the surrounding gas. By probing various pressure, this experiment scanned Kramer's turnover with a maximal hopping rate for a pressure of ca. 1500 Pascals, in agreement with theory. This experimental work is a example of the combination of the high-resolution and flexible character of modern optical trapping experiments with the broad descriptive character of Brownian motion.

Developments such as cavity cooling for quantum-ground state manipulation or high-vacuum Kramers turnover, inspired by quantum optomechanics are highly promising for future fundamental work. Yet they do not replace a continuous effort within the -apparently simpler- framework of overdamped optically trapped Brownian motion at ambiant temperature. This parallel development with an increasingly refined connection with the complexity of natural systems is still providing numerous new results, often linked to soft-matter and biological systems.

A large body of work in this field is grounded on the notions of small scale thermodynamics and out-of-equilibrium physics, where Brownian motion is useful for making physical processes visible and intuitive. Indeed, by connecting the laws of thermodynamics with Langevin equations, the field of stochastic energetics, initiated by Ken Sekimoto [45, 46] is endowing mechanistic equations with a thermodynamics content. Especially suited to describe small systems, this new field of research experienced an important development during the last two decades [47, 32, 48], which we do not intent to review here. It is the core of the understanding of the laws governing energy exchanges in biological systems at microscale, as for example a bacterium propelling itself by consuming chemical fuel [49].

Such systems are called *active* because of their ability to convert an energy available in the environment, (glucides [49], ATP [50, 51]) into another thermodynamic form of energy such as heat, or work necessary for directed motion [26]. The non-equilibrium nature of active systems [52, 53, 54] raised many fundamental questions on the nature of thermodynamic equilibrium [55], the ingredients necessary to be out-of-equilibrium [56, 57], and the tools to characterize this departure [58, 59, 60, 31, 61]. Even though the concept of active matter applies to many different fields and ranges across many different scales, key features can be approached using microscopic Brownian systems

[62, 63, 55, 64]. Brownian models are easily described theoretically and studied experimentally, eventually replacing actual living samples, that are harder to manipulate. A large body of theoretical work has been published on the characterization of the nature of active matter, and its non equilibrium thermodynamics [65, 66]. Recently, an appealing interpretation has been proposed, with the idea that most of the specificities of active matter can be encapsulated in the concept on non-reciprocal coupling.

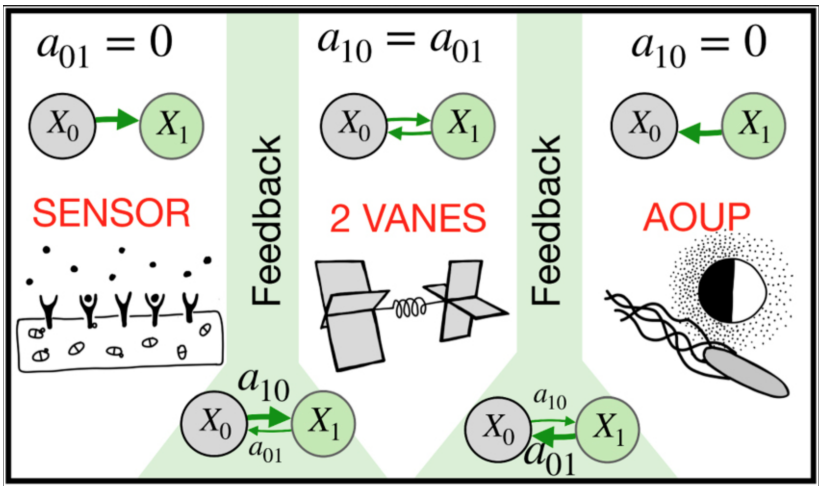

Figure 1.5: From [67], for the simple case of a set of two coupled stochastic equations : the terms a_{01} and a_{10} are the coupling coefficients injecting the solution of one equation into another, as for example the state of the propulsion mechanism into the position dynamic for a self-propelled object (AOUP on the right panel). A similar set of equations can describe a sensing mechanism [68] (left panel). The case where $a_{01} = a_{10}$ describes two variables symmetrically coupled but immersed in two independent baths, as the examples of coupled vanes (middle panel). The intermediate cases, are generic feedback systems.

The work of Sarah A. M. Loos and Klaus Kroy [67], as well as some earlier work [66, 69] put forward the very broad consequences of asymmetrically coupled Brownian dynamics. If we focus on the aforementioned example of a self-propelled micro-scale bacterium, its position is well described by a random variable obeying a Langevin equation driven by two independent noises [66]. A first uncorrelated noise (white noise) simulates thermal fluctuations of the surrounding fluid. A second correlated noise (colored noise) simulates the effects of the self-propulsion mechanism such as the bacterium flagella. Such correlated noise is itself the solution of a second Langevin

equation, driven by a “virtual" white noise. The system is thus well described by a set of two stochastic equations, with one coupling term, injecting the random propulsion variable into the stochastic position equation. This case is called active Ornstein-Uhlenbeck particle (AOUP) and will be described in details in Chap. 4, as a limit case of unidirectional coupling, as shown in Fig. 1.5 (right, panel) where the only coupling term is referred to as a_{01}.

We see that non-reciprocally coupled stochastic processes is an operative way of solving apparently complicated problems: in the previous example, it allow to get rid of the colored noise, by treating it explicitly as an independent variable, instead of a random term. Yet this framework is richer than only simplifying the description of self-propelled objects. As seen in Fig. 1.5, the same framework applies to many different systems, from biophysics [70] to optomechanics [71], by simply changing the coupling terms. It enables a two-dimensional description of the process, which can be a subtle way of revealing the irreversibility of the system, with visible steady-state currents that break the detailed balance condition.

1.3 Towards analogues

In the previous section, we introduced the idea that optically trapped Brownian motion is an excellent way to tackle statistical mechanics problems, lying in various fields of physics, chemistry or biology. This can be brought one step further by implementing genuine analogues.

The idea of analogy in physics has a history in itself, with celebrated examples, as Maxwell’s analogies [72, 73] in his derivations of the laws of electrodynamics. As analyzed by Francesco Nappo [74], Maxwell’s analogies seem to possess a double nature. On the one side, they have a pedagogical and interpretative power as they *“serve to clarify the equations proposed for an unfamiliar domain with a working interpretation drawn from a more familiar science"*, but in the other side, they are *“sources of defeasible yet relatively strong arguments from features of the more familiar domain to features of the less"*.

Analogies are also used in experimental physics, in order to achieve quantitative statements on systems that are hard to access directly [75, 76, 77]. As an illustrative example, the group of Chunquan Sheng [78] used a microsphere, embedded in a polymer waveguide to mimic the curved space-time in the vicinity of massive object.

Their experimental setup allows to explore several regimes, from weak to strong lensing effects. The results are in agreements with simulations based on the geodesic path of massless particle in curved space. We represent on Fig. 1.6 the analogy presented in this work as well as an example of bended light beam. This illustrative example shows how table-top experiments can serve to study hard-to-access physical systems.

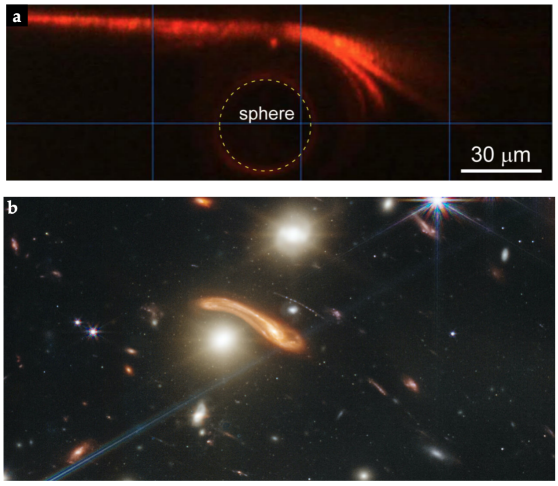

Figure 1.6: (a) Adapted from [78]: deflected light beam around a microsphere in a polymer waveguide is the analogue to gravitational lensing. (b) Recent image from James Webb telescope [79], displaying gravitational lensing on a galaxy.

Formal analogies will be the core of Chap. 4 and Chap. 5, to study two very different physical systems: living active matter in the first case and quantum open systems in the second. We will rely on the flexibility of optically trapped Brownian motion to build analogue experiments and extract quantitative measurements.

The possibility to use optically trapped Brownian motion to simulate statistical mechanics or build analogues as presented throughout this introduction relies on strict assumptions regarding the reliability of the experimental setup, as well as fundamental properties, such as the ergodic nature of the stochastic process. The experimental verifications of those properties will be the scope of Chap. 2 and Chap. 3.

1.4 Content of the thesis

In this thesis, we use a versatile optical trapping setup to probe the properties of various stochastic processes. Our control on the parameters, combined with the formal simplicity of Brownian dynamics allowed us to probe fundamental aspects such as diffusivity and ergodicity of a Langevin process. By adding well controlled external driving, we then designed two analogue experiments where optically trapped Brownian motion is applied to two a priori disconnected fields, namely active matter and open quantum systems. In the following, we briefly overview the content of the thesis, chapter by chapter.

Chapter 2 is dedicated to the main experimental, numerical and analytical methods to study Brownian motion in an optical trap. We introduce the experimental and numerically methods used to study such optically trapped microparticle and follow its time-dependant position. The Langevin process is connected to the deterministic Fokker-Planck equation. For a harmonic confinement, Fokker-Planck equation simplifies to an ordinary differential equation for the motional variance. It is explored with statistical ensemble, built by cutting and re-assembling a long time-series of recorded positions. This method is used for looking at the response of the trapped microsphere to a quench in the optical potential: by applying the same quench sequentially we built an ensemble of sub-trajectories on which deterministic quantities, such as the position probability distribution and its moments are derived. The Power Spectral Density (PSD) of positions is used to calibrate our optical setup and recover the trajectory of the microsphere from the recorded signal. The Mean-Square-Displacement is used to study the normality of the diffusion, by probing the short-time linear increase of squared displacements, as predicted by Einstein theory of Brownian motion. Finally, we introduce the framework of stochastic thermodynamics, connecting Langevin equation with the first law of thermodynamics.

In **Chapter 3**, we focus on two subtle and complementary observables of stochastic processes at play. First, we implement an operative test to demonstrate the ergodic nature of the stochastic process in our optical trap. This ergodic criterion is applied to a Brownian trajectory in our optical trap, proving its ergodicity, before being applied to an experimental stochastic resetting process [80], known theoretically to be non-ergodic [81]. This counter-example clarifies the meaning of the ergodic criterion, and also unveils an original method to correct long-time drift of very small amplitudes. In a second time, the long-time stability of the experimental setup is demonstrated using an Allan-variance based test.

Equipped with such tests, **Chapter 4** explores an active matter analogue built with an external optical force. We introduce the experimental methods needed to build an auxiliary bath with a stochastic radiation pressure before focusing on the case of exponentially correlated noise, which is known to be a minimal model to emulate effects of active matter. The trajectories of the microsphere under such a noise are shown to be superdiffusive and to break the equipartition theorem, unveiling the non-equilibrium steady state (NESS) nature of the process. We take advantage of the color-dependent response of the microsphere dynamics to design color-based protocols where the correlation time of the noise is used as a time-dependent parameter to drive the system through a NESS-to-NESS transition. The ergodic nature of the trajectories is verified before applying a STEP-like changes of color and observe the dynamical responses through the time-evolution of the motional variance. The non-equilibrium nature of the trajectories is explored. A rheological experiment demonstrates the violation of the fluctuation-dissipation theorem and a stochastic thermodynamics analysis gives a quantification of the heat released in the fluid bath by the particle under colored noise. Finally, an information thermodynamics interpretation of the process is proposed and discussed.

Chapter 5 deals with a classical stochastic analogue of an open quantum system, modeled through the so-called quantum drift-diffusion equation. This model is applied to the special case of harmonic confinement, where the exact results of a Wigner kinetic model are recovered at first order in Planck's constant, providing a validation of the drift-diffusion model. After noting the formal similarity between the quantum drift-diffusion model and a Fokker-Planck equation, we derive the associated stochastic equation, which has the peculiar property of depending on the probability density itself through the quantum Bohm potential (McKean-Vlasov process). The McKean-Vlasov process is first explored a numerically, by reconstructing the quantum potential through an ensemble of classical processes. Through the example of diffusion in a Duffing double-well potential, we discuss the impact of the quantum potential on the statistics of the residency times. The mean residency time is significantly shorter in the quantum case, which is reminiscent of the tunnel effect in standard quantum mechanics. Finally, we implement experimentally this stochastic process and study non-equilibrium potential protocols through the relaxation of the motional variance, from an initial equilibrium state to a different final equilibrium state.

Chapter 6 gives a general conclusion to this thesis, putting the main results in perspective with current challenges and ongoing projects.

Chapter 2

Brownian motion in an optical trap

2.1 Introduction

This chapter introduces the main experimental and numerical techniques as well as the theoretical observables used to explore Brownian motion in an optical tweezer. The development of optical tweezer over the last decades [2, 3, 82] gave access to the dynamics of single micron-sized objects. It allowed to study the nature of the optical field [83], to measure small forces [84, 85, 86] *e.g.* Casimir force [87], or, by studying the mechanical trajectories themselves, to probe the Brownian dynamics of micro-objects [88, 89, 90, 91]. The latter point, by providing individual stochastic trajectories in a defined energy landscape and bath, was used to investigate experimentally the interplay between the diffusive dynamics and its environment. For example, the application of optical tweezer to biological matter unveiled anomalous diffusive properties due to the complex active environment [92, 93, 94]. Various observable can be constructed with the stochastic trajectories to access their properties. For example, the spectral analysis of the trajectories though the power spectral density unveil different diffusive regimes, and can be used to calibrate an optical trap [95]. In the time-domain, the mean-squared displacement of the position in the trap is used for example to discriminate normal Brownian diffusion from anomalous diffusion [96, 97, 98]. As a last landmark, optically trapped Brownian objects allowed experimental tests in the recent development of stochastic thermodynamics [32, 99] and Brownian engines [100, **?**, 101] where thermodynamic quantities such as work, heat and entropy are derived and probed at the level of single stochastic trajectories.

Here we start by presenting the optical trapping experimental setup used throughout the thesis as well as the associated measurement, calibration and analysis techniques. The experimental platform is complemented by numerical simulations of

stochastic trajectories. As a model for the Brownian motion at play, we discuss the Ornstein-Uhlenbeck process, with specific constrains put on the nature of the thermal noise, that we carefully assess. Standard quantities like correlation, spectral density and mean-squared displacement are implemented and studied and the same quantities will be used again in the Chap. 4 and Chap. 5 to understand the nature of more complex diffusion processes. In the final section, we explain how the recorded stochastic trajectories can be studied from a stochastic thermodynamics point of view.

2.2 Langevin dynamics in an optical trap

2.2.1 Optical setup

Our experiment consists in trapping a single Brownian object in the harmonic potential created at the waist of a focused laser beam. A schematic view of the setup is given in Fig. 2.1.

A linearly polarized Gaussian beam (OBIS Coherent, CW 785 nm, 110mW) is focused by a water immersion objective (Nikon Plan Apochromat 60×, Numerical Aperture 1.20) into the sample that consists of a cell made of a glass slide and a coverslip, separated by a 120 μm thick and 13 mm wide adhesive spacer (Grace Bio-Labs SecureSeal). The cell is filled with a colloidal dispersion of polystyrene microspheres (in this chapter: ThermoFisher FluoSpheres polystyrene microspheres, 1 μm diameter $\pm$2%, in Chap 4: Duke Scientific Corp. 3 μm diameter) diluted in deionised water. We start with a solution of concentration of 10^{10} beads/mL that we dilute with a ratio 1:10^5 (N.B. this leads to about a thousand beads in the whole volume of the sample, leading to approximately one bead per 0.5 mm^2 if we consider a quasi 2D cell ; this allows easily to work with a single bead). The cell is then taped to a metal holder mounted in our optical setup. The instantaneous position of the trapped single bead is recorded using an additional low-intensity counter-propagating laser beam (Thorlabs HL6323MG CW 639 nm, 30 mW, but here used at low power $\approx$ 1mW), focused on the bead using a second objective (Nikon Plan-fluo Extra Large Working Distance 60×, Numerical Aperture 0.7). Within the small trapping volume defined by our setup, the intensity of the light scattered by the microsphere scales linearly with its displacement x_t along the optical axis. This scattered intensity signal is collected through the trapping objective and sent to a P.I.N. photodiode (Thorlabs, model Det10A2). The output signal goes through the data acquisition chain schematised on Fig. 2.2.

Another way to record the instantaneous position of the microsphere is to collect the part of the trapping 785 nm beam that is back-scattered by the microsphere.

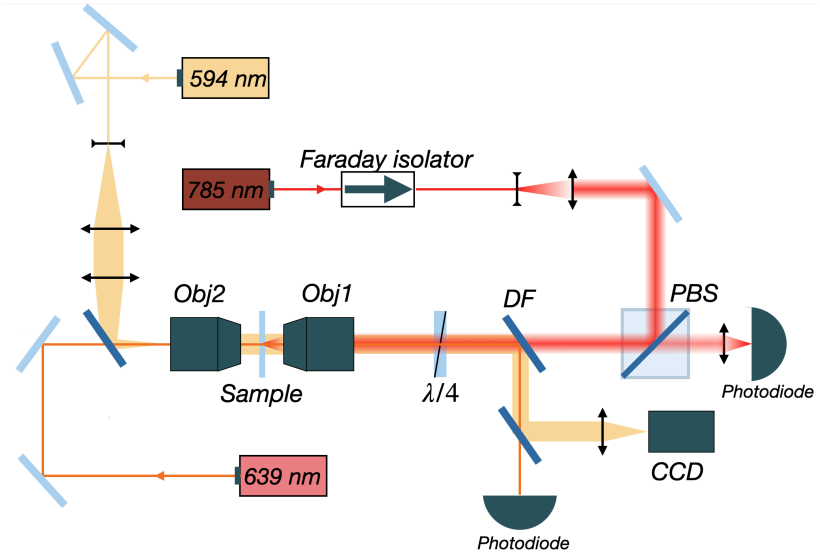

Figure 2.1: Simplified optical setup: the 785 nm trapping laser beam, drawn in red, is optically isolated with a Faraday isolator, expanded with a telescope to overfill the input lens of the microscope objective Obj.1 (Nikon Plan-Apo VC, 60×1.20 Water Immersion) thus focused on the sample. A second low-power 639 nm laser beam is used as a passive probe to measure the position of the bead. The beam is sent to the sample via a low-NA objective Obj.2 (Nikon Plan-fluo ELWD 6×0.70) and the light scattered by the sphere is collected by Obj.1 and sent to a photodiode (Thorlabs Det10a). A third low-power 594 nm laser beam is used to image the sphere, focused at the back focal plane of Obj. 2 to go through the sample as a plane wave. The light is collected by Obj. 1 and send to a CCD camera using a dichroic filter (DF).

It is collected by Obj.1 and transmitted though the PBS, it can then be sent to a photodiode (photodiode on the right of Fig. 2.1). However, as detailed later, the trapping beam is often modulated in intensity during experiments, in order to act on the microsphere, therefore, this detection method rely on some signal separation, that can be unpractical. Yet an important result of this alternative detection, is precisely to verify that the probing 639 nm beam is not modifying the dynamics of the bead. To do so, we verify with a recording from the back-scattered light, that a trajectories measured with or without the 639 nm laser beam have the same properties.

The photodiode output in Volt is sent to a low noise amplifier (Stanford Research, SR560); it is filtered through a 0.3 Hz high-pass filter at 6 dB/oct in order to remove the DC component of the output signal and through a 100 kHz low-pas filter at 6

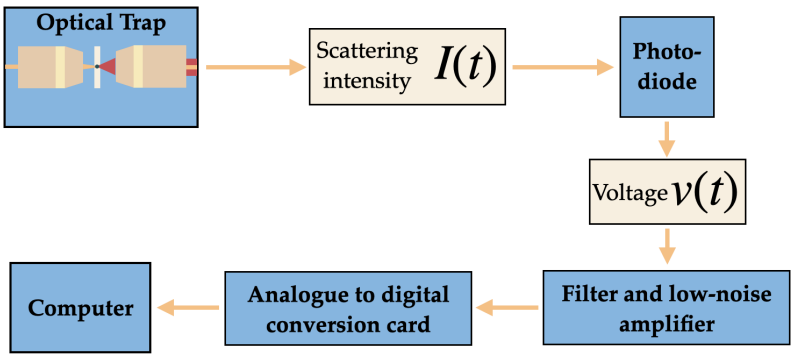

Figure 2.2: Schematic representation of the data acquisition chain, from scattered light intensity to voltage digitalised traces recorded on a computer.

dB/oct to prevent aliasing. It is finally acquired by an analog-to-digital card (National Instrument, PCI-6251) and stored as a time-series of voltage in a computer. The scattering intensity is linear with the position of the bead i the vicinity of the trapping laser waist. Since we work with small light intensity, the output voltage of the photodiode is also linear with the input light intensity. It is again linearly scaled by the amplifier, to yield an overall linear relation between the voltage values stored in the computer and the position of the bead $v(t) = ax_t + b$. It will later be explained how to experimentally calibrate this linearity to obtain positions in meter.

In our experiment, it is crucial to trap only one bead at a time. To achieve this, we rely on (i) a low concentration of beads in the solution as detailed above and (ii) a direct imaging of the vicinity of the trap (approximately 100 µm) with a transmission microscopy system; a low power 594 nm laser beam is extended using a telescope and focused in the back-focal-plane of the low numerical aperture objective. It enters the fluidic cell as a plane wave and the light scattered by the suspended fluid is recorded by the trapping objective, then separated from the other beams using a dichroic filter and sent to a CCD camera. This allows us to have an instantaneous image of the colloidal dispersion, helpful for searching a sphere to trap and for ensuring that only one object is actually trapped. A second important point is ensured by the thickness (120 µm)of the cell: the trapping region must be localised far enough from the walls to keep fluid parameters constant. The choice of the trapping wavelength (785 nm) also avoids heating locally the fluid, since it corresponds to the visible transparency window of water.

The optical force created by the focused 785 nm laser beam is responsible for the

trapping of the microsphere. Several frameworks have been used to describe optical trapping forces, depending on the size of the particle with respect to the wavelength. As explained in Appendix 8.1, the Rayleigh regime [102] provides a good framework to physically interpret the experiment. It is a dipolar approximation of the particle, suited for objects very small with respect to the wavelength of the trapping beam. As shown in [103], it can operatively be extended for the gradient force (trapping) term, up to particle of radius of the same order as the trapping beam waist. Within this framework and for small enough displacements $\boldsymbol{r}$ around the waist of the trapping beam, the gradient force is linear $\boldsymbol{F}_{trap}(\boldsymbol{r}) = -\kappa\boldsymbol{r}$. This linear conservative force can be written as the gradient of a potential

$$V(\boldsymbol{r}) = \frac{1}{2}\kappa\boldsymbol{r}^2, \tag{2.1}$$

where the stiffness κ is proportional to the optical power of the trapping laser. The OBIS laser used here can be driven via an input voltage that we generate with a function generator (Agilent 33220A, 20MHz). This allows to control the stiffness of the optical trap. Using this technique, we can dynamically change the potential by modifying the optical power and record the instantaneous trajectory experiencing this change of energy landscape. We will refer to this process as a *protocol* of stiffness, that can be set to follow various time-dependant profiles $\kappa(t)$.

2.2.2 Brownian dynamics and Ornstein-Uhlenbeck process

The microsphere is diffusing in three dimensions within in the optical potential. We however probe only its motion along the optical axis (along the 639 nm and 785 nm laser beams on Fig. 2.1) that we denote x. We will therefore only work in one dimension of interest x for all the work presented in this thesis.

The microsphere in the optical trap is subjected to different forces. As discussed above, the optical force that stems from the 785 nm laser beam derives from a harmonic potential that writes, in one dimension

$$V(x) = \frac{1}{2}\kappa x^2, \tag{2.2}$$

fully characterised by its stiffness κ, leading to a restoring force $F_{trap} = -\frac{dV(x)}{dx} = -\kappa x_t$

Since the microsphere is immersed in water, it will also experience two forces from the fluid.
(1) at room temperature, the water molecules forming the surrounding bath are thermally agitated and, by bouncing on the microsphere, produce a noisy force. The fluid

correlations in water at ambiant temperature are in the terahertz range [104], hence when the dynamics is measured at lower frequencies, this thermal noise appears as uncorrelated. It can be model as force of random amplitude whose values ξ_t at a time t and ξ_s at a time s are δ-correlated: $\langle \xi_t \xi_s \rangle = \delta(t-s)$ where $\langle . \rangle$ means the average over many realisations of the noise. Since the Fourier transform of the Dirac δ-function is a constant, this uncorrelated noise possesses a flat spectrum, which is called *white noise*. The amplitude of the noisy thermal force induced on the microsphere by the fluid is given by the diffusion coefficient D.
(2) the microsphere pushed by the random thermal force in the fluid will then experience a drag force that will be opposite to its velocity as $F_{viscous} = -\gamma \dot{x}_t$ where $\dot{x}_t$ is the derivative of the position and γ is the viscous drag of the tracer in the fluid, computed with the Stokes formula $\gamma = 6\pi\eta R$ where η is the viscosity of the fluid and R is the radius of the sphere.

The fluctuation induced by the agitation of the water molecules and the drag opposing to the velocity stems from the interaction with the same fluid bath and their properties are connected. This is clearly expressed by the Einstein relation, special case of the fluctuation-dissipation theorem relating the amplitude of the thermal force, imprinted in the diffusion coefficient, to the viscous drag through $D = k_B T/\gamma$, where $k_B T$ is the thermal energy, Bolzmann's constant multiplied by fluid temperature. The thermal force writes $F_{th} = \sqrt{2k_B T\gamma}\xi_t = \sqrt{2D}\gamma\xi_t$. The overall equation of motion is obtained with Newton's law for a sphere of mass m

$$m\ddot{x}_t = -\gamma\dot{x} - \kappa x_t + \sqrt{2k_B T\gamma}\xi_t. \tag{2.3}$$

Equilibrium canonical statistical mechanics teaches us that this system eventually reaches thermal equilibrium with the bath, where the energy provided by the thermal fluctuations are dissipated by the viscous forces. The positions and velocities then follows the Maxwell-Boltzmann distribution. The canonical distribution for the two quadratic degrees of freedom $\dot{x}$ and x connected to kinetic energy $m\dot{x}_t^2/2$ and potential energy $\kappa x_t^2/2$ thus writes as:

$$\rho(x_t, \dot{x}_t) = \frac{1}{\mathcal{Z}} e^{-\beta\left(m\dot{x}_t^2/2 + \kappa x_t^2/2\right)} \tag{2.4}$$

where $\beta = 1/k_B T$ is the inverse thermal energy and $\mathcal{Z} = \int dx \int d\dot{x} e^{-\beta\left(m\dot{x}_t^2/2 + \kappa x_t^2/2\right)}$ is the partition function. The two marginal distributions along position and velocities are simply partial integrals of this bivariate distribution. For example, the partial integration on velocities $P(x) = \int \rho(x_t, \dot{x}_t) d\dot{x}_t$ leads to the position probability density

$$P_{eq}(x) = \frac{1}{\mathcal{Z}_x} e^{-\beta\kappa x^2/2}, \tag{2.5}$$

where the normalisation constant is $\mathcal{Z}_x = \sqrt{2\pi k_B T/\kappa}$. This distribution is a Gaussian with zero mean and variance $\sigma_x^2 = k_B T/\kappa$.

The thermalisation time τ_{th} needed for the velocities to reach thermal equilibrium distribution is given by the ratio between the mass and the viscous drag $\tau_{th} = m/\gamma$. For a polystyrene microsphere of diameter of 1 μm, the mass is 5.5×10^{-16}kg the Stokes drag is $\gamma = 8.9837 \times 10^{-9}$ kg/s this time is of the order of 10^{-7} s. On the other hand, the time needed for the position to reach thermal equilibrium distribution is given by the ratio between the viscous drag γ and the stiffness κ, for typical experimental parameters, $\kappa \sim 10^{-6}$ N/s^2, this time is of the order of the millisecond $\tau_{relax} = \gamma/\kappa \sim 10^{-3}$ s. We note here the clear separation of time scales between velocity and position relaxation, both also well separated from the bath correlation time $\sim 10^{-12}$s (therahertz range discussed above).

This separation of time scales define different regimes: first, both thermalisation time τ_{th} and relaxation time τ_{relax} needs to be large with respect to the correlation time of the fluid to ensure the validity of the coarse-grained equation Eq. (2.3). Furthermore if the experimental bandwidth does not includes the fast degree of freedom τ_{th}, the velocities will always appear at equilibrium, one thus cannot probe their relaxation. This regime, known as overdamped limit is a consequence of the clear separation of τ_{th} and τ_{relax} due to the small mass and large viscosity of the fluid, hence low Reynolds number. In this case, the inertial term in Eq. (2.3) is much smaller than the other terms and can be disregarded. The dynamics of the microsphere in the optical trap is then defined by the following overdamped dynamic, corresponding to an Ornstein-Uhlenbeck stochastic process

$$\gamma \dot{x}_t = -\kappa x_t + \sqrt{2k_B T\gamma}\xi_t, \tag{2.6}$$

which can be written under a more convenient form by using the diffusion coefficient $D = k_B T/\gamma$ and introducing the inverse relaxation time (typical pulsation) $\omega_0 = \kappa/\gamma$ and the Wiener increment $dW_t = \xi_t dt$

$$dx_t = -\omega_0 x_t + \sqrt{2D}dW_t. \tag{2.7}$$

The stochastic process x_t describing the instantaneous position of the microsphere in the trap is the solution of the stochastic differential equation Eq. (2.6) or (2.7). It can be conveniently computed via Laplace transform as detailed in Appendix 8.2. This transformation has the advantage of making explicit the initial conditions of the dynamic. This leads to the solution

$$x_t = x_0 e^{-\omega_0 t} + \sqrt{2D}\int_0^t e^{-\omega_0(t-s)}\xi_s ds, \tag{2.8}$$

where x_0 is the initial position at time $t = 0$. The integral over time shows the correlation or memory kernel of the position x_t with respect to a position in the past x_s, characterized by the relaxation time $\omega_0^{-1} = \tau_{relax}$ in the exponential.

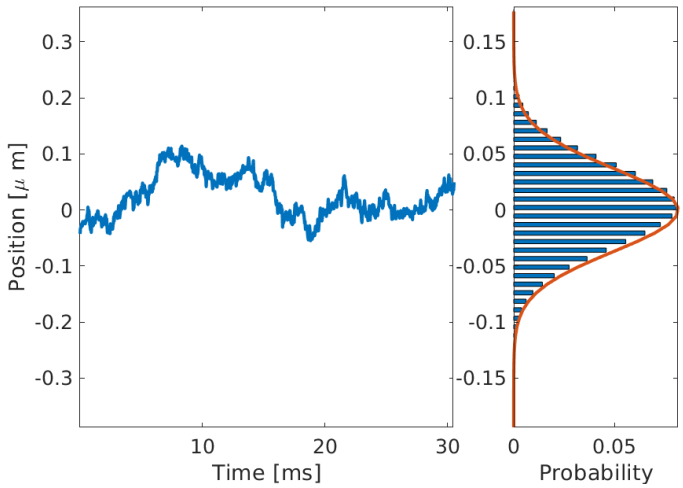

Figure 2.3: Stochastic trajectory x_t obeying to Eq. (2.7) recorded for 10 minutes at a rate of 2^{15} Hz, shown here over 30 ms. This trajectory is recorded with a trap of stiffness $\kappa = 2.9614 \pm 0.0673$ pN/µm, at room temperature, $T \approx 295$ K. The 1 µm bead experiences a drag coefficient $\gamma = 6\pi\eta R$ kg/s where $\eta \approx 0.95 \cdot 10^{-3}$ Pa s, hence $\gamma = 8.9837 \times 10^{-9}$ kg/s. Probability distribution (blue bars) of the whole ten minutes trajectory, along with the theoretical distribution Eq. (2.5) (red line). The data presented on this figure will be used in this chapter and the following. The same 10 minutes-long trajectory will serve to illustrate the stationary tools developed in the following sections and for the studies of the next chapter, that are used in [105].

On Fig. 2.3 we represent a trajectory recorded with our optical setup within the experimental conditions detailed in Sec. 2.2.1. In this experimental example, a 1 µm polystyrene microsphere is trapped using an optical power of 40 mW leading to a stiffness κ of 2.96 pN/µm. On the right panel, we display the corresponding probability distribution, a histogram of the ten minutes-long trajectory along with the Gaussian $P_{eq}(x)$ computed with experimental parameters. On the figure, we see the good agreement between the histogram and the theoretical Gaussian density. We emphasize that it is the same 10 minutes-long trajectory presented Fig. 2.3 that will be used in this chapter and the following as well as in [105].

Further, more subtle features can be derived that characterise further the properties of the trajectory, as we will detail is Sec. 2.5. Before doing that, we introduce two important concepts in the following sections. First we will describe how to numerically simulate such Brownian trajectoires. These simulations will be useful both to test and verify experimental results, but their derivation also gives deep insight on the nature of the stochastic process associated with Eq. (2.7). Then, we will focus on the non-equilibrium dynamics at play when looking at the transient response of Brownian trajectories. This will lead us to introduce the notion of ensemble of trajectories.

2.3 Numerical simulations of Langevin dynamics

The time evolution of our process is described by a stochastic differential equation. Let us first summarize how ordinary differential equations are generally numerically simulated by approximating the time derivative by a finite difference, and using this difference to evaluate the solution at a time-step i as a function of its value at step $i-1$. The approximation of the process gets closer to the exact solution as the size of the time-step diminish. Formally, the discretisation procedure is a consequence of a Taylor expansion of the trajectory for small time increments. By taking into account more terms in the expansion, the derivatives can be approximated with increasing precision while keeping the same time-step. For the ordinary differential equation

$$\frac{dx_t}{dt} = a(x,t), \tag{2.9}$$

the Taylor expansion until second order in time-increment Δt writes

$$x_{t+\Delta t} = x_t + \Delta t \frac{dx_t}{dt} + \Delta t^2 \frac{d^2x_t}{dt^2} + \mathcal{O}(\Delta t^3). \tag{2.10}$$

A numerical approximation Y_i of the solution x_t can therefore be obtained by truncating the Taylor expansion at a given order. For example, the first-order approximation of Eq. (2.9) writes

$$Y_{i+1} = Y_i + a(Y_i)\Delta t \tag{2.11}$$

know as Euler scheme for a given initial condition. The next order will involve the derivative $a'(Y_i)$, leading to a better approximation of the exact process x_t.

For a stochastic differential equation as

$$\frac{dx_t}{dt} = a(x,t) + b(x_t)\xi_t, \tag{2.12}$$

that can be more conveniently we written

$$dx_t = a(x_t)dt + b(x_t)dW_t, \tag{2.13}$$

with a drift term $a(x_t)$ and a diffusion term $b(x_t)$, the main issue is to evaluate the random Wiener increment dW_t. More formally, the question is how to generalise the aforementioned procedure of discretisation to the stochastic case. A large body of literature is available on the derivation of algorithm for stochastic differential equations [106, 107, 108, 109], here, we mostly underline what differ from an ordinary differential equation.

Similarly to the ordinary case a first order approximation of Eq. (2.13) can be written as

$$Y_{i+1} = Y_i + a(x_i)\Delta t + b(x_i)\Delta W_i, \tag{2.14}$$

where the Wiener increment $\Delta W = \int_t^{t+\Delta t} dW$ can be simulated by $\Delta W = \xi\sqrt{\Delta t} \equiv \mathcal{N}(0,1)\sqrt{\Delta t}$. It is known as Euler-Maruyama scheme.

An important difference between the ordinary and stochastic cases, is that the scaling $\Delta W \propto \sqrt{\Delta t}$ implies that the "order" of approximation of a given truncation of Taylor expansion is less clear for a stochastic process. Therefore, the question of the convergence of an approximated solution to the exact result must be addressed with quantitative tools. Two criteria are used. The *strong convergence* criteria [107] evaluates the average absolute difference of the Y_N and x_{t_f} at final time $t_f = N\Delta t$. If there are constant C and n such that

$$\mathbb{E}(|x_{t_f} - Y_N|) \leq C\Delta t^n \tag{2.15}$$

the algorithm is said to converge in the strong sense with order n [107]. However, when the quantities of interest are mostly average, variances or other low order moments, such criteria is not necessary. We can instead rely on the criterion of *weak convergence* [108], i.e. convergence of the means. We say that an algorithm has a weak order of convergence n is there exist a constant C such that for all function $f(X_t)$

$$|\mathbb{E}\left(f(x_t)\right) - \mathbb{E}\left(f(Y_i)\right)| \leq C\Delta t^n. \tag{2.16}$$

In our case we will test the weak convergence of the algorithm on the variance and use $f(x_t) = x_t^2$. To evaluate the weak order of convergence of our codes, we therefore run the algorithm for a set of parameters and for different discretization precision Δt and compare the resulting sample variance to its theoretical value. Since we wish to build algorithm the simulates the dynamics of our experimental setup where $a(x,t) = -\kappa x_t$ and $b(x,t) = \sqrt{2D}$, the equilibrium variance is given by $k_B T/\kappa$. Hence the error is evaluated as $e_{weak} = |1 - \mathbb{E}(Y_i^2)/(k_B T/\kappa)|$, and the order of convergence is the scaling of e_{weak} with Δt.

Furthermore, in this case, all first derivatives of $b(x_t)$ and second derivatives of $a(x_t)$ are zero, which drastically simplifies the Taylor expansion of the differential equation. As detailed in Appendix 8.4, the next order approximation of Eq. (2.13) writes

$$\begin{aligned} Y_{i+1} = Y_i + a_i\Delta t + b_i\sqrt{\Delta t}\eta \\ + b_i a_i' \frac{1}{2}\left(\eta + \frac{1}{\sqrt{3}}\theta\right)\Delta t^{3/2} + a_i a_i' \Delta t^2 \end{aligned} \tag{2.17}$$

where η and θ are two uncorrelated random numbers $\mathcal{N}(0,1)$.

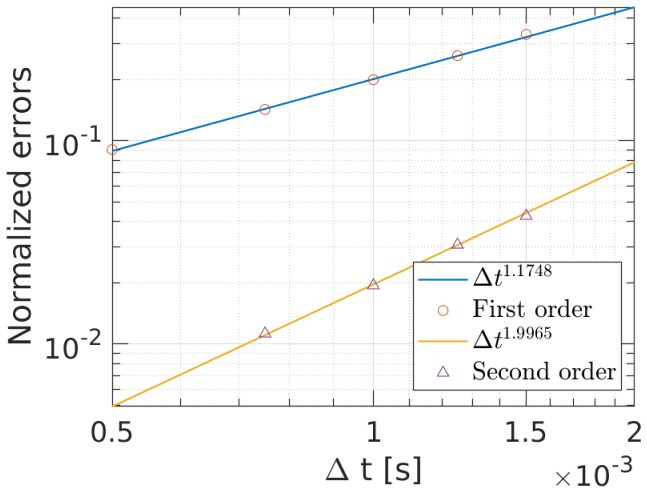

Figure 2.4: Weak convergence test of both Euler-Maruyama and second order algorithms. We plot the errors evaluated as the normalized difference between the measured variance and the theoretical result derived from equipartition k_BT/κ. Namely $e_{weak} = |1 - \mathbb{E}(Y_i^2)/(k_BT/\kappa)|$ for different values of the time increment Δt. We observe that the slopes of $\Delta t^{1.1748}$ and $\Delta t^{1.9965}$ are close to the expected ones of Δt^1 and Δt^2 respectively.

The weak order of convergence of Euler-Maruyama algorithm is known [107] to be $n = 1$ while second order approximation is supposed to converge with order $n = 2$. On Fig. 2.4 we show the result of the weak convergence criterium for both first order approximation Eq (2.14) and second order approximation Eq. (2.17). We see a convergence of order $n = 1.1748$ for the former, close to the expected value of 1 and $n = 1.997$ for the latter close to the expected value of 2.

This result means that the error we get on the variance evaluated on a trajectory simulated with the second order code Eq. (2.17) vanishes faster for the same discretiza-

tion Δt. This can allow to reach high precision while keeping reasonable computation cost, since a fine discretization demands more time-steps to probe the same dynamics. In most cases, this first-order scheme is good enough to provide reliable numerical results, it will be used in Chap. 4 and 5. In the following however, and in Chap. 3 we study stationary properties of trajectories on long times and with fine precision. The aim is to evaluate the long-time properties of the trap, such as stability as well as the short-time transition from free-like to trapped diffusion. In this case, precision is needed and an algorithm with higher efficiency is useful.

2.4 From random trajectories to deterministic ensemble distributions

To study out-of-equilibrium dynamics with deterministic (averaged) quantities we will rely on building *statistical ensemble of stochastic trajectories* x_t. As seen Fig. 2.3, associated probability densities converge to known distributions, characterised by the physical parameters of the process, in our case, the stiffness κ and the diffusion coefficient D. More generally, a given distribution $P(x_t, t)$ is time-dependent and its deterministic dynamics obeys the Fokker-Planck equation associated [110] with the process Eq. (2.7):

$$\frac{\partial P(x,t)}{\partial t} = -\frac{\partial}{\partial x}\left(\frac{\kappa x_t}{\gamma}P(x,t)\right) + D\frac{\partial^2}{\partial x^2}P(x,t). \tag{2.18}$$

If the physical parameters κ and D are constant, the system eventually reaches the time-independant equilibrium solution Eq. (2.5). But when the system is out-of-equilibrium and is undergoing a transient or forced evolution, the time dependence of $P(x,t)$ appears. The simplest case to discuss here is the response to a sudden change of one parameter in the process Eq. (2.7) as the potential energy in which the process evolves. By abruptly changing κ, one modifies the potential, going from an initial V_i, for which the bead is at equilibrium to a final potential V_f with different parameters. The initial density of position $P_i(x) \sim e^{-\beta V_i}$ is not the equilibrium solution of the new potential and the process x_t will undergo a transient evolution to a new state, with equilibrium density $P_f(x) \sim e^{-\beta V_f}$. In our case, the optical potential is locally harmonic, and as detailed Sec. 2.2.1, its stiffness κ can be controlled by varying the intensity of the trapping laser.

If many useful information can be extracted from single stochastic trajectories [111, 112, 47, 32, 48], the mechanical relaxation of the system from an initial to a

final equilibrium state is best understood though distributions and moments. Therefore, it is crucial to build large ensembles, over which we can measure for example the time-dependent ensemble-variance, that contains all information on the dynamics of the relaxation of the microsphere under a change of κ.

As detailed in Sec. 2.2.1, our experiments allow us to record the successive positions of the trapped bead, forming one single trajectory x_t. Ensembles are built by relying on the ergodic hypothesis, which will be carefully discussed in the next chapter. Ergodicity allows us to gather subparts of the trajectory x_t as independent individual shorter trajectories x_t^i and regrouped to build an ensemble $\{x_t^i\}$, from this collection.

To study the response of our system to a parameter change , such as an abrupt STEP-like change of stiffness κ, we apply the desired protocol sequentially, at a low-enough repetition rate, in order for the system to reach equilibrium between each event. With a typical relaxation time of a millisecond, the period of repetition is usually a few tens of milliseconds. We record synchronously both the trajectory experiencing the sequence of protocol and the imposed stiffness evolution $\kappa(t)$, through the voltage sent to the trapping laser. The simultaneous knowledge of x_t and $\kappa(t)$ allows, around each change of κ, to draw a sub-trajectory, long enough to include equilibrium before and after the protocol.

Fig. 2.5, shows the method used to build the ensemble for such a STEP-like change of stiffness. We only show a small excerpt of the five minutes long time-series of position recorded, experiencing in total $\approx 10^4$ changes of potential energy. The resulting ensemble $\{x_t^i\}$ corresponds to all the synchroniszed sub-trajectories associated STEP-like changes of stiffness κ going from 9.6 to 13.6 pN/µm On this ensemble $\{x_t^i\}$, we can compute a time-dependent instantaneous density $P(\{x_t^i\}, t)$, as a histogram of the position (defining a grid of bins and counting the individual positions measured in each bin). This histogram is normalized and converges to the probability distribution $P(x, t)$ solution of Eq. (2.18) for a large ensemble of trajectories.

On Fig. 2.6 (a), we show a contour plot of the time-dependant probability distribution $P(x, t)$ computed as an histogram on the ensemble. At each time, the distribution follows a Gaussian profile as in Fig. 2.3 and the width of the Gaussian goes from an initial variance for negative time to a final variance for long times. In between, around 0 to a few ms, it undergoes a quench. Since the distribution is Gaussian with zero mean, it is well described by its time-dependant variance $\sigma_x^2(t)$, it obeys a deterministic equation that can be derived by injecting a zero-mean Gaussian Ansatz in the

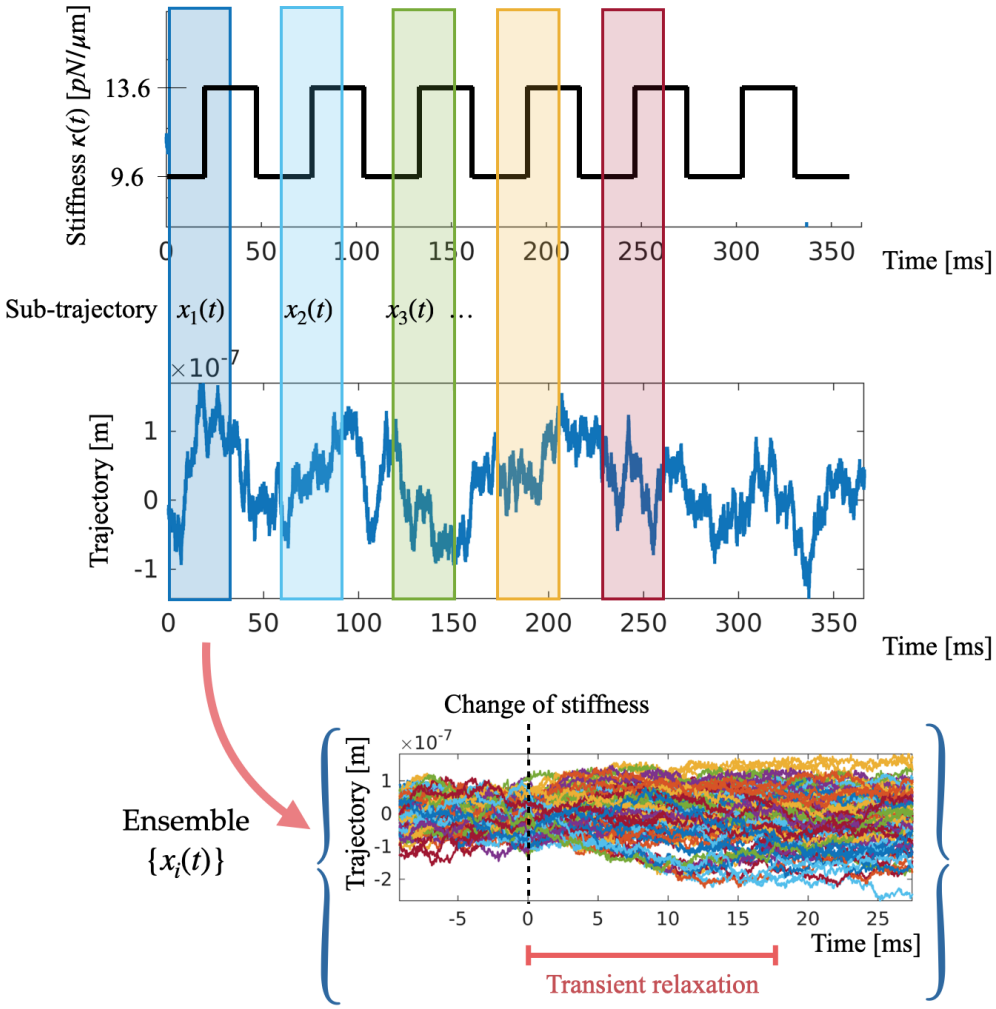

Figure 2.5: Schematic view of the method implemented to build an ensemble. A long time-series of position experiencing some sort of protocol at a low repetition rate (here STEP-like change of the potential energy every circa. 30ms shown on the top graph) is cut is sub-trajectories centred around one protocol. The ensemble is the reunion of the synchronised sub-trajecotries.

Fokker-Planck Eq. (2.18) leading to

$$\frac{d\sigma_x^2(t)}{dt} = -\frac{2\kappa}{\gamma}\sigma_x^2(t) + 2D, \tag{2.19}$$

a simple first order ordinary differential equation. When the initial condition is different from the stationary result k_BT/κ, it undergos an exponential evolution on a time-scale $2\gamma/\kappa$ from initial condition to the equilibrium variance.

For a STEP-like change of stiffness with initial equilibrium $\sigma_x^2(t < 0) = k_BT/\kappa_i$,

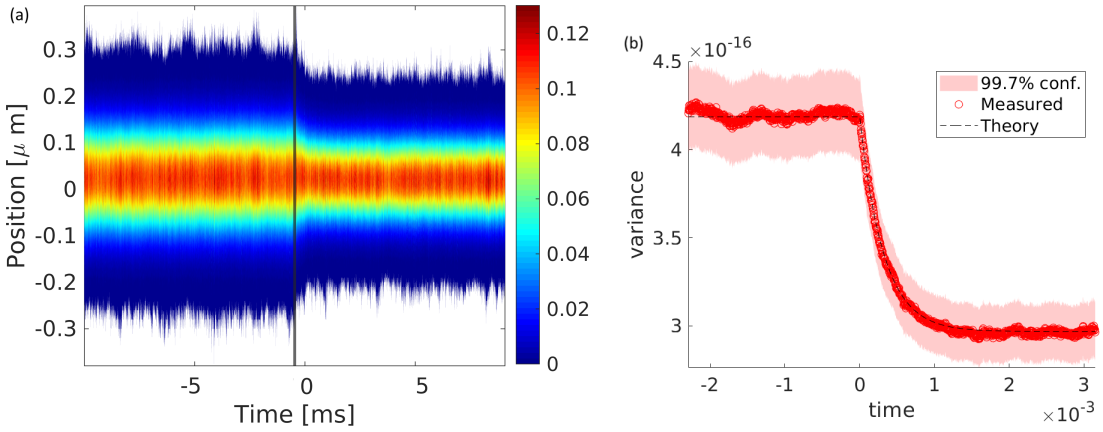

Figure 2.6: (a) Contour plot of the time dependent probability distribution of $\approx 10^4$ trajectories experiencing a step-like change of stiffness. At time 0, the stiffness is increased from 9.6 to 13.6 pN/µm and the density is quenched, with a smaller final variance. (b) Time-dependent variance of the ensemble of trajectories experiencing a step-like change of stiffness. The colored patch corresponds to 99.7% confidence interval, with error computed as the sum of the systematic errors performed on the radius of the bead and temperature of the fluid, as well as the statistical error on the estimator of the variance, evaluated with a χ^2 test at 3σ. The black dotted line corresponds to the analytical solution of Eq. (2.19) evaluated experimental parameters $\kappa(t)$ and D. The data presented here belong to the series of measurement presented in details Chap. 3 and in [113]. The calibration method and errors evaluations is more detailed in Chap. 5.

the solution of Eq. (2.19) writes

$$\sigma_x^2(t) = \left(\frac{k_B T}{\kappa_i} - \frac{k_B T}{\kappa_f}\right) e^{-\kappa_f t/2\gamma} + \frac{k_B T}{\kappa_f}. \tag{2.20}$$

On Fig. 2.6 (b), we represent the variance of the aforementioned distribution around the quench. We can clearly observe the decrease of variance when the stiffness is increased, this transient evolution is well fitted by the analytical Eq. (2.20). The method to calibrate the data and obtain an agreement between the experimental result and the analytical solution is detailed Chap. 5 when the data presented here are explored in more details.

In this section, we detailed how non-equilibrium transient evolutions can be probed using an ensemble of trajectories constructed from a sub-sampled a single long trajectory. In this case, the time-dependant Gaussian distribution is characterised by

its variance that obeys an ordinary differential equation. Here we focused on time-dependent case. In stationary state also, statistical tools are available to characterise the nature and the physical properties of the trajectory. By Fourier transforming the Brownian trajectory, one can compute the corresponding power spectral density and describe the nature of the thermal noise driving the dynamics. Using composed averages, one can also derive the autocorrelation function of the position and the mean-square-displacement that characterise the diffusivity of the tracer. Those quantities can be measured on an ensemble, or as time-averaged quantities taken on a single long stationary trajectory. In the next section, we will detail how to derive their analytical expressions and how to evaluate them on a trajectory to get useful information on its properties.

2.5 Stationary spectra, correlation functions and mean-square-displacements

While in the stationary state, the distribution of position and its variance are constant, other observables are available to characterise the nature of the process. In this section, we show that the power spectral density, autocorrelation function and mean-square-displacement of the position of the microsphere inside the trap constitute such observables and how they can be evaluated using experimental data, numerical simulations and analytical results.

2.5.1 Spectral representation and calibration

An essential feature of Brownian systems is given by their power spectral density (PSD). PSDs are largely used [114, 95] to characterise the nature of a noisy dynamical system or to calibrate optical tweezers. The PSD of our process is obtained by Fourier transforming Eq. (2.6)

$$-i\omega x[\omega] = -\omega_0 x[\omega] + \sqrt{2D}\xi[\omega] \tag{2.21}$$

where $x[\omega]$ is the Fourier transform of x_t. Isolating $x[\omega]$ gives

$$x[\omega] = \frac{1}{\omega_0 - i\omega}\sqrt{2D}\xi[\omega] \equiv \chi[\omega]F_{th}[\omega] \tag{2.22}$$

where we introduced the mechanical susceptibility $\chi[\omega]$ of the system (the diffusing microsphere) to the thermal force $F_{th}[\omega]$

$$\chi[\omega] = 1/(\kappa - i\gamma\omega) \tag{2.23}$$

which will be used in Chap. 4 to probe fluctuation-dissipation relation via rheology measures. The one-sided PSD $S_x[\omega]$ is obtained as the squared norm of $x[\omega]$

$$S_x[\omega] = |x[\omega]x^*[\omega]| = \frac{2D}{\omega_0^2 + \omega^2} \tag{2.24}$$

this Lorentzian profile is often evaluated as a function of frequency $2\pi f = \omega$, leading to $S_x[f] = D/(\pi^2(f_c^2 + f^2))$ where $f_c = \kappa/2\pi\gamma$ is known as the roll-off frequency. It separate a low-frequency regime where the spectrum is flat -reflecting the long-time stationary state where the bead has explored all the potential landscape- from a high-frequency $1/f^2$ regime reflecting the free-like short-time diffusivity of the bead.

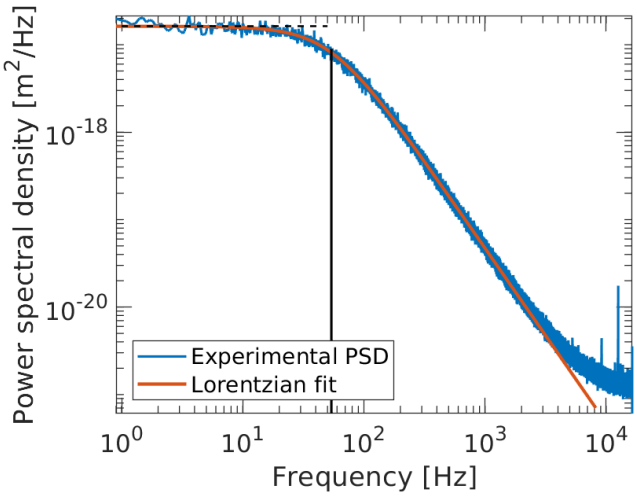

Figure 2.7: Experimental power spectrum density (PSD) evaluated for a trajectory $x(t)$ measured from 0.03 Hz to 100 kHz, displaying a large signal-to-noise ratio, spanning over 4 decades. We also note the transition (vertical black continuous line), at the roll-off frequency (53.6511 Hz) between the high frequency, almost-free, regime and the low frequency trapped regime. The thermal noise plateau $2k_BT\gamma/\kappa$ (horizontal black dashed line) agrees well with the low frequency limit of the PSD, as expected. From the Lorentzian fit performed on the PSD, we can extract the stiffness $\kappa = 2.9614 \pm 0.0673$ pN/µm. The experiments are performed at room temperature, with $T \approx 295$ K.

On Fig. 2.7 we show the spectrum from the same 10 minutes-long trajectory shown Fig. 2.3 and studied throughout this chapter and the following. We superimpose a fit performed with the analytical Lorentzian Eq. (2.24). With a vertical black line we indicate the roll-off frequency f_c and with an horizontal black dashed line we underline the amplitude of the low-frequency plateau $k_BT\gamma/\pi^2\kappa^2$.

A PSD can be used to calibrate our optical setup. As detailed in Sec. 2.2.1, the physical signal recorded is a voltage, amplified and filtered at the output of the photodiode. This voltage is proportional to the instantaneous position of the bead in the trap and the main calibration procedure is the extraction of the calibration factor β in meters per volts relating the measured voltage $V_{meas.}(t)$ to the position as $V_{meas.}(t) = \beta x_t$. This can be done if we assume known some physical quantities such as the radius of bead and the temperature and dynamical viscosity of the fluid, allowing to fix the diffusion coefficient $D = k_B T/\gamma$. The calibration procedure then consists in computing the PSD of the measured voltage and fit it with a Lorentzian of the form $D_v/(\pi^2(f_c^2 + f^2))$. The extracted diffusion coefficient D_v is expressed in V^2/Hz. The ratio between the latter and the a priori physical diffusion coefficient gives the calibration factor

$$\beta = \sqrt{D/D_v}. \tag{2.25}$$

A second calibration step is the calibration of the optical trapping potential, connecting the controllable parameters such as the optical power (or the voltage sent to the diode) and the stiffness of the harmonic potential experienced by the bead.

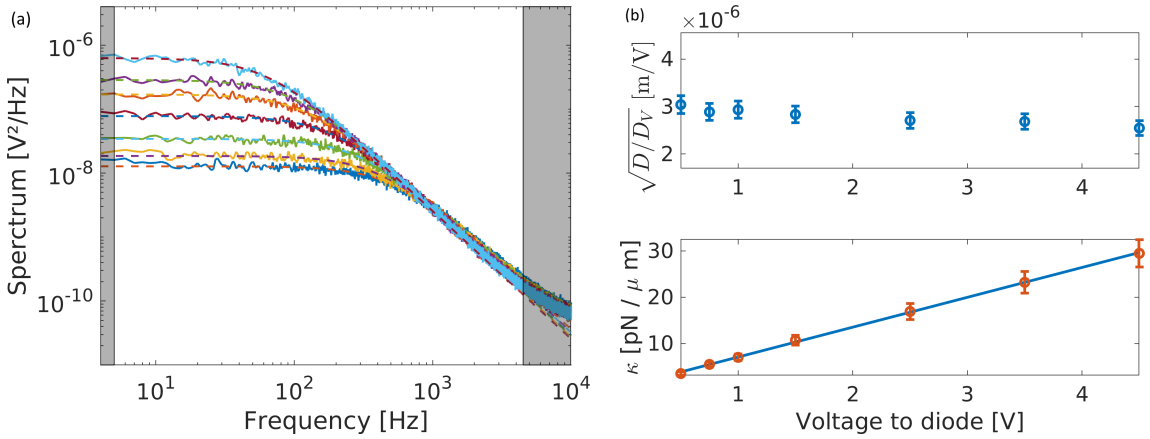

Figure 2.8: (a) Measured PSD and their respective fits for 7 values of voltage spanning the dynamical range of the laser diode input, from 0.5 to 5 V. (b) Parameters extracted from the Lorentzian fit. On the top pannel, the position calibration factor β as a function of the voltage remains as expected almost constant, with a mean value of 2.804×10^{-6} V/m. On the lower pannel, the stiffness κ expressed in pico Newton per micron, linearly increases, as expected, with the imposed voltage with a slope of 6.44 pN/µmV.

On Fig. 2.8 (a) we plot the measured PSD as evaluated from the voltage output measured at the photodiodes (and the Lorentzian fits) for 7 different trapping laser

optical intensities, expressed here as the voltage sent to the diode (i.e. as what the experimentalist controls). We stress with grey patches low and high-frequency regions that are discarded for the fitting procedure, considering that the very low-frequency points can suffer from some drifts (yet this will be carefully addressed in the next chapter) and that the high-frequency region is dominated by detection electronic noise above 10 kHz. The fit performed with the model $D_v/(\pi^2(f_c^2+f^2))$ allows to extract the value of D_v and f_c for each optical power. On Fig. 2.8 (b) we show those parameter as a function of the imposed voltage. We observe that $\beta = \sqrt{D/D_v}$ is nearly constant and κ scaling, as expected, linearly with the voltage, with proportionality constant 6.44 pN/µmV.

Other methods are of course available for calibration. Indeed, the calibration method proposed here which yields a volt-to-meter calibration is done by comparing a measured quantity (the amplitude of the PSD) to a theoretical prediction derived using physical parameters of the system. This method can be applied to other quantities than the PSD, arguably, simpler to compute and to compare to theory. This is the case for example of the sample variance $\langle x_t^2 \rangle$, which is known by the equipartition theorem to be equal to $k_B T/\kappa$. The ratio between the measure variance $\langle V_{meas.}(t)^2 \rangle$ and the equipartition result also gives a calibration factor. By the same token, inverting the relation gives an estimation of the stiffness κ for each measurement.

However, this method is less reliable in general, mostly for the estimation of κ. Indeed, the measured voltage is necessarily suffering from some artefacts such as contribution stemming from the high-frequency electrical noise, due to the acquisition and amplification chain. It is not a physical signal, and will have little influence on the physical conclusions drawn from the experiments (mostly, it does not influence the dynamics). It however can degrade a calibration done through equipartition. Indeed, this additional noise will artificially increase the variance, therefore decrease the value of the extracted stiffness κ. In contrast, the stiffness extracted from the PSD does not suffer from artefacts or ambiguity since it is a frequency measurement, and is independent from the amplitudes of the measured signals (the high-frequency saturation of the measured PSD does not influence the result of the fit on Fig. 2.7).

Fig. 2.9 displays the linearity between stiffness and applied voltage obtained with the two methods and where a net difference of slope is observed (4.26 pN/µmV for equipartition, 6.44 pN/µmV for PSD fit). The Lorentizan fitting method should therefore be chosen for the estimation of the stiffness. Although, as we will see in Chap. 5, more alternatives are possible. In this chapter, we propose a method based on the dynamical measurement. We apply to a the system a STEP-like change in stiffness

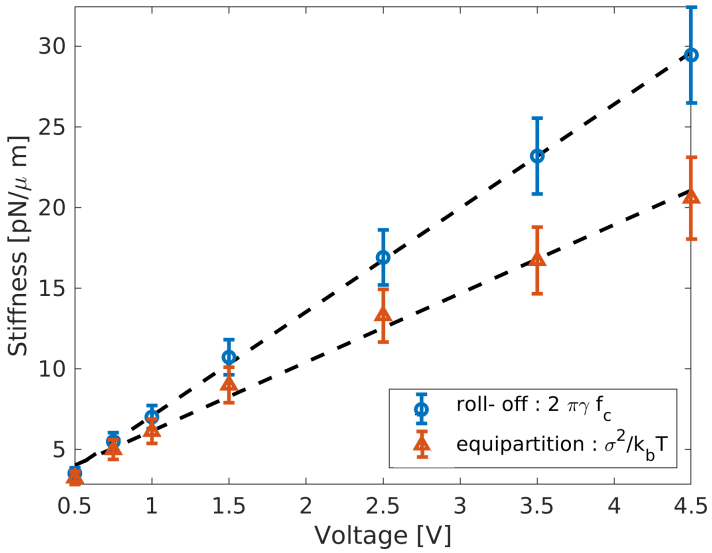

Figure 2.9: Comparaison between the calibration of stiffness performed with the Lorentzian fit of the PSD and with the equipartition theorem method.

$\kappa(t)$ as discussed above in Sec. 2.4. The variance therefore evolves as an exponential, whose characteristic time is uniquely defining the final stiffness of the STEP. By fitting the relaxation of the measure variance in volt $\sigma_v^2(t)$ we can extract a (time-domain) measurement of the stiffness. This alternative will also provide satisfying results.

2.5.2 Covariance and MSD, diffusivity and normality

To compute statistical observables such as mean-square-displacements (MSD) or autocorrelations, our method is to directly use the analytical solution Eq. (2.8) of the stochastic differential equation Eq. (2.6). We note however that the correlation function can also be obtained from the PSD via the Wiener-Khintchine theorem and that MSD can be derived from correlation if one knows the variance.

As discussed above, the solution Eq. (2.8), for the harmonically trapped Brownian motion possesses a short exponential memory, due to the presence of the potential. This also appears in the PSD, where the characteristic roll-off frequency f_c shows that, in contrast with the free Brownian motion, the process at play here has a characteristic time-scale. An apposite tool for studying the way the process depends on its past state is the autocorrelation function, given as the average on many realisations of the product of the process itself, evaluated at two different times $C_{xx}(t,s) = \langle x_t x_s \rangle$. This quantity

can be computed directly from Eq. (2.8) as:

$$\begin{aligned} C_{xx}(t,s) &= \langle x_t x_s \rangle \\ &= \langle x_0^2 \rangle e^{-\omega_0(t+s)} + 2D \int_0^t \int_0^s e^{-\omega_0(t+s-t_1-t_2)} \langle \xi_{t_1} \xi_{t_2} \rangle dt_1 dt_2 \\ &= e^{-\omega_0(t+s)} \left(\langle x_0^2 \rangle + 2D \int_0^{\min(t,s)} e^{2\omega_0 t_1} dt_1 \right) \\ &= e^{-\omega_0(t+s)} \left(\langle x_0^2 \rangle - \frac{D}{\omega_0} e^{2\omega_0 \min(t,s)} \right), \end{aligned} \tag{2.26}$$

where $\min(t,s)$ is the minimum between t and s. We can simplify this expression using the fact that $|t-s| = t+s-2min(t,s)$ to express the correlation as a function of $|t-s|$

$$C_{xx}(t,s) = \frac{D}{\omega_0} e^{-\omega_0|t+s|} + e^{-\omega_0(t+s)} \left(\langle x_0^2 \rangle - \frac{D}{\omega_0} \right). \tag{2.27}$$

Furthermore, when the system is in thermal equilibrium, it obeys the equipartition relation, stating that every quadratic degree of freedom equals $k_B T/2$. In our case, the only quadratic degree of freedom is the potential energy $\kappa x_t^2/2$ so that the variance at thermal equilibrium writes as

$$\langle x_t^2 \rangle_{eq.} = k_B T/\kappa. \tag{2.28}$$

If we consider the process initially at thermal equilibrium, namely $\langle x_0^2 \rangle = k_B T/\kappa = D/\omega_0$, the correlation function simplifies to a function of the lag $|t-s|$ only. In this stationary case where $C_{xx}(t,s) = C_{xx}(|t-s|)$, it is more convenient to express the correlation function as a function of a lag Δ as

$$C_{xx}(\Delta) \equiv \langle x_\Delta x_0 \rangle = \frac{D}{\omega_0} e^{-\omega_0 \Delta}. \tag{2.29}$$

The correlation function of the 10 minutes-long trajectory showed Fig. 2.3 measured in the optical trap is displayed Fig. 2.10. We superimpose the analytical result of Eq. (2.29) where a good agreement is seen, with a clear exponential decay to 0 with a time constant $\tau_{relax} = \kappa/\gamma$. We also show a numerical simulation performed with a second order algorithm, as detailed in Sec. 2.3 (red line). In the inset we show the covariance of the displacement $\langle dx_t dx_s \rangle$ which is computed in the Appendix 8.3. The displacement autocorrelation is an other, yet equivalent, way to characterize the stochastic process Eq. (2.6), by its increment.

From the covariance expression Eq. (2.29) and the equilibrium variance (2.28) one

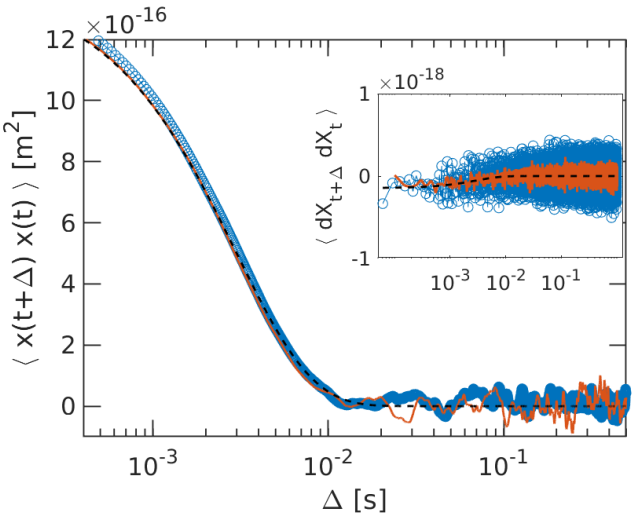

Figure 2.10: Time average covariances of positions (main graph), experimental data are plotted (blue open circles) together with the simulation results performed with a second-order algorithm (orange continuous line) and the analytical prediction of Eq. (2.29) (black dashed line). In the inset, we represent the autocorrelation function evaluated on displacements $\langle dx_t dx_s \rangle$ along with an analytical result derived in Appendix 8.3.

can compute the mean-square-displacement $\langle \delta x^2(\Delta) \rangle \equiv \langle (x_{t+\Delta} - x_t)^2 \rangle$

$$\begin{aligned} \langle \delta x^2(\Delta) \rangle &= \langle x(t+\Delta)^2 \rangle - 2\langle x(t+\Delta)x(t) \rangle + \langle x(t)^2 \rangle \\ &= \frac{D}{\omega_0} - 2\frac{D}{\omega_0} e^{-\kappa\Delta/\gamma} + \frac{D}{\omega_0}, \end{aligned} \tag{2.30}$$

giving

$$\langle \delta x^2(\Delta) \rangle = 2\frac{D}{\omega_0} \left(1 - e^{-\kappa\Delta/\gamma}\right). \tag{2.31}$$

On Fig. 2.11 we show the MSD of the same trajectory along with the analytical result of Eq. (2.31) and the numerical simulation results. We observe the $\sim \Delta$ increase at short times and the exponential saturation to a constant value of twice the equilibrium variance for long times. The first regime corresponds to the free-like diffusion obeying the well known diffusion equation, where the variance increase as $2D\Delta$, where D is given by Einstein's relation. The latter regime is determined by the influence of the harmonic trap, confining the motion of the microsphere and preventing the free-diffusion growth of the variance. The two regimes again are separated by the relaxation time τ_{relax}.

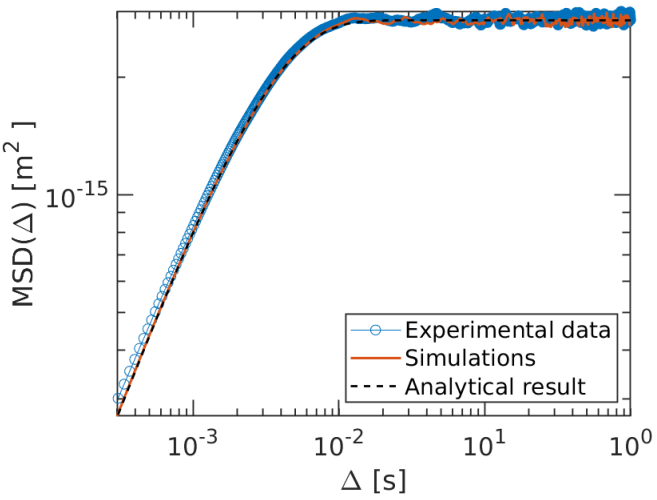

Figure 2.11: Comparison between the measured mean square displacements (MSD) (blue open circles) and the analytical expression given in Eq. (2.31) obtained in the stationary regime (black dashed line). The comparison with simulation results is also displayed (orange continuous line). The very good agreement with both theory and simulations shows that the measured process can be considered as stationary. We note the same relaxation time of $3 \cdot 10^{-3}$ s for all data, revealing the crossover between the free (Wiener) and trapped (Ornstein-Uhlenbeck) diffusion regimes.

The MSD is an other observable characterizing the diffusivity of the process. Indeed, its short-time increase serves as a measure of the (a)normality of diffusion [96, 115], which reveals the (non)-Brownian nature of the dynamics. If the effect of the conservative force $-\kappa x_t$ deriving from potential is easily analysed via the long-time contribution on the shape of the stationary distribution, the effect of diffusive forces that can differ from $\sqrt{2D}\xi_t$ is less simple to diagnose. MSD measure of how the tracer explores available space at short time and is useful to analyse the influence of non-trivial noises that do not modify the energy landscape but the nature of the diffusion within it. In our case, the linear scaling $\lim_{\Delta\to 0}\langle \delta x^2(\Delta)\rangle \sim \Delta^1$ is confirming the Brownian nature of the diffusion. It is related to the uncorrelated nature of the thermal noise. We will see in Chap. 4 that this is no longer the case when the microsphere experiences a noise η_t that is correlated $\langle \eta_t \eta_s \rangle \neq \delta_{t-s}$.

The observables presented in this section are mostly *stationary* observables in the sense that they explore the properties of a trajectory diffusing in a stationary state, where the probability density has relaxed to a constant distribution. All three quan-

tities, spectrum, autocorrelation and mean-square-displacement are giving similar but complementary information about the trajectory, since they are related to each other by simple transformations. Each observable is connected more accurately to specific effects, or are more useful for precise tasks than others. For example, the PSD is a quantity that is used for the calibration of the cut-off frequency and of the acquisition chain with a reasonable computational cost: using a fast Fourier transform on a small set of data already gives precise results [95]. On its side, the MSD can be used very conveniently to diagnose the nature of the diffusion process at play putting aside the influence of the external potentials applied. By observing the short-time limit of the MSD, one can measure the (a)normality of the diffusion.

2.6 Stochastic thermodynamics

The field of stochastic thermodynamics [46, 32, 48, 47] aims at adapting the concepts of macroscopic thermodynamics to mesoscopic systems, where fluctuations are important. Its applications range from molecular motors of a few tens of nanometers up to micron sized systems, such as our colloidal particle. The method of stochastic thermodynamics have been used in many different contexts, to derive thermodynamical observables relevant for small systems [54], as biological objects [26], micromechanical oscillators [116], RC circuits [117], small non-equilibrium [118, 31] and active systems [119]. Its application to optically trapped colloidal systems enabled the possibility to build microsized thermodynamic engines [100, **?**, 101], that exchange work and heat with an optical potential and a temperature-controlled thermal bath.

The first key step of stochastic thermodynamics is to endow Langevin equation with an energetic interpretation as done by Ken Sekimoto [46, 45]. A parallel development was the derivation of fluctuation theorems and energetic equalities [120, 121, 122, 123], with the remarkable possibility to extract quantitative features, such as the free energy by more accessible observables, like the work derived from a single trajectory [124]. The development of a trajectory-dependent entropic description [112, 47] add an even more refined understanding of the reversibility of stochastic trajectories Finally, the connexion to information theory [125, 126, 127] led to a better understanding in the physical nature of information, with experimental verifications of the finite cost of erasing information, so called Landauer limit [36, 35].

In Chap. 4 we will characterise the energetics of a specific type of protocol. To do so, we will rely on the Sekimoto's framework, starting from Langevin equation in a

harmonic potential of stiffness κ and in the overdamped limit

$$\gamma \dot{x}_t = -\kappa x_t + F_{th}(t) \tag{2.32}$$

where $F_{th}(t) = \sqrt{2k_B T \gamma}\xi_t$ is the thermal random force with ξ a white noise. Grouping the terms related to the interaction of the microsphere with the bath and multiplying by an increment dx, it is possible to draw an energy balance

$$\left(\gamma \dot{x}_t - F_{th}(t)\right) dx = -\kappa x_t dx \tag{2.33}$$

where the left-hand side, seen as the energy exchanged between the sphere and the bath under dissipative forms, is interpreted as minus the heat. The right-hand-side is $-\partial_x V dx$ where the potential is $V = \kappa x_t^2/2$. Since the stiffness of the potential can be controlled, it should be considered as a variable just as x_t leading to write the total differential of the potential as:

$$dV = \frac{\partial V(\kappa, x)}{\partial x} dx + \frac{\partial V(\kappa, x)}{\partial \kappa} d\kappa \tag{2.34}$$

a form interpreted by Sekimoto as the total change of internal energy under a variation of stiffness $d\kappa$ and with a displacement dx. Adding the remaining term on both side of Eq. (2.33) gives

$$\left(\gamma \dot{x}_t - F_{th}(t)\right) dx - \kappa x_t^2 d\kappa = -dV. \tag{2.35}$$

The variation of potential energy with respect to the external action of the parameter κ is interpreted as work. Identifying the change of heat δq, of internal energy du and of work δw is Eq. (2.35) gives an formulation of the energy balance that corresponds to the first law of thermodynamics

$$du = \delta w + \delta q. \tag{2.36}$$

The thermodynamic quantities derived here are stochastic, since they depend on the random variable x_t. Their distributions obeys fluctuation theorems [124, 111, 116, 47] and their average values can be derived by the methods presented above, leading to deterministic measure of the mean energy exchanged in the system. For example, one can compute the average work and heat exchanged during a STEP-like change of stiffness as described above [128]. The quantities derived here will be mostly used Chap. 4 to evaluate the thermodynamic nature and cost of a specific external process applied on the trapped microsphere.

2.7 Conclusion

In this chapter, we detailed our experimental optical trapping platform, that allows measuring Brownian trajectories in a controllable harmonic potential. After reviewing the experimental and numerical techniques to obtain Brownian trajectories, we introduced the methods to build statistical ensembles of independent trajectories, necessary to extract deterministic observables and study the response of the system to any external action. The main observables associated with a stationary dynamics, spectra, correlation functions and mean-square-displacements are derived and experimentally studied. Finally, we introduced the tools of stochastic thermodynamics that will be used is Chap. 4.

Our methods developed to build ensembles rely on the possibility of manipulating single long trajectories and turning them into ensembles of independent equivalent trajectories. This implies two key hypotheses. First, the experiment is stable in time: to study e.g. STEP-like change of stiffness by changing periodically κ at a rate of ten times the relaxation time, five minutes-long experimental trajectories are necessary to get good statistics of ca. 10^4 events. This implies that the experiment must remain stable over hundreds of seconds, ensuring that the same parameters κ and D and the same calibration factor β are fixed through time. Then the trajectory must be ergodic. This second hypothesis corresponds to the possibility to transform a trajectory into ensemble of sub-trajectories. These assumptions of stability and ergodicity and their verifications will form the core of Chap. 3.

Chapter 3

Noise properties of an optically trapped Brownian object, ergodicity, stability

In this chapter, standard quantities that are routinely used to study the properties of noise are complemented by more subtle measures of the noise properties. The first is an ergodic parameter [97, 129] that allows us to prove the validity of the ergodic hypothesis for our trajectories, paving the way to the construction of ensembles. The second is the Allan variance [114, 130] that evaluates the stability of the whole experiment with respect to drift over long integration times.

Both observables are derived analytically in the case of the Ornstein-Uhlenbeck process and applied on experimental trajectories in the optical trap, over a large frequency bandwidth. This allows to probe again the transition between different regimes, already unveiled in the previous chapter on PSD, correlation and MSD, separating a high-frequency free-like diffusion regime from a low-frequency saturation in the trapped regime. We observe a smooth crossover between the two regimes that are unified with both Allan variance-based test and the ergodic analysis.

Both observables are important to access for assessing the properties of a given optical trap. Indeed, as presented in the previous chapter, the study of the response of a Brownian object to an external action, goes with the building of a statistical ensemble out of a single time-series of positions. This ensemble is necessary to obtain well defined deterministic quantities out of the stochastic process at play. It relies on strong assumption regarding the ergodic nature of the process, but also its stability. The need for long-time stability of the optical trap is also very clear in the context

of metrology and weak forces measurements. In metrological measurements, a high resolution in force detection is achieved by integrating a high sensitivity over an integration time as long as possible. This is naturally relying on the long-time stability of the experiment.

In this chapter we explicitly show how ergodicity and stability assumptions can be tested for an overdamped harmonically trapped Brownian particle, paving the way to reliable experiments involving large integration times, with well-controlled ergodic properties. The tools proposed here are general and can be applied to more complex systems, as it will be the case in Chap. 4 where the bath is not anymore a thermal white noise. It can also be exploited to reveal the non-ergodic nature of specific systems, as discussed in the case of stochastic resetting in Sec. 3.1.5, or in the case of complex environments and glassy systems.

3.1 Ergodicity

As introduced in the previous chapter, the response of the system to a perturbation (*e.g.* a change of stiffness κ), is studied using deterministic averaged quantities (such as the mean and variance of position) or the time-dependant probability density. To do so, we need to build a statistical ensemble of independent trajectories out of a single long time-series of positions.

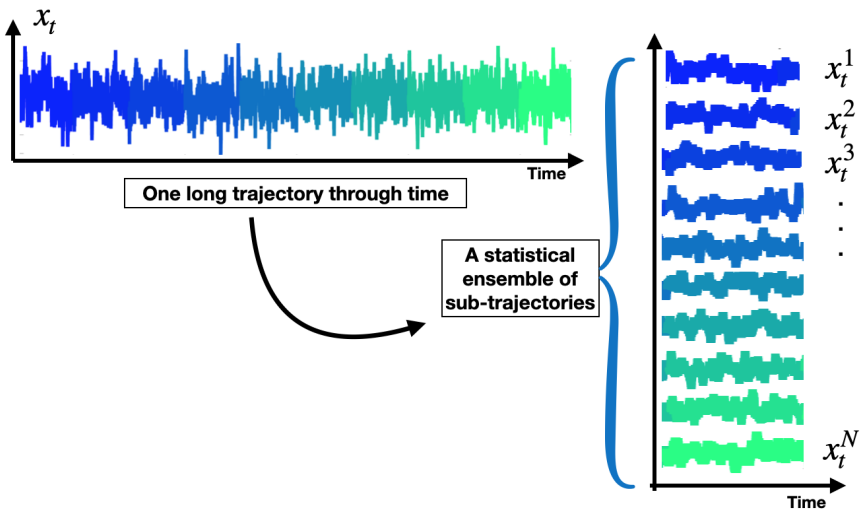

Figure 3.1: Schematic representation of the method to build an ensemble of sub-trajectories out of a long time-series of position. In this example, we show a 2.5 ms-long trajectory, cut into an ensemble of 10 individual 0.25 ms-long subtrajectories.

On Fig. 3.1 we schematize this procedure where a long trajectory is cut into an ensemble of shorter sub-trajectories. In this section, we wish to asses the validity of this procedure, namely, the ergodic nature of the ensemble. The question can be summarised as: *is one sub-trajectory a good representative of the whole ensemble?* For this to be true, the process first of all needs to be stationary. Ergodicity then states that time averages of a single trajectories must converge to instantaneous ensemble averages in the limit of infinite time and infinite ensemble. Remarkably, this general definition can be adapted to finite samples and thus made quantitative for experimental results, as first discussed by Metzler et. al [97, 129]. In the following sections we sill further develop the framework of ergodicity testing and apply it to the trajectories actually recorded in our optical trap.

3.1.1 Time and ensemble averaging for mean square displacement

Ergodicity is evaluated on averaged quantities. Since the first moment for centred process trivially vanishes (in our case any averaged position is $\langle x_t \rangle = 0$) the second moment is a suited observable to study averaging process. Furthermore, for a stationary process, the simple sample variance $\langle x_t^2 \rangle$ is a constant and cannot be used to asses the dependancy of ergodicity on the length of time sample and the size of the time steps. Therefore, we will turn to the mean-square displacement. This quantity is the first non-trivial moment of stationary Brownian displacement.

The mean square displacement (MSD) of a Brownian trajectory can be evaluated as an ensemble average performed on many realisations of the same process, as introduced in the previous chapter. Such an ensemble-averaged mean-square-displacement EA-MSD writes explicitly as:

$$\text{EA-MSD} \equiv \langle \delta_x^2(\Delta) \rangle = \langle (x_{t+\Delta} - x_t)^2 \rangle \equiv \frac{1}{N} \sum_{i=0}^{N} \left(x_{t+\Delta}^i - x_t^i \right)^2 \tag{3.1}$$

where we call x_t^i the i-th trajectory taken from the ensemble composed by these N independent sub-trajectories and where t is an arbitrary (yet in stationary state) initial time. On the other hand, on a single trajectory x_t^i, one can compute a time-averaged mean-square-displacement TA-MSD by integrating on the initial time t where the trajectory is evaluated

$$\text{TA-MSD} \equiv \overline{\delta_x^2}(\Delta) \equiv \frac{1}{\mathcal{T} - \Delta} \int_0^{\mathcal{T}-\Delta} \left(x_{t+\Delta}^i - x_t^i \right)^2 dt \tag{3.2}$$

where $\mathcal{T}$ is the total time of the measured i-th subtrajectory. If different such sub-trajectories in the ensemble are not equivalent to each other, then the TA-MSD of one

sub-trajectory may be significantly different from another This is the case for example if the sub-trajectories are produced with different tracers, whose properties, as size, may vary. Then TA-MSD will also be different from EA-MSD since the latter averages the dispersion of parameters over the ensemble. Nevertheless, even when the ensemble is drawn from a single long trajectory, where this tracer dispersion does not exist, both quantities can differ. Indeed, if a drift happens on an experimental parameter, such as temperature or on a mechanical object, then the long recorded trajectory is not stationary anymore, and the sub-trajectories obtained at different absolute times will differ. In that case again TA-MSD is not equal to EA-MSD.

These examples illustrate cases where the system under study in not ergodic, in the sense that one sub-trajectory of a statistical ensemble is not representative of the whole ensemble. For a stationary process, ergodicity of a given observable such as MSD, corresponds to the equality taken in the infinite time limit $\mathcal{T} \to \infty$, between the time average and the ensemble average of the quantity. In that case, every sub-trajectory's TA-MSD is equal to every other and to the EA-MSD. Although simple, this definition is however hardly operative in real experiments that only yield finite ensembles of finite-time trajectories. When $\mathcal{T}$ is finite, each TA-MSD is computed on a finite amount of data, and as such therefore remains a random quantity whose dispersion needs to be characterised.

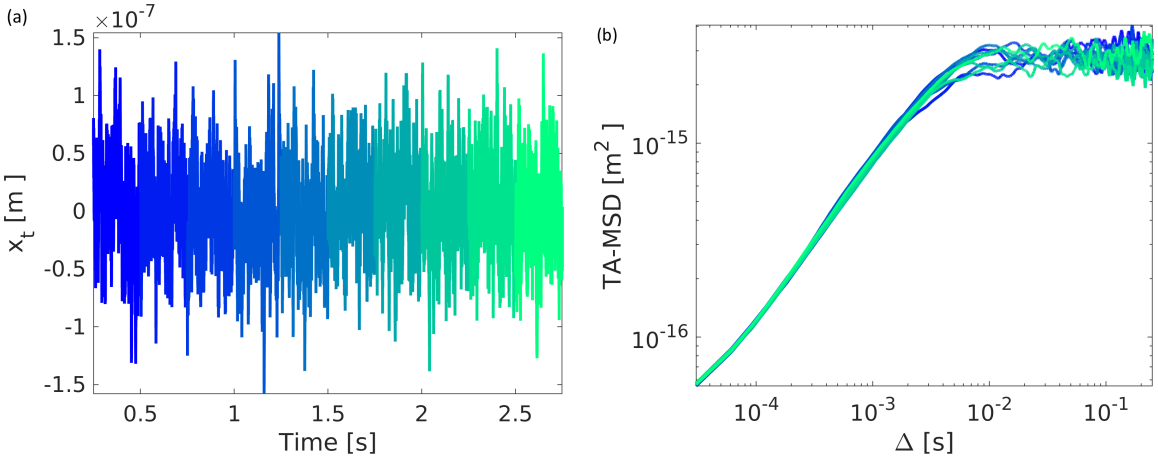

Figure 3.2: (a) One $\mathcal{T} \approx 2.5$ s long can be cut into an ensemble of 10 short trajectories of $\mathcal{T}_i \approx 0.25$ s. The process is represented here with 10 shades from blue to green. (b) On each short sub-trajectory, TA-MSD can be evaluated. The 10 resulting TA-MSD are represented with the same colouring, and the dispersion due to finite sample size is visible, mostly for long time-lag Δ.

As an illustration, on Fig. 3.2 (a) we plot one 2.5 seconds long trajectory and show how it can be cut into a finite ensemble of shorter trajectories. For each sub-trajectory x_t^i we can compute the TA-MSD, that is represented on Fig. 3.2 (b) with the same color coding as in Fig. 3.2 (a). We see that the individual TA-MSD slightly differ from one another. At this stage, this can be due either to a drift on the system or to the finite size of the sampled trajectories. If the latter is unavoidable and does not represent a physical issue, the former would be the sign of non-stationarity, which would forbid the building of a statistical ensemble from one single long trajectory. A more precise study of the ensemble of TA-MSD is necessary to decipher between these two very different phenomena.

On an ensemble, one can do both averaging operation sequentially and average the TA-MSD on the ensemble, obtaining the time-ensemble averaged mean-square-displacement TEA-MSD

$$\text{TEA-MSD} \equiv \langle \overline{\delta_x^2}(\Delta) \rangle \equiv \frac{1}{N} \sum_{i=0}^{N} \left[\frac{1}{\mathcal{T} - \Delta} \int_0^{\mathcal{T}-\Delta} \left(x_{t+\Delta}^i - x_t^i \right)^2 dt \right]. \tag{3.3}$$

This corresponds on Fig. 3.2 (b) to the averaging at every time-lag Δ of the different TA-MSD. Naturally, ergodicity demands the TEA-MSD to be equal to the EA-MSD. This represent a first approach to demonstrate the ergodic nature of the trajectories. However, this equality is only a necessary condition for ergodicity [97, 129], since TEA-MSD can hide a large dispersion of individual TA-MSD resulting of the non-equivalence of the sub-trajectories. Instead, a necessary and sufficient condition for ergodicity is the vanishing of the TA-MSD dispersion when integration time is large. This allows to define an observable of ergodicity on finite sample, where the comparaison of the TA-MSD dispersion with an analytical prediction assesses the ergodic nature of the ensemble. In the two following sections, we will study both the necessary condition on TEA-MSD and the necessary and sufficient condition of the dispersion of TA-MSD.

3.1.2 Necessary condition for ergodicity on finite sample

Using a ten minutes long trajectory (i.e. 1.97×10^7 successive position measurements acquired at a frequency of $2^{15} = 32768$ Hz) we build a statistical ensemble of $N = 1200$ trajectories of 0.5 second each. Therefore each trajectory is long with respect to the millisecond relaxation time of the bead in the trap. On this large ensemble, the can compute 1200 individual TA-MSD as well as the instantaneous EA-MSD. Both quantities can be compared with the analytical result for mean-square displacement

of the Ornstein-Uhlenbeck process

$$\langle \delta_x^2(\Delta) \rangle = \frac{2D}{\omega_0} \left(1 - e^{-\omega_0 \Delta}\right) \tag{3.4}$$

where we recall the relaxation time $\omega_0^{-1} = \gamma/\kappa = 2.1$ ms in the trap of stiffness $\kappa = 2.96$ pN/µm and $D = k_B T/\gamma$ the diffusion coefficient in the thermal bath.

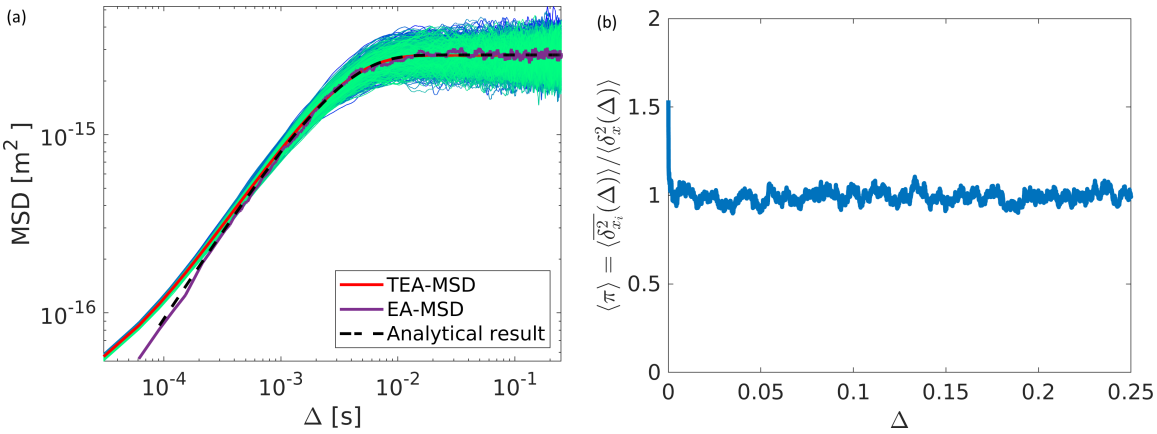

Figure 3.3: (a) From blue to green is an ensemble of $N = 1200$ individual TA-MSD, the red line is the ensemble average of the latter: the TEA-MSD. The blue line is the instantaneous EA-MSD, the black dotted line is the analytical MSD given by Eq. (3.4). (b) Necessary condition for ergodicity, on which the ratio between TEA-MSD and EA-MSD is one for all time. The short time-deviation is due to the difference seen on the left plot between TEA and EA-MSD where the values measured are very small time-laps Δ and subjected to tracking errors, as discussed in the main text.

On Fig. 3.3 (a) we represent the ensemble of TA-MSD as well as the associated TEA-MSD. The resulting function is compared with the instantaneous EA-MSD as well as analytical result Eq. 3.4. We can observe a neat equality of both TEA-MSD and EA-MSD for a large bandwidth of circa. 4 order of magnitudes of time-lag. However, for short time-lag, we observe a discrepancy, with an overestimated TEA-MSD. This can arise from tracking errors, as studied in [131] as well as in our own previous work [105]. Such errors are detailed in appendix 8.7. Tiny errors are mostly visible on short time-lag since the values of displacement measured at these time-scales are small. Typically the shortest measured displacement for a time-lag inverse of our acquisition frequency f_{acq} is $\sqrt{\langle \delta_x^2(\Delta = 1/f_{acq}) \rangle} \approx 7.43$ nm. This small displacement corresponds to a voltage measured on the photodiode (obtain by inverting the acquisition chain modelization detailed Chap 1., namely by dividing the displacement

$\sqrt{\langle \delta_x^2(\Delta = 1/f_{acq})\rangle}$ by the calibration factor and the gain of the low-noise amplifier) of $\delta V \approx 2.04$ µV. Since we use a 50 Ω resistor in parallel at the output of the photodiode, it corresponds to a current $\delta I = \delta V/50 \approx 40.7$ nA. This value is below the typical 100 nA dark current of a Thorlabs Det100A. This order of magnitude suggest that the values of displacement measured at those short time-lag are very likely subjected to errors as tracking errors [131] and that the discrepancy between TEA-MSD and EA-MSD at these values cannot be interpreted as a physical break of ergodicity. Since EA-MSD is computed on all the ensemble of 1200 sub-trajectories while each TA-MSD is computed on a single sub-trajectory, we can suppose that the latter is more likely to be affected by errors. This could explain why the EA-MSD is very neatly following the expected trend at very short-time while the TA-MSD are deviating.

The superimposition of TEA-MSD with EA-MSD clearer by forming their ratio, represented on Fig. 3.3 (b). This ratio is one for all time-lag, with a small deviation for very short Δ that corresponds to the short time-lag difference between EA and TA-MSD discussed above.

More precisely, we define π as this ratio between TA-MSD and EA-MSD At the level of a single i-th trajectory, the ratio π_i is a random quantity but the ensemble-averaged value $\langle \pi \rangle$ is deterministic

$$\langle \pi \rangle = \left\langle \frac{\overline{\delta_x^2}(\Delta)}{\langle \delta_x^2(\Delta)\rangle} \right\rangle = \frac{\langle \overline{\delta_x^2}(\Delta)\rangle}{\langle \delta_x^2(\Delta)\rangle} \equiv \frac{\text{TEA-MSD}}{\text{EA-MSD}}. \tag{3.5}$$

If TEA-MSD converges to EA-MSD, one expects $\langle \pi \rangle = 1$, as shown on Fig. 3.3 (b). Note that this value provides a necessary condition for ergodicity: if it where not the case, the consequence would imply that one cannot use a single trajectory to assess the properties of the ensemble, regardless of the length of the integrated time. But we stress, following [129] that this cannot be a sufficient condition for ergodicity, since the TEA-MSD can hide individual pathological trajectories, whose contributions though the ensemble averaging are minute while individually showing strong deviation from the expected behaviour. In the next section we focus on the dispersion of TA-MSD at a single trajectory level, hence of π_i, to build a necessary and sufficient condition for ergodicity [97, 129, 132, 105].

3.1.3 Sufficient condition for ergodicity on finite samples

As we discussed above, ergodicity of an ensemble of sub-trajectories demands the convergence of the ensemble of TA-MSD to the EA-MSD. A first quantification of this convergence was discussed in the previous section by the averaged ratio $\langle \pi \rangle$ between

TEA-MSD and EA-MSD, that should be equal to 1. We underlined that $\langle \pi \rangle = 1$ is not a sufficient condition for ergodicity. A more refined quantification of the convergence of TA-MSD to the EA-MSD, is the vanishing of the dispersion of individual TA-MSD on a single trajectory level. It implies that not only the probability distribution of the individual ratios π_i is centred around 1, but also that it tends to a Dirac distribution for long times, or as $\mathcal{T}/\Delta \to \infty$.

A sufficient condition for ergodicity is therefore that the dispersion of this ratio goes to zero in the limit $\mathcal{T}/\Delta \to \infty$. In this section we focus on the dispersion of individual TA-MSD by studying the probability distribution of $\phi(\pi)$ for the ensemble of $N = 1200$ individual TA-MSD. Furthermore, experimental result for the ergodic parameter are compared with numerical simulations performed with a weak-order 2 algorithm as detailed Chap 2. This comparaison gives an additional way of deciphering the limitations due to the finite sample sizes and experimental errors.

On Fig. 3.4 we represent $\phi(\pi)$ for different time-lags Δ. Yellow lines corresponds to long Δ and blue lines to short Δ. We can see that the distribution sharply converges to a peaked density around 1 as Δ decreases. As shown in inset, the kurtosis of $\phi(\pi)$ stays close to 3, the condition for a normal distribution. The distribution can therefore be characterised with its variance $\langle \pi^2 \rangle - \langle \pi \rangle^2$. The quantity $\epsilon(\Delta) = \langle \pi^2(\Delta) \rangle - \langle \pi(\Delta) \rangle^2$ is the ergodicity breaking parameter introduced in [97, 129]. The vanishing of $\epsilon(\Delta)$ for large $\mathcal{T}/\Delta$ serves as a necessary and sufficient condition for ergodicity. Indeed, it fully characterizes the convergence of the ensemble of individual TA-MSD to its mean value, the TEA-MSD. Comparing the evolution of $\epsilon(\Delta)$ as a function of finite $\mathcal{T}/\Delta$ with an analytical expression will allow to verify that the ensemble of TA-MSD is ergodic on this finite sample.

One very appealing aspect of the quantity $\epsilon(\Delta)$ is that it can be analytically computed for an Ornstein-Uhlenbeck process. In its expression

$$\epsilon(\Delta) \equiv \langle \pi^2 \rangle = \frac{\left\langle \left(\overline{\delta_x^2}(\Delta) \right)^2 \right\rangle - \left\langle \overline{\delta_x^2}(\Delta) \right\rangle^2}{\langle \overline{\delta_x^2}(\Delta) \rangle^2}, \tag{3.6}$$

the first term is the ensemble average of the square of TA-MSD over the square of TEA-MSD

$$\langle \left(\overline{\delta_x^2}(\Delta) \right)^2 \rangle = \frac{1}{(\mathcal{T} - \Delta)} \int_0^{\mathcal{T}-\Delta} dt_1 \int_0^{\mathcal{T}-\Delta} dt_2 \langle (x_{t_1+\Delta} - x_{t_1})^2 (x_{t_2+\Delta} - x_{t_2})^2 \rangle \tag{3.7}$$

thats using Wick's theorem for a normal distribution as detailed in Appendix and the

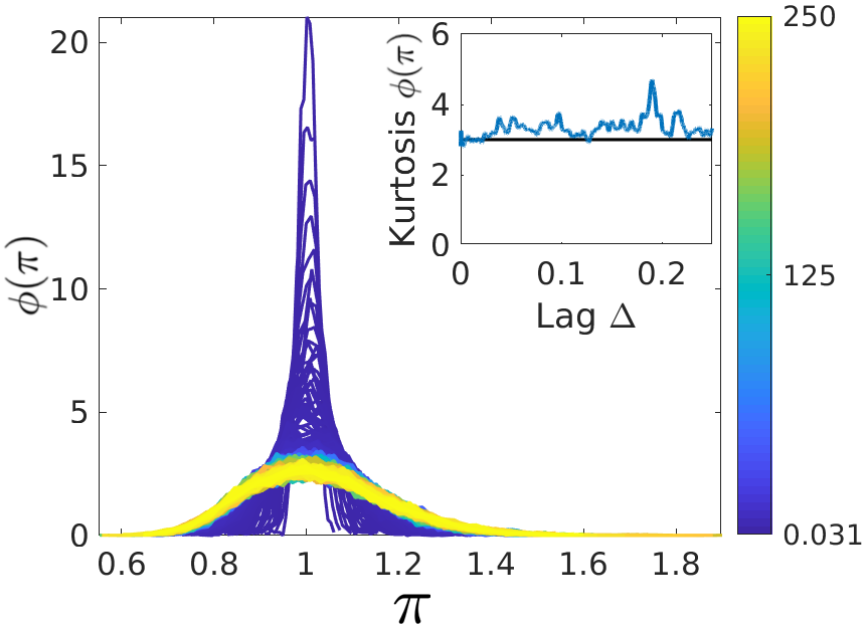

Figure 3.4: Probability distribution of TA-MSD. Each line from yellow ($\Delta = 250$ ms) to blue ($\Delta = 0.031$ ms) is the histogram of the ratio π between TA-MSD and TEA-MSD. Each line on this plot corresponds to a histogram of the TA-MSD along a vertical cut in Fig. 3.3 for different values of Δ. As expected, this distribution collapses to a Dirac distribution for small Δ, hence in the long $\mathcal{T}/\Delta$ limit. On the colorbar, the scale is Δ in milliseconds. In the inset, we plot the evolution of the kurtosis of the distribution of π as a function of the lag-time Δ. We observe that is stays close to the normal value of 3, validating the Gaussian nature of $\phi(\pi)$ for every time. the distribution can therefore be fully characterised by its second moment, the variance of π

stationary correlation function $\langle x_{t+\Delta} x_t \rangle = D\omega_0^{-1} e^{-\omega_0 \Delta}$ gives

$$\langle \left(\overline{\delta_x^2}(\Delta) \right)^2 \rangle = \frac{2D^2}{(\mathcal{T}-\Delta)^2 \omega_0^2} \int_0^{\mathcal{T}-\Delta} dt_1 \int_0^{\mathcal{T}-\Delta} dt_2 \Big(2e^{-\omega_0 |t_1 - t_2|} - e^{-\omega_0 |t_1 - t_2 + \Delta|} - e^{-\omega_0 |t_2 - t_1 + \Delta|} \Big)^2 . \tag{3.8}$$

As detailed in Appendix 8.5, we call I this variance of TA-MSD. By furthermore recalling that the TEA-MSD given by $\langle \overline{\delta_x^2}(\Delta) \rangle = 2D\omega_0^{-1}(1 - e^{-\omega_0 \Delta})$, we can write the ergodic parameter as

$$\epsilon(\Delta) = I \frac{D}{4\omega_0 (1 - e^{-\omega_0 \Delta})} \tag{3.9}$$

that can be explicitly calculated as done in Appendix 8.5.

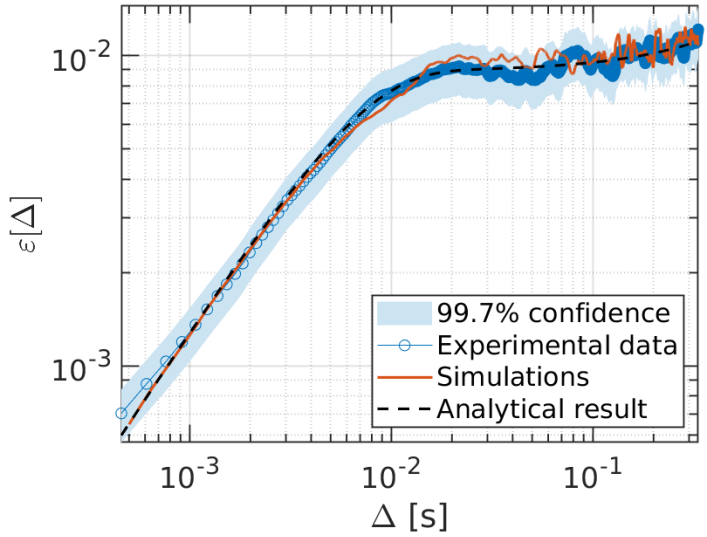

Figure 3.5: The normalized variance $\epsilon(\Delta)$ playing the role of an ergodic parameter is displayed for the Ornstein-Uhlenbeck process at play in our optical trap. Experimental results (blue open circles) for $\epsilon(\Delta)$ are compared to the theory (black dashed line) within a 99.7% confidence interval. We also show the results of a numerical simulation using $\mathcal{O}(3/2)$ algorithm (red continuous line). The slight deviation at short times between the experiment and the theory comes from two intertwined sources. (1) from the position tracking errors as discussed in appendix 8.7 and (2) to long-time drift as discussed below. In Sec. 3.1.5 we will show how the long-time drift can be quantified to correct this deviation.

On Fig. 3.5 we show the evolution of $\epsilon(\Delta)$, variance of the distribution $\phi(\pi)$ as a function of the time-lag Δ. We superimpose to the experimental results (blue circles) the analytical expression of Eq. (3.9) (black dashed line) as well as the result of numerical simulations (red line). The variance goes to 0 for small Δ as expected for an ergodic ensemble. This, together with the good agreement between experimental and analytical result over the whole bandwidth accessible to the experiment proves the ergodic character of the ensemble built from the sub-trajectories. We can use this ensemble of 1200 trajectories as an ergodic statistical ensemble of sub-trajectories and exploit is as such.

One can observe a smooth crossover between the long time-lag trapped regime and the short time-lag free-like diffusion, we probed in detail in [132] the linear increase of ϵ with Δ. The transition between both regimes is governed by the relaxation time of the trap ω_0^{-1}. Since $\epsilon(\Delta)$ is a variance, the quality of its estimator on a finite-size

ensemble is quantified using a χ^2-test. On Fig. 3.5, the error (shaded region) are the sum of systematic errors and this test up to a 3σ level of confidence.

The small deviation at short time-lag stems from two effects. The first, discussed in Sec. 3.1.2 is associated with the magnitudes of the displacement (measured here at ≈ 7.43 nm) that are so small that they can be dominated by small effects such as tracking errors (see 8.7). The second effect is more subtle. When computing $\epsilon(\Delta)$ we do measure the variance of the ensemble of TA-MSD. This ensemble being drawn out of a long time-series of position, the different TA-MSD correspond to different instants of time throughout all the 10 minutes of the experiment. A drift occurring during that 10 minute-long experiment, will necessarily induce an overestimation of the variance $\epsilon(\Delta)$.

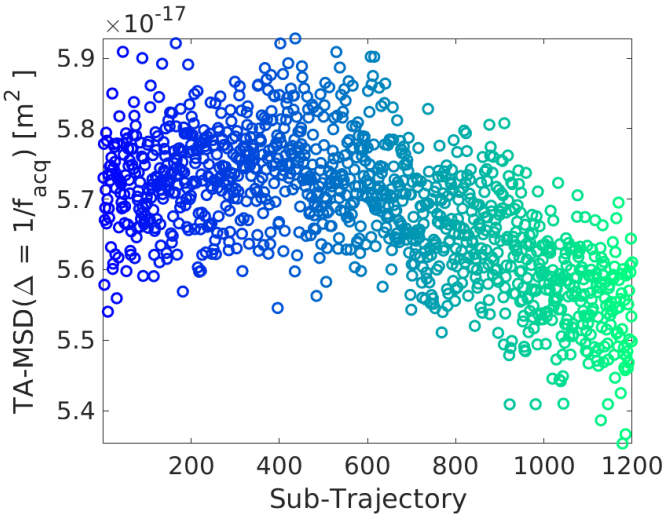

Figure 3.6: Cross-cut of the ensemble of TA-MSD for the shortest time-lag $\Delta = 1/f_{acq}$ unveiling a long time drift of the order of a nanometer between average displacements measured 10 minutes apart. The color coding corresponds to the time-ordered 1200 individuals TA-MSD.

On Fig. 3.6 we represent the ensemble of TA-MSD for the shortest time-lag $\Delta = 1/f_{acq} = 0.031$ ms (inverse of the acquisition frequency f_{acq}). It corresponds to a vertical cut of Fig. 3.3 (a) at the shortest Δ. As in the latter, the color coding corresponds to the 1200 individual and chronologically ordered TA-MSD. Therefore, the first blue circle corresponds to $\overline{\delta_x^2}(\Delta = 1/f_{acq})$ averaged over 0.5 s evaluated at the beginning of the experiment and the last green circle corresponds to the same quantity evaluated 599 s later. We can observe that the first half of the values are centred around a constant carrier as expected, whereas the second half is linearly de-

creasing. This clearly reveals a long-time drift of the experiment, where the measured value of the short-time displacement is evolving in time. This naturally leads to an overestimation of the variance of the TA-MSD at this time-lag Δ, as seen of the plot of the ergodic parameter $\epsilon(\Delta)$.

However, the value of this drift remains of the order of 1.31 nm of average displacement only. It therefore only affects the observables for very small magnitudes, and hence very short time-lag, as seen Fig. 3.5. This drift is visible only on very short time-lag and stems from differences of very long absolute times (above 2/3 of the total time as seen on Fig. 3.6), and will therefore not be captured by an Allan variance-based test of stability that, by definition, is a test performed at maximum on 1/2 of the total time as discussed in the next section.

The subtle comparaison of short time-lag displacement at very distant absolute experimental times appears as a precise tool to quantify drifts. This is necessary when deciphering between a physical ergodicity breaking from a spurious deviation, due to a drift in the experimental setup. In Sec. 3.1.5, we will quantify this drift in order to asses the ergodic nature of one trajectory, in contrast with the non-ergodic nature of another.

3.1.4 Study of the ergodic parameter

In this section we study more extensively the ergodic parameter ϵ both as a function of the lag-time Δ and as a function of the total time $\mathcal{T}$, an important parameter, since it determines TA-MSD. The data plot of Fig. 3.5 are the result of one specific choice of the total time of the trajectories $\mathcal{T} = 0.5$ s, this choice leading to an ensemble of size $N = 1200$. We can however verify that other choices are possible and that the ergodic nature of the trajectory is robust with respect to this choice.

On Fig. 3.7 (a) we represent the experimental and analytical ergodic parameter $\epsilon(\Delta)$ as a function of the time-lag Δ for different choice of the total time $\mathcal{T}$ ranging from 0.2 s to 5 s. We can observe a good agreement for all cases. Two aspects are modified when we increase the total integration time: first obviously the longer time-lag accessible for the observable increases but by the same token, the size of the ensemble decreases (from $N = 3000$ to $N = 120$), leading to a poorer definition of the variance with more fluctuations and a larger error for short time-lag. This does not however prevent the trajectory to follow the respective analytical trends and therefore to keep an ergodic character upon all the studied transformation (from a trajectory of length L to an ensemble of a N sub-trajectories of length L/N). This shows that one

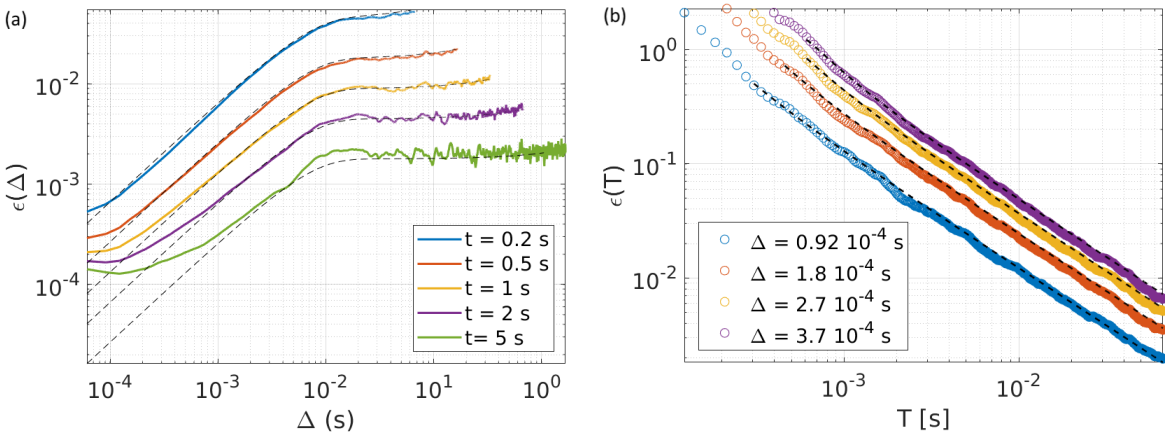

Figure 3.7: (a) Experimental ergodic parameter $\epsilon(\Delta)$ for different choices of the trajectories arrangements. Respectively we have, 3000 trajectories of 0.2s (blue), 1200 of 0.5s (red), 600 of 1s, 300 of 2s and 120 of 5s. (b) Experimental ergodic parameter $\epsilon(\mathcal{T})$ as a function of the total time $\mathcal{T}$ for different values of the lag Δ

long trajectory can serve to build various ensembles of different size and length, while keeping an ergodic nature.

The ergodic parameter ϵ can be represented as we just shown against the time-lag Δ for a fixed total time $\mathcal{T}$, but it can also be represented as a function of the time $\mathcal{T}$ for a fixed time-lag Δ as it is done in [129]. In that case it takes a simple $\epsilon(\mathcal{T}) \sim 1/\mathcal{T}^2$ dependancy as discussed in [129, 105]. Again, the choice of the fixed lag-time Δ is arbitrary. On Fig. 3.7 (b) we represent the ergodic parameter as a function of the total time for various choices of Δ ranging from $\Delta = 0.09$ ms to $\Delta = 0.37$ ms. We see a good agreement between the experimental data and the analytical result for every choice of Δ and for all $\mathcal{T}$. Again this equivalent representation of the ergodic parameter ϵ demonstrates the ergodic nature of the trajectory and show its robustness with respect to the choice of the transformation applied. This representation however misses to display the interesting crossover between free-like diffusion on small time to trapped-diffusion on long time as it is the case in the lag-time representation.

3.1.5 Example of ergodicity-breaking trajectories

In this section, we discuss an example of non-ergodic trajectories, characterized with the different observables introduced above. The trajectories under study are subjected

to a process of Stochastic Resetting (SR) [133, 80, 134, 135]. The principle of resetting it to let a Brownian object diffuse for a given time τ before reinitialising its position to a reference point in space x_0. If the reinitializing times form a stochastic sequence, i.e. if the resetting happens at random instants, then the trajectory is said to undergo a process of SR.

In a work still under preparation, we implemented an approximation of SR by swiching our optical potential from a very shallow trap to a very stiff trap at random times. The trap is kept shallow, $\kappa = \kappa_{min} = 2.9 \pm 0.15$ pN/µm for a random time τ and the particle diffuses in the potential. It is then abruptly increased to $\kappa = \kappa_{max} = 83.1 \pm 2.1$ pN/µm and the particle exponentially relaxes to a very small region of space $\sigma_x = \sqrt{k_B T/\kappa} = 7.04$ nm, mimicking a resetting event. The times τ are drawn out of an exponential law $P(\tau) \propto e^{-\lambda\tau}$ where $\lambda = 20\gamma/\kappa_{max} = 6.1$ ms is the resting rate. The time-series of positions x_t is recorded over 5 minutes and therefore subjected to a large amount of resetting events. To get closer to an ideal SR process, we remove the points from the time series x_t when the trapping laser in increased to κ_{max}. Those points corresponds to transient relaxation sequence and waiting times that we discarded to mimic an instantaneous resetting. The resulting trajectory is out of thermal equilibrium [136] and is theoretically known to break ergodicity [137, 138, 81]. Our tools allow us to demonstrate this experimentally.

In our experiment, we record a 300 second-long time-series x_t at an acquisition frequency of $2^{15} = 32768$ Hz. After removing the waiting times, we obtain a trajectory of ca. 239 seconds. This long trajectory can be cut and reassembled into a statistical ensemble of circa. 800 trajectories of 0.3 s as described above and illustrated Fig. 3.1; each individual trajectory contains many resetting events. We can compute the TA-MSD for each trajectory, the associated TEA-MSD and the standard EA-MSD.

On Fig. 3.8 (a), we show individual TA-MSD for the statistical ensemble of trajectories as well as the associated TEA-MSD and EA-MSD. Remarkably, TEA-MSD and EA-MSD still coincide, therefore the necessary condition for ergodicity $\langle \pi(\Delta)\rangle = 1$ is still satisfied. However, one can note that the dispersion of individual TA-MSD does not collapse to 0 for short time-lag as it was the case for standard Brownian motion in the previous sections (compare to Fig. 3.3). As a consequence, the necessary and sufficient condition for ergodicity on the variance $\langle \pi(\Delta)\rangle$ will not be satisfied. This is visible Fig. 3.8 (b) where the ergodic parameter $\epsilon(\Delta)$ is plotted as a function of Δ for both a normal trajectory diffusing in a potential (blue squares) and a trajectory experiencing SR (orange squares). The strong deviation of the SR process ergodic estimator from a decay to 0 for short time-lag Δ is the signature of the non-ergodic

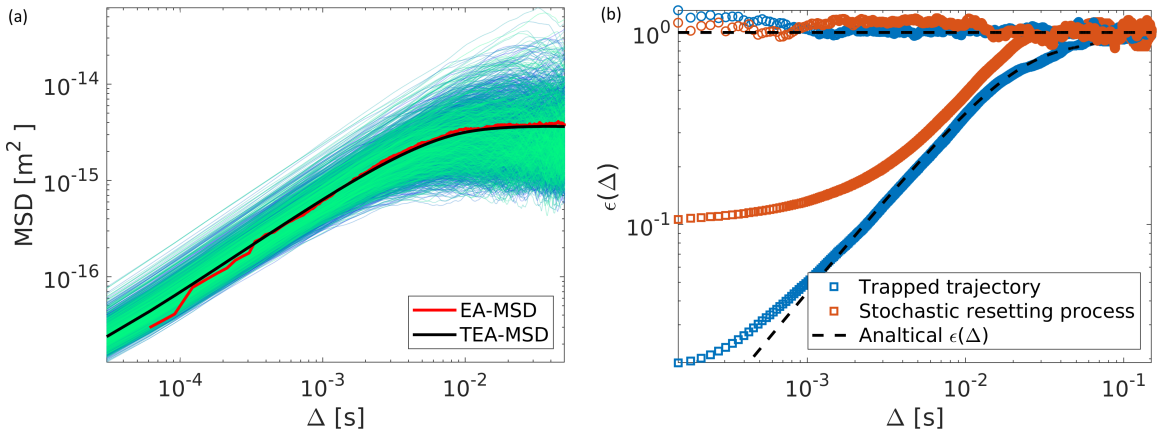

Figure 3.8: (a) Individual TA-MSD (blue to green) for each of the ca. 800 trajectories experiencing stochastic resetting, associated TEA-MSD (black line) and EA-MSD (red line) evaluated for the ensemble (b) We show there the necessary ergodic condition $\langle \pi(\Delta) \rangle = 1$ expected for both a standard trajectory in the optical trap with $\kappa = \kappa_{min}$ (blue circles) and also for a trajectory experiencing stochastic resetting in the same potential (orange circles). Together with this, we show the sufficient condition $\epsilon(\Delta)$ as a function of the time-lag Δ for both a standard trajectory in the optical trap (blue squares) and a trajectory experiencing stochastic resetting (orange squares). For the latter we see that the standard Brownian motion follows the expected behaviour on a large time-lag region, whereas the SR process strongly deviates, as a consequence of the non-vanishing dispersion of TA-MSD for large $\mathcal{T}/\Delta$. We note that the parameter $\epsilon(\Delta)$ deviates from the analytical curve also for the normal trajectory when looking at short time-lag Δ. We will show below, that this deviation is due to drift in the experiment, while the strong deviation visible for the SR process is a physically meaningful ergodicity-breaking.

nature of the trajectory under SR.

On Fig. 3.9 (a) we show the value of TA-MSD at $\Delta = 0.061$ ms from blue to green for each chronologically ordered sub-trajectory as a function of the absolute time of the experiment. It corresponds to a vertical cut in a TA-MSD plot such as displayed Fig. 3.3 (a). We can observe, superimposed to the expected dispersion a systematic evolution, that reveals a drift in the experimental setup. We fit the behaviour with a guess function $f(t)$, combination of negative constant slope and a slow sinusoidal oscillation. The fit gives the black continuous line on Fig. 3.9 (a) and is used to correct

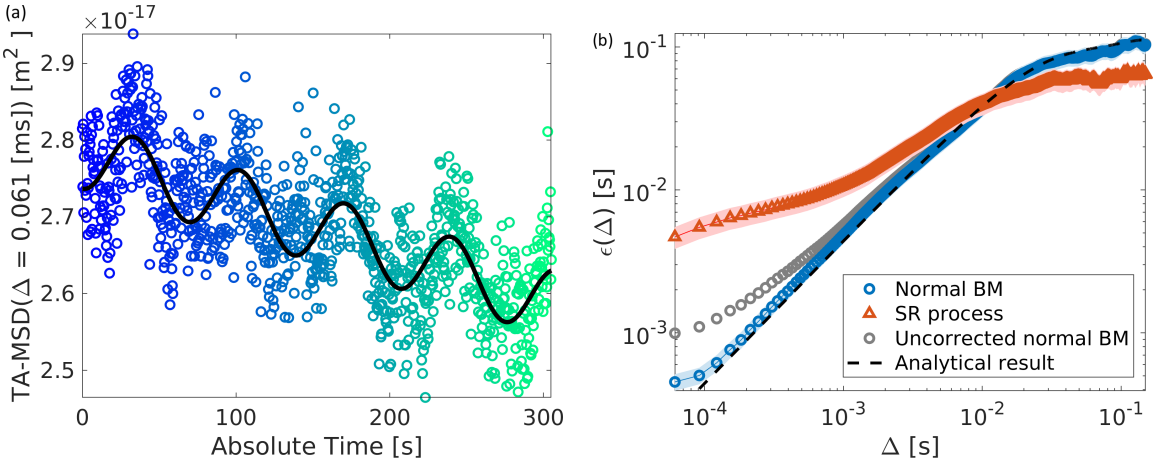

Figure 3.9: (a) Short time-lag TA-MSD $\overline{\delta^2_{x_i}}(\Delta = 0.061[\text{ms}]))$ for each individual chronologically ordered sub-trajectories as a function of the absolute time in seconds. We clearly observe a systematic trend, that is well captured by the combination of linear decrease and a ≈ 80 s sinusoidal evolution. The magnitude of the drift is of the order of 1.4 nm of mean displacement. (b) Associated ergodic parameter computed on a trajectory corrected by the fit of the 1.4 nm mean displacement drift on the 300 s. We show ϵ both for a normal Brownian motion in a potential of stiffness κ_{min} (blue circles) and for a SR process in the same potential (orange triangles). This method neatly corrects the deviation observed for the normal trajectory (the uncorrected $\epsilon(\Delta)$ for the normal trajectory is also displayed in grey), clearly reveals the difference between the ergodicity-breaking of the SR process and the error-induced deviation seen in the normal trajectory, that keeps its ergodic character.

as a function of time the calibration factor β used to convert the measured voltages into meter. We apply this (very small 1.4 nm mean displacement) correction to our experimental trajectory by replacing β by $\beta * \sqrt{f(t)}$ both for the normal trajectory and the SR process. Due to the small value of the correction, the resulting corrected trajectories are similar to the uncorrected ones on most observable (variance, probability distribution, MSD). Remarkably, when we compute again the ergodic parameter $\epsilon(\Delta)$, the short-time deviation of ϵ for the normal trajectory is neatly corrected, and falls back on the expected trend even for short time-lag Δ. The ergodic parameter for the SR process is almost unaffected by this correction, since its very strong deviation keeps it at a larger magnitude, un-sensitive to the drift. This ergodic test, complemented by this drift correction allow us to very neatly demonstrate the non-ergodic

nature of an SR process, while a normal trajectory in the same (but constant) optical trap is ergodic.

The example described in this subsection underlines the importance of both $\langle\, \pi(\Delta)\rangle$ and $\langle\, \pi(\Delta)^2\rangle$ approaches to ergodicity, enabling to unveil ergodicity breaking mechanism, as seen here with the example of an experimental SR process.

In the previous sections, we explored how to derive and apply an ergodicity estimator that yields both necessary and sufficient conditions for ergodicity. It can be analytically computed and experimentally measured and the excellent matching on all spectral ranges between theory and experiment and irrespective of the choice of the transformation (length of each sub-trajectory i.e. size of the ensemble drawn out of a single trajectory) applied to build the ensemble allow to clearly assess the ergodic nature of the trajectories recorded in our setup. It also allows to discriminate ergodic stochastic processes from non-ergodic trajectories such as demonstrated with the example of stochastic resetting. This test is central to our work, since it grounds the validity of our method chosen for building ensembles.

This being emphasized, a final aspect to be discussed, that still constrains the validity of the building of statistical ensembles, is the long-time stability of the experiment. Indeed stability is the necessary condition for stationarity of the process, which itself constrains the ergodic nature. Indeed, in the general case, ergodicity means that any trajectory of an ensemble is equivalent to all other (any observable will be the same for every trajectory if they are long enough). It is only in the stationary case that it takes the operative definition of convergence of time and ensemble averages, that we used to assess it experimentally. In the next section, we therefore asses the stability of our experimental setup on long times with an Allan-variance [139, 140] based test.

3.2 Allan variance and stability

In this section we present a stability test based on the Allan variance [139] that can be directly used at the level of our experimental trajectories and long integration times.

3.2.1 Temporal versus spectral property: Allan variance and power spectral density

In the previous chapter, observables like the autocorrelation function, power spectral density (PSD) and mean-square-displacement (MSD), led us to characterize the nature of the stochastic process at play. Namely, we verified its Brownian nature and the normal character of the diffusion within the short-time limit of the MSD. This is also encapsulated in the Lorentzian profile of the PSD which integral reveals the thermal nature of the noise through the fluctuation dissipation theorem. These properties are consequence of the dynamical equation driving the position x_t including the nature of the driving noise that stems from the thermal bath. With these observables, we verify the uncorrelated (*i.e.* white) nature of the thermal noise in our optical trap. However, the spectral analysis of the PSD as well as the relative time-lag analysis of MSD and autocorrelation are exposed to low frequency drifts [132, 114, 130] that can modify noise or trapping properties.

Therefore, another important characteristic that must be checked is the stability in time of the experiment. In order to draw physical conclusions from measurements that have been integrated (recorded) over long times, it is critical to demonstrate and verify that the white and thermal nature of the noise remains constant throughout this time, as well as the properties of the trapping potential. In this section we analyse the time-stability of the measured trajectories through an Allan-variance based test [139, 140], in continuation of previous work done in our group [86]. The strong difference of this approach with respect to a spectral analysis (over frequencies) or a displacement measurement (over time-lag) is that it is defined in the absolute time-domain and is able to reveal low frequency drifts within a stochastic signal. This allow us to verify unambiguously the stationary and thermally limited properties of the noise at play as well as the stability of the trapping potential properties in an experiment.

The Allan variance $\sigma^2(\tau)$ is defined as

$$\sigma^2(\tau) = \langle(\overline{y}_{k+n} - \overline{y}_k)^2\rangle \tag{3.10}$$

where the variable $\overline{y}_k$ at time $t_k = kdt$ is the time average of the displacement $\Delta x_t = x_{t+dt} - x_t$ on an interval of length $\tau = ndt$

$$\overline{y}_k = \frac{1}{\tau}\int_k^{k+\tau} \Delta x_t dt. \tag{3.11}$$

Here the displacement fluctuations Δx_t can be understood as analogous to the frequency fluctuation in the classical use of Allan variance on the stability of atomic

clocks [140]. The position of the Brownian object at a time t can thus be understood as the phase fluctuation of a clock. It is given by

$$x_t = \int_0^t \Delta x_s ds \tag{3.12}$$

and allows to rewrite the Allan variance as

$$\sigma^2(\tau) = \frac{1}{2\tau^2}\langle (x_{(k+2)\tau} - 2x_{(k+1)\tau} + x_{k\tau})^2 \rangle. \tag{3.13}$$

This quantity can therefore be expressed as a combination of correlation functions at different times. Conveniently, it can be connected to the noise PSD $S(f)$ through the following relation [140]:

$$\sigma^2(\tau) = \frac{4}{\pi\tau^2}\int_{-\infty}^{+\infty} S_x(f)\sin^4(\pi f\tau)df \tag{3.14}$$

and can therefore be explicitly evaluated analytically for the Ornstein-Uhlenbeck PSD $S_x(f)$

$$\sigma^2(\tau) = \frac{k_B T}{\kappa\tau^2}\left(4\left[1-e^{-\kappa\tau/\gamma}\right] - \left[1-e^{-2\kappa\tau/\gamma}\right]\right), \tag{3.15}$$

as detailed in Appendix 8.6 and in [114, 141].

3.2.2 Probing Allan variance on experimental data

We use the same 10 minutes-long experimental trajectory studied in the previous section and in Chap. 2 to apply the Allan variance based test.

On Fig. 3.10 we plot the Allan deviation (square root of the Allan variance) measured on the experimental trajectory. We superimpose the experimental data with the result of numerical simulations as well as the analytical result Eq. 3.15. From its definition, the Allan deviation can be evaluated at most on half the total acquired time, here 300 seconds. We can observe on the figure the very good agreement between the experimental data and both numerical and analytical results, showing the high level of stability over more than 6 decades in time, up to 300 seconds. This is emphasised on Fig. 3.10 where we show the long time limit of Allan deviation with the analytical result. We observe the fluctuations due to the smaller statistics of the averaging process for such long times, but still with a very close agreement of the experiments with the expected trend.

These data also reveal how the Ornstein-Uhlenbeck and the short-time limit of Wiener processes are characterized by different Allan variance signatures. Indeed, we identify on Fig. 3.10 two different asymptotic regimes. The short time regime

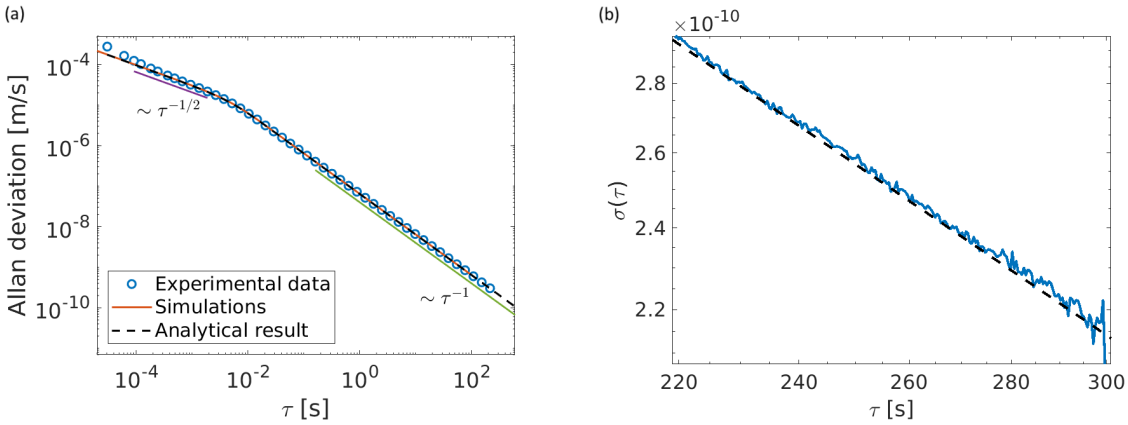

Figure 3.10: (a) Allan standard deviation evaluated for the long trajectory experimentally recorded (blue open circles). We plot the simulated Allan standard deviation (orange continuous line) superimposed to the analytical result (black dashed line). We highlight the slopes in both free (purple continuous line) and trapped regimes (green continuous line). We observe that the whole time range from $\sim 10^{-4}$ s up to 300 s is perfectly captured by the theoretical expression built with experimental parameters $-\gamma, T, \kappa$, – with a very high level of agreement. (b) Zoom made on the long-time limit of Allan standard deviation, showing thermally limited behaviour of the noise with no drift over all probing times.

($\omega_0^{-1} \ll \gamma/\kappa$) falls on the $\sigma_{\text{free}} \sim \tau^{-1/2}$ slope, which is known to corresponds to the thermal white noise limit of free Brownian motion [114, 132]. Interestingly, in the long time limit ($\omega_0^{-1} \gg \gamma/\kappa$) of the Ornstein-Uhlenbeck process where the trapping action dominates the motional dynamics, the Allan variance shows a different slope with $\sigma_{trap} \sim \tau^{-1}$. This change of signatures between the two regimes, accounting for the presence of the harmonic force field in the long time limit, is continuous and well captured by a single analytical expression Eq. 3.15. We observe a very good match between the experiments and theory in the transition between asymptotic regimes.

The stability shown in this section using the Allan variance-based test is key to access long experiments in well controlled condition. Such an access is central when using optical trap for weak forces measurement and more generally each time large statistics are needed.

3.3 Conclusion

The combination of an ergodic analysis with mean-square-displacements and a stability analysis with Allan variance, leads to characterize the nature of the noise and optical potential in our experimental setup and this through a wide spectral range. These tests are highly operative since they serve as rigorous ground for the methods involved in exploiting our platform to study the properties of controlled trajectories and for the other perspectives detailed in Chap 4 and 5. In addition, the application of these observables reveals the specific features of both the ergodic parameter and the Allan variance between the short-time free-like diffusion and the long-time trapped regime. The methodology proposed in our work is also relevant to many experiments involving Brownian systems coupled to non-thermal noise, and more complex environments [62] as discussed in Chap 4.

The tools presented in this chapter are more than mandatory verifications that assess the validity of our experimental method since they also reveal fundamental properties of the stochastic processes. In Sec. 3.1.5, the application of an ergodicity test to stochastic resetting process unveiled a non-ergodicity induced by a simple stochastic modulation of the potential. The demonstrated non-ergodicity is connected to other fundamental properties of the process. It is, for example, a necessary condition for memory processing [125], key aspect in information thermodynamics of microscopic stochastic systems. Experimentally probe the non-ergodic nature of a process can open new possibilities of applications, showing the vast range of consequences of the tests studied in this chapter. This is an example of how ergodicity is saying more than the possibility to build ensembles. Similarly, our Allan-variance based test is indeed providing a verification of the stability of the experimental setup over long time, but, by its slope, it also provides informations on the nature of the stochastic process at play.

Chapter 4

Bath engineering, active matter and information harnessing

4.1 Introduction

In the previous chapter, we explored how a noise and the statistical properties of a Brownian trajectory in an optical trap can be characterised. A strong emphasis was put on the Brownian, stable and ergodic nature of the trajectories but also on the verification of the Gaussian and white nature of the random force $\sqrt{2k_BT\gamma}\xi_t$ driving the process. This force stems from the thermal bath in which the bead is immersed and, even though we have a flexible control on the optical conservative forces $-\nabla V$ acting on the bead, the thermal forces are imposed by the environment. Yet many physical systems evolves in bath of different nature, or simply thermal baths with time varying parameters, *e.g.* temperature. For example biological systems at the micron scale experience a noisy environment, but the complexity of the surrounding medium [142] induces correlations in the noise, departing from a white nature.

The large field of active matter [143] deals with systems able to convert a source of energy into directed motion. These system typically exhibit non-Brownian diffusion [49, 63, 55] that is effectively well modelled by correlated noise bath [66, 144]. Active matter is intrinsically out-of-equilibrium, but quantifying and describing it with the tools of statistical mechanics has been challenged by an important theoretical work [145, 56, 119, 146, 61, 147, 148, 65, 58, 60, 149, 150]. Experimental studies with biological active matter [151, 98, 57, 152] are limited by the complexity of manipulating real living systems, restraining the range and flexibility of the experiments. Along this line, having an artificial way to engineer the properties of the bath for simple white noise [153, 154] or more complex noises [155, 156, 157, 27] is very valuable since

it does lead to test and explore the out-of-equilibrium nature of active matter with more flexibility and control. Such tuneable baths can allow one to act on the diffusive properties of the trajectories through ways that remain inaccessible by using solely conservative forces.

The aim of this chapter is to propose an optical method to couple to an optical trap an additional artificial bath whose properties can be dynamically chosen by the experimentalist. Using a secondary laser beam whose intensity is driven by an accousto-optic-modulator, we can act on the trapped microsphere through radiation pressure force. We use this force to exert on the sphere an external stochastic force F_{ext} that plays the role of an additional bath. The time-series building this stochastic force is generated numerically and therefore of arbitrary nature. We will mainly focus on the case of exponentially correlated noise, where the values of the force F_{ext} at two time instant t and s obeys $\langle F_{ext}(t)F_{ext}(s)\rangle \sim e^{-\omega_c|t-s|}$. We use this example of colored noise [158, 159, 66] as a minimal model to tackle the questions mentioned above on the non-Brownian and out-of-equilibrium properties of active matter.

In Sec. 4.2 we describe how to experimentally implement the external bath and control its properties as amplitude or correlations of the noisy forces. Following this optomechanical perspective, Sec. 4.3 focuses on the nature of the trajectories followed by the microsphere and how strongly it depends on the properties of the bath. The studied case of exponentially correlated Gaussian noise exhibits superdiffusion and breaks equipartition of energy, forbidding the definition of an effective temperature. Since the motional variance of the trapped micro-sphere depends on the color of the noise imposed, the latter can thus become a parameter used to make the system transient from on state to another. We therefore study color-driven protocols in Sec. 4.4. Finally, Sec. 4.5 focuses on the thermodynamic description of the out-of-equilibrium process and emphasizes the strong connexion with biological active matter. The fluctuation-dissipation theorem is studied via rheological measurement and the thermodynamic observables of the trajectories are computed. The heat released during a color protocol is shown to be generated by the informative content of the bath, revealing a robust connexion between energy and information. To further reveal the distance to equilibrium, an alternative representation of a colored-noise driven trajectory is given, considering the noise variable as an additional dimension and building a two dimensional pseudo phase-space. This description studied in Sec. 4.3.3 unveils the broken detailed-balance and net current associated with such colored noise, bringing to light the non-equilibrium nature of the process.

4.2 A secondary artificial bath

In this section, we experimentally show how the radiation pressure can be used for inducing an artificial bath with tuneable color, intensity and distribution.

4.2.1 Radiation pressure as an additional stochastic optomechanical force

Radiation pressure can act on the bead as a bath when it is injected as a stochastic time-dependant external force. Our experimental setup, shown on Fig.4.1 (the setup, appart from the radiation pressure is the same as detailed in Chap 2), is composed of a single 3µm dielectric bead harmonically trapped with a focused laser beam (785 nm, 110 mW). The bead is immersed in water at room temperature and undergoes Brownian motion due to the thermal fluctuations ξ. The fluid, as carefully explored in Chap. 3 is a thermal white noise, with no time correlation $\langle \xi_t \xi_s \rangle = \delta(t-s)$.

An additional radiation pressure force is applied using a second 800 nm high-power laser Spectra Physics Ti:Sa (model 3900s CW) tuneable laser, with a maximal output power of 5 W. The beam passes through an accousto-optic-modulator (AOM, Gooch and Housego 3200s). The first order diffracted beam, spatially selected, has its intensity depending on the acoustic wave in the cristal and therefore on the voltage sent to the AOM. This beam is sent to a telescope where the second lens can be precisely positioned in three dimensions. Since the role of the laser is to add an independent force, without trapping effects despite optical powers that can be comparable to the power of the trapping laser, the key point is to minimise the amplitude gradient in the vicinity of the bead. This can be achieved by focusing the laser in the back focal plane of the objective such that broad plane wave is transmitted through the objective. This leads to levels of transmission implying that measurable forces need high powers. Instead of this approach, we choose to send the laser as a thin light beam, that will concentrate the power on the bead. To avoid trapping, we use a lower NA objective and strongly underfill its entrance with the thin beam, to minimise focusing effect as much as possible. The role of the telescope is therefore to reduce the diameter of the beam, but also, with the precise x-y-z positioning of the second lens, to carefully tune the divergency of the beam. This control of the divergency allow us to position the focus of the laser inside the cell, and to make it coincide with the one of the probing 639nm laser. We will see in the following sections that the radiation pressure does not modify the trapping potential, by verifying for example that the corner frequency of the motional power spectral density of the trapped bead does not change when the

additional radiation pressure is injected inside the trap.

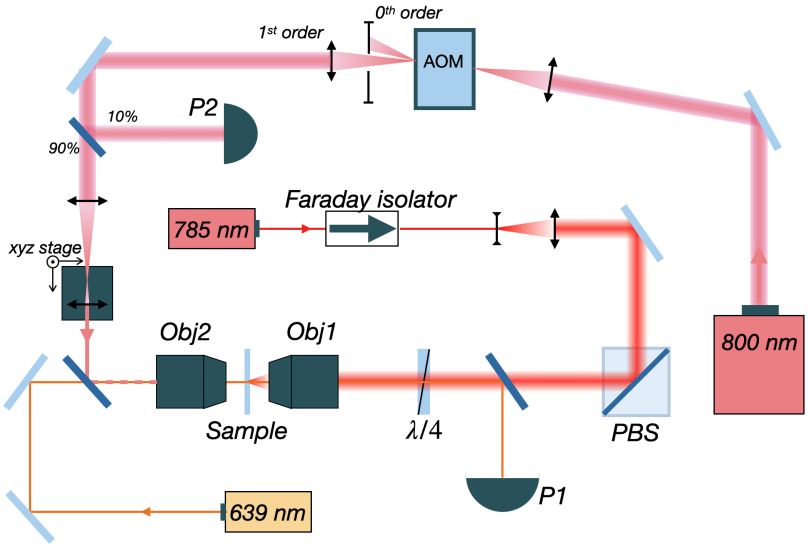

Figure 4.1: Schematics of the optical setup: the 785 nm trapping laser, drawn in red is optically isolated with a Faraday isolator, expanded with a telescope to overfill the input lens of the microscope objective Obj.1 (Nikon Plan-Apo VC, 60 × 1.20 Water Immersion) focusing the trapping beam on the bead. The radiation pressure in applied using the 800 nm beam, drawn in purple. It is focused into an AOM and then sent to a telescope to reduce its diameter and control its divergency, with a precise positioning of the output lens. The beam is sent in the trapped bead via a low-NA objective Obj.2 (Nikon Plan-fluo ELWD 60 × 0.70). A third low-power 639 nm laser is used as a passive probe to measure the instantaneous position of the bead: the light scattered by the bead is collected by Obj.1 and sent to a photodiode (Thorlabs Det10a).

The voltage of the AOM is controlled with a PYTHON code via a digital to analogue card (NI PXIe 6361). The signal generation procedure is detailed in the next section. Using this technique, any waveform that can be produced numerically can be send as an external force on the bead.

4.2.2 Noise modulation and active diffusion coefficient.

To play the role of a bath, the waveforms that we are interested in here are stochastic signals. Such signals stems from a noise η_t generated numerically with chosen properties. The signal is then processed following the sequence described in Fig. 4.2.

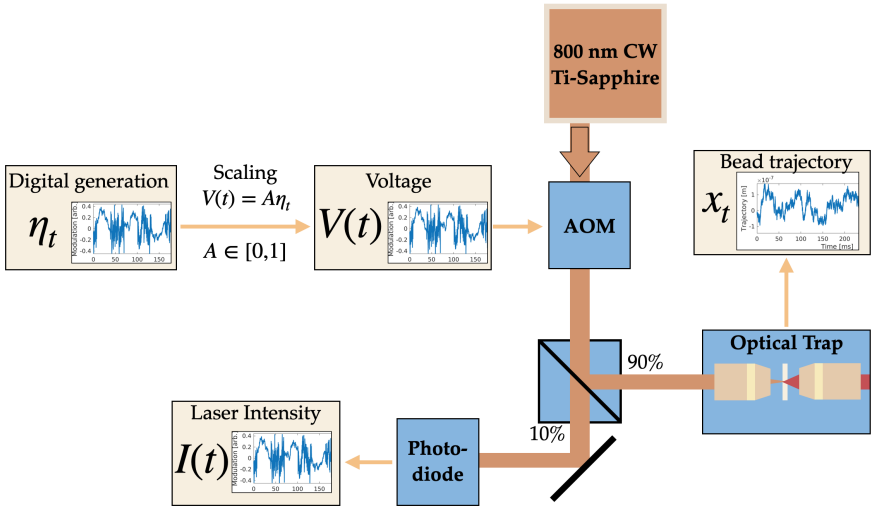

Figure 4.2: Schematic representation of the signal and data acquisition processing implemented in our experiments. The noise η_t is digitally generated, scaled to a voltage $V(t)$ that can be sent to the acouto-optic modulator (AOM), producing a diffracted beam whose intensity varies linearly with this input voltage. The laser beam diffracted through the AOM exerts a radiation pressure on the optically trapped sphere, whose position is recorded. A beam splitter sends 10% of the laser beam into a photodiode for monitoring and evaluateing the noise η_t as it enters the trap.

Its amplitude is scaled between 0 and 1V to fit with the input of the radiofrequency driver that drives the AOM. The AOM is calibrated by interpolating its response to a linear increase over its whole dynamical range with a polynomial function, which is then inverted and applied to the initial signal η_t to obtain a linear relation between the desired signal and the light intensity. The output beam is separated using a 90 : 10 beam splitter to probe and record its time trace $I(t)$ with the 10% arm. The 90% arm is sent into the optical trap as detailed in the previous section. This results in an external radiation pressure force that we denote $F_{ext} = F_0 + \delta F(t)$ centred around a mean value $\langle F_{ext} \rangle = F_0$ and with a fluctuating time dependant part $\delta F(t)$. This noise will then enter into the Langevin equation as an external random force field

$$\gamma \dot{x} = -\kappa x_t + \gamma\sqrt{2D}\xi_t + F_{ext}(t) \tag{4.1}$$

with κ the stiffness of the optical potential, $D = k_B T/\gamma$ the diffusion coefficient in the thermal bath, where k_B is Boltzmann's constant, T the fluid bath temperature and γ Stokes drag coefficient. The effect of the DC component of the external force F_0 is simply to shift the equilibrium position of the bead in the trap as described on Fig. 4.3.

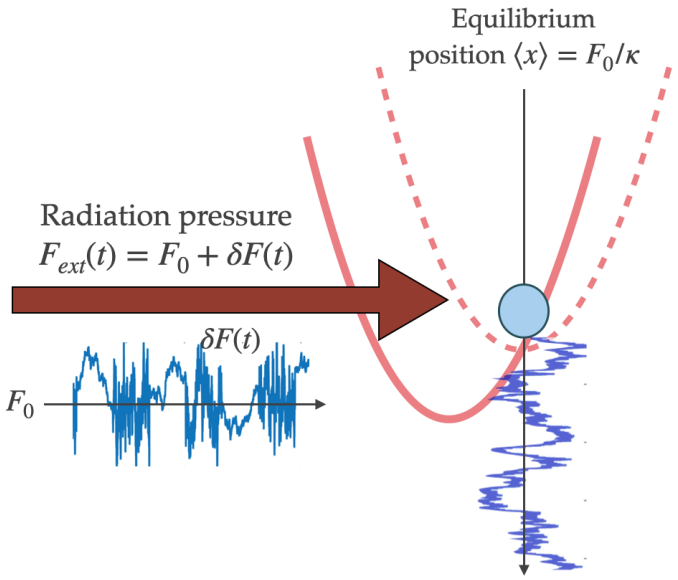

Figure 4.3: Effect of the external radiation pressure: the average position of the bead is shifted away from the center of the trap by F_0/κ. The bead fluctuates around this new equilibrium position under the influence of both the thermal bath $\sqrt{2k_BT\gamma}\xi_t$ and the fluctuating part of the radiation pressure $\delta F(t)$.

The magnitude of the force is kept small enough to maintain the bead in the linear response area of both the trapping and probing lasers. Therefore, the contribution of F_0 vanishes trivially when looking at the centered process $x_t - \langle x_t \rangle = x_t - F_0/\kappa$, which is always what happens in our experiments, due to the low-frequency filter.

Since we aim at treating the fluctuating part of the radiation pressure as a bath, we will write it in a more convenient form as $F_{ext}(t) = \gamma\sqrt{2D_a}\eta_t$, *i.e.* on the same footing as the thermal force $F_{th}(t) = \gamma\sqrt{2D}\xi_t$ where D is in m^2/s and ξ (the time derivative of a Wiener process) is in $\sqrt{\mathrm{Hz}}$. This leads us to introduce an *active* diffusion coefficient D_a having the same dimension as D, associated with the noise η_t. This choice for D_a gives to the noise a dimension $[\eta_t] = \sqrt{\mathrm{Hz}}$, just like the thermal noise term ξ_t. The word *active* is used to distinguish the "natural" diffusion due to the fluid thermal bath, and the additional "artificial" diffusion associated with the auxiliary bath. It will become clear when we will the study active matter with such an external noise.

4.2.3 The white noise case for the second bath

The noise that we generate is characterised by three parameters, *(i)* its amplitude $\sigma_\eta(t)$ *(ii)* its probability distribution $P(\eta, t)$ and *(iii)* its time correlation $\langle \eta_t \eta_s \rangle$. We obtain a

flexible system by keeping independent the amplitude and the correlation of the noise. The amplitude can be fixed by scaling to an arbitrary value the signal sent to the RF driver (as detailed on Fig. 4.2), but also by adjusting the power of the laser beam entering the AOM. The correlation depends on the mathematical generation of the noise.

A first instructive case is white noise. Such $\delta-$correlated noise $\langle \eta_t \eta_s \rangle = \delta(t-s)$ possesses a flat spectrum, where all frequencies are represented with an equal magnitude. It can easily be generated numerically with build-in random number generator that produces a series of independent random values between 0 and 1. The distribution of the noise can be chosen arbitrarily, since its consist in a series of independent and identically distributed random variable. By the virtue of the central limit theorem, it will induce a Gaussian distribution for the bead. Of course, this will be different when the noise is correlated. It should be noted that since the noise is generated with a finite generation frequency f_{gen}, its spectrum is flat over a finite bandwidth and its white character is valid only within this bandwidth. We use the PYTHON build-in random number generator provided by the library *Numpy*. To choose the generation frequency, we compromise between two contradictory needs. First, one needs to choose f_{gen} as high as possible to achieve the best possible white noise On the other hand, a very high f_{gen} means that a significant part of the optical power will be used in very high frequencies, where the bead does not respond, leading to an effective decrease of the amplitude of the noise on the useful bandwidth. By looking at the response of the bead, for example on its Lorentzian power spectral density, one sees that the response decreases rapidly after a few kHz. Around 10kHz the signal starts to be dominated by the electronic noise. We therefore choose to use $f_{gen} = 20$kHz to obtain a correct white character of the noise over the selected bandwidth while minimising the power loss at high frequencies.

The effect of such a well-behaved white noise should not be distinguishable from the effect of the thermal bath and should therefore simply lead to an increase of the variance of the bead response, without changing any other parameter. More precisely, the natural thermal noise $\sqrt{2D}\xi_t$ and the additional noise $\sqrt{2D_a}\eta_t$ can be recast in one single noise $\sqrt{2(D+D_a)}\theta_t$ where $\langle \theta_t \theta_s \rangle = \delta(t-s)$ is a white noise. The increase of variance can be described as an increase in kinetic temperature, defined through equipartition as $T_{kin} = \kappa \langle x^2 \rangle / k_B$. Hence an additional white noise can be used to control the temperature of the bead. The additional force, with its average and fluctuating components is bringing the microsphere in a non-equilibrium state, displacing its position from the bottom of the potential well and increasing the width of its probability distribution by a constant feed in energy. However, in this simple white noise

case, the two noises combine in an effective temperature and the system can still be described with the tools of equilibrium states [153].

In the next section, we will turn to a colored noise, where the temporal correlation can take arbitrary values. While in this case the tools of equilibrium statistical mechanics cannot be used anymore, the constrains that we detailed for white noise related to the generation frequency still hold to obtain the desired correlation on the used bandwidth.

4.3 Exponentially correlated Gaussian noises

In this section, we focus on exponentially correlated Gaussian noises [160, 56, 142]. Such noises are characterised by an exponentially decaying correlation function and can serve as a minimal model for memory or persistence effects, in strong connection with biological matter [151, 98, 66, 60]. Using radiation pressure to engineer an additional bath, we study the statistical mechanics properties of trajectories driven by exponentially correlated noise. We derive and measure useful observables and analyse their deviations from standard Brownian motion at thermal equilibrium.

4.3.1 Colored noise as a solution of a numerical Ornstein-Uhlenbeck process

Exponentially correlated noise has the same mathematical structure as a standard Brownian motion in an optical trap, where the correlation time ω_c^{-1} is connected to a virtual "stiffness" and "viscosity". This colored noise [159, 158] can therefore be generated as the solution η_t of the Ornstein-Uhlenbeck process

$$d\eta_t = -\omega_c \eta_t dt + \sqrt{2\alpha\omega_c} dW_t, \tag{4.2}$$

where ω_c is the inverse correlation time of the noise, $\sqrt{\alpha}$ is its amplitude (the variance of such a process is $\langle \eta_t^2 \rangle = \alpha$) and dW_t is a Wiener process. We will refer to it as Ornstein-Uhlenbeck noise, or OU-Noise for now on.

An important asset of our work is the flexibility of our scheme for controlling the color and the amplitude of the noise, which demands to keep ω_c and α independent. This is different from the choice made in [98] for instance, where α scales as the square root of the inverse correlation time of the noise. The latter choice necessarily induces an interplay between both correlation times and amplitudes that we precisely want to avoid for reasons that will be clear below. In our experiments, this noise is obtained by simulating numerically Eq. 4.2 in PYTHON with time-step $dt = 1/f_{gen} = 50\mu s$, scaling

and sending it to the AOM, as previously detailed. This numerically generated noise is thereby encoded into a radiation-pressure force sent to the bead. The incoming beam intensity acting on the bead depends both on the gain of the AOM-diffracted beam and on the choice of the radiation-pressure laser intensity. Furthermore, the actual amplitude of the force experienced by the bead depends not only on this radiation-pressure laser intensity but also on the optomechanical coupling between this laser beam and the trapped sphere It will be taken into account in F_{ext} via the active diffusion coefficient D_a. Choosing $\alpha = 1$ as the simplest option simply means that the optomechanical coupling is entirely "incorporated" in D_a. However, we keep the α term for clarity, as a purely dimensional constant.

As OU-noise has the same structure as a trapped Brownian motion it is defined by the same Gaussian distribution $P(\eta) = e^{-\eta^2/2\alpha}/\sqrt{2\pi\alpha}$ and exponential correlation function $\langle \eta_t \eta_s \rangle = \alpha e^{-\omega_c|t-s|}$.

It is also characterised by the same Lorentzian spectral profile that we can derive by Fourier transforming Eq. (4.2)

$$-i\omega\eta[\omega] = -\omega_c\eta[\omega] + \sqrt{\alpha\omega_c}\xi[\omega] \tag{4.3}$$

taking the squared norm leads to the active noise power spectral density (PSD)

$$S_\eta(\omega) \equiv \eta[\omega]\eta^*[\omega] = \frac{\alpha\omega_c}{\omega_c^2 + \omega^2}. \tag{4.4}$$

with a corner frequency of $f_c = 2\pi\omega_c$ separating a low-frequency flat (white) part from a high-frequency $1/\omega^2$ part.

Fig. 4.4 displays we show the spectrum of the resulting fluctuations of the laser intensity before it enters the microscope objective, both for a white noise and an OU-noise. We can observe the flat spectrum of the white noise over the desired bandwidth, as well as the Lorentzian profile of the colored noise.

Colored noise can be considered as almost white for large (but finite) ω_c. Indeed, the low frequency part of the colored noise being flat one can retrieve an almost white noise by increasing ω_c. As we shall see later on the bead response, the effect of a colored noise with ω_c of the order of 10 kHz can hardly be distinguished from the one of a white noise. However, our choice of keeping ω_c and α independent forbids to take formally the limit of $\omega_c \to \infty$ as a usable white noise limit. Indeed, keeping a constant variance α, means that the integral of the spectral density does not changes when the cutoff pulsation increases. As a consequence the amplitude of spectrum on finite bandwidth decreases as one increases ω_c and in the limit, an infinite ω_c leads to

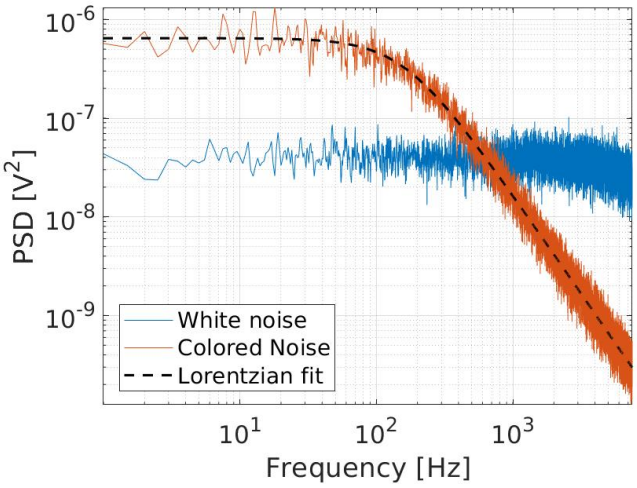

Figure 4.4: Power spectral density of the noise η_t sent to the bead. The blue curve corresponds to a white noise, with $f_{gen} = 20$ kHz, its spectrum is flat throughout the whole studied bandwidth as expected, with a slight decrease at frequencies ~ 10 kHz as the signal approaches the generation limit. The red curve is an exponentially correlated Gaussian noise with a corner frequency $\sim 10^2$ Hz along with a Lorentzian fit $\propto 2\pi f_c/(f_c^2 + f^2)$.

a zero amplitude. Therefore it is crucial to keep in mind the limits imposed on the finite bandwidth when taking limits.

4.3.2 Non-Brownian trajectories x_t

The noise generated numerically is injected onto the bead as previously described. The sphere subjected to this additional noise obeys to the stochastic process

$$dx_t = -\omega_0 x_t + \sqrt{2D}\xi_t + \sqrt{2D_a}\eta_t \tag{4.5}$$

where $\omega_0 = \kappa/\gamma$ is the inverse relaxation time of the sphere in the trap. We have $\langle \xi_t \xi_s \rangle = \delta(t-s)$ and $\langle \eta_t \eta_s \rangle = \alpha e^{-\omega_c |t-s|}$. In the following experiments, we use an average optical power for the 800 nm pushing laser ranging from 10^1 to 10^2 mW and correlation times ω_c^{-1} ranging from 0.1 to 100 ms. The fluid is considered to be at room temperature, varying between 296−298 K for the different experiments, but varying less than a degree during a given experiment. We use polystyrene microspheres, with a radius of 3 µm (Duke Scientific Corp. 3 µm) leading to a drag coefficient $\gamma = 2.699 \times 10^{-8}$ kg/s. The trapping stiffnesses κ range from a few to a few tens of pN/µm, leading to relaxation times $\omega_0^{-1}$of the order of the ms. This means that the noise correlation ω_c^{-1} can be both smaller or larger than the sphere relaxation time

ω_0^{-1}, allowing us to probe various regimes of correlation. The trajectory of the bead is recorded at an acquisition frequency of $2^{15} = 32768$ Hz following the procedures presented in Chap. 2.

We want to asses the nature of these trajectories. To do so, we analyse, as in Chap. 2, the diffusivity, correlation and spectral properties of the trajectories. Measuring the power spectral density, autocorrelation function and Mean-Square-Displacement (MSD) of the trajectories under a colored noise and under a white noise of the same amplitude, leads to discriminate the effects of the color only. Indeed, we expect the trajectories subjected to a white noise to behave "normally", namely, with only a change in amplitude of the different observables but no change of nature (*e.g.* time or frequency dependance and scaling). In other words, these trajectories can be described with the tools of Chap. 2 with a higher effective temperature (or effective diffusion coefficient D_{eff}). To contrast, the data driven by a colored noise of same amplitude yields different features for all the aforementioned observables, this discrepancy being solely due to the correlation of the noise.

We present here the theoretical results for PSD, autocorrelation and MSD evaluated with a colored noise, and the corresponding experimental data. The solution x_t of Eq. 4.5 can be obtained using Laplace transform (see details in Appendix 8.8).

$$x(t) = x_0 e^{-\omega_0 t} + \int_0^t \left(\sqrt{2D}\xi_{t'} + \sqrt{2D_a}\eta_{t'}\right) e^{-\omega_0(t-t')} dt'. \tag{4.6}$$

The additional noise η_t enters the equation similarly to the thermal noise, but with a non-δ correlation. It induces an additional memory kernel in the integral of the right-hand-side of Eq.(4.6). By Fourier transforming Eq. 4.5 as detailed in Appendix 8.9 and using the Lorentzian spectrum of η, the PSD of the bead position writes

$$S_x(\omega) \equiv x[\omega]x^*[\omega] = \frac{1}{\omega_0^2 + \omega^2}\left(2D + \frac{2D_a\alpha\omega_c}{\omega_c^2 + \omega^2}\right) \tag{4.7}$$

that clearly departs from a simple white noise-driven Lorentzian profile. We show on Fig. 4.5 the measured PSD for both a white noise and colored noise driven trajectory, with $T = 296$ K, $\omega_0^{-1} = 1.2$ ms. The correlation time of the colored noise η_t set to $\omega_c^{-1} = 1$ ms.

Both experimental data are fitted with the according theoretical result. We use a standard Lorentzian for the white noise driven trajectories (see Chap 2 Eq. 2.24), leading to an effective diffusion coefficient $D_{eff} = 0.29$ µm^2/s (while the thermal diffusion coefficient at room temperature is $D = 0.16$ µm^2/s). The colored noise driven spectrum is fitted with Eq. 4.7 keeping $D = 0.16$ µm^2/s, leading to $D_a = 1.44$ µm^2/s.

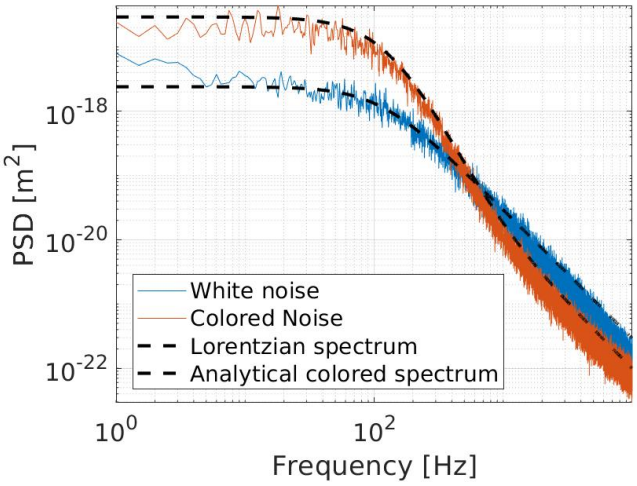

Figure 4.5: Motional PSD $S_x[\omega]$ plotted as a function of the frequency for the white noise driven process (blue) and the colored noise driven process (red) along with the associated theoretical PSD (black dashed curves).

We clearly observe the non-Lorentzian profile of the latter spectrum, with a slope higher than $1/f^2$ after the corner frequency.

The autocorrelation function of the position $C_{xx}(\Delta) \equiv \langle x_{t+\Delta} x_t \rangle$ can be computed from the spectrum via the Wiener-Khintchine theorem, as detailed in appendix 8.9, leading to

$$C_{xx}(\Delta) = \frac{D}{\omega_0} e^{-\omega_0 \Delta} + \frac{D_a \alpha \omega_c}{\omega_0(\omega_c^2 - \omega_0^2)} \left(e^{-\omega_0 \Delta} - \frac{\omega_0}{\omega_c} e^{-\omega_c \Delta} \right) \tag{4.8}$$

Finally the MSD can be computed from the autocorrelation and the variance as $\langle \delta x^2(\Delta) \rangle = \langle (x_{t+\Delta} - x_t)^2 \rangle = 2\langle x_t^2 \rangle - 2C_{xx}(\Delta)$ in the stationary regime, leading to

$$\langle \delta x^2(\Delta) \rangle = \frac{2D}{\omega_0} \left(1 - e^{-\omega_0 \Delta}\right) + \frac{2D_a \alpha \omega_c}{\omega_0(\omega_c^2 - \omega_0^2)} \left(1 - e^{-\omega_0 \Delta} - \frac{\omega_0}{\omega_c}(1 - e^{-\omega_c \Delta}) \right). \tag{4.9}$$

Both quantities are evaluated experimentally in the same condition as the PSD, for white noise and colored noise driven trajectories, and are fitted with the theoretical corresponding expressions. We show on Fig. 4.6 (a) the normalised autocorrelations with a good agreement with the fits, where again diffusion coefficients are the only fitting parameters. We note the longer lasting correlations of the colored noise driven trajectories, that also depart from a simple exponential decay while still decaying to zero correlation for long times

On Fig. 4.6 (b) we show the MSD in both cases, where again good agreement with the fits can be observed. The short-time limit of MSD can be used to asses the diffusive

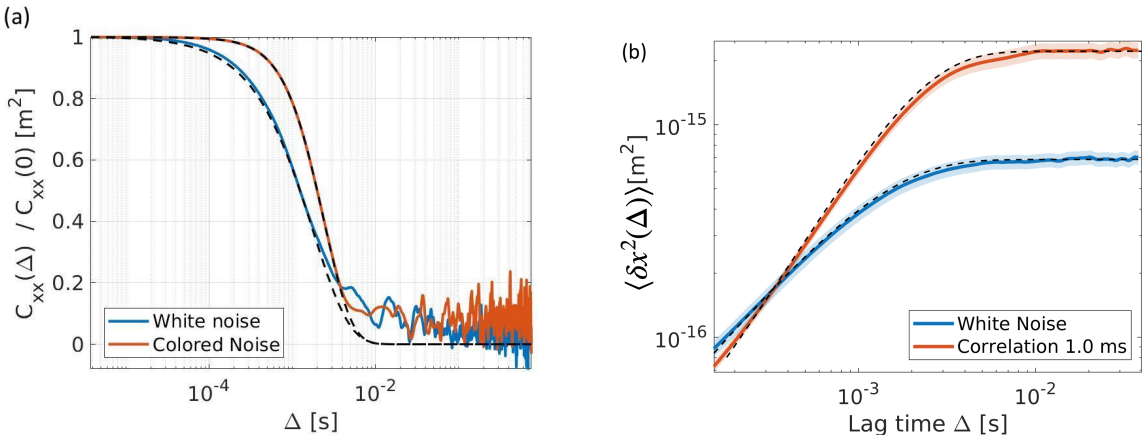

Figure 4.6: (a) Autocorrelation function $C_{xx}(\Delta) = \langle x(t+\Delta)x(t) \rangle$ plotted as a function of the lag Δ for the white (blue curve) and colored (red curve) noise driven processes both with physical parameters $T = 296$ K and $\omega_0^{-1} = 1.2$ ms and normalised to the zero-delay $\Delta = 0$ correlation function $C_{xx}(0)$. The theoretical expressions derived in appendix 8.9 are displayed as dashed black curves for both cases. (b) Mean square displacement measured experimentally for a white noise added to the existing thermal fluctuations inside the fluid (blue line), showing a short-time diffusive limit, and a correlated noise with $\tau_c = 1$ ms (red line), yielding a short-time superdiffusive limit; the superimposed dashed lines are the MSD expected from theory, with a Ornstein-Uhlenbeck MSD evaluated for the white noise case and the modified MSD in the correlated-noise case. The shaded regions accounts for the uncertainties associated with the fitting error in determining ω_0 and the systematic error in the sphere radius determination.

nature of the process. Indeed for small enough time-lag Δ, the bead does not respond to the trapping potential and explores the available space inside the trap according to the free diffusive motion $\langle \delta x^2(\Delta) \rangle \sim \Delta^\beta$, with $\beta = 1$ for normal diffusion and $\beta \neq 1$ for anomalous diffusion [96, 115]. We can observe on Fig. 4.6 that the white noise driven trajectories are undergoing normal diffusion, by fitting the short-time limit, obtaining an MSD $\sim \Delta^{0.94}$. On the other hand, the colored noise driven trajectories clearly shows a superdiffusive short-time limit, with $\sim \Delta^{1.5}$. The superdiffusivity of a Brownian object subject to an exponentially correlated noise was observed with a colloid suspended in a fluid saturated in *E. coli* bacteria [98]. However, in this biological example, the experimental contrains limited the flexibility and control to study the influence of the correlation time of the noise ω_c^{-1} on superdiffusion and the

deviation to equilibrium-like behaviour are small. To contrast, in the section 4.3.4 we extensively observe the importance of the value of ω_c^{-1} with respect to the relaxation time ω_0^{-1}.

4.3.3 Alternative representation of the trajectories

In the previous section, we explored the non-Brownian nature of the trajectories x_t, subjected to correlated noise. An alternative approach [66] is to consider the colored noise η_t as a genuine variable, on the same footing as the position x_t. Eq. 4.5 and 4.2 are a couple of differential equation, and the vector (x_t, η_t) describes the evolution of this coupled system. The advantage of this method is to recover a couple of white-noise baths, driving the evolution of the two variables, that becomes Markovian again. The idea of increasing the number of dimension to recover Markovian dynamics was already suggested by Uhlenbeck in [161].

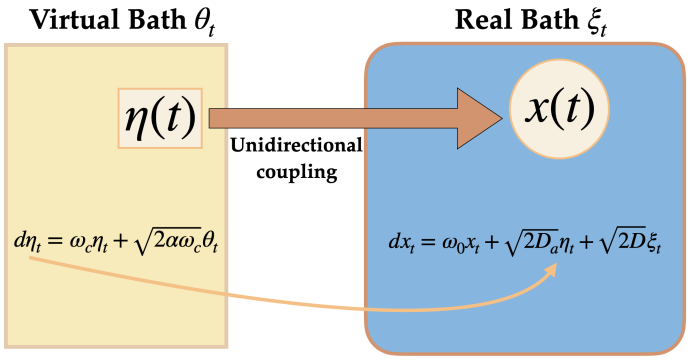

Figure 4.7: Schematic view of the system considered : x and η are now considered as two variables, immersed in two different δ-correlated baths. Furthermore, the two systems are coupled in an asymmetrical way since x depends on η but the reverse is not true.

On Fig. 4.7 we schematize this alternative representation of the problem: x_t and η_t are two random processes, driven by two independent white noise baths ξ_t and θ_t respectively. Both equations are coupled in a unidirectional way by the term $\sqrt{2D_a}\eta_t$ in the equation for x_t. As shown in [67] non-reciprocal systems are inherently out-of-equilibrium, with breaking of detailed-balance condition, fluctuation-dissipation relation and non-vanishing steady-state currents. Because of the unidirectional coupling, studying the system in the (x_t, η_t) space vividly reveals the non-equilibrium nature of the process, by showing net currents and detailed-balance violation. As shown in [69], the probability density for (x_t, η_t) in steady-state takes is Gaussian both in x and η

projections, but with a cross term correlating the two variables, giving an elliptical shape to the probability densities in 2D-space. The ellipticity is proportional to $1/\omega_c$ and grows with increasing correlation in the noise; it disappears for white noise.

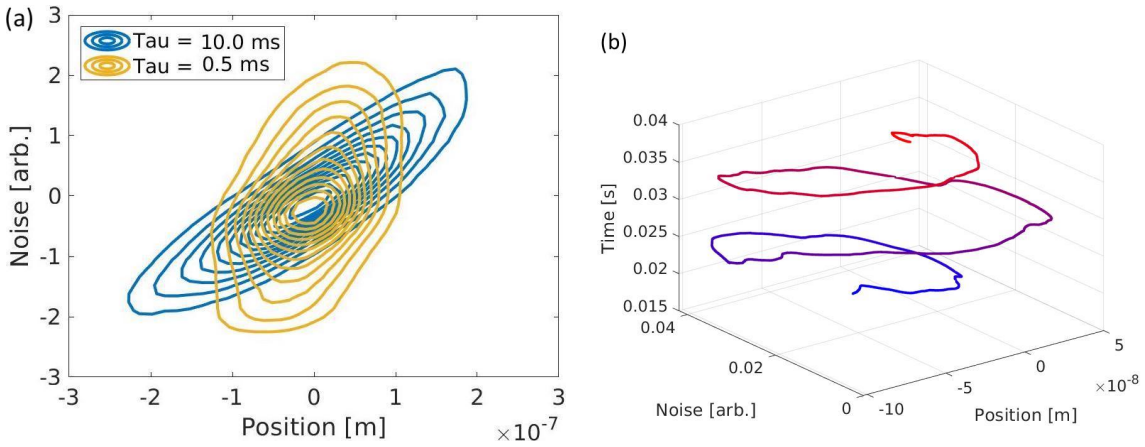

Figure 4.8: (a) Experimental (x, η) parameter space stationary distributions for the colored-noise driven trajectory with different correlation time, from almost white (blue line) to strongly colored (yellow line). (b) moving-average smoothened trajectory $\{x_t, \eta_t\}$ in the (x, η) parameter space (with time on the vertical axis) for a colored-noise driven process ($\omega_c^{-1} = 1$ms) showing a net rotation, unveiling the broken detailed-balance condition.

On Fig. 4.8 (a) we represent two steady-state distributions for almost white noise ($\omega_c^{-1} = 0.5$ ms) and strongly colored noise ($\omega_c^{-1} = 10$ ms). We can make several observations: *(i)* as we choose $\langle \eta^2 \rangle = \alpha$, we ensure a constant input noise variance, this is visible by the constant width of the distributions on the noise axis; *(ii)* the marginal variance along the position axis in increasing with ω_c^{-1}, as a consequence of the increasing mechanical coupling, as studied in more details in Section 4.3.4 and 4.4.2 *(iii)* the ellipticity of the distributions is increasing with correlation time ω_c^{-1}.

Furthermore, as studied in [66, 67, 69], the unidirectional coupling between x_t and η_t induces a non-vanishing probability current in the two dimensional space. This current, necessarily rotational, since it does not exist in the one-dimensional x-space, is visible by plotting a smoothed trajectory in (x_t, η_t)-space, as shown Fig. 4.8 (b). This is revealing the broken detailed balance [69] in this space: the jump-probability connecting two arbitrary points (x_t, η_t) and (x'_t, η'_t) is not equal to its time-reversed twin $P(x, \eta \mid x', \eta') \neq P(x', \eta' \mid x, \eta)$ if there is a net current.

However, this signature of non-equilibrium is not a direct consequence of the colored nature of the process η_t, it is only due to the asymmetrical coupling between both equation. In the case where η_t is a white noise, the same currents exist and the resulting trajectories x_t are out-of-equilibrium. The main difference between white and colored noise is therefore not the equilibrium nature of the joint-process: we know that even a white noise drive is still maintaining the system in a NESS, but this one can, in the x-space, be described with the tools of equilibrium states (with and effective temperature) which is impossible for colored noise.

This alternative description allows to get insight on the mathematical process and how the coupling between stochastic processes induces non-equilibrium properties. However in most experimental cases the stochastic process η_t is not accessible, as for example when it stems from the many collisions of a passive tracer with surrounding bacterias [98]. In that case, one cannot build a bi-dimensional space, and the "physical" process remains solely x_t, driven by a colored noise. In the next sections, we therefore go back to this framework, where the non-equilibrium nature of the process will appear through other observables.

4.3.4 Exploring the effect of correlation time: from almost white to strongly colored noises

Our flexibility regarding the color of the noise allows us to explore the effect of the correlation time from 0.1 to 50 ms one the trajectories of the trapped bead. We monitor the corresponding modification on the bead dynamics using the MSD of the trajectories.

On Fig. 4.9 (a), we show the power spectral densities of different noises, from white to strongly colored noises. The blue curve in Fig. 4.9 (a) corresponds to a white noise generated over the desired bandwidth where we see its flat spectrum covering all the response region of the bead, up to the 20 kHz limit of the generation sampling frequency. The other curves are the different colored noises, with correlation times spanning from 0.1 ms (orange line) to 50 ms (deep red line).

On Fig. 4.9 (b), we show the mean squared displacement (MSD) associated with each noise. The black dashed line shows the DC case with $F_{ext} = F_0$ where no noise is added. The blue curve corresponds to the white noise drive (blue spectrum of Fig. 4.9 (a)). It is similar to the thermal MSD black dashed line, but with a higher amplitude, as a consequence of the increase in effective temperature. The orange curve gives the first colored noise case, with correlation time $\omega_c^1 = 0.1$ ms (orange spectrum of Fig.

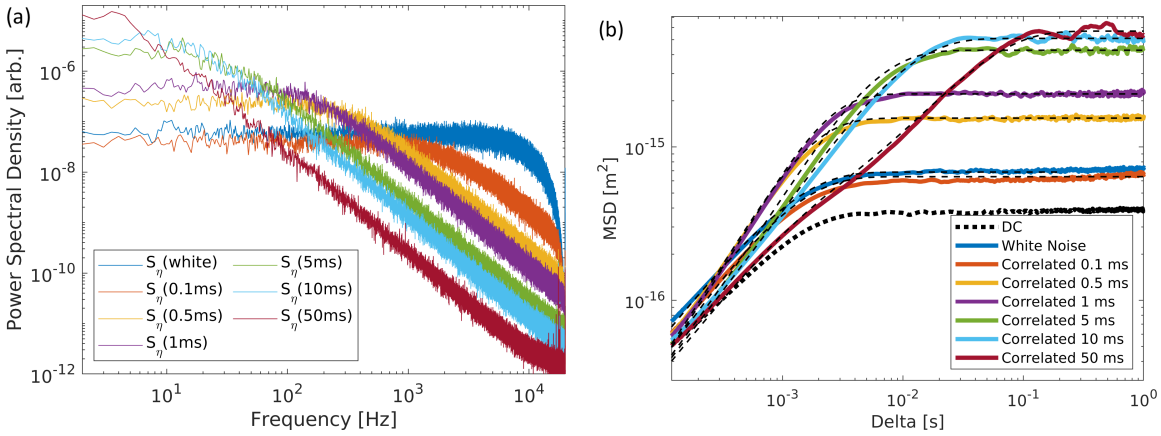

Figure 4.9: (a) Power spectral density associated with different noises η_t (for each colored curves, the corresponding correlation time is indicated within brackets in the legend). These spectra are measured directly from the laser intensity signal that is sent on the trapped bead as a radiation pressure. (b) Mean squared displacement of the sphere for each of the noises presented in panel (a). The DC case corresponds to the absence of additional noise, with $F_{ext} = F_0$. We observe that the white noise case and the first colored noise case (correlation time 0.1ms) are almost identical. Superimposing the fit performed with the analytical expression for the mean squared displacement enables one to extract the active diffusion coefficients D_a for each case.

4.9 (a)). We can note that this response is similar to the response to white noise : this colored noise is almost white considering that its correlation time falls off the bead's response bandwidth. Hence, longer correlation time $\omega_c^1 > 0.1$ ms are needed to make a clear difference between the white and colored cases (as seen for the next colored noise with correlation time 0.5 ms). The other curves are the MSD corresponding to the different noises of Fig. 4.9 (a). We can note that for strongly colored noise, the MSD takes a complex shape, where two time-scales characterising the problem starts to be visible. See on the purple line for $\omega_c^{-1} = 50$ ms for instance, we can see two inflections around 1 ms and ≈ 50 ms, corresponding respectively to the bead's relaxation time $\omega_0^{-1} = 1.2$ ms and the correlation time ω_c^{-1} of the noise.

The flexibility on choosing correlation times while preserving a good agreement between experimental data and theory allows us to study various regimes, departing from normal Brownian motion. This possible discrepancy with standard Brownian motion is connected to the out-of-equilibrium nature of the process, and it increases as the distance from equilibrium increases [56]. We will see later when looking at the

connexion to active matter, that this control of distance to equilibrium allows us from witness when and how the laws governing equilibrium states break.

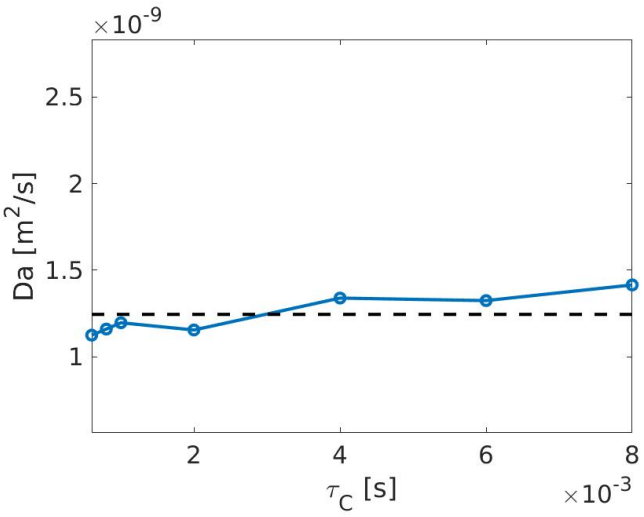

Figure 4.10: The active diffusion coefficient D_a is fluctuating around a constant value when the correlation time of the bath ω_c^{-1} changes from $\tau_c = 0.1$ ms to $\tau_c = 0.8$ ms, with relaxation time inside the optical trap fixed at $\omega_0^{-1} = \gamma/\kappa \approx 1.2$ ms.

The active diffusion coefficient is taking into account the optomechanical coupling of the radiation pressure onto the bead. It thus depends on the intensity and focalisation of the beam as well as on the optical response of the microsphere. In our case, this (complicated) dependency is circumvent by extracting D_a from the fit of the experimental MSD with the analytical expression Eq. (4.9) where all other parameters are known. In the case when the intensity of the force applied (amplitude of η_t sent to the AOM and intensity of the laser beam passing through it) is constant, the coefficient D_a is a constant under changes of correlation time, as seen on Fig. 4.10. The fluctuations of D_a around the mean value comes from experimental errors, since it is the only fitting parameter.

4.3.5 Breaking of equipartition and absence of effective temperature

As we see on Fig. 4.9, when the noise gets more colored, i.e. the correlation time increases and the overall amplitude of the MSD increases. When the correlation time increases, the microsphere explores a larger volume. This is reminiscent of an increase of temperature, as in the case of an additional white noise discussed in Sec. 4.2.3.

In the colored noise case, seen on the MSD, this increase is not a simple change in amplitude, but goes with a modification of the scaling of MSD with respect to the lag-time (superdiffusion). This prevents one to describe the system with a unique constant effective temperature [31]. As a way to highlight this strong difference with a simple temperature change, we show that the law of equipartition of energy fails to describe the bead response.

Equipartition states that every quadratic degree of freedom contributes on average to $k_BT/2$ to the energy of the system. In our case, the only quadratic term is the potential $\kappa x^2/2$ hence equipartition imposes $\kappa\langle x^2\rangle = k_BT$. Introducing the diffusion coefficient $D = k_BT/\gamma$ and the inverse relaxation time $\omega_0 = \gamma/\kappa$, we can write equipartition as $\langle x^2\rangle = D/\omega_0$, linearly relating the variance with the diffusion coefficient. Of course, when a second noise is added, this relation cannot hold, since the variance increases with a fixed fluid temperature. However, for a white noise, the microsphere is driven by two uncorrelated white noises and a generalised equipartition relation can be obtained as $\langle x^2\rangle = D_{eff}/\omega_0$, where we introduce an effective diffusion coefficient $D_{eff} = k_BT_{eff}/\gamma$ connected to an effective temperature. This is what we do for the white noise driven trajectories in Sec. 4.2.3. When the noise is colored, the stationary variance ceases to be defined by a linear relation with a single diffusion coefficient, but rather obeys to

$$\langle x^2\rangle = \frac{D}{\omega_0} + \frac{D_a\alpha}{\omega_0(\omega_c+\omega_0)} \tag{4.10}$$

where α is a dimensional constant in m^{-1}. When $\omega_c \gg \omega_0$ (but finite), the noise is almost white *i.e.* we can again recover a generalised equipartition relation [98] where an effective temperature can be defined to describe the system. However, our ability to control the color of the noise to arbitrary values allows us to explore strongly correlated noise, where this approximation fails. In this case, the relation between the motional variance and the total diffusion coefficient $D + D_a$ is Eq. 4.10, where the explicit dependency on ω_c prevents one to define an effective temperature. On Fig. 4.11, we plot the variance against the total diffusion coefficient along with a naive equipartition result that assumes linearity and the actual relation 4.10. We observe a very clear departure from an effective equipartition, but a good agreement with the theoretical expression.

One consequence of equipartition breaking is thus the absence of an effective temperature. To be more precise, it is the impossibility to describe the system over all time-scales using a single temperature. If one can use the long-time stationary variance to define an effective temperature [151], the short-time superdiffusive character

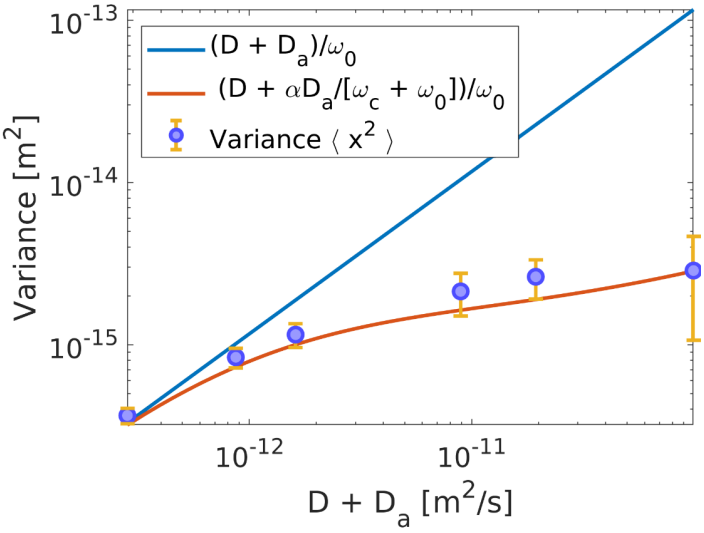

Figure 4.11: The relation between the motional variance $\langle x_t^2 \rangle$ and the $D + D_a$ diffusivity is measured on a 99.7% confidence level (blue dots and 3-σ bars) for different correlation times ranging from $\omega_0^{-1} = 0.1$ ms to $\omega_0^{-1} = 100$ ms, and with a relaxation time inside the optical trap fixed to $\omega_0^{-1} = \gamma/\kappa \approx 1.2$ ms. A naive equipartition result (straight blue line) that would assimilate the correlated noise to a white noise of same amplitude clearly departs from the experimental results, except for very short correlation times. The correct estimation of the variance for the correlated noise drawn in red is given by Eq. 4.10 with D_a value extracted from the correlated noise MSD. It fits well the experimental data.

is however not captured by this description. In fact, this impossibility is a first strong observable of the out-of-equilibrium nature of the process, connected to the violation of fluctuation-dissipation theorem (FDT) that will be discussed in section 4.5.3. The latter, consequence of Onsager regression principle, connects the response function of the system to an external perturbation to the spontaneous correlation function [162] through $k_B T$. Out-of-equilibrium, both response function and correlation have generally different dynamics cannot be connected by a constant $k_B T$ factor. In that case [31], a quasi-FDT can allow to define an effective temperature via a non-constant $k_B T_{eff}[\omega]$ here expressed as a frequency dependence as in [163] to contrast with a constant T_{eff} that would allow an equilibrium-like description.

4.4 Noise color for protocols

In the previous section we observed that the motional variance of the microsphere can be modified by changing the color of the noise. We studied in details that this a change, not only of the amplitude of all observables (such as MSD, PSD, autocorrelation) but of their nature, like the superdiffusive character of MSD. These changes in nature are summarised in the break of equipartition relation that shows no more a linear relation between variance and one given unique temperature. The monotonic increase of variance with the correlation time of the bath could however still be used in a similar way to a change in temperature or volume for controlling the system. Color of the bath is an experimental parameter on which time-dependant functions can be imposed, modifying through time the environment of the bead and the volume of the space it explores. As such, it provides a direct path to so-called 'bath engineering" techniques [153, 154].

In this section, we propose to use correlation time as a parameter to perform protocols on the trapped bead without modifying at all the trap features themselves. We monitor in real time the dynamical response of the bead to this change of bath. The simplest protocol that one can design is a sudden change in color at a given time instant, instantaneously modifying the bath properties. This is reminiscent of more standard thermodynamical protocols, like volume changes, that are performed in optical traps by a change in stiffness [33, 128], change in kinetic temperature, for example via noisy electrical forces [153, 154], or a combination of both [101, 99].

In our case the protocol has a different nature for two reasons. First, it does not only change the amplitude of observables (such as MSD, PSD, autocorrelation) but modifies the nature of the diffusion of the bead. Then, it does not demand any change in the amplitude of the forces applied. Changes in trap stiffness, in striking contrast need a change in the laser power sent in the trap, and temperature changes are assisted trough changes in the amplitude of an external noisy force. In our case, we propose to change the color of the noise while keeping its amplitude (variance) constant. A constant external noise variance means a constant constant overall energetic cost since the same laser power is needed to produce the force. In this sense, both first and second points give the nature of the process : we modify the spectral properties of the bath, tuning it more or less to the mechanical response of the bead, leading to a change in diffusivity. As a consequence, one obtain a change in amplitude at constant input energy. We will observe in the last section of this chapter, through a thermodynamic study of the process, that this apparent paradox resolves when interpreting such a

colored-based protocol as a relation between information and heat, where the former us converted into the latter.

In this section we will study the effect of a change in color on the motional variance. The latter being an average quantity, we need an ensemble of Brownian object experiencing the same protocol to build the average response. In order to build this ensemble out of a single trajectory, we will rely on the ergodic hypothesis that states the equivalence between time and ensemble averaging processes. Ou method consists in sending the same protocol sequentially on the bead, at a low enough repetition rate so that stationarity is reached between each event. The resulting long time-series of event is then reshaped into an ensemble of synchronised trajectories experiencing the same protocol. In order to validate our method, we must first assess that the ergodic nature of the trajectories is not broken by the non-Markovian nature of the additional noise.

4.4.1 Ergodic nature of the obtained trajectories

An ensemble of processes is said to be ergodic when each individual trajectory can represent the whole ensemble. This means first that individual trajectories explores the whole phase-space available to the ensemble, it also implies that any time-averaged quantity computed on this trajectory is the same as computed for any other trajectory. If furthermore the process is stationary, meaning that any ensemble-averaged quantity or distribution is constant in time, then ergodicity simply is the equality of time and ensemble averages in the limit of long time $\mathcal{T} \to \infty$ and infinite ensemble. As detailed in Chap. 3 and [105], appropriate tools exist that can assess the ergodic nature of trajectories $\{x_t\}$ on finite samples and finite times. The important point for our work is that once one has assessed the ergodic nature of a stationary process, an ensemble can be used to study non-stationary dynamical events.

In this section, we aim at verifying that the additional white or colored noise does not modifies the ergodic nature of a long stationary process. To do so, we rely on an estimator [96] corresponding to the ensemble variance of the ratio between time averaged mean squared displacement (TA-MSD) and ensemble averaged mean square displacement (EA-MSD). This ratio $\epsilon(\Delta)$ (see Eq. 3.6 from chap 3) should becomes Dirac-like for long-time (or short time lag Δ in the MSD). Therefore, as discussed Sec. 3.1.3 a necessary and sufficient condition for ergodicity is the vanishing of the variance of ϵ, corresponding to the vanishing of the dispersion of individual TA-MSD [164, 105].

The result, plotted in Fig. 4.12 (a) with fixed $\mathcal{T} = 0.5$ s and varying Δ, decays

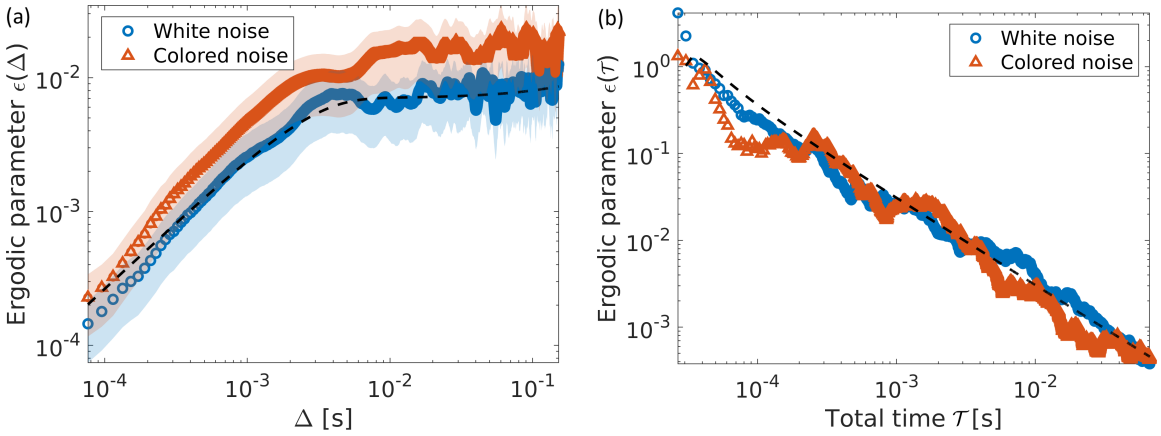

Figure 4.12: (a) The ergodic parameter (i.e. the normalised variance $\epsilon(\Delta)$ presented Sec. 3.1.3) is shown as a function of the time lag Δ for both the white noise driven process (blue circles) and the colored noise driven process (red triangles) along with the analytical prediction for the white noise case (black dashed line). The red and blue hazes measure the 95% confidence intervals. (b) The same ergodic parameter $\epsilon(\mathcal{T})$ plotted as a function of the total time $\mathcal{T}$ for both the white-noise driven process (blue circles) and the colored-noise driven process (red triangles) along with the analytical prediction for the white noise case (black dashed line).

to zero for short time-lag as expected. With fixed $\Delta = 0.183$ ms, varying $\mathcal{T}$, the expected decrease towards 0 in the long time limit, with a $1/\mathcal{T}$ trend, is also clearly seen in Fig. 4.12 (b). These two results validate our ergodic assumption for the time-series of position x_t, and therefore our treatment when it comes to building trajectory ensembles.

4.4.2 Looking at a color STEP protocol through variance

We study the response of the system to a dynamical change in the inverse correlation time $\omega_c(t)$ of the bath. The simplest protocol one can design is a sudden change of inverse correlation time from an initial ω_c^i to a final value ω_c^f. We will refer to this protocol as a STEP protocol. We expect the system (the bead) to start in a steady state characterised by a trap stiffness κ, a thermal bath temperature T and immersed in a secondary correlated bath characterised by a diffusivity D_a and inverse correlation time ω_c^i. When only the correlation time is modified, the system will reach another steady state, characterised by the same parameters and the new correlation ω_c^f. As we saw in Sec. 4.3.4 this new state will have a different probability distribution, still Gaussian but with different widths. It will also have different diffusivity and it

will be at a different distance of equilibrium as detailed through the thermodynamic description given in Sec. 4.5.5.

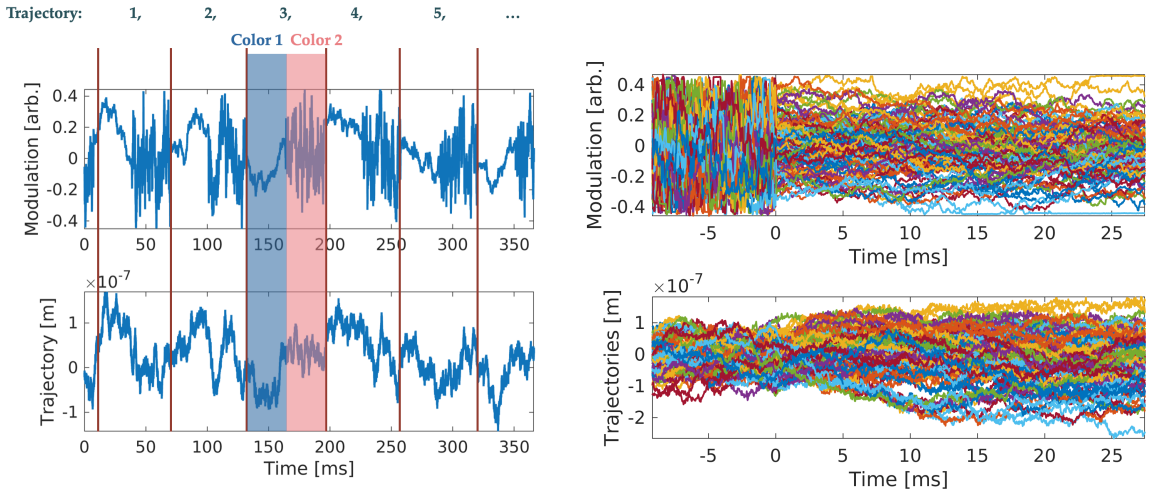

Figure 4.13: (left) Temporal noise series η_t modulated between two correlation times (two colors) following a 20 Hz square modulation function (top) and the resulting trajectory x_t (bottom). (right) Each long trajectory is reshaped as an ensemble. In the upper panel, the $\{\eta_t^i\}$ ensemble clearly displays at $t = 0$ the instantaneous change in correlation with constant amplitude. In the lower panel, the ensemble of trajectories $\{x_t^i\}$ of the bead shows the progressive change in the motional variance that results from the step-like change of the correlation times of the secondary, correlated bath.

To study the response to the STEP-protocol, we need an ensemble of independent trajectories all experiencing the same parameter changes. With one single bead in the optical trap, the ensemble is drawn out of a long time series, for which the ergodic hypothesis is crucial and was carefully checked as discussed in Sec. 4.4.1. We produce two long noise sequences η_t, one with ω_c^i and the other with ω_c^f. Both sequences are then interspersed synchronously with a ω_c^i/ω_c^f square modulation. This way we obtain a periodic STEP between two stationary noises with two different correlations at a low enough repetition rate (a few tens of Hertz). The detailed procedure is described in Fig. 4.13 (a). This modulated sequence of noise η_t is sent to the bead via the radiation pressure laser. The corresponding trajectory x_t of the bead relaxes to one steady-state between each change on ω_c. The long trajectory is cut and reshaped into an ensemble of trajectories $\{x_t^i\}$ that, each, experience a step-like change in correlation time. We will see in Sec. 4.4.3 that other methods for producing protocols are possible and each impacting differently the response of the system.

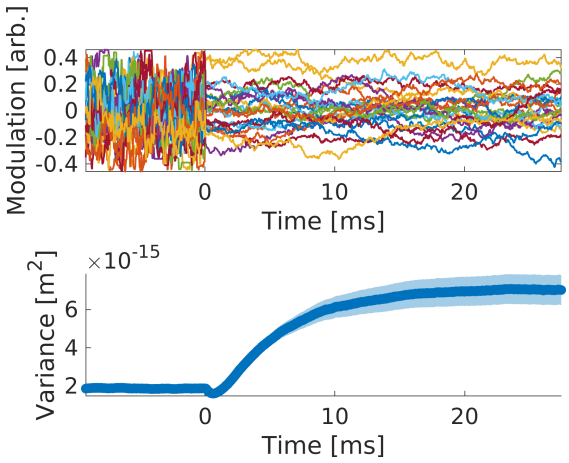

Figure 4.14: STEP protocol using the noise correlation time as a control parameter. (top panel) 25 digital realisations of the noise variable η_t, undergoing a change in the correlation time at $t = 0$, from $\tau_c = 0.8\,\text{ms}$ before the STEP to $\tau_c = 40\,\text{ms}$ after. (bottom panel) Corresponding experimental ensemble variance $\langle x_t^2 \rangle$ of the position of the bead from the trajectory associated with each noise realisation; the shaded area represents the 99.7% confidence interval.

In Fig. 4.14 (b), we show the results of a STEP protocol where the correlation time is suddenly changed from $\omega_c^{-1} = 0.8$ ms to $\omega_c^{-1} = 40$ ms, while $\omega_0^{-1} = 2.1$ ms. A squence of realisations of the noise variable η_t is displayed in Fig. 4.14 (a): the change in correlation time at $t = 0$ is clearly visible. In Fig. 4.14 (b), we represent the variance of the position of the bead evaluated on the trajectory associated with the noise realisation, which undergoes a threefold increase when the correlation time is changed. The small dip right after the STEP is due to the way we build the protocol by interspersing two uncorrelated noise time-series as detailed in the following section and in Appendix 8.11

The above STEP protocol has the same effect (increase in the variance $\langle x_t^2 \rangle$) as a protocol where the noise remains white, but its amplitude (temperature encapsulated in $D + D_a$) increases [99, 101]. The important difference is that, in our case, we do not change the amplitude of the noise, but only act on its spectrum by modifying the correlation time. In this sense, the protocol can seem costless from the experimentalist's point of view, as no additional power is provided to the laser source at the transition time. As a comparison, we estimated the equivalent power needed to induce the same increase in variance as in Fig. 4.14 (b) through a change in the noise amplitude, i.e., by changing the diffusivity D_a. The result is that one would need a laser intensity of 70 mW, whereas we used only 36 mW in our color-based protocol.

4.4.3 How to change color ? Experimental details.

As we have pointed out in the previous section, our method to build the protocol is not unique. We recall that we generate two uncorrelated time-series of noise η_t with different correlation times and reshape the two sequences into one single long periodic change between two noises. One obvious consequence of this choice is that all correlations in the noise are lost after the protocol: if the change happens at time $t = t_0$ then we have $\langle \eta(t_0 - \epsilon)\eta(t_0 + \epsilon)\rangle = 0$ for any short delay ϵ. Consequently, the bead experiences at each STEP a "new" noise which explores its available parameter space from an initial condition, without memory from its past values. The bead therefore uses a finite time to "measure" the whole amplitude of the noise $\eta(t_0 + \epsilon)$ and for this time the corresponding trajectory will decrease in amplitude. This can be captured by numerical simulations as well as an analytical expression of the variance. To build this theoretical result, detailed in Appendix 8.11, we solve the differential equation for x with a noise build in two parts $\theta(t - t_0)\sqrt{2D_1}\eta_1 + \theta(t_0 - t)\sqrt{2D_2}\eta_2$, where $\theta(t - t_0)$ is Heavside's distribution centred in t_0 and D_1, D_2 are the active diffusion coefficient for respectively η_1 and η_2. In our case we are able to change the correlation time constant, while keeping the amplitude constant, we therefore choose $D_1 = D_2 \equiv D_a$. The solution computed in Appendix 8.11 exhibits a local decrease after the STEP just like shows the experimental data. This can be understood from the full expression of $\langle x_t^2\rangle$ where we see just after t_0 the simultaneous exponential decrease of x_t associated with η_1 and the exponential increase of x_t associated with η_2. This combination results in a local minimum in the variance evolution.

We test the obtained analytical result on numerical simulations done with a first order algorithm for the position stochastic differential equation Eq.4.5. We simulate 10^4 independent trajectories with the following parameters : a stiffness $\kappa = 6\times10^{-6}$ kg/s^2, a viscous drag of $\gamma = 8 \times 10^{-9}$ kg/s, leading to a thermal diffusion coefficient $D = 0.52 \times 10^{-12}$ m^2/s with a strong active diffusion coefficient $D_a = 5 \times 10^{-8}$ m^2/s, . The protocol goes from $\omega_{c,initial}^{-1} = 1$ ms to $\omega_{c,final}^{-1} = 40$ ms. We simulate a total time of 0.1 s with a sampling rate of 2^{14} Hz We then compute the instantaneous ensemble variance of all these trajectories and plot the result along with the analytical result of Fig. 4.15 (a). The very good agreement can be seen.

An alternative way of producing the STEP would have been to simulate one single time-series of noise η_t where the correlation time $\omega_c^{-1}(t)$ is changed dynamically in the simulation. Since the variance of the process is conserved by the independence of α. There is no relaxation observed in the properties of η_t. This method preserves the correlations of the noise around t_0 and thereby no decrease in the motional variance

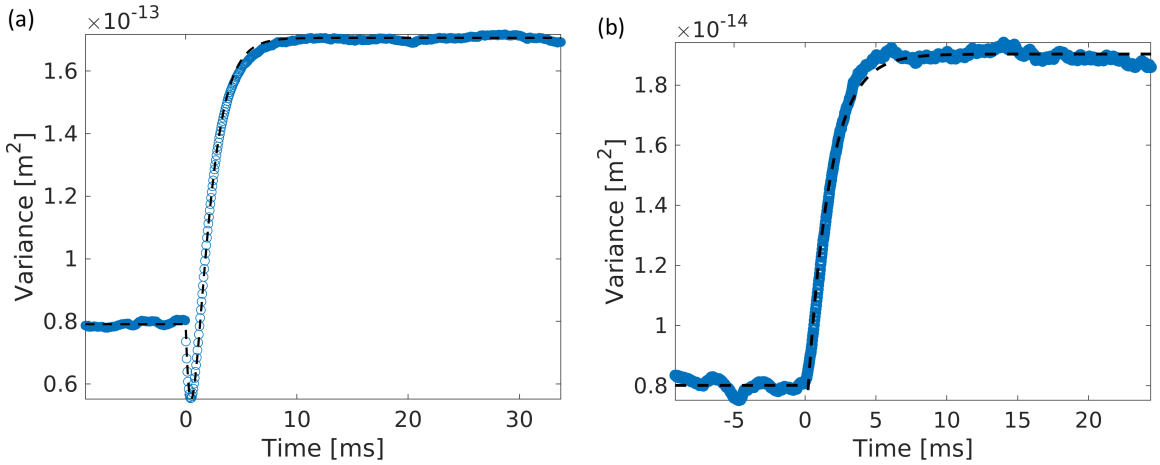

Figure 4.15: (a) Comparison between the analytical result for the time-evolution of the variance under a color STEP protocol and the numerical simulations performed with the first method: appending two independent noise time-series, hence loosing correlations at $t = 0$. The blue circles are the ensemble variance of 10^4 independent trajectories and the black dotted line is the analytical result, combination of Eq. 8.98 and Eq. 8.97. (b) Numerical variance $\langle x_t^2 \rangle$ that experiences a color STEP done by changing dynamically $\omega_c(t)$ this time, and in contrast with (a), without loosing the correlations around the STEP, as described in the main text as a second alternative method, along with a simple exponential fit.

of x_t will be observed. A simulation done in such conditions is shown on Fig. 4.15 (b) where we observe indeed the monotonic behaviour of the time-evolution of $\langle x_t^2 \rangle$, in contrast with the result plotted in Fig. 4.15 (a).

The existence of the dip after a STEP can be obtained in situations simpler than a color protocol. Indeed, it is a consequence solely of the abrupt change from one noise to another, uncorrelated with the initial one. The two noises can have the same color but differ, for example in amplitude (*i.e.* "temperature"). In this case, just like what is studied in [165] we can do a "temperature quench" by decreasing D_a in a STEP like way. The result is a local *overcooling* as shown in that publication. Again, we understand this decrease to be a consequence of the method used to perform the protocol. Even if the color of the noise is not modified in this example, all correlations are lost during the protocol since it is the combination of two independent noises. Therefore, the bead experiences a combination of exponentials just as in the color steps, but this time, both parametrised by the same ω_c.

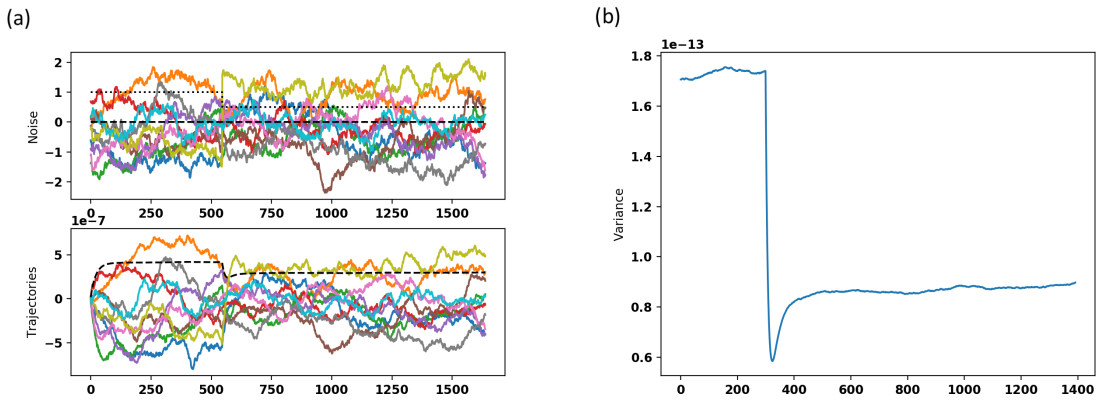

Figure 4.16: (a) Noise realisations η_t and trajectories x_t when the protocol is done by appending two noises of same color, but entering the dynamics of x multiplied by $D_a(t)$ that is a decreasing STEP (black dotted line). bottom : response x_t along with standard deviation (b) Response variance of trajectories $\langle x_t^2 \rangle$ that shows a decrease after the STEP.

In this section we studied the response of the system in terms of motional variance $\langle x_t^2 \rangle$ of the trapped microsphere to a STEP change of correlation time of the secondary bath. Another important aspect lies in the evaluation of the distance of the system to equilibrium. Indeed, as already mentioned, the colored noise drives the system in non-equilibrium steady-states (NESS), and the STEP protocol is an example of dynamical NESS-to-NESS transient. The out-of-equilibrium properties of the trajectories are modified in the process and the two NESS will be characterised by different distances to equilibrium. In the following section we focus on the characterisation of non-equilibrium through different observables, such as fluctuation-dissipation theorem or heat and entropy. We also propose a connexion with active matter-like systems.

4.5 Out-of-equilibrium with colored noise: probing active-matter-like physics.

In this section, we will look at the out-of-equilibrium nature of colored-noise driven trajectories and how our system can be used, in this colored noise environment as a minimal model to study the properties of active matter.

4.5.1 Active matter in biological systems

Active matter is a state of systems able to convert an energy provided by the surrounding (or an internal source) into forces and motion, leading for example to propulsion or self-organisation [145, 149, 56, 58, 61, 119]. The most striking example of active systems are found in biology. Living systems being intrinsically thermodynamically open and operating far from equilibrium [59] are characterised by a constant flow of energy and information.

This is clear at macroscopic scales, where collective organisation of living systems such as schools of fish or flocks of birds are described by the tools of active matter [166]. At this scale, a large part of these peculiar aspects are due to collective effects and can be modelled by the statistical behaviour of large ensembles of self-propelled objects [167] which do not obey to the laws of equilibrium thermodynamics. Macroscopic structures with directional motion are clearly breaking the time-reversal symmetry and it fundamentally stems from their non-equilibrium nature, due to energy consumption and dissipation. At mesoscopic scales in living systems, the cytoskeleton network of filaments and motors collective behaviour maintains the cell architecture and enables motility [52, 53, 144, 15, 16]. The capacity of cells to perform motion and apply forces enables the formation of large structures by physical stresses, as is happening during embryonic morphogenesis [168]. Again these process are happening out-of-equilibrium. Just as embryonic structuration shows an irreversible evolution with energy consumption and dissipation, cells are displaying non-thermal active motion breaking the fluctuation-dissipation theorem.

It is at microscopic scales that exotic effects are more vividly showing the importance of energy and information circulation. For instance, molecular motors such as kinesin walking on microtubules are converting chemical energy (by hydrolysis of adenosin triphosphate) into mechanical forces [51, 50]. At this scale, directional motion is not necessarily happening, as in the case of the active fluctuations of a cell membrane [59]. Here, irreversibility [65] and detailed-balance violations [66] -that are obvious at larger scales- are hidden. Understanding how and where detailed balance is broken can be more subtle. One way to unveil non-equilibrium is to notice that these microscopic active system are always the consequence of the non-reciprocal coupling on several variables [67, 69]. One can think for example of the position of a self-propelled bacteria and the state of its propulsion mechanism: the first is determined by the second, whereas the latter can be totally independent of the former. The behaviour of the self-propelled object can be suitably described by the position-propulsion couple of variables and more generally, the parameter space opened by the different variables

-as we did in Sec. 4.3.3- unveils the breakdown of time-reversal symmetry [66].

However, other observables explicitly shows the non-equilibrium nature of the systems. A consequence of non-thermal activity is for example to break the equipartition of energy, preventing the use of simple effective temperature [98] to describe the system. This was carefully studied in Sec. 4.3.5. Another measure of departure from equilibrium is the violation of fluctuation-dissipation theorem, stating that equilibrium fluctuations are related to mechanical response [59]. This aspect can be tackled by performing microrheology experiments to probe experimentally both the mechanical susceptibility and the fluctuation correlations of the system. Distance from equilibrium can also be evaluated via energy dissipation [58, 56]. At these roughly micron-scales, where thermal fluctuation plays a central role, quantities are random variables and all information and energy exchange happens in a fluctuating environment. The framework of stochastic energetics [46, 45, 54, 119] emerges as a suited tool to investigate the energy dissipation of unique microscopic active systems by assessing heat and entropy productions [112, 47].

In this chapter, we use our colored-noise driven trajectory as a genuine implementation of self-propelled object. The latter serves as simple model that exhibits most of the non-equilibrium properties shared by the examples above. We use our optomechanical analogue to investigate the rules connecting non-equilibrium with energy and information exchange in active matter.

4.5.2 The minimal model of an active Ornstein-Uhlenbeck particle

These examples of active matter are sharing many common features and simple models can be derived to access a large part of the key aspects described. The model of Active Ornstein-Uhlenbeck Particle (AOUP) has emerged as a minimal but rich model for self propelled object [60, 150]. It describes for example a bacteria or sperm cell evolving in a fluid influenced by both the thermal fluctuations and an additional force due to the active flagella or other propulsion mechanism [49]. This propulsion induced an exponential persistence in the motion of the object, which is not diffusing as a passive Brownian object anymore. But interestingly, a passive colloid can exhibit the same properties if it is immersed in an active bath such as a fluid saturated with bacterias [151, 98, 142], whose collective effective action on the colloid turns out to be an exponentially correlated force. This stems from the exponential persistance of each bacteria building the active bath. Such a system has been extensively studied

numerically [60, 160, 65, 150] and used as a model for biological experiments. Recently, it has also been used as a model to build experimental mechanical analogues of living systems [155, 156, 157, 27], our experiments are precisely in this framework. In our case, the external radiation pressure force induces this activity, and can be interpreted either as a self-propulsion mechanism or as an active bath. This analogy between our optomechanical system and active matter is sketched on Fig.4.17.

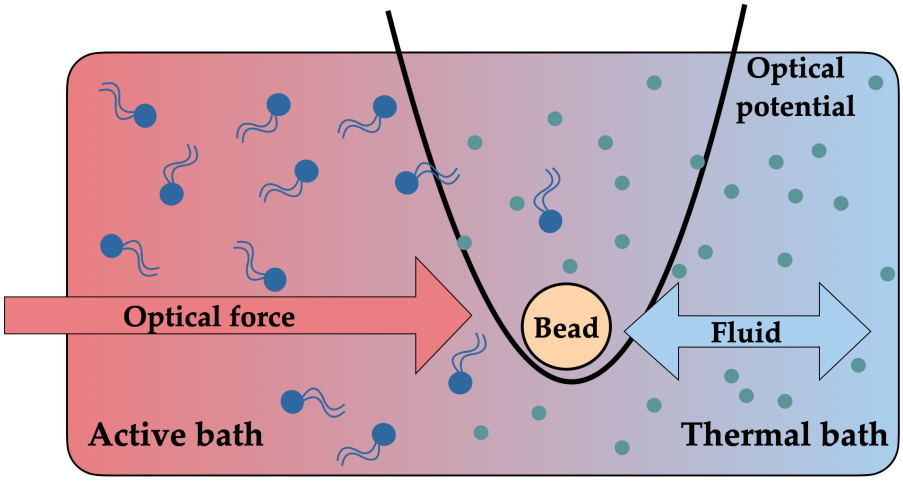

Figure 4.17: A schematic view of the experimental realisation of the active Brownian particle. An optically trapped bead is connected to two baths : a thermal bath by the surrounding fluid and an athermal active bath, by the external force.

The active system is modelled with the same Langevin equation Eq. 4.5 that we presented above, where added to thermal fluctuation, a secondary colored bath is driving the many different features (superdiffusion, breaking of equipartition, NESS-to-NESS transitions) that we described in previous sections. We recall here the differential equation driving the dynamics of the bead

$$dx_t = -\omega_0 x_t + \sqrt{2D}\xi_t + \sqrt{2D_a}\eta_t \tag{4.11}$$

where $\omega_0 = \kappa/\gamma$ is the inverse relaxation of the object in the potential, the thermal noise obeys to $\langle \xi_t \xi_s \rangle = \delta(t-s)$ and the colored noise to $\langle \eta_t \eta_s \rangle = \alpha e^{-\omega_c |t-s|}$. In the following, we will focus on aspects more directly connecting this model to active matter and unveiling the implication of its non-equilibrium nature. This will underline the properties of different observable of non-equilibrium but also resole the aforementioned paradox, by an information analysis, again emphasising the dependance of active matter on information flows.

4.5.3 FDT breaking and microrheology

We probe the non-equilibrium nature of the active fluctuations and the validity of the Fluctuation Dissipation Theorem (FDT) by comparing the dynamical responses of our bead to Active MicroRheological (AMR) and Passive MicroRheological (PMR) excitations, respectively [59, 148]. AMR corresponds to the response of the system to an external excitation, typically, a sinusoidal force at a given frequency, while PMR corresponds to the recording of the spontaneous fluctuation of the system, with no external drive. When a small perturbation $a(t)$ is applied on the bead, its average position is modified. The amplitude of this motion is given at first order by

$$\langle x_t \rangle = \int_{-\infty}^{t} R(t-s)a(s)ds \tag{4.12}$$

where $R(t)$ is called the mechanical response function or susceptibility of the system. At thermal equilibrium, under detailed balance conditions (equality of the probability of transition between two microstates and its time-reversed transition), FDT [169] connects the response function to the equilibrium correlations of fluctuations according to

$$\frac{\partial C_{xx}(t)}{\partial t} = k_B T R(t), \tag{4.13}$$

where $C_{xx}(t) = \langle x(t)x(0) \rangle$ is the motional autocorrelation function. This important equation enables to probe the response function of a system via its spontaneous fluctuations. Furthermore, when both response function and autorrelation function can be measured, it is used to verify if a system is -or not- at thermal equilibrium. For example, in an active biological system, the fluctuations are not only due to the mechanical response of the object to thermal fluctuations, but also to internal energy-consuming mechanisms. In this case Eq. 4.13 is not verified, proving the non-equilibrium nature of the system [59].

In experiments, the mechanical susceptibility of often probed by measuring the amplitude of the response to a small sinusoidal force. In that case FDT is more conveniently expressed in the frequency domain, which can be obtained by Fourier transforming Eq. 4.13. It can also be obtain directly from the Langevin equation. To do so, we will start from Eq. 4.5 and combine both thermal and active noises into a single term, that represents the fluctuating excitation. Then the bead is driven by a single noise of unit variance ϕ_t. To recover FDT, we will assume a white noise η_t, therefore equilibrium. According to Eq. 4.5 the overall noise takes in our case the form $\phi_t = \xi_t + \sqrt{D_a/D}\eta_t$, defining an effective temperature $T_{eff} = T(1 + \sqrt{D_a/D})$ for a white noise driving. In such a case, the Fourier transform of the corresponding

Langevin equation writes as:

$$-i\omega\gamma x[\omega] = -\kappa x[\omega] + \sqrt{2k_BT\gamma}\phi[\omega], \tag{4.14}$$

where κ is the stiffness of the potential, γ the Stokes friction drag. The equation can be written in terms of a mechanical susceptibility $\chi[\omega]$ as

$$x[\omega] = \chi[\omega]\sqrt{2k_BT\gamma}\phi[\omega] \tag{4.15}$$

where $\chi[\omega]$ can be decomposed into real and imaginary parts as:

$$\chi[\omega] = \frac{\omega_0}{\gamma(\omega_0^2+\omega^2)} + i\frac{\omega}{\gamma(\omega_0^2+\omega^2)} \equiv \chi'[\omega] + i\chi''[\omega]. \tag{4.16}$$

Fluctuation dissipation is recovered by comparing the imaginary part $\chi''[\omega]$ with the power spectral density of a thermal, white noise driven Brownian motion $S_x[\omega] = 2k_BT_{eff}/\gamma(\omega_0^2+\omega^2)$. This leads to the expression of the FDT in the Fourier space:

$$\chi''[\omega] = \frac{\omega}{2k_BT_{eff}}S_x[\omega] \tag{4.17}$$

where the spectrum $S_x[\omega]$ is the Fourier transform of autororrelation function $C_{xx}(t)$ (Wiener-Khinchine theorem) and $\chi[\omega]$ is the Fourier transform of the mechanical response. Of course, for a colored noise, the PSD will differ from the PSD of white-noise driven process, according to Eq. 4.7.

If now one adds a small sinusoidal perturbation on the bead by means of an external force (which corresponds to radiation pressure in our experiments), the FDT can be tested experimentally by measuring the response function. Under the sinusoidal *ac* drive of the AMR mode at pulsation ω_{ac}, the PSD takes the following form [86]

$$S_x^{ac}[\omega] = \frac{1}{\omega_0^2+\omega^2}\left(2D_{eff} + \frac{F_{ac}^2}{2\gamma^2}\delta(\omega-\omega_{ac})\right) \tag{4.18}$$

where $D_{eff} = k_BT_{eff}/\gamma$ for a white noise driven trajectory and F_{ac} is the Fourier force component of the drive, while the unperturbed PSD of the PMR mode writes

$$S_x[\omega] = \frac{2D_{eff}}{\omega_0^2+\omega^2}. \tag{4.19}$$

By computing the ratio $S_x[\omega]/S_x^{ac}[\omega_{ac}]$ at the pulsation ω_{ac} for a bead on which a white noise radiation pressure is exerted (hence maintaining it close to thermal equilibrium but at an effective temperature T_{eff} higher than room temperature), we can extract the value of F_{ac} by taking the mean value of all realisations. This value can then be used to calibrate the response function $\chi''[\omega]$ and compare it with the steady-state fluctuation PSD $S_x[\omega]$.

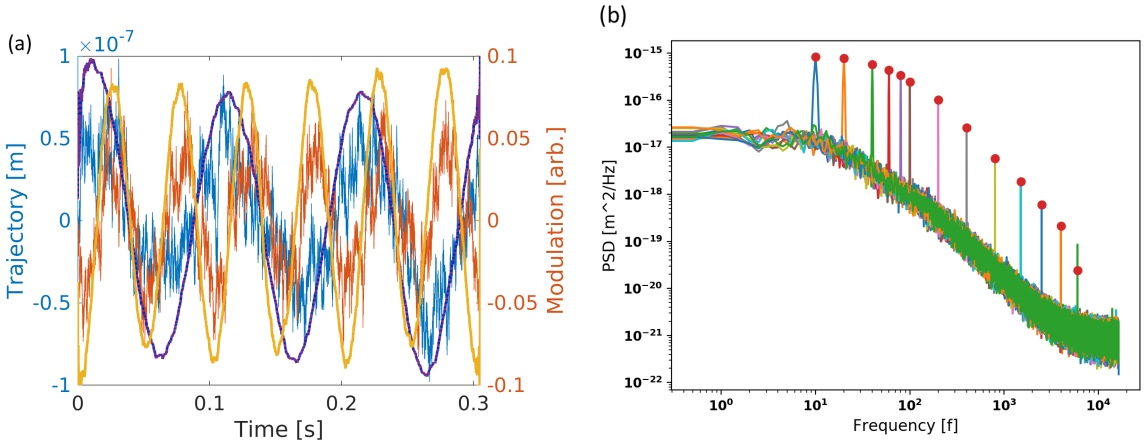

Figure 4.18: (a) Active micro-rheological (AMR) experiment where the sinusoidal forcing of the system is monitored in the time domain. The recorded trajectories of the bead inside the trap are superimposed to the sinusoidal traces of the force for two different modulation frequencies. (b) Power spectral densities displayed together for different modulation frequencies of the external force drive. The Fourier components of each harmonic forcing at different ω_{ac} from 10 Hz to 6 kHz are clearly seen as peaks in the PSD.

On Fig. 4.18 (a), we show the external drive in the time-domain and the motional response of the bead inside the trap for two different modulation frequencies. By repeating the procedure for frequencies ranging from 10 Hz to 6 kHz, the response of the bead is characterized over all the useful bandwidth (see Fig. 4.18 (b)). On Fig. 4.19, the values of $\omega S_x[\omega]/2k_BT_{eff}$ and $\chi''[\omega]$ are plotted together for the probed frequencies, for both the white noise and colored noise driven processes. We clearly observe that in both cases, the response functions associated with the mechanical susceptibilities fall back on the same trend. This can be understood since the susceptibility $\chi''[\omega]$ depends only on the mechanical properties of the system under study. Here, the bead immersed in the fluid bath (γ solely corresponds to the viscosity of the surrounding water), the additional bath is not inducing any mechanical response, since the sphere does not dissipate in it. Therefore, the mechanical response is not modified by an additional colored noise. This trend is exaclty the one associated with the white noise driven PSD as expected from Eq. (4.17). In contrast, the spectral density of the colored noise driven process significantly departs from the FDT in Eq. (4.17), and more particularly for the low frequencies of the active fluctuation spectrum. This is in agreement with other observations made recently on active systems [59], where the active mechanical processes mostly appear at low frequency, while the FDT is recovered for the thermally dominated high-frequency part.

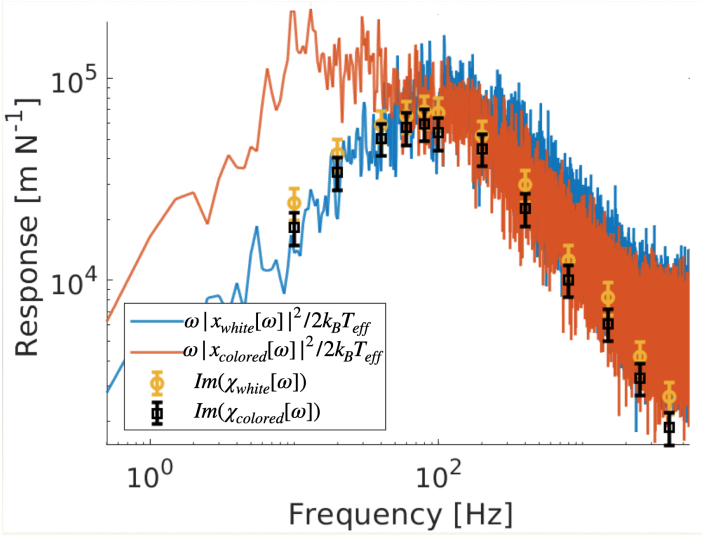

Figure 4.19: We compare the measured values of $\chi''[\omega]$ for white (open circles) and correlated (open squares) noise for different modulation frequencies ω_{ac} and small sinusoidal perturbations with the stationary correlation spectra plotted as $\omega S_x[\omega]/2k_BT_{eff}$ for white (blue curve) and correlated (orange curve) noises. One immediately remarks the breaking of the FDT for the colored-noise driven process. This can be understood since the susceptibility $\chi''[\omega]$ depends on the mechanical properties of the bead, that are not modified by the addition of a second noise.

We note here that a simple observation of the breaking of the FDT can already be seen in our model described by Eq. (4.5), where the fluctuating forces associated with the added noises ξ_t and η_t now possess an intrinsic correlation time due to the correlated nature of η_t, while the friction kernel γ is taken as instantaneous $\Gamma(t,t') = \gamma\delta(t,t')$. This choice has been shown to be valid in the experimental case [152], where the fluctuations of the active bath are not compensated through dissipation with the same rate. In the limit of vanishing correlation times, the FDT is recovered as the noise is white (δ-correlated) and its only effect is an effective change in temperature, as was already observed using a different experimental technique [153, 154].

4.5.4 Recovering a frequency-dependent effective temperature

The breaking of the equipartition relation for a colored-noise driven trajectory, demonstrated in Sec. 4.3.5, prevents the definition of a simple constant effective temperature T_{eff} to characterize the system. Furthermore, in the previous section, we showed in Fig. 4.19 that imposing a constant T_{eff} breaks the fluctuation-dissipation theorem

(FDT).

Notwithstanding, the writing of FDT in Fourier space Eq. (4.17) suggest a possible definition of a richer effective temperature [59]. By releasing the constraint of a *constant* effective temperature, one invert the FDT to define

$$T_{eff}[\omega] = \frac{\omega S_x[\omega]}{2k_B \chi''[\omega]} \tag{4.20}$$

where the effective temperature is now a function of pulsation, or equivalently, of frequency. Furthermore, we can rewrite this expression, by replacing the mechanical susceptibility $\chi''[\omega]$ by its expression via FDT in a case where it holds. Here, we can use FDT on an equilibrium trajectory with no additional noise (standard Ornstein-Uhlenbeck equilibrium process at room temperature[1] in a trap) as an evaluation of the susceptibility $\chi''[\omega] = \omega S_x^{eq}[\omega]/2k_B T_{room}$. Then, the effective temperature can be expressed as

$$T_{eff}[\omega] = T_{room}\ \frac{S_x[\omega]}{S_x^{eq}[\omega]}, \tag{4.21}$$

ratio between the power spectral density in the out-of-equilibrium studied case $S_x[\omega]$ and an equilibrium case $S_x^{eq}[\omega]$ with same trap stiffness $\kappa = 23.8$ pN/µm.

Of Fig. 4.20 (left axis) we represent the effective temperature, expressed as a function of frequencies for two cases. For a white noise-driven process (blue circles), we recover a nearly constant value, centred around the effective temperature of 1182 K extracted from equipartition theorem (black dashed line). We believe that the slight decrease at high frequency is due to the electronic noise in the PSD, as in Fig. 2.7 in Chap. 2. This result confirms that white noise-driven Brownian motion can be described with the tools of equilibrium statistical physics. This constant effective temperature is of course connected to the recovering of FDT using the simple noise scaling used in the previous section for a white noise-driven trajectory.

For a colored noise-driven process (red circles) in contrast, the effective temperature strongly depends on frequency, reaching very high values (around 30.000 K) at low frequency. This again is a striking proof that this process cannot trivially be rationalized with the tools of equilibrium statistical mechanics. Remarkably, for high frequencies, the effective temperature decreases to room temperature, below the effective temperature of the equivalent white-noise driven trajectory. This comes from the fact that at such frequencies, the colored-noise has a smaller amplitude than the white noise (see the injected PSD Fig. 4.4). The decreasing amplitude of the colored-noise above a

[1] In this subsection, we explicitly write room temperature T_{room} to avoid confusion.

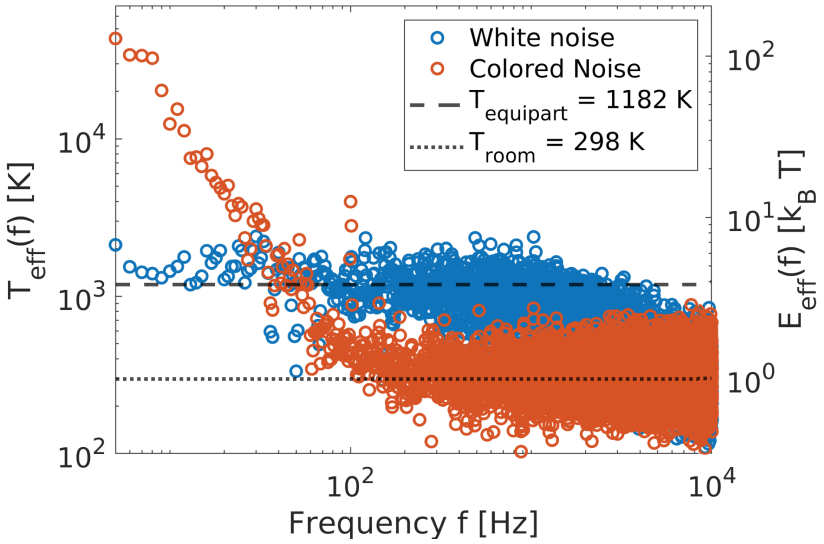

Figure 4.20: (left axis) Frequency dependent effective temperature $T_{eff}(f)$ for a white noise driven process (blue circles), and for a colored noise (of same amplitude, with correlation time $\omega_c^{-1} = 3$ ms) driven process (red circles). We superimposed the temperature extracted from equipartition theorem for the white noise $T_{equipart} = \kappa\langle x^2\rangle_{white}/k_B$ (black dashed line) as well as the room temperature $T_{room} = 298$ K (black dotted line). (right axis)Following [59], visual representation of the spectral repartition of the injected effective energy. We see that for a colored-noise driven trajectory, the energy is mostly injected at low frequency, with values up to 100 $k_B T_{room}$.

few hundred Hz cannot augment the microsphere's motion, that falls back at its room temperature agitation level.

On the same Fig. 4.20 (right axis), we show the spectral repartition of the injected energy in units of $k_B T_{room}$. This is a simple rescaling of $T_{eff}(f)$ by T_{room} but it provides insightful information. We can observe that for the white noise driven case, the energy is evenly injected over all bandwidth, the horizontal dashed line now corresponding to the average energy $\kappa\langle x^2\rangle_{white} = 3.99\ k_B T$. On the other hand, for the colored-noise driven case, energy is injected mostly at low frequencies and for high frequencies it actually injects less energy than in the white noise case. Again this is consistant with the spectral profile of the injected power Fig. 4.4. Yet it will have non-intuitive consequences, studied in the next section, that can be anticipated with the question: which of those two cases will induce, for the microsphere, the largest energy dissipation rate in the fluid? On one side, a naive equipartition applied on the colored-noise driven trajectory (which we know to be invalid) would give a temperature larger than the

white noise equivalent by a factor 12, consequence of the large mechanical response of the microsphere at low frequencies. On the other side, integrating the effective energy in the spectral domain gives an energy injection rate larger in the white noise case (0.197 fW) than in the colored-noise case (0.175 fW) which are relatively close to typical biological rates [59]. The relation between injected and dissipated energy will be explored in the next section with the tools of stochastic thermodynamics.

4.5.5 Stochastic thermodynamics of AOUP and heat release through a STEP protocol

The trajectories of the microsphere driven by the colored noise are out-of-equilibrium, as observed in various ways in the sections above. The breaking of fluctuation-dissipation theorem implies energy exchanges with the medium to maintain the system in a steady-state. A suited way to probe the deviation from equilibrium is the measure of energetic quantities, such as the heat dissipated in the medium. The application of stochastic thermodynamics to active matter has already been studied theoretically [147, 148, 119, 146, 65] and experimentally in some cases [57]. In this section, we describe in detail how the stochastic heat can be efficiently used to describe and characterize the processes at play in our active matter analogues.

We first note that, in our experiments, our system is brought to a Non-Equilibrium Steady-State (NESS) where the stationary stochastic laser drive maintains – through the action of radiation pressure – the system out of its equilibrium state at a given temperature and stiffness κ. Following the standard methods of stochastic energetics [46, 45] and Eq. 4.5, we write, for our process

$$\left(\gamma \dot{x}_t - \gamma\sqrt{2D}\xi_t dt\right) dx = -\left(\kappa x_t - \gamma\sqrt{2D_a}\eta_t\right) dx. \tag{4.22}$$

The left-hand side is interpreted as the heat exchanged between the microsphere and the thermal bath $\delta q = -\left(\gamma \dot{x} - \sqrt{2D}\xi_t dt\right) dx$. The internal energy is defined by the potential energy $dU = -\kappa x_t dx$. The remaining term $\gamma\sqrt{2D_a}\eta_t dx$ is the energy exchanged with the active bath. Interpreted as a heat term [65], it can be evaluated from the right-hand side of Eq. (4.22) as

$$\delta q(t) = \frac{1}{2}\kappa\frac{dx^2}{dt}dt - \gamma\sqrt{2D_a}\eta_t \dot{x}_t dt, \tag{4.23}$$

which can be integrated to give the stochastic heat evaluation

$$q(t) = \frac{1}{2}\int_0^t \kappa\frac{dx_s^2}{ds}ds - \gamma\int_0^t \sqrt{2D_a}\eta_s \dot{x}_s ds. \tag{4.24}$$

The ensemble average heat can be expressed in terms of variance and cross-correlations

$$\begin{aligned} Q(t) \equiv \langle q(t) \rangle &= \frac{1}{2} \int_0^t \kappa \frac{d\langle x_s^2 \rangle}{ds} ds - \gamma \int_0^t \sqrt{2D_a} \langle \eta_s \dot{x}_s \rangle ds \\ &\equiv Q_{EX}(t) + Q_{HK}(t). \end{aligned} \tag{4.25}$$

The first term Q_{EX} is zero in a steady-state, i.e. when the motional variance of position is constant $\frac{d\langle x_s^2 \rangle}{dt} = 0$. We identify it with the *excess* (EX) heat well known in stochastic thermodynamics [47]. The second term Q_{HK} is non-zero even in steady state, as it will be detailed later. We identify it as the *housekeeping* (HK) heat [47]. We will address both quantities independently because they are relevant in different context.

The excess heat is easily applied to non-stationary transient states: when the microsphere undergoes a change of motional variance because of an external action. As detailed in Sec. 4.4.2, we can use the color of the noise, i.e. its correlation time ω_c^{-1} to drive such a transient, that connects an initial NESS defined by $\omega_{c,\text{initial}}^{-1}$ to a final NESS defined by $\omega_{c,\text{final}}^{-1}$. Under such change of correlation time, we observed above that the variance evolves from an initial to a final stationary value. The excess heat associated with this transient can be computed as $Q_{EX}(t) = \int_0^t \frac{1}{2} \kappa \frac{d\langle x_s^2 \rangle}{ds} ds$ and is plotted on Fig. 4.21 for a STEP-like change in correlation time from $\omega_{c,\text{initial}}^{-1} = 0.8$ ms to $\omega_{c,\text{final}}^{-1} = 40$.

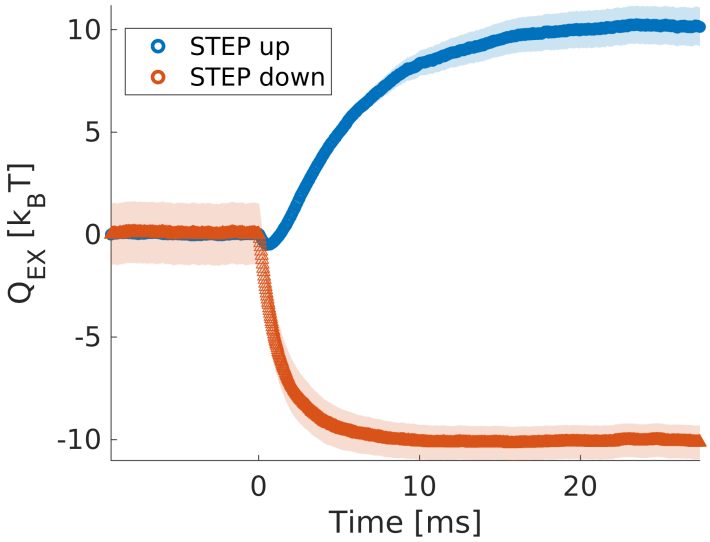

Figure 4.21: Released heat measured in units of k_BT through the transient both for an increasing correlation time (blue circles) from $\omega_{c,\text{initial}}^{-1} = 0.8$ ms to $\omega_{c,\text{final}}^{-1} = 40$ and equivalently for the corresponding decreasing correlation time (red triangles).

We observe the exponential evolution of the excess heat, following the behaviour of the motional variance described in Sec. 4.4.2. It is remarkable to stress that the quantity of heat $\approx 10 k_B T$ exchanged is the same for both cases. The total amount of excess heat exchanged during such STEP protocol can be evaluated as

$$\Delta Q_{EX} = \int_{t_i}^{t_f} \frac{1}{2}\kappa \frac{d\langle x_s^2 \rangle}{ds} ds = \frac{1}{2}\kappa \left(\langle x_s^2 \rangle_f - \langle x_s^2 \rangle_i \right) \tag{4.26}$$

where t_i is chosen before the change in correlation time ω_c^{-1} and t_f is chosen after a time long enough so the system has reached steady-state again. $\langle x_s^2 \rangle_i$ is the stationary variance in the initial steady-state and $\langle x_s^2 \rangle_f$ in the final steady-state.

In contrast, the houskeeping heat Q_{HK} is non-zero even in the steady-state. We will therefore study its behaviour in the case where the system has reached a stationary regime with constant probability distribution and explore how housekeeping heat can characterize this steady-state. The explicit calculation of the correlation term $\langle \eta_s \dot{x_s} \rangle$ is done in Appendix 8.10, and leads, after a short time exponential transient to a linear evolution

$$Q_{HK}(t) = 2\gamma D_a \alpha \left(\frac{\omega_0}{\omega_0 + \omega_c} - 1 \right) t \tag{4.27}$$

where the system is stationary. Housekeeping heat for a stationary system is therefore well described in terms of heat production rate

$$\dot{Q}_{HK} = 2\gamma D_a \alpha \left(\frac{\omega_0}{\omega_0 + \omega_c} - 1 \right) \tag{4.28}$$

On Fig. 4.22 we represent the housekeeping heat production rate in $k_B T$ per millisecond for various correlation times ω_c^{-1}. Remarkably the absolute heat production rate is decreasing when the correlation time increases, which can seem counter-intuitive when one recalls that the motional variance of the microsphere is increasing. One could expect that a larger variance would imply a larger dissipation, imprinted in the housekeeping heat production rate (which is the total heat production rate in a stationary state, since there is no excess heat). This behaviour can however be understood by looking more carefully on the changes occuring when the correlation time is modified.

A very small correlation time (a close-to-white noise limit) has very sharp time-evolution (large increments $d\eta_t$) as seen Fig. 4.14 (top before $t = 0$). In contrast, a large correlation time (a very colored noise) has a smooth time-evolution as seen Fig. 4.14 (top after $t = 0$). It is not surprising that the smoother colored noise is inducing a smaller dissipation rate: it induces less “collisions" with the microsphere per unit of time. This smooth colored noise is however better coupled to the mechanical response

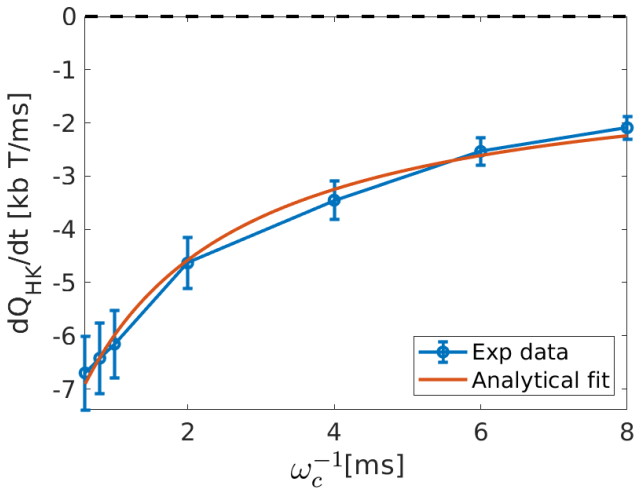

Figure 4.22: Housekeeping heat production rate $\dot{Q}_{HK}$ in units of k_BT/ms for various correlation times, ranging from $\omega_c^{-1} = 0.1$ ms to $\omega_c^{-1} = 0.8$ ms. Experimental data are shown as blue circles and a fit (to correct an offset with experimental points, described in the main text) with analytical expression Eq. (4.28) is shown as a red line. The error bars correspond to the sum of the dispersion of D_a and the uncertainty remaining on the radius of the microsphere.

of the bead and induces a larger response variance. This could explain qualitatively why the heat production rate decreases when the correlation time increases. On Fig. 4.22 we show the experimental values along with a fit realized with the analytical expression of the heat production rate Eq. (4.28). The fit is a linear transformation necessary to correct for an offset between the experimental points and the raw expression given by Eq. (4.28). This offset is probably coming from the need to evaluate experimentally $\langle \eta_s \dot{x}_s \rangle$ which is, because of $\dot{x}_t$, not a well behaved quantity. It remains however clear, as the main point, that the increase of the heat production rate with the correlation time of the noise is captured by both the experimental and analytical results.

Another interpretation of this results is to connect it with the frequency-dependent energy injection, shown Fig. 4.20 (right axis). The colored-noise energy injection is far from uniform, and shows smaller values than a white noise at high frequencies: a colored noise-driven trajectory receives less energy at short-time, leading to a smaller dissipation rate.

The heat production rate, however is not the same quantity as the heat itself. To

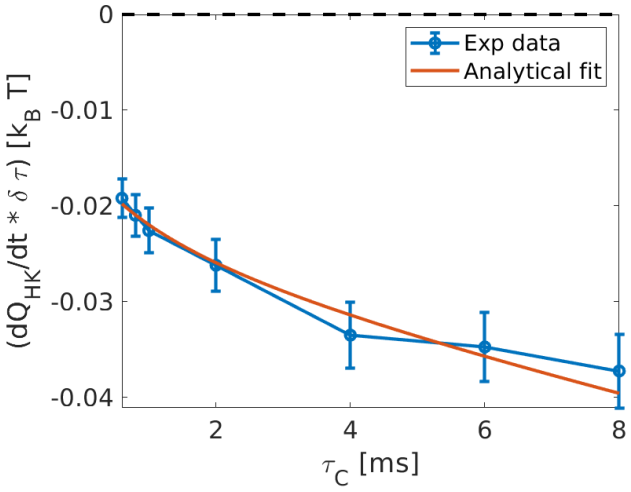

Figure 4.23: Integrated housekeeping heat production rate in units of k_BT for various correlation times, ranging from $\omega_c^{-1} = 0.1$ ms to $\omega_c^{-1} = 0.8$ ms. The integration time corresponds to $\delta\tau = \omega_0^{-1} + 2\omega_c^{-1}$, empirical time needed for the MSD to reach stationarity, hence for the microsphere to have explored all available space in the potential. Experimental data are shown as blue circles as well as a fit with the analytical expression Eq. (4.28), shown as a red line.

obtain the heat discarded by the microsphere in the fluid bath, one needs to integrate the heat production rate over a given time. As seen on the evolution of the MSD as a function of the time-lag for various correlation times (Fig. 4.9 (b)) the MSD takes longer to reach stationarity when the correlation time is larger i.e. the microsphere takes longer to explore the available space. With this in mind, a reasonable measure of the heat dissipated by the microsphere in a given correlated bath, is the heat production rate, integrated over the time needed to explore the available space, in this case $\delta\tau = \omega_0^{-1} + 2\omega_c^{-1}$. On Fig. 4.23 we show the heat production rate multiplied by the respective time intervals $(\omega_0^{-1} + 2\omega_c^{-1})$ for the same cases as in Fig. 4.22. We see that in this case, we recover an increasing dissipated heat when the correlation time increases and the microsphere explores a larger space.

The exchange of heat between the Brownian object and the fluid bath (white noise bath) implies [65] an exchange of entropy $S = -Q/T$ that follows the same decomposition into a linear housekeeping term and an exponential release during the transient. This quantity is the entropy dissipated in the form of heat by the motion of the colloidal particle in the passive fluid.

Note that an alternative expression for the heat can be found in the context of active matter and active Ornstein-Uhlenbeck processes. These different approaches lead all to similar results, since Sekimoto's definition of heat as

$$\delta q = -\left(\gamma \dot{x} - \gamma\sqrt{2D}\xi_t dt\right) dx \tag{4.29}$$

is uniquely defined [46, 155]. The differences stem from the way to evaluate this quantity. In the description of non-reciprocal systems [67], the steady-state heat is computed as a sum of correlation between variables and velocities. In our case of unidirectional coupling, this simplifies to a term $\sim \langle \eta_t \dot{x}_t \rangle$ which is the term we also obtain. Another definition is based on the deviation from the fluctuation dissipation relation, the Harada-Sasa relation [118] used in [155, 148], which, similarly to our calculations, gives a constant rate of heat production in the steady state.

4.5.6 Energy-information connection: the spectral entropy

The color protocols performed in Sec. 4.4.2 and their energetics characterisation done in Sec. 4.5.5 rise a paradox since the protocols induce a release of heat in the medium, which stems from work injected by the active force onto the microsphere, while the driving force is kept at constant amplitude. The driving thus appears costless, where *cost* is meant as an experimental quantity : no additional laser or electrical power is needed to make the system transient to a state with higher dissipation. From a thermodynamic point-of-view, there is a clear amount of energy exchanged through the protocol: the active forces produce an energetic input characterized in Sec. 4.5.5 as $\gamma\sqrt{2D_a}\eta_t \dot{x}_t dt$. This input will induce a mechanical response from the bead and therefore will dissipate heat inside the medium. What appears surprising is that the value of these two energetic terms can be varied without changing force amplitudes, but only force correlations.

This paradox can be resolved by different ways. A first simple explanation stems from a purely mechanical point of view: since the microsphere has a non-flat spectral mechanical response, it is clear that the same force amplitude will induce different response amplitudes depending on the overlap between the spectral profile of the motion and the spectral profile of the force. Another path to resolve this paradox comes when looking at correlations for what they are: part of the information content of the bath. Indeed, with respect to a white noise, built of independent random numbers, a correlated noise in containing a non-zero quantity of information. This solution draws a direct connexion between information and thermodynamics. We propose to quantify the informational content of the active bath and relate it to the thermodynamic

quantities exchanged during a STEP protocol.

The information content of the injected noise is measured by the spectral entropy H_s [170], which is precisely the Shannon entropy measured in the frequency domain. To evaluate this quantity and its relation to heat, we perform a series of measurements varying the correlation time of the noise ω_c^{-1} while keeping the other parameters constant, and we test the robustness of the result for different sets of parameters (stiffness and noise intensity). For each experiment, an equivalent white noise experiment is also performed, that allows us to extract an effective temperature evaluated through equipartition: $T_{eff} = \kappa\langle x^2\rangle_{white}/k_B$. We then compare $\Delta Q_{EX}/k_B T_{eff}$ to ΔH_s. The evaluation of H_s is done on the normalised power spectral density of the noise itself. In Fig. 4.24 (a), we represent the normalised power spectral densities (PSD) for white and colored noises generated at 20 kHz, along with the spectral boundaries used to get rid of the nonphysical part of the signal (high frequency noise of the electronics).

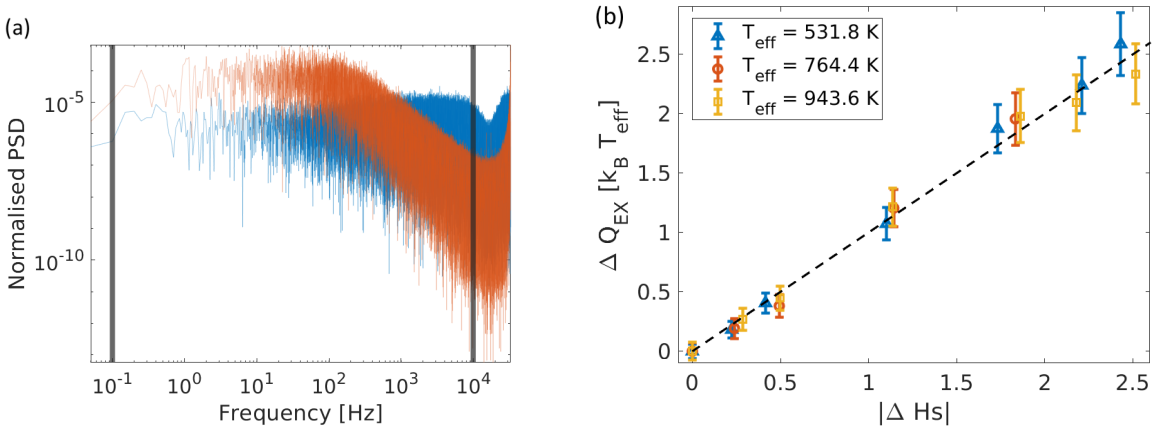

Figure 4.24: (a) Measured spectra of the white noise (blue line) and colored noise (orange line). The vertical black lines are the limits imposed on the calculation of the spectral entropy at 0.1 Hz and 10^4 Hz. (b) Measured excess heat between two NESS (in units of $k_B T_{eff}$) plotted as a function of the calculated spectral entropy, for three values of the noise amplitude, each characterized by an effective temperature T_{eff}. The dashed line has a slope equal to unity.

On this noise PSD, the spectral entropy is then evaluated as:

$$H_s = -\sum_{i=1}^{N} P(\omega_i) \ln P(\omega_i), \tag{4.30}$$

where $P(\omega_i) = S_\eta[\omega_i]/\sum_i S_\eta[\omega_i]$, and $S_\eta[\omega_i] = 2|\eta[\omega_i]|^2$ denotes the PSD value of the signal $\eta[\omega]$ at frequency ω_i. We compare this quantity to Q_{EX} which can be deduced

by the difference in variance between a reference and the state under study. On Fig. 4.24 (b) we plot Q_{EX}/k_BT_{eff} as a function of H_s. Remarkably, the plot shows that both quantities coincide over all the probed region, leading to a relation falling on the dashed line of slope 1.

We wish to test the relation between H_s and Q_{EX} in various conditions of stiffness and noise amplitude. Here we present the data from three different experiments. The first one is set with $\kappa = 33.2$ pN/µm and a pushing laser maximal power of 150 mW, leading to a white noise effective temperature of 764.4 K. The second experiment is performed with $\kappa = 14.8$ pN/µm, pushing laser power 19 mW, leading to $T_{eff} = 531.8$ K. The third experiment is done with $\kappa = 21.4$ pN/µm, pushing laser power 40 mW, leading to $T_{eff} = 943.6$ K. The strong influence of both the stiffness and noise intensity on the effective temperature is clear. This influence however does not break the central relation shown in the main text between Q_{EX} and H_s. We stress here that this relation is displayed without any fitting or adjusting parameters.

From this result, it is clear that injecting more information in the system implies a larger amount of heat dissipated during the NESS-to-NESS transient. Over the probed region, the relation is even a one-to-one relation and all the injected information is turned into heat with a meaningful dimensional factor k_BT_{eff}. However, this correlation of ΔQ_{EX} and ΔH_s is not a causality relation. The expression of both quantities can be explicitly derived in the case studied here of exponentially correlated noise. The difference of excess heat is given by the difference of variance multiplied by $\kappa/2$, leading to

$$\Delta Q_{EX} = \frac{D_a}{\omega_0}\frac{\omega_1 - \omega_2}{(\omega_0+\omega_1)(\omega_0+\omega_2)} \tag{4.31}$$

where we used the notation $\omega_1 = \omega_{c,\text{initial}}$ and $\omega_2 = \omega_{c,\text{final}}$. On the other hand, the spectral entropy can be computed analytically. We define a normalized pulsation $\Omega = \omega/\omega_c$, and write the normalized spectrum as

$$P(\Omega) = \frac{S_\eta[\Omega]}{\int S_\eta[\Omega]d\Omega} = \frac{2}{\omega_c}\frac{1}{1+\Omega^2}. \tag{4.32}$$

Therefore, the continuous spectral entropy writes:

$$\begin{aligned} H_s &= -\omega_c \int P(\Omega)\log(P(\Omega))d\Omega \\ &= 2\int \frac{\log(1+\Omega^2)}{1+\Omega^2}d\Omega + \log(\omega_c/2)\int \frac{2}{1+\Omega^2}d\Omega \\ &= 4\pi\log(2) + \log(\omega_c/2) \end{aligned} \tag{4.33}$$

where we recognised for the first integral the entropy of a Cauchy distribution ([171, 172]) and for the second integral the unit variance of the normalized process. It leads to a simple expression

$$H_s = log(\omega_c) + C \tag{4.34}$$

where $C = (4\pi - 1)\log(2)$. Therefore the difference of spectral entropy between two correlated bath writes as:

$$\Delta H_s = -\log(\omega_2/\omega_1). \tag{4.35}$$

From this derivation, it is clear that both quantities are not formally equal, one having a logarithmic profile, while the other is a ratio of polynomials. On Fig. 4.25 we plot the experimental result for excess heat and spectral entropy along with the analytical result. The excess heat explicitly depends on D_a (as seen on Eq. (4.31)) which itself depends on the amplitude of the noise sent (each noise amplitude characterized by an effective temperature T_{eff} will give another D_a, but the exact relation between D_a and T_{eff} is not known in our model). Therefore, the excess heat is not unique, but the different effective temperature T_{eff} give a family of curves, represented here as a shaded red area. The spectral entropy, in contrast is uniquely defined for all effective temperatures (black solid line).

We can observe that, despite their very different mathematical natures, both functions are very close over a wide frequency bandwidth, making them experimentally indistinguishable within our resolution. They depart from each other for high frequencies (as seen on the inset, that scans a larger bandwidth), that are out of range of the spectral mechanical response of the microsphere: as seen Sec. 4.3.4, a noise with a correlation time of 0.1 ms (hence $\omega_c = 10$ kHz) cannot be distinguished from a white noise. Finally, our experimental data spans over most of the accessible bandwidth, and the deviations appear for frequencies that are hard to access and have therefore less physical relevance in the context of microscopic mechanical systems. Tthe simplicity of the correlation between heat and information is experimentally true within our resolution and over our experimental bandwidth.

Although very close, normalized heat and spectral entropy differ, hence no causality can be deduced from information to heat. What is however formally true for all correlation times, is that both quantities vary monotonically in the same direction. Injecting more information in the system will always induce more heat dissipated during the NESS-to-NESS transition, even if both quantities are indirectly connected.

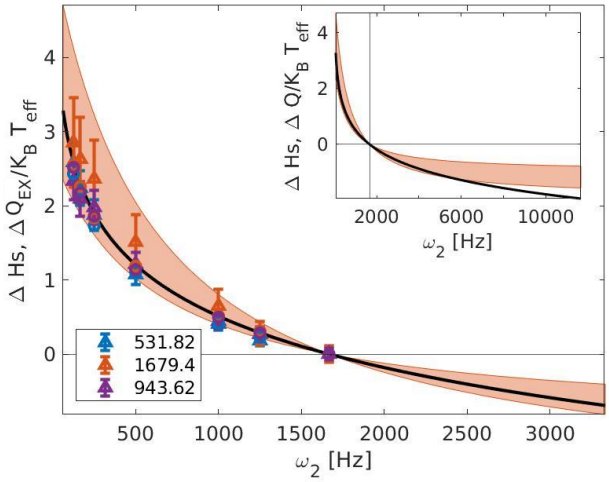

Figure 4.25: Experimental change in excess heat $\Delta Q_{EX}/k_B T_{eff}$ (triangles) and spectral entropy ΔH_s (circles) as a function of the final correlation pulsation ω_2 with constant $\omega_1 \approx 1666$ Hz (vertical black thin line in the inset). We superimpose the analytical results for the spectral entropy Eq. (4.35) (black line). We also show the excess heat difference Eq. (4.31). Since each noise amplitude (characterizd by T_{eff}) induces another value of D_a, which itself gives a different curve for ΔQ_{EX}, we represent the family of curves as a shaded area for the different values of D_a. In the inset, we plot the same analytical result but on a very large bandwidth of final pulsations.

4.6 Conclusion

In this chapter, we used radiation pressure to build a secondary artificial bath and tune its properties. We observed how the nature of this artificial bath strongly influences the properties of the trajectory of the immersed microsphere. With the case of exponentially correlated Gaussian noise, we observed a non-Brownian behaviour with superdiffusion at short time, the breaking of the law of equipartition of energy and of the fluctuation-dissipation theorem. The color of the noise was then used as a parameter to perform NESS-to-NESS transitions and the thermodynamics of the transformation was studied in the framework of stochastic energetics. This led us unveiling a remarkable connexion between the entropic content of the bath and the energy dissipated by the bead diffusing through this transition. Adding a bath with controllable properties extend the possibilities to use Brownian object as an analogue for exploring the properties of complex systems such as active matter with a strong flexibility. In the next chapter, we will explore another analogy, by playing on the de-

terministic trapping potential. Doing so, we will emulate Bohm's quantum potential and build an analogue of an open quantum system.

Chapter 5

Classical stochastic analogue of a quantum process

In this chapter we devise a classical stochastic analogue of a quantum process. Analogies in physics constitute a powerful tool for the understanding of complex phenomena. Since James Clark Maxwell ideas that an analogy is a two-folded reasoning, mirror symmetric of a pun, as *"Now, as in a pun two truths lie hid under one expression, so in an analogy one truth is discovered under two expressions"* [73] analogies have been extensively used to reformulate scientific questions within a different framework. Not only they enable us to apply our knowledge and intuition of a specific domain to a different field, but also offer the possibility to transfer experimental results from one branch of physics to another. For instance, table-top experiments have been used to get insight into complex – and experimentally unreachable – domains such as quantum gravity and black holes, using acoustic [75] or optic [173] analogs. Of particular interest here are classical analogs of quantum systems [76], based on optic [77] or hydrodynamic [174, 175] experiments. These analogs rely on the Madelung representation of the wave function and the corresponding "hydrodynamic" evolution equations for its amplitude and phase, as in the de Broglie-Bohm version of quantum mechanics [176, 177, 178].

When a quantum particle is immersed in a thermal bath, and taking the limit of vanishing mass, the hydrodynamic model can be cast in the form of a quantum drift-diffusion (QDD) equation [179, 180], which is often used to describe charge transport in semiconductor devices. Here, the QDD equation will be the starting point of our quantum-classical analogy. Indeed, the QDD model has the form of a classical Fokker-Planck equation with the addition of an extra quantum Bohm potential $Q = -\frac{\hbar^2}{2m}\frac{\Delta\sqrt{n}}{\sqrt{n}}$, which depends on the position probability distribution $n(x,t)$ of the particles and carries the information about quantum correlations. As is well know, any Fokker-Planck

equation is equivalent to a stochastic process described by a Langevin equation.

Our goal here is to use such underlying classical stochastic process to emulate the evolution of a quantum system. For the present case, the situation is somewhat more complicated, because the Bohm potential depends on the position probability distribution, making the process nonlinear, as the random variable depends on its own probability density. These types of stochastic processes are known as McKean-Vlasov processes [181] and have been extensively studied in the past [182].

Here, we devise a classical analog of this process by reconstructing the probability distribution by statistical means. Our strategy is based on the possibility of simultaneously manipulating many classical objects, whose ensemble distribution $n(x,t)$ is used as an input to construct the Bohm potential, thus recovering the results of the QDD model. This can be achieved numerically by simulating $\mathcal{N}$ stochastic trajectories, but, most importantly, can also be realized experimentally, by means of multiple optical trapping of micron-sized Brownian particles [183], as illustrated schematically in Fig. 5.1. Experimentally, up to a few thousand traps can be realized in practice [184, 185].

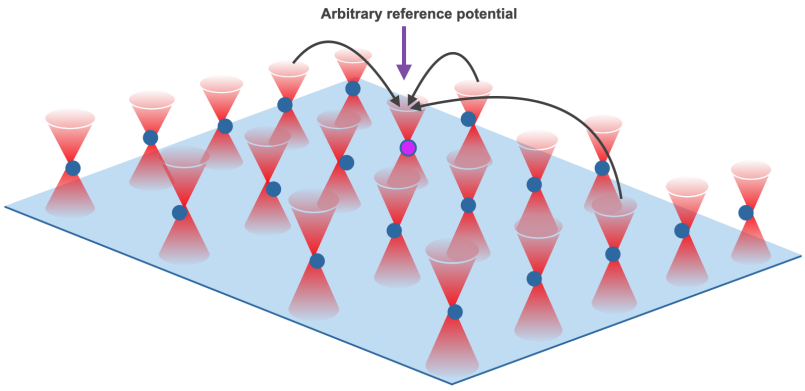

Figure 5.1: Schematic view of a possible implementation of the quantum-classical analogs in a multiple optical trapping system. Each identical trap contains a single Brownian particle and the trapping potential, shared among all traps, is controllable. All the particle positions are recorded and the information is collected at each time-step to build the quantum Bohm potential. The latter is then added to the optical trapping potential, thereby acting on all trajectories. This information transfer is represented by the black arrows pointing to one chosen trap.

In the first two sections, we introduce the framework of quantum hydrodynamics and the QDD model. We compare it to an exact kinetic result for the case of a harmonic

potential and then develop our analogue model, through the associated stochastic process. In the two next sections, we focus on three configurations that nicely capture some typical quantum effects: (i) a quantum increase of the position autocorrelation time, (ii) an analog of the quantum tunnelling effect, and (iii) a departure from the classical dynamics for out-of-equilibrium states. These effects will be investigated with both numerical simulations – (i) and (ii) – and optical experiments (iii).

5.1 Quantum hydrodynamic

5.1.1 Madelung transformation: a set of fluid equations for a quantum state

In this section we describe how the Madelung transormation [176, 186] allows one to build a set of fluid equations for a quantum state reminiscent of classical hydrodynamics. The Schrodinger equation of an isolated time dependent wavefunction $\Psi(x,t)$ writes

$$i\hbar\frac{\partial\Psi(x,t)}{\partial t} = \frac{-\hbar^2}{2m}\frac{\partial^2\Psi(x,t)}{\partial x^2} + V_{\text{ext}}(x)\Psi(x,t), \tag{5.1}$$

where $\hbar$ is Planck's constant, m the mass of the quantum object and $V_{\text{ext}}(x)$ an external potential. The wavefunction $\Psi(x,t)$ can be written in a polar form

$$\Psi(x,t) = \sqrt{n(x,t)}e^{i\phi(x,t)/\hbar} \tag{5.2}$$

where $n(x,t)$ is the probability density and $\phi(x,t)$ the phase. Injecting this structure into Schrodinger equation and separating the real and imaginary parts gives a system of two equation :

$$\begin{cases} \dfrac{\partial n(x,t)}{\partial t} = -\dfrac{\partial j}{\partial x} \\ -\dfrac{\partial\phi(x,t)}{\partial t} = \dfrac{1}{2m}\left(\dfrac{\partial\phi(x,t)}{\partial x}\right)^2 + V_{ext}(x) - \dfrac{\hbar^2}{2m}\dfrac{\Delta\sqrt{n(x,t)}}{\sqrt{n(x,t)}}. \end{cases} \tag{5.3}$$

where the current $j(x,t) = n(x,t)u(x,t)$ depends on the mean velocity $u(x,t) = \nabla\phi(x,t)/m$. The first equality is a conservation equation for the probability density $n(x,t)$. The second relates the time evolution of the phase to three energetic contributions. First, with the definition of the mean velocity, we see that the term $\frac{1}{2m}\left(\frac{\partial\phi(x,t)}{\partial x}\right)^2$ is the kinetic energy of the particle. The second term $V_{\text{ext}}(x)$ is the external potential and the third term a "quantum" potential

$$Q(x,t) = \frac{-\hbar^2}{2m}\frac{\Delta\sqrt{n(x,t)}}{\sqrt{n(x,t)}}, \tag{5.4}$$

due to the curvature of the wavefunctions amplitude. This quantum potential $Q(x)$, also called Bohm potential because of its use in de-Broglie-Bohm formalism of quantum mechanics encapsulates the non-local effects of quantum nature of the wavefunction, with an explicit dependency on the density $n(x,t)$. Finally, by taking the gradient of the second equation on $\phi(x,t)$ and recalling the mean velocity $u(x,t)$, we obtain a set of equations that resemble the classical conservation and Euler equations for a fluid:

$$\begin{cases} \dfrac{\partial n(x,t)}{\partial t} = -\dfrac{\partial n(x,t)u(x,t)}{\partial x} \\ \dfrac{\partial u(x,t)}{\partial t} + u\dfrac{\partial u(x,t)}{\partial x} = -\dfrac{1}{m}\nabla\left(V_{ext}(x) + Q(x,t)\right). \end{cases} \tag{5.5}$$

The Madelung transformation shows, on the simple example of an isolated quantum state $\Psi(x,t)$, how its dynamics can be described with a hydrodynamic model on the probability density $n(x,t)$. It introduces the quantum potential $Q(x,t)$ that contains all information about the quantum nature of the system, it is the only difference with a classical set of hydrodynamic equation. In the next section, we turn to the case of an open quantum system, strongly coupled to a classical thermal environment. In this context as well, a hydrodynamical model can be derived and the same quantum potential will appear.

5.1.2 Open quantum system, moment expansion of the Wigner-Boltzmann equation

To describe the dynamics of a quantum particle interacting with a classical thermal environment, we cannot use Madelung formalism anymore. A quantum particle interacting with a thermal environment is not described by a pure state $\Psi(x,t)$ but by a statistical mixture, framed as a density matrix

$$\rho(x,x',t) = \sum_{\alpha=1}^{N} w_\alpha \Psi_\alpha^*(x,t)\Psi_\alpha(x',t) \tag{5.6}$$

where w_α is the probability of state Ψ_α. In order to build a phase-space tool similar to the classical phase-space distribution describing the evolution of a probability density, we use the Wigner transform of the density matrix

$$f(x,p,t) = \frac{1}{2\pi\hbar}\int d\lambda e^{ip\lambda/\hbar}\rho(x_+,x_-,t) \tag{5.7}$$

where $f(x,p,t)$ is Wigner's quasi-distribution and $x_\pm \equiv x \pm \lambda/2$. The dynamics of the Wigner function is described by the Wigner equation

$$\frac{\partial f}{\partial t} + \frac{p}{m}\frac{\partial f}{\partial x} = \frac{i}{2\pi\hbar^2}\int e^{\frac{i(p-p')\lambda}{\hbar}}\left[V_{\text{ext}}\left(x_+\right) - V_{\text{ext}}\left(x_-\right)\right] f(r,p',t)d\lambda\, dp' \tag{5.8}$$

that relates the hydrodynamic derivative $\frac{\partial f}{\partial t}+\frac{p}{m}\frac{\partial f}{\partial x}$ to the potential energy. We furthermore introduce a general collision operator $\Theta(f)$, similarly to the Boltzmann equation approach to represent the effects of the classical environment. Then the dynamics of a quantum particle interacting with a classical thermal environment can be described, in a first approximation, by a Wigner-Boltzmann equation [187]

$$\frac{\partial f}{\partial t}+\frac{p}{m}\frac{\partial f}{\partial x}-\frac{i}{2\pi\hbar^2}\int e^{\frac{i(p-p')\lambda}{\hbar}}\left[V_{\text{ext}}\left(x_+\right)-V_{\text{ext}}\left(x_-\right)\right]f(r,p',t)d\lambda\, dp'=\Theta(f). \quad (5.9)$$

The collision operator will be taken, in this first approximation, as $\Theta(f)=-(f-f_0)/\tau$ where f_0 is the thermal equilibrium distribution and τ a characteristic relaxation time that will be defined later.

An hydrodynamic framework similar to the Madelung equations can be retrieved by taking moments of Wigner equation [188, 189, 187]. The moments of order k of the Wigner distribution, defined as $m_k=\int f(x,p,t)p^k dp$ are connected to physical fluid quantities. For example, the zero-th order moment is the density

$$n(x,t)=\int f(x,p,t)dp, \quad (5.10)$$

the first order moment is the current

$$j(x,t)=\frac{1}{m}\int pf(x,p,t)dp, \quad (5.11)$$

connected to the mean velocity $u(x,t)=j(x,t)/n(x,t)$.

The dynamics governing the moments can be derived by taking integrals of Wigner's equation (5.9). The zero-th order moment gives

$$\frac{\partial n}{\partial t}+\frac{\partial(nu)}{\partial x}=0, \quad (5.12)$$

which is a continuity equation, denoting the conservation of mass. The dynamics of the mean velocity $u(x,t)$ appearing in this equation will be given by the next order moment of Wigner equation, starting an infinite hierarchy of coupled partial differential equations. The first order moment of Wigner equation Eq. (5.9) yields

$$\frac{\partial(nu)}{\partial t}+\frac{\partial(nu^2)}{\partial x}=-\frac{1}{m}\frac{\partial P}{\partial x}-\frac{n}{m}\frac{\partial V_{\text{ext}}}{\partial x}-\frac{nu}{\tau} \quad (5.13)$$

where

$$P=\frac{1}{m}\int f(x,p,t)(p-m\langle u\rangle)^2 dp \quad (5.14)$$

the pressure, second order momentum moment of Wigner distribution, with only the statistical fluctuations of momentum $p-m\langle u\rangle$.

As shown in [190], the pressure can be decomposed into $P = P_C + P_Q$ with a classical part P_C and a quantum part P_Q by reintroducing the polar form used in Madelung derivation of Sec. 5.1.1 for each wavefunction Ψ_α. Then the classical pressure takes the form of a velocity dispersion as in a classical gas and can, as for a Maxwell-Boltzmann equilibrium at temperature T be written as

$$P_C = nk_BT, \tag{5.15}$$

where k_B is Boltzmann's constant. The quantum part P_Q, proportional to $\hbar$ has no classical counterpart. It can be expressed as a combination of gradients of the density $n(x,t)$ and identifies with the quantum potential introduced in the Madelung formalism

$$\partial_x P_Q = n\partial_x Q, \tag{5.16}$$

see [190].

Using these expressions, one arrives at a set of two quantum hydrodynamic equations for the density $n(x,t)$ and the mean velocity $u(x,t)$:

$$\frac{\partial n}{\partial t} + \frac{\partial (nu)}{\partial x} = 0, \tag{5.17}$$

$$m\left[\frac{\partial (nu)}{\partial t} + \frac{\partial (nu^2)}{\partial x}\right] = -n\left(\frac{\partial V_{\text{ext}}}{\partial x} + \frac{\partial Q}{\partial x}\right) - \frac{mnu}{\tau} - k_BT\frac{\partial n}{\partial x}, \tag{5.18}$$

Quantum effects are contained in the Bohm potential $Q[n(x,t)]$, whereas the effects of the environment contained in the temperature-dependant term and the damping term (the last two terms in the RHS of Eq. (5.18)).

5.1.3 QDD as large friction or small mass limit of QHD

In this subsection, we take a viscous limit of the quantum fluid equations Eq. (5.17) and (5.18). It is natural to choose for τ the classical thermalization time of velocities: $\tau = m/\gamma$, where γ is the drag coefficient of the object in the fluid that makes up the thermal bath. Finally, taking the limit $\tau \to 0$ and $m \to 0$, while $m/\tau = \gamma$ remains finite, enables us to drop the inertial terms [left-hand side of Eq. (5.18)] an isolate $n(x,t)$ as

$$n(x,t) = \frac{u}{\gamma}\left[k_BT\frac{\partial n}{\partial x} + n\frac{\partial}{\partial x}\left(V_{\text{ext}} + Q\right)\right]. \tag{5.19}$$

Injecting the expression for nu into the continuity equation ((5.17)), leads to a single quantum drift-diffusion (QDD) equation for the density [180]:

$$\frac{\partial n}{\partial t} = \frac{1}{\gamma}\frac{\partial}{\partial x}\left(n\frac{\partial}{\partial x}\left(V_{\text{ext}} + Q\right)\right) + \frac{k_BT}{\gamma}\frac{\partial^2 n}{\partial x^2}. \tag{5.20}$$

This is a first-order equation for the time-evolution of the density n is given by a drift term $\sim \partial_x[n \times \text{force}]$ and a diffusion term $\sim \partial_x^2 n$. It has the structure of a classical Fokker-Planck equation for Brownian motion, and differs from it only by the presence of the Bohm potential Q. This is an important difference, however, as the Bohm potential is itself a functional of the probability density $n(x,t)$ and its derivatives. This analogy with a classical diffusion equation will be exploited later in Sec. 5.2.

5.1.4 Harmonic oscillator

When the external potential V_{ext} is quadratic in position x, simple analytical solutions can be derived. As the classical thermal equilibrium distribution in a quadratic potential is a Gaussian, we inject here a Gaussian Ansatz for the QDD model described above for the case of harmonic confinement. Remarkably, this Ansatz is an exact solution and the distribution stays Gaussian for all times. In this case, the QDD model, which is an equation on probability distributions, simplifies to a simple first order differential equation for its variance. We furthermore verify that in that special case, we recover in the stationary regime and at first order in $\hbar$ the same result as the momentum integral of the corresponding Wigner function. The latter is an exact result for a harmonic oscillator in a thermal bath, and the agreement with the stationary regime of QDD strongly validates the latter model.

We consider a harmonic external potential $V_{ext} = \frac{1}{2}\kappa x^2$ with stiffness κ, and a Gaussian probability distribution

$$n(x,t) = \frac{1}{\sqrt{2\pi S(t)}} e^{-x^2/2S(t)} \tag{5.21}$$

where $S(t)$ is the time dependent variance. Within the Gaussian assumption the Bohm potential can be analytically derived

$$\begin{aligned} Q(x,t) &= \frac{-\hbar^2}{2m} \frac{\Delta\sqrt{n(x,t)}}{\sqrt{n(x,t)}} \\ &= \frac{-\hbar^2}{2m} \left(\frac{-1}{2S(t)} + \frac{x^2}{4S^2(t)} \right) \end{aligned} \tag{5.22}$$

where we notice the quadratic form in position x. The Bohm force will therefore be linear in x, similar to the external force. If we inject the Gaussian Ansatz and the harmonic assumption in the QDD model and solve for $S(t)$, we obtain

$$\frac{1}{2}\frac{dS(t)}{dt}\beta n = -\frac{2\kappa}{\gamma} S(t)\beta n + \frac{\hbar^2}{2m\gamma S(t)}\beta n + \frac{2k_B T}{\gamma}\beta n \tag{5.23}$$

with $\beta \equiv \left[\frac{x^2}{S^2} - \frac{1}{S}\right]$ and n that can be simplified leading to the variance ordinary differential equation (ODE):

$$\frac{dS(t)}{dt} = -\frac{2\kappa}{\gamma}S(t) + \frac{\hbar^2}{2m\gamma S(t)} + \frac{2k_BT}{\gamma}. \tag{5.24}$$

This result shows that any Gaussian initial distribution injected in the QDD model will remain Gaussian at any time, as shown in the general QHD case in [191]. Therefore, the QDD model within these assumptions can be fully described by the simple first order differential equation of its variance (for a zero mean). Eq. (5.24) is non-linear and the term $\hbar^2/2m\gamma S(t)$ that encapsulates the quantum effects adds a non-trivial dependence on the variance, and therefore on time.

The equilibrium variance is the stationary $dS(t)/dt = 0$ solution of this differential equation

$$S^{eq}_{QDD} = \frac{k_BT}{2\kappa} + \frac{1}{2}\sqrt{\left(\frac{k_BT}{\kappa}\right)^2 + \frac{\hbar^2}{m\kappa}}. \tag{5.25}$$

The classical limit where $\hbar$ vanishes is the standard variance of a Brownian motion in an harmonic potential i.e. k_BT/κ. Here the quantum nature of the object adds a correction that increases the value of equilibrium variance.

Next, we wish to verify the validity of the model used here. The result obtained for the variance is the consequence of a strong friction limit of the quantum hydrodynamic model. However, an exact result can be obtained for this special case of the harmonic oscillator. The Wigner function of a harmonic oscillator in contact with a thermal bath is derived in [192]. One starts from the unnormalized density operator in the canonical ensemble $\hat{\Omega} = e^{-\beta\hat{H}}$, where $\beta = 1/k_BT$ and $\hat{H} = \frac{1}{2m}\hat{p}^2 + \frac{m\omega_{ho}^2}{2}\hat{x}^2$ is the Hamiltonian of the system. $\hat{\Omega}$ obeys to the Bloch equation for the density operator in the canonical ensemble. It can be translated it into an equation for phase-space function $\Omega(x,p)$. Applying it to the special case of harmonic oscillator, one can solve for $\Omega(x,p)$ obtaining

$$\Omega(x,p) = \operatorname{sech}\left(\frac{\hbar\omega_{ho}}{2k_BT}\right) e^{-\frac{2}{\hbar\omega_{ho}}\tanh\left(\frac{\hbar\omega_{ho}}{2k_BT}\right)H(x,p)} \tag{5.26}$$

where ω_{ho} is the characteristic frequency (hence $m\omega_{ho}^2 = \kappa$, the stiffness). Finally, normalising the resulting expression gives the Wigner function of a harmonic oscillator at temperature T

$$P_w(x,p) = \frac{1}{\pi\hbar}\tanh\left(\frac{\hbar\omega_{ho}}{2k_BT}\right) e^{\frac{-2}{\hbar\omega_{ho}}\tanh\left(\frac{\hbar\omega_{ho}}{2k_BT}\right)\left[\frac{p^2}{2m} + \frac{m\omega_{ho}^2}{2}x^2\right]}. \tag{5.27}$$

This distribution is Gaussian both in position and momentum variables. It has the form of the classical canonical distribution $\frac{1}{\mathcal{Z}}e^{-H/k_BT_{eff}}$ with an effective temperature $T_{eff} > T$ depending on $\hbar$. The effective temperature accounts for the quantum broadening of the distribution, similarly to the increase of variance in the QDD result.

By integrating over the momentum p we obtain the density $n(x,t)$:

$$n(x,t) = \int P_w(x,p)dp = \sqrt{\frac{m\omega_{ho}}{\pi\hbar}\tanh\left(\frac{\hbar\omega_{ho}}{2k_BT}\right)}e^{\frac{-m\omega_{ho}}{\hbar}\tanh\left(\frac{\hbar\omega_{ho}}{2k_BT}\right)x^2}. \tag{5.28}$$

In the case where quantum effects, related to the quanta of energy $\hbar\omega_{ho}$ are very small with respect to thermal energy k_BT, we can consider $\frac{\hbar\omega_{ho}}{k_BT} \ll 1$ and Taylor expand the result for the distribution. More precisely, we expand both hyperbolic tangent terms, using $\tanh(\epsilon) \approx \epsilon - \frac{\epsilon^3}{3}$, and we obtain

$$n(x,t) \approx \sqrt{\frac{m\omega_{ho}}{2\pi k_BT} - \frac{\hbar^2 m\omega_{ho}^2}{24\pi(k_BT)^3}}e^{\left(\frac{-m\omega_{ho}}{2k_BT}+\frac{\hbar^2m\omega_{ho}^2}{24(k_BT)^3}\right)x^2} \tag{5.29}$$

which is a Gaussian distribution in position x as the solution of the QDD model. We can note that if we had only kept the first order $\tanh(\epsilon) \approx \epsilon$, we would have recovered the classical result. To the next order and with $\kappa = m\omega_{ho}^2$, the variance becomes:

$$S_{ho} = \left(\frac{m\omega_{ho}^2}{k_BT} - \frac{\hbar^2m\omega_{ho}^2}{12(k_BT)^3}\right)^{-1} \approx \frac{k_BT}{\kappa} + \frac{\hbar^2}{12mk_BT}. \tag{5.30}$$

This result corresponds up to a factor 1/3 to the first order term in the stationary solution of the variance obtained from QDD model:

$$S_{QDD}^{eq} = \frac{k_bT}{2\kappa} + \frac{1}{2}\sqrt{\left(\frac{k_BT}{\kappa}\right)^2 + \frac{\hbar^2}{m\kappa}} \approx \frac{k_BT}{\kappa} + \frac{\hbar^2}{4mk_BT}. \tag{5.31}$$

We observe a factor 1/3 in the first-order quantum correction between the hydrodynamic model (QDD) and the exact kinetic model (Wigner function). To understand this discrepancy we discuss again the closure relation used in Sec. 5.1.2 on the pressure P to break the infinite hierarchy of moment equations. We saw that the pressure can be separated in two components, a classical pressure and a quantum pressure. For both we assumed a simple closure relation, for the classical pressure we wrote $P_C = nk_BT$ and for the quantum part, we identified its gradient $\partial_x P = n\partial_x Q$ with the gradient the quantum potential Q. As discussed in [190] (Sec. 3.1), these closure relations are not universal, but rather part of a family of relations, governed by two parameters (γ, ζ) as

$$P_C = n_{eq}k_BT\left(\frac{n}{n_{eq}}\right)^{\gamma} \tag{5.32}$$

and

$$\frac{\partial P_Q}{\partial x} = \zeta n \frac{\partial Q}{\partial x}. \tag{5.33}$$

The values of γ and ζ are not always equal to unity but rather depend on the specific system under study. As shown in [190], two extreme cases (high-frequency plasmons and low-frequency phonons) can be investigated to derive values for γ and ζ. In the case of low-frequency acoustic waves (which is relevant here), phonons propagates in the lattice with a phase velocity small in comparaison with the electronic thermal velocity. The dispersion relations derived from the exact kinetic model and the fluid equations coincide if $\gamma = 1$ (because we work at constant temperature T) and $\zeta = 1/3$ as in our case. The fact that our "viscous" fluid limit coincides with the phononic picture more than with the plasmonic case is not surprising.

The comparaison of the equilibrium variance derived from the QDD model with the kinetic result derived from Wigner equation, together with the proposed explanation for the 1/3 difference validates the accuracy of QDD to describe the properties of a quantum object evolving in a classical environment.

By anticipating the numerical and experimental implementations of this model later in this chapter, we stress that this 1/3 factor will be absorbed into an adimensional parameter, governing the strength of quantum effects.

5.2 Fokker-Planck equation and classical analogue

5.2.1 Drift and diffusion equation: analogous to Fokker-Planck

The quantum drift diffusion (QDD) model Eq. (5.20) derived above and studied for the special case of a harmonic oscillator has the structure of a Fokker-Planck equation describing the evolution of the probability density of a Brownian object in a potential, under the random action of thermal forces. Such Fokker-Planck equation was discussed in the classical regime in Chap. 2. In this section we use this formal analogy between the quantum model and a classical equation to devise an operative analogue.

We recall the one-dimensional Fokker-Planck equation for a probability density $n(x,t)$ [110]:

$$\frac{\partial n(x,t)}{\partial t} = -\frac{\partial}{\partial x}\left[A(x,t)n(x,t)\right] + \frac{1}{2}\frac{\partial^2}{\partial x^2}\left[B(x,t)n(x,t)\right] \tag{5.34}$$

with a general drift coefficient $A(x,t)$ and a general diffusion $B(x,t)$. For a classical harmonic oscillator, A is the gradient of the external potential V_{ext} divided by the

viscosity γ and $B(x,t) \equiv 2D = 2k_BT/\gamma$, is a constant. We therefore obtain:

$$\frac{\partial n(x,t)}{\partial t} = -\frac{\partial}{\partial x}\left[\frac{\kappa(t)}{\gamma}x\ n(x,t)\right] + D\frac{\partial^2}{\partial x^2}\left[n(x,t)\right] \tag{5.35}$$

that is Eq. 2.18.

The QDD model Eq. (5.20) takes this form (5.34) as well, if $A(x,t) = \frac{1}{\gamma}\frac{\partial}{\partial x}(V_{ext}(x) + Q[n])$ while keeping $B(x,t) = 2D$. We know that the specificity of the quantum potential is that it explicitly depends on the probability density $n(x,t)$. Therefore, we emphasise this dependence by writing it explicitly as a functional $Q[n]$. This dependence of course induces a strong difference between the classical Fokker-Planck equation and the QDD model: the drift coefficient A explicitly depends on the density for the QDD whereas it was a simple function of position x in the classical case.

Despite this important difference, writing the QDD under this form (5.34) suggest that it can be emulated by classical means if one can mimic the quantum potential $Q[n]$. This will be made more clear in the next section where we discuss the stochastic process underlying the QDD model.

5.2.2 Associated McKean-Vlasov stochastic process

From classical statistical mechanics, we know that the Fokker-Planck equation governs the evolution of the probability distribution of a diffusive object. The latter can equivalently be described at a microscopic level by a Langevin equation, governing its stochastic trajectory. By the same token, we propose here to study the stochastic process that is associated with the Fokker-Planck point-of-view of QDD model. The Langevin equation associated with the general Fokker-Planck equation Eq. (5.34) characterised by the drift $A(x,t)$ and the diffusion B is

$$dx_t = A(x,t)dt + \sqrt{B}dW_t, \tag{5.36}$$

where dW_t is the Wiener increment, white noise, with zero mean: $\langle dW_t \rangle = 0$ and no memory: $\langle dW_t dW_s \rangle = \delta(t-s)dt$. This stochastic differential equation describes the dynamics of the position x_t as a fonction of time, its solution can be computed via Laplace transform, as it was done in the first chapter Chap. 2. The probability distribution of the random variable x_t obeys to the associated Fokker-Planck equation. Hence an experimental or numerical realisation of the stochastic process Eq. (5.36) allows to obtain the result of the Fokker-Planck equation Eq. (5.34).

Here, we propose to use the stochastic process associated with the QDD model to emulate the dynamic of the quantum density $n(x,t)$. The stochastic process associated with the QDD model Eq. (5.20) can be written as

$$dx_t = -\frac{1}{\gamma}\frac{\partial}{\partial x}\left(V_{\text{ext}}(x,t) + Q[n]\right)\,dt + \sqrt{\frac{2k_BT}{\gamma}}dW_t, \tag{5.37}$$

where again, we emphasise the functional dependency of the quantum potential on the probability density as $Q[n] = -\frac{\hbar^2}{2m}\frac{\Delta\sqrt{n}}{\sqrt{n}}$. For a quantum particle evolving in the potential V_{ext}, the quantum potential in an intrinsic effect, arising, as we have seen in Sec. 5.1.2 from the quantum component of the pressure. Yet we see here that it takes the simple form of an additional force in a Langevin equation.

A large number of trajectories x_t obeying Eq. (5.37) are needed to probe the evolution of the density $n(x,t)$, yet the evaluation of the quantum potential rely on the instantaneous knowledge of $n(x,t)$ itself. Therefore, in order to emulate Eq. (5.37) the key issue is to be able to inject instantaneously the probability distribution $n(x,t)$ into the random process. This can be achieved if one can generate (numerically or experimentally) an ensemble of $\mathcal{N}$ simultaneous trajectories in order to reconstruct $n(x,t)$, at each time-step. Then, the quantum potential is derived from the measured density and injected as a force for the next time-step. This method is detailed on Fig. 5.2. The ensemble of trajectories can be initiated with an arbitrary distribution and will converge towards the solution $n(x,t)$ of the QDD model. Experimentally, this may be implemented using a multiple optical trapping system (see Fig. 5.1) where the ensemble of particles are used to probe the distribution. Stochastic equations of this type, where the microscopic random variable depends on its own probability distribution are called McKean-Vlasov processes.

5.2.3 Non-dimensional equations

Deriving a non-dimensional writing of both the QDD model and the associated McKean-Vlasov process underlines two points. Firsts it shows that all physical constants can be neatly described by a single parameter ϵ that simplifies numerical and experimental implementation. Second, this parameter has a clear physical meaning, which clarifies the relation between quantum and classical effects.

In order to derive a non-dimensional description of the dynamical equations for

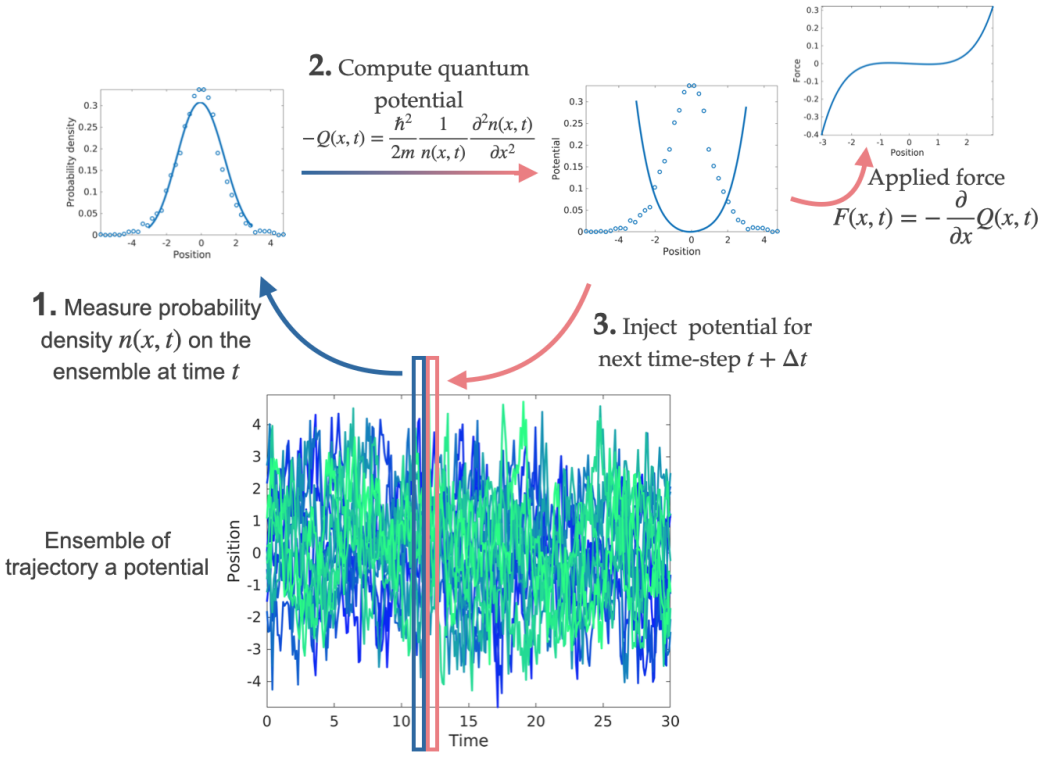

Figure 5.2: Method used to implement a McKean-Vlasov process using a statistical ensemble. First $\mathcal{N}$ random variable are drawn in an initial probability distribution, e.g. the solution of a simple Langevin equation without the quantum potential. Then at each time-step, the probability distribution of positions $n(x,t)$ is measured as a histogram on the ensemble. From this evaluation of the density, the quantum potential $Q[n]$ is derived and applied on all the particles for the next time-step $t + \Delta t$. For any arbitrary initial condition, the system will relax towards the quantum solution of the QDD model. The parameters driving the dynamic of the system are the external potential and the properties of the thermal environment encapsulated in the diffusion coefficient. If they are varying in time, the ensemble of particles will undergo a transient evolution out of equilibrium, from which we can probe the time evolution of the non-stationary density.

$n(x,t)$ and for x_t, we start with the QDD

$$\frac{\partial n}{\partial t} = \frac{k_B T}{\gamma}\Delta n - \frac{\hbar^2}{2m\gamma}\nabla\left[n\nabla\left(\frac{\Delta\sqrt{n}}{\sqrt{n}}\right)\right] + \frac{1}{\gamma}\nabla\left[n\nabla V\right], \tag{5.38}$$

and make the following change of variables, focusing on a quadratic external potential $V_{ext} = \frac{1}{2}\kappa(t)x^2$ for simplicity:

$$\begin{cases} t \to \tilde{t} = t/\tau_{relax}, \\ x \to \tilde{x} = x/\lambda_\kappa, \\ V = \dfrac{1}{2}\kappa x^2 \to \tilde{V} = \dfrac{1}{2}\kappa x^2/\kappa_i \lambda_\kappa^2. \end{cases} \tag{5.39}$$

Here, κ_i corresponds to the initial stiffness, $\tau_{relax} = \gamma/\kappa_i$ is the corresponding relaxation time and $\lambda_\kappa \equiv \sqrt{\frac{k_B T}{\kappa_i}}$ the classical width of the harmonic oscillator at thermal equilibrium fixed by equipartition. This change of variables leads to

$$\frac{\partial n}{\partial \tilde{t}} = \Delta n - \epsilon^2 \nabla \left[n \nabla \left(\frac{\Delta \sqrt{n}}{\sqrt{n}} \right) \right] + \nabla \left[n \tilde{\kappa}(t) \tilde{x} \right], \tag{5.40}$$

where

$$\epsilon \equiv \sqrt{\frac{\hbar^2 \kappa_i}{2m(k_B T)^2}} \tag{5.41}$$

is a dimensionless parameter that can be described as half the ratio between the de Broglie thermal length $\lambda_{\mathrm{dB}} = \sqrt{2\pi\hbar^2/mk_BT}$ and the classical width of the harmonic oscillator at thermal equilibrium λ_κ as

$$\epsilon = \frac{\lambda_{dB}}{2\lambda_k}. \tag{5.42}$$

Another possible interpretation can be given as the ratio between the quantum decoherence time and the thermal relaxation time $\tau_{relax} = \gamma/\kappa$. Following [193], the loss of quantum coherence is governed by a typical time scale $\tau_D = \tau_{relax} \left(\frac{\hbar^2}{2mk_BT\Delta x^2} \right)$ where Δx is a typical length scale of motion. In our case, we propose $\Delta x = \lambda_\kappa = \sqrt{k_B T/\kappa}$. This gives

$$\epsilon^2 = \frac{\tau_D}{\tau_{relax}}, \tag{5.43}$$

hence the ratio between the decoherence time and the relaxation time.

Finally, the non-dimensional stochastic McKean-Vlasov process becomes

$$d\tilde{x}_t = -\nabla \tilde{V}_{ext} d\tilde{t} + \epsilon^2 \nabla \left(\frac{\Delta \sqrt{n}}{\sqrt{n}} \right) d\tilde{t} + \sqrt{2} d\tilde{W}_t. \tag{5.44}$$

Here again, ϵ measures the importance of quantum effects with respect to thermal fluctuations. This non-dimensional process will be studied numerically in the next section. Note that for simplicity, the tildes $\tilde{x}$ and $\tilde{t}$ denoting non-dimensionality will be dropped in the numerical work.

One can ask how this model relates to the experimental framework of this PhD thesis described in the previous chapters. In an experimental scheme like our optical

trapping setup, it is possible to study the evolution of a Brownian object obeying the Langevin equation (Ornstein-Uhlenbeck process in this case of harmonic confinement). The typical size of the microsphere trapped is the micron. For such an object at room temperature, the magnitude of the quantum effects due to its a priori quantum nature are minute and ϵ is typically of the order of 10^{-17}. In this case, the quantum potential can be neglected and we retrieve of course the classical Ornstein-Uhlenbeck process study in details Chap. 2.

However, the form of the non-dimensional writing of QDD, with all parameters contain in ϵ, suggests that an arbitrary rescaling of the process is possible, keeping all the specificities of the quantum dynamic of QDD, while working at room temperature. This is the nature of the analogue proposed here: in our classical analog, ϵ is no longer related to Planck's constant, but can be adjusted at will, within the practical limits of the experimental or numerical realization. The classical case, i.e. standard Brownian motion, corresponds to $\epsilon = 0$, while when $\epsilon \approx 1$ "quantum" effects play a significant role.

5.3 Numerical simulation in arbitrary potentials

5.3.1 Numerical method for a McKean-Vlasov process

Our numerical approach is based on the Euler-Maruyama stochastic algorithm [106, 194] already detailed in Chap. 2. It consists in a discretisation of the stochastic differential equation up to $\mathcal{O}(\Delta t^{1/2})$ in time increment. For the stochastic equation Eq. (5.44) where all variables are non-dimensional, it takes the form

$$y_{i+1} = y_i - \nabla V_{ext}(y_i)\Delta t + \epsilon^2 \nabla \left(\frac{\Delta \sqrt{n(y_i)}}{\sqrt{n(y_i)}} \right) \Delta t + \sqrt{2\Delta t}\xi_i, \tag{5.45}$$

where y_i is the numerical approximation of x_t (non-dimensional) and ξ_i is a normally distributed random variable. Our numerical approach is the following: as for a classical stochastic algorithm, we compute one time-step for $\mathcal{N}$ Brownian particles simultaneously and then we evaluate the forces for the next time-step.

As detailed above, the specificity of this McKean-Vlasov process arises from the evaluation of the quantum force, which demands an evaluation of the density $n(y_i)$. The density can be probed as a histogram on the ensemble of particles. However, the quantum force contains a third order derivative of the density and some care needs to be taken on the shape of the measured probability density to avoid divergence of

the algorithms. We use a *particle in cell* method to evaluate n: to each particle of the ensemble, we associate a Gaussian kernel, their sum being a reasonably smooth evaluation of the density. From the evaluation of $n(y_i)$ we are able to compute the quantum force $\nabla\left(\frac{\Delta\sqrt{n(y_i)}}{\sqrt{n(y_i)}}\right)$, used to compute the next time-step.

One important parameter here is the width of the Gaussian kernel used to represent each particle of the ensemble. The kernel can range from zero where the each Gaussian goes to a Dirac distribution and the full width of the histogram, that leads simply to a Gaussian fit of the distribution. Therefore, a too large kernel is not capturing the specific shape of the distribution if it differs from a Gaussian. Yet, for finite ensemble, a too small kernel will lead to a noisy evaluation of the density, that will become unpractical because of the three derivatives and the division by n occurring in the quantum force. This can result in a divergence of the algorithm.

Of course, a localized kernel can still be used if the number of particles is very large, in which case the distribution will remain smooth. The question only arises when small statistics are used. In the numerical results shown here, we wish to stay close to the existing experimental platform that contains at most a few thousands of trapped objects. In our case, we use 3000 trajectories and we therefore compromise between a kernel of size close to zero (sum of Dirac delta functions) and of size equal to the whole width of the distribution (Gaussian approximation, exactly true only for harmonic external potential, as detailed later).

On Fig. 5.3 we show an example of instantaneous probability distribution of positions in a non-harmonic external potential, computed with 3000 independent positions. We superimpose the result of a density estimation via a sum of Gaussians for various kernels, varying from 0.1 (blue line) that follows the irregularities of the measured histogram to the full width of the distribution (yellow line), a Gaussian approximation of the distribution. In the following, we use the conventional arbitrary units where the size of the kernel is 0 for a sum of Dirac peaks and 1 (arbitrary units) when it spans the full width of the distribution. For the numerical study of next subsection, we use a value between 0.6 and 0.8: large enough to smooth out irregularities arising from the small statistics, but small enough to account for the difference of the distribution with respect to a Gaussian.

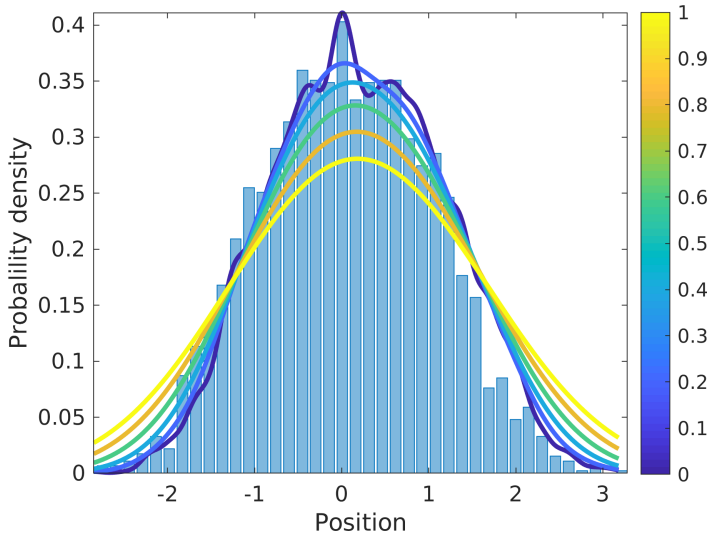

Figure 5.3: Probability density for 3000 trajectories. Measured histogram (blue bars) and its estimation by a sum of Gaussian kernels of width varying in arbitrary units from 0.1 (blue line) to 1 (yellow line: this value of 1 a.u. corresponds to the Gaussian approximation of the distribution)

5.3.2 Anharmonic potential and autocorrelation

In this subsection and in the following, we focus on two cases, studied using numerical simulations. In both cases, we use a quartic external potential $V_{\text{ext}} = \alpha x^2 + \beta x^4$. In this subsection we consider $\alpha > 0$ which makes V_{ext} an anharmonic single-well potential. We focus on the features of the equilibrium distribution and stationary observables, such as the autocorrelation function of positions $\langle x_t x_s \rangle$. Non-equilibrium transients will be analyzed later using an experimental protocol. We simulate the adimensional process with 3000 trajectories on 300 time-steps of duration $\Delta t = 0.1$. The potential is parameterized as $V_{\text{ext}} = 0.6x^2 + 0.2x^4$. We simulate three different cases:

- a classical Langevin process in the quartic potential, with $\epsilon = 0$ (referred to as "Classical Quartic" in the following)
- a quantum McKean-Vlasov process Eq. (5.44) in a quartic potential, with $\epsilon = 4$ (referred to as "McK-V Quartic")
- a classical Ornstein-Uhlenbeck process in a harmonic potential $V_{\text{ext}} = x^2/2$ (referred to as "Ornstein-Uhlenbeck")

These three cases are important to highlight to highlight, by contrast, different effects. Our aim is both to underline the specificity of the quantum effects, but also the

specificity of anharmonicity. The first and second are compared to show the modifications induced only by the quantum effects. The third classical harmonic case, is used in contrast, to underline the effect of anharmonicity of the potential in the two first.

We take as initial condition for both the classical quartic and McKean-Vlasov quartic processes the stationary distribution of a classical quartic process (Eq. (5.44) with $\epsilon = 0$), then turn on quantum effects for the McKean-Vlasov process ($\epsilon = 4$) and let both systems evolve. As expected, the classical process will stay stationary while the quantum McKean-Vlasov will evolve towards a new equilibrium. At each time-step, a smooth distribution $n(x,t)$ is constructed from the $\mathcal{N}$ trajectories by softening the particle positions $x(t)$ with a Gaussian kernel as discussed above.

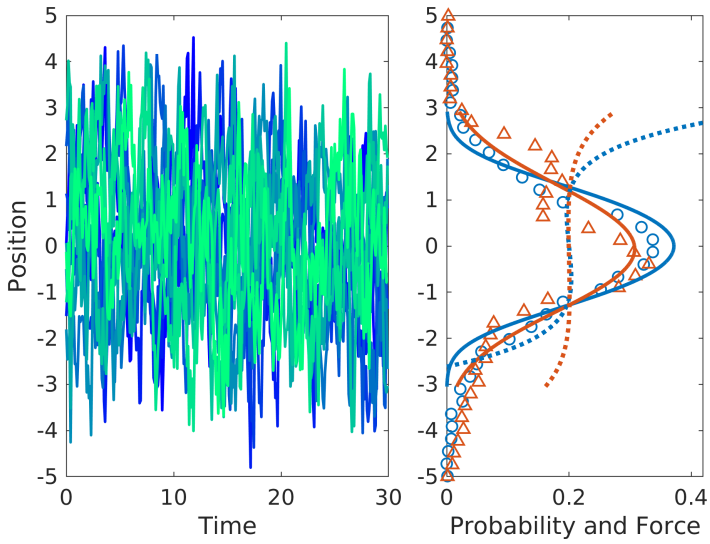

Figure 5.4: (Left) Evolution of 15 simulated trajectories, initially distributed according to the classical stationary state in the quartic potential $V_{\text{ext}} = \alpha x^2 + \beta x^4$, where $\alpha = 0.6$ and $\beta = 0.2$, computed with a total $\mathcal{N} = 3000$ trajectories with $\epsilon = 4$, for 300 time-steps with $dt = 0.1$; (Right) Histograms of the initial (classical, $\epsilon = 0$, blue circles) and final (quantum, $\epsilon = 4$, red triangles) equilibrium distributions, together with their density estimation with a sum of Gaussian (continuous line) and respective Bohm force (dotted line).

In Fig. 5.4 we represent some simulated trajectories for the quantum McKean-Vlasov process on the left as well as their ensemble probability distributions at the initial time (blue) and final time (red). After a certain relaxation time, the system stabilizes around a quantum equilibrium distribution, which differs significantly from the initial classical Boltzmann equilibrium. This departure from the classical result

is due to the action of the Bohm force, which works against the external confinement and extends the width of the distribution. We superimpose the quantum force derived from the respective densities (dotted line), which takes a cubic profile.

As explained above, an important point in the performed simulations is the choice of the kernel of the Gaussian used to approximate the density. It needs to stay small enough to allow each distribution to keep its specificities. Here we go in more details on this point to show that the resulting distribution significantly differ from a Gaussian.

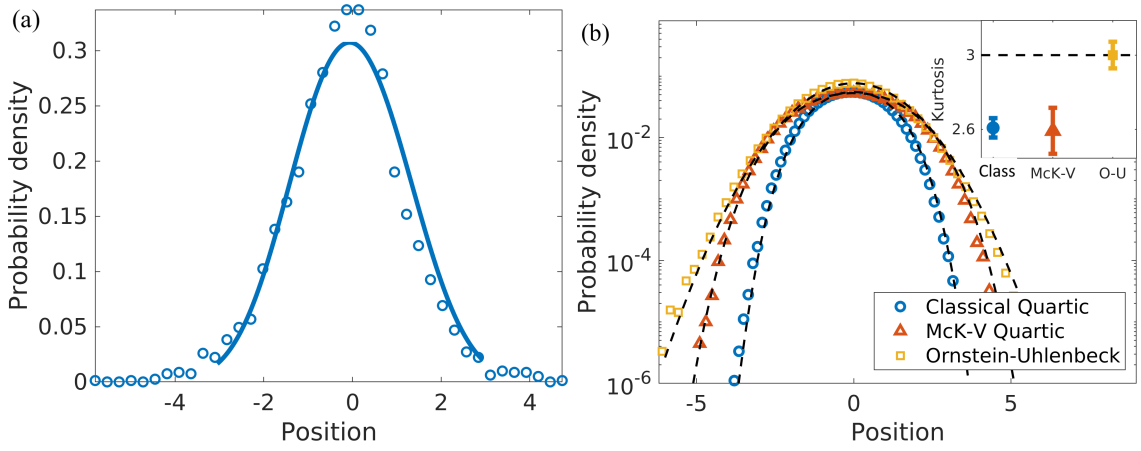

Figure 5.5: (a) Numerical distribution as well as its approximation by a sum of Gaussian kernels of width 0.8 (arbitrary units). We observe that this approximation flattens the top of the distribution. (b) Total probability distribution of the trajectories on 300 time-steps for the three cases. The classical quartic position distribution (blue circles) and McKean-Vlasov quartic distribution (red triangles) are fitted with a Maxwell-Boltzmann distribution with quartic energy and the Ornstein-Uhlenbeck distribution (yellow squares) is superimposed with the expected Gaussian shape. In the inset we show the time-averaged ensemble-kurtosis (4^{th} moment) of all three cases with the same color code. The kurtosis of the Gaussian distribution of the Ornstein-Uhlenbeck process is 3 as expected for a normal distribution. The kurtosis of both quartic processes differs significantly, the error bars correspond to one sigma of dispersion of the ensemble-kurtosis on the 300 time-steps.

On Fig. 5.5 (a) we show a typical probability distribution evaluated on the ensemble of trajectories with its approximation as a sum of Gaussian of width equal to 0.8 (a.u.). Although this choice of kernel is not an approximation as crude as a Gaussian fit, it still visibly departs from the measured distribution. A kernel of width $0.6 - 0.8$ is however the smallest kernel that can be used with such a small statistics: indeed,

with a smaller width, the third derivative of the distribution contained in the quantum force would be too noisy causing the algorithm to diverge.

To evaluate the effect of anharmonicity of both quantum and classical processes in the quartic potential, we evaluate the kurtosis of the respective distributions. Kurtosis of a centered random variable, is its fourth moment normalized by the squared variance $K \equiv \mathbb{E}[x^4]/\sigma^4$. Since for a normal distribution $\mathbb{E}[x^4] = 3\sigma^4$, the kurtosis is $K = 3$. A statistically significant deviation from this value is therefore a measure of non-Gaussianity.

We show on Fig. 5.5 (b) that the probability distribution of the McKean-Vlasov process (red triangles) is keeping its non-Gaussian nature (in contrast with the yellow squares Gaussian distribution) as measured with the kurtosis $K < 3$ and also significantly differ from its classical counterpart (blue circles). $K < 3$ distributions, referred to as *platykurtic* are typically displaying less outliers than a normal distribution, as one can see on the shape of both blue and orange distributions, that show smaller tails than the Gaussian yellow distribution.

More precisely, the probability distribution function (PDF) of both classical processes are expected to converge to the Maxwell-Bolzmann statistics $n(x,t) = \frac{1}{\mathcal{Z}} e^{-V_{\text{ext}}/k_B T}$. Harmonic confinement V_{ext} leads to a Gaussian PDF $\propto e^{-x^2/2\sigma^2}$ while quartic confinement V_{ext} leads to a non-Gaussian shape $\propto e^{-(\alpha x^2+\beta x^4)/k_B T}$. On Fig. 5.5 (b) we show the three distributions. We superimpose to both classical distributions the expected Botzmann PDF. We note the good agreement for the classical PDF, while the distribution of the quantum McKean-Vlasov process significantly differs from both classical counterpart and Gaussian distribution. The latter is fitted with a general Boltzmann distribution in a quartic potential $\propto e^{-(\alpha' x^2+\beta' x^4)/k_B T}$ with different parameter α' and β' as fitting parameter. It shows that the total potential, sum of V_{ext} and Q keeps a quartic shape, with different coefficient.

In Fig. 5.6, we show the normalized autocorrelation at equilibrium: $\langle x(t+\Delta)x(t)\rangle / \langle x^2(t)\rangle$, where the averaging is done over all the trajectories, as a function of the lag-time Δ. The initial time is set at an instant t, when the distribution has already relaxed to its quantum equilibrium. We note that the addition of the quantum Bohm potential induces longer-lasting correlations compared to the classical case. A straightforward interpretation is that the McKean-Vlasov trajectories are correlated with one another through the action of the Bohm force.

The result of this subsection validates our method on the example of a quartic

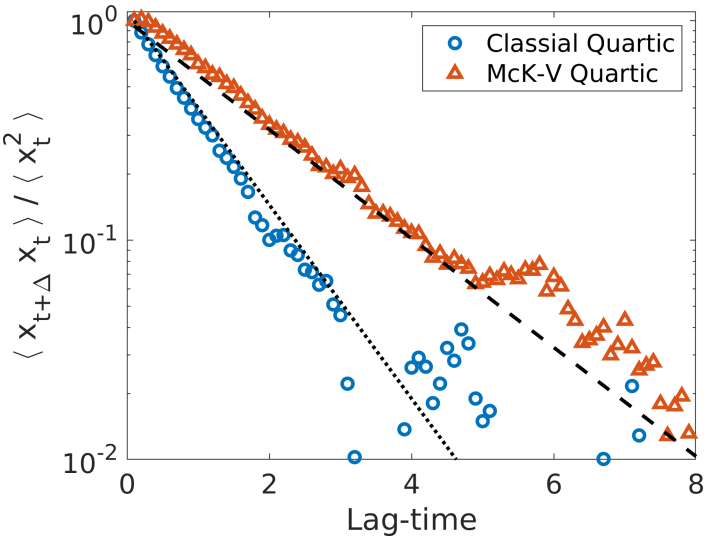

Figure 5.6: Semi-logarithmic plot of the normalized ensemble-averaged correlations $\langle x(t+\Delta)x(t)\rangle/\langle x^2(t)\rangle$ as a function of the lag time Δ, for trajectories $x(t)$ undergoing a quantum McKean-Vlasov (orange triangles) or classical (blue circles) stochastic process. In both case we superimpose an exponential fit (black dashed and dotted lines respectively).

potential. We are able to emulate the McKean-Vlasov process, while keeping a reasonable statistics and can unveil some specific effect, here visible on the equilibrium correlation function.

5.3.3 Bistable Duffing potential

We now turn to the case $\alpha < 0$, for which the confining potential is a bistable double well parametrized as $V_{\text{ext}} = -x^2 + 0.1x^4$. Using the same numerical method, we simulate again $\mathcal{N} = 3000$ trajectories for both the classical ($\epsilon = 0$) and the McKean-Vlasov ($\epsilon = 2$) stochastic processes. On Fig. 5.7 (left) we represent individual trajectories in the potential for 2000 time-steps of duration $\Delta t = 0.1$. We can see that in the classical case (blue trajectory), the particles linger in one of the wells for a relatively long residency time τ_R, before occasionally jumping to the second well due to thermal fluctuations. In contrast, in the McKean-Vlasov case (red line) these jumps occur much more frequently. As a consequence, the probability distribution of the McKean-Vlasov process is less sharply peaked on the two minima (Fig. 5.7, right panel). The classical distribution is well fitted by a Boltzmann law $\propto e^{+\alpha x^2 - \beta x^4}$ with the chosen $\alpha = 1$ and $\beta = 0.1$. The quantum McKean-Vlasov distribution is also fitted with a Boltzmann distribution, $\propto e^{+\alpha' x^2 - \beta' x^4}$ where α' and β' are fitting parameters, showing that the total potential takes the same analytical form as the external potential, but

with modified coefficients.

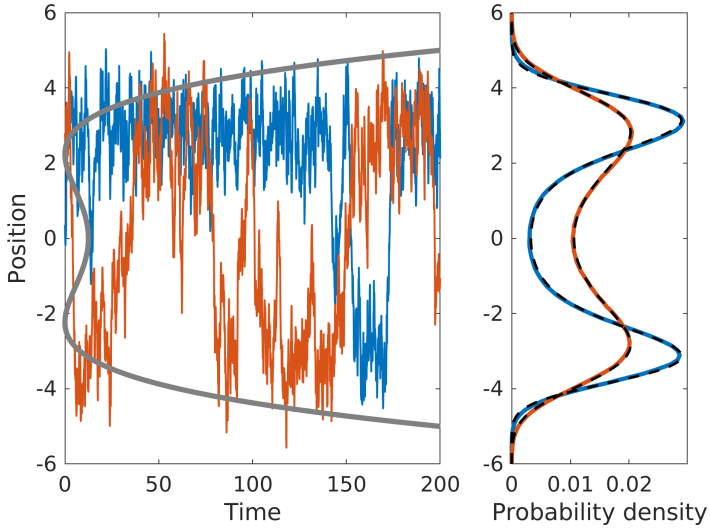

Figure 5.7: (left) Classical ($\epsilon = 0$, blue line) and McKean-Vlasov ($\epsilon = 2$, red line) trajectories in a double-well potential ($\alpha = -1$, $\beta = 0.1$, grey line) along with (right) their respective probability distributions for $\mathcal{N} = 3000$ trajectories simulated for 2000 time-steps with $dt = 0.1$

The main difference between classical and quantum processes is therefore well captured by the difference in residency time in each minima of the potential. Here we study in more details the jump statistics. On Fig. 5.8 (a) we represent a part of trajectory x_t for both classical (blue) and quantum (red) processes. We wish to study the statistics of the time τ_R that the position x_t spends in one well (e.g. $x_t > 0$). We superimpose on the trajectories x_t a rolling average smoothing (smoothing on 20 time-steps). This smoothing allows to avoid counting very short events that are not bringing the particle to the other minima. We then scan the trajectory and detect all crossing events (that are rezpresented on Fig. 5.8 (a) as circles on the $x = 0$ line). The residency times are then defined on the times between each crossing event. With this method, we collect $\sim 10^4$ residency times τ_R and build their probability distributions.

The jump events from one minima to the other are correctly described by Poisson statistics [195, 196] and the probability distribution of the residency times obeys an exponential decay law [197] $P(\tau_R) = \lambda e^{-\lambda \tau_R}$, where $\lambda \equiv 1/\langle \tau_R \rangle$. The results shown in Fig. 5.7 (b) are in good agreement with this exponential law, both for the classical and for the McKean-Vlasov processes, albeit with different values of λ, the effect of the Bohm potential being to decrease the mean residency time. The enhanced mobility between the two wells is clearly seen in the probability distribution of the particle po-

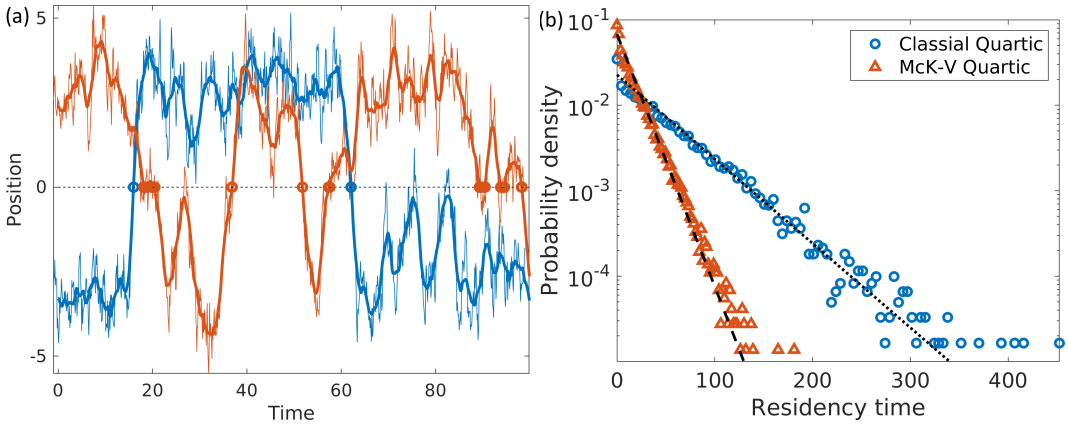

Figure 5.8: (Left) Classical ($\epsilon = 0$, blue) and McKean-Vlasov ($\epsilon = 2$, orange) trajectories (thin lines) and a rolling averaged smoothing (thick line) in a double-well potential ($\alpha = -1$, $\beta = 0.1$). We emphasize the crossing events detected with thick circles on the $x = 0$ line. (Right) Probability distribution of the residency times τ_R for the classical (blue circles) and quantum (orange triangles) cases. The straight lines represent the corresponding Poisson distributions, with $\langle \tau_R \rangle = 42.9$ for the classical and $\langle \tau_R \rangle = 8.4$ for the McKean-Vlasov case.

sitions (Fig. 5.7 (right)), which signals a decrease of the effective potential barrier due to the quantum Bohm potential. This result can be interpreted as a manifestation of quantum tunnelling, which increases the frequency of barrier-crossing events beyond the classical thermally-induced probability.

The effective decreasing of the potential barrier is shown on Fig. 5.9 where we display the external potential (blue line), the time-averaged ensemble-measured quantum potential (red line), as well as the total potential (yellow dashed line), sum of the external and the quantum potentials. The total potential is what the particles actually experience along their trajectories. We clearly see on the figure that the addition of the quantum potential decreases the height of the potential barrier separating the two minima. This was already visible on the flattening of the probability distribution function on Fig. 5.7 (right). We also show the profile of the force (external, quantum and total with the same color code). This again underlines the softening induced by the quantum nature of the McKean-Vlasov process.

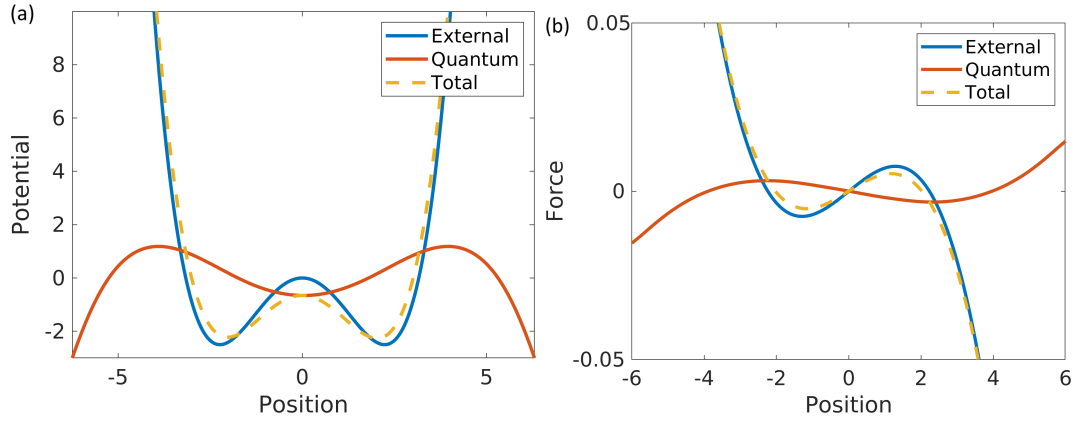

Figure 5.9: (a) External potential applied $V_{\text{ext}} = -x^2 + 0.1x^4$ (blue line), ensemble-measured quantum potential $Q = -\epsilon^2 \frac{\Delta\sqrt{n}}{\sqrt{n}}$ (red line, scaled for visibility) averaged on all time-steps and total potential $V_{\text{ext}} + Q$ (yellow dashed line). (b) Associated external force $F_{\text{ext}} = -\nabla V_{\text{ext}}$ (blue line), $F_{\text{Bohm}} = -\nabla Q$ (red line, scaled for visibility) and total $F_{\text{ext}} + F_{\text{Bohm}}$ (yellow dashed line).

5.4 Experimental realisation in a harmonic potential

In this section we implement McKean-Vlasov process experimentally in our single Brownian object optical trap. Since we have only one microsphere in one trap, we cannot use the method proposed above to probe the distribution on an ensemble. Instead we use a simple analytical result for harmonic potential to circumvent the need of an ensemble. This approach will be used to study the effect of the Bohm potential in an out-of-equilibrium configuration.

5.4.1 Quantum effect in a single potential

Our experimental setup, shown in Fig. 5.10 and presented in detail in Chap. 2 is composed of a single 1 µm dielectric bead optically trapped by a 785 nm Gaussian laser beam. The optical potential created by the gradient forces at the waist of the beam is harmonic, $V_{\text{ext}} = \kappa x^2/2$ with a stiffness κ proportional to the intensity of the laser beam that can thus be controlled precisely. The bead is immersed in water at ambient temperature and undergoes Brownian motion due to the thermal fluctuations. The overall motion is consistent with an Ornstein-Uhlenbeck process and is therefore suited to implement our model.

We have seen in Sec. 5.1.4 that in the case of harmonic potential, the quantum potential can be analytically derived and takes a harmonic shape as the external

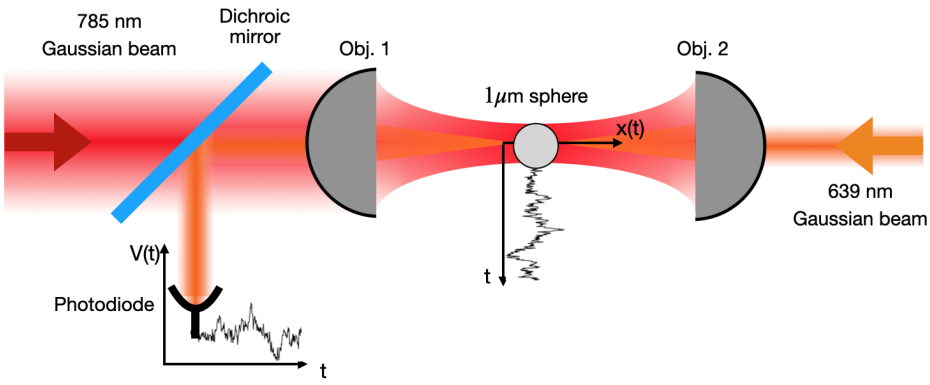

Figure 5.10: Schematic representation of the experimental setup: a 785 nm Gaussian laser beam is tightly focused on the 1 µm polystyrene bead with a 1.2 N.A. microscope objective Obj. 1. A second low-power 639 nm is sent through a 0.7 N.A. objective Obj.2. The scattered 639 nm light by the microsphere is collected by Obj.1 and sent to a photodiode. The intensity fluctuations are linear with the position x_t and is calibrated to measure the trajectories. More details are given Chap. 2

potential, leading to a force $-\partial_x Q[n(x,t)] = \frac{\hbar^2}{4m\gamma}\frac{x_t}{S^2(t)}$. In this case, both the Bohm force and the external force $-\kappa x_t$ have the same functional form, linear in the stochastic variable x_t. Furtherfmore, a Gaussian probability distribution

$$n(x,t) = \frac{1}{\sqrt{2\pi S(t)}} e^{-x^2/2S(t)}, \tag{5.46}$$

where $S(t)$ is the time-dependent variance of the distribution, is an exact solution of the McKean-Vlasov process (5.37), provided the variance obeys the following equation:

$$\frac{dS(t)}{dt} = -\frac{2\kappa}{\gamma}S(t) + \frac{\hbar^2}{2m\gamma S(t)} + \frac{2k_BT}{\gamma}. \tag{5.47}$$

This equation can be written as

$$\frac{dS(t)}{dt} = -\frac{2}{\gamma}\left[\kappa(t) - \frac{\hbar^2}{2m\gamma S^2(t)}\right] S(t) + \frac{2k_BT}{\gamma}. \tag{5.48}$$

where the term between bracket is a single modified stiffness

$$\bar{\kappa}(t) \equiv \kappa(t) - \frac{\hbar^2}{4m\gamma S^2(t)}. \tag{5.49}$$

Hence, the quantum McKean-Vlasov process can be expressed as an ordinary (Ornstein-Uhlenbeck) stochastic process:

$$dx_t = \frac{-\bar{\kappa}(t)}{\gamma}x_t dt + \sqrt{\frac{2k_BT}{\gamma}}dW_t. \tag{5.50}$$

Despite this apparent mathematical simplicity, all the physical richness of the analog model is preserved, with the modified stiffness $\bar{\kappa}(t)$ still depending on the ensemble variance $S(t)$ as a consequence of the quantum nature of the problem. Moreover, in this harmonic case, as already discussed Sec. 5.2.3 the dimensionless parameter governing quantum effects takes the form: $\epsilon^2 \equiv \frac{\hbar^2\kappa}{2m\,(k_BT)^2} = \lambda_{\mathrm{dB}}^2/2\lambda_\kappa^2$, i.e. half the ratio between the de Broglie thermal wavelength and the classical width of the harmonic oscillator at thermal equilibrium.

The specificity of the harmonic confinement is that the variance need not be measured out of a collection of trajectories taking place simultaneously in $\mathcal{N}$ identical traps, as in Fig. 5.1. Instead, $S(t)$ can be computed from Eq. (5.47) and then used to construct the Bohm potential or force, thus avoiding the necessity of using many optical traps in the experiment. This approach of computing analytically the variance however relies on a very neat calibration of the optical setup. The motional variance of the microsphere depends on the stiffness κ of the optical potential, needs to be known with high precision before doing the experiment.

5.4.2 An alternative calibration method

In our experimental implementation, the optical potential created by the focused laser beam is locally harmonic. The stiffness of the harmonic potential $\kappa(t)$ is proportional to the laser power $P(t)$ and can be controlled by the experimentalist. Our experimental method and calibration are based on the theoretical results obtained in the harmonic and Gaussian case, mainly the relation between the stiffness $\kappa(t)$ and the variance $S(t)$ given by the classical variance ODE Eq. (2.19). It makes it possible to realise the McKean-Vlasov process using one single trajectory and to use this system to probe out-of-equilibrium states, with a given protocol $\kappa(t)$. The method is the following: first a protocol $\kappa(t)$ is defined, a value of the parameter ϵ is chosen and is transferred to an arbitrary Planck constant $\hbar_{arb}^2 = \frac{2m(k_BT\epsilon)^2}{\kappa_i}$. Then the variance ODE is solved for this protocol and the modified stiffness $\bar{\kappa}(t) = \kappa(t) - \hbar_{arb}^2/4mS^2(t)$ is injected as a laser intensity protocol. The different steps of the procedure, including the calibration, are summarized Fig. 5.11.

This procedure relies on a precise calibration of the system: in order to use the variance differential equation Eq. (5.47), we need to know with the best possible precision the stiffness $\kappa(t)$ at play in the trap. In this section, we detail our method.

In order to predict the stiffness of the trap, we first calibrate the linear relation

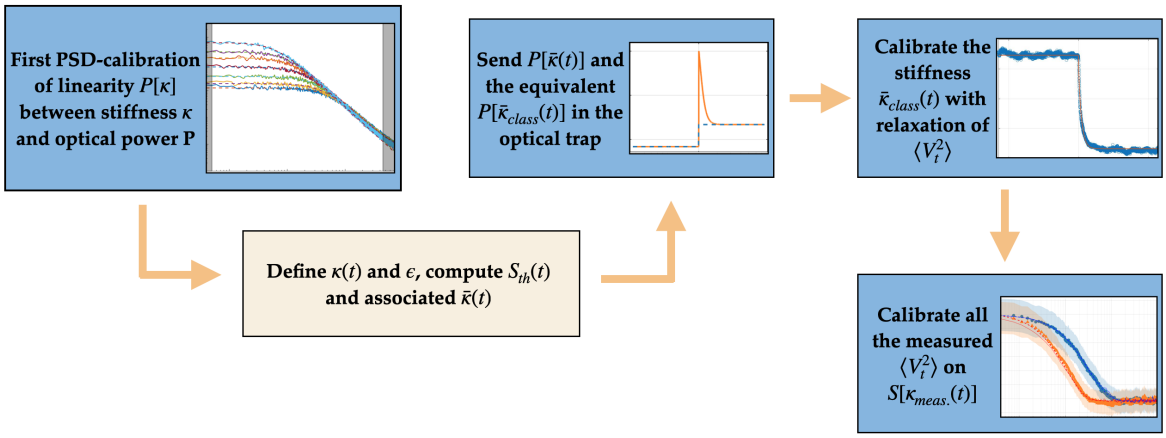

Figure 5.11: Schematic sequence of the different steps of our experimental calibration procedure. P is the trapping laser power, κ the stiffness of the harmonic potential, $\bar{\kappa}$ is the modified stiffness that includes quantum effects through $\bar{\kappa}(t) = \kappa(t) - \hbar^2_{arb}/4mS(t)^2$. $\bar{\kappa}_{cl}$ is the step-like protocol connecting the same initial and final stiffnesses, $V(t)$ is the voltage signal of the photodiode recording the beads position along the optical axis $x(t)$, κ_{meas} is the stiffness obtained by the relaxation calibration and $S[\kappa_{meas}]$ is the solution of the variance ODE for $\kappa(t) = \kappa_{meas}(t)$.

between the trapping laser power $P(t)$ and $\kappa(t)$. We use the power spectral density (PSD) method [95]. As detailed Chap. 2, the Ornstein-Uhlenbeck process describing the Brownian motion in the trap

$$dx_t = -(\kappa/\gamma)x_t dt + \sqrt{2k_B T/\gamma} dW_t,$$

can be spectrally analysed with the position PSD:

$$S_x(f) = \frac{D}{\pi^2(f_c^2 + f^2)}. \tag{5.51}$$

where the roll-off frequency $f_c = \kappa/2\pi\gamma$ separates the high frequency regime $S_x(f) \sim D/\pi^2 f^2$ of free Brownian motion from the low frequency trapping regime $S_x(f) \sim D/\pi^2 f_c^2 = 4k_B T\gamma/\kappa$. By recording a trajectory with a certain laser power, one can obtain the stiffness κ from the roll-off f_c, by a Lorentzian fit of the spectrum. On Fig. 5.12 (left) we represent the PSD and fit for different trapping strengths, which yields the linear relation between κ and the laser power. It is then possible to send a designed protocol of stiffness $\kappa(t)$ by inverting the relation.

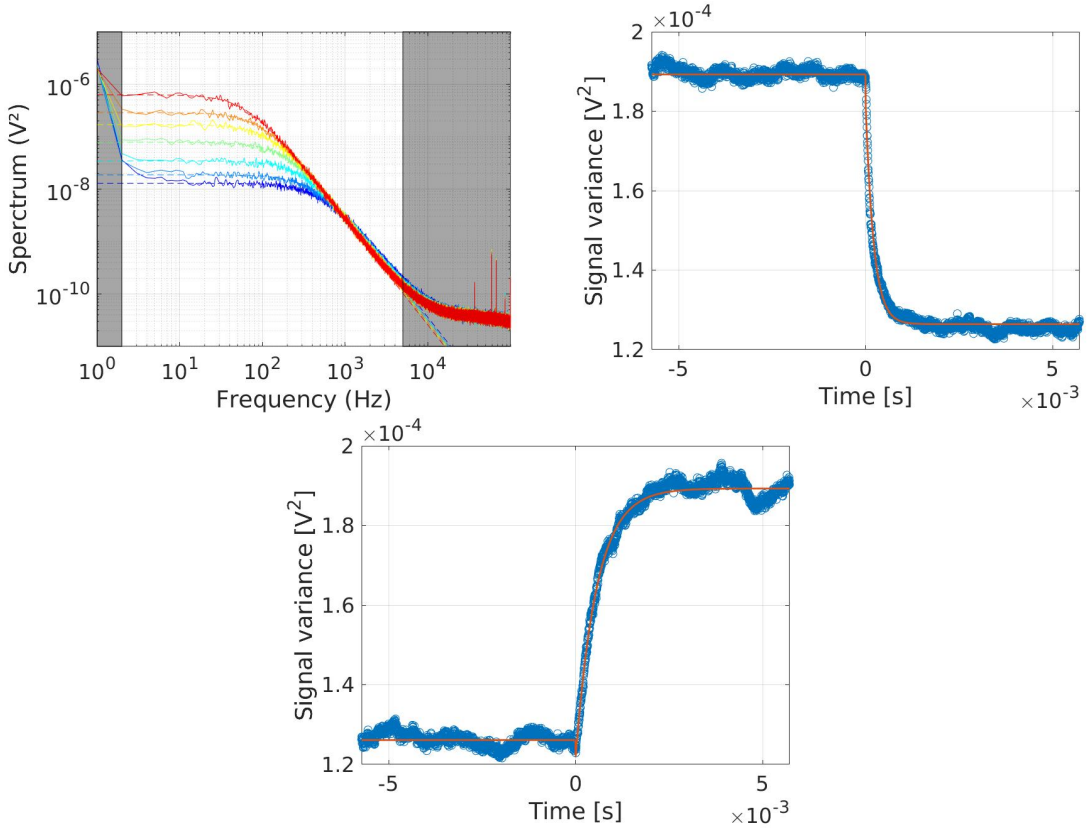

Figure 5.12: (top left) power spectral densities of the measured photodiode voltages for different trapping stiffnesses with Lorentzian fit, (top right) exponential decay fit of the "up" step from κ_i to κ_f ($\kappa_f > \kappa_i$), allowing us to obtain a measure of κ_f, (bottom) exponential decay fit of the "down" step from κ_f to κ_i, allowing us to obtain a measure of κ_i.

In order to build an ensemble of synchronised trajectories experiencing a defined protocol, we rely on the ergodic hypothesis. From one long trajectory experiencing a series of protocols, we build an ensemble of $N_{exp} \approx 2 \cdot 10^4$ trajectories. We start by defining a step-like protocol where $\kappa(t)$ goes abruptly from κ_i to κ_f and send it as $P(t)$ to the trapping laser. From the obtained ensemble of trajectories experiencing a transient relaxation, we extract the photodiode signal variance $\langle V^2(t) \rangle$ that follows an exponential decay (solution of the classical Fokker-Planck equation). This decay $\sim e^{-\kappa_f t/\gamma}$ is fully characterising the final stiffness. With an exponential fit of both the "up" and "down" stiffness steps, we recover a measurement of the stiffness performed in the time-domain. This allows us to measure, during the experiments the actual stiffness that can depart slightly from the expected value, due to small drifts or fitting errors of the Lorentzian [95]. Since we pair each McKean-Vlasov process experiment

with an equivalent classical step, we can perform this dynamical calibration for each experiment.

After the first step-like protocol experiment, we define a value of ϵ and perform both the quantum and the classical analog experiments. The dynamical calibration gives the values of κ_i and κ_f, that yield an ϵ that can slightly differ from the predicted value. These values correspond to the parameters needed to compute the analytical results.

Furthermore, the variance $S(t)$ and the stiffness $\kappa(t)$ are unambiguously connected by the variance differential equation $\frac{dS(t)}{dt} = -\frac{2\kappa(t)}{\gamma}S(t)+\frac{2k_BT}{\gamma}$. Hence, once we know the stiffness, we can compute $S(t)$ and can then calibrate our measured voltage variance $\langle V^2(t)\rangle$ to $S(t)$. We fit the transformation by a linear relationship $S(t) = \alpha\langle V^2(t)\rangle + \beta$ which implies that the position transforms according to $x_t = \sqrt{\alpha}V(t) + \sqrt{\beta}\mathcal{N}(0,1)$ where the first term represents the linear response of the photodiode and the second the sum of all experimental noises (which we approximate as a resulting white noise). This method allows a precise calibration of the variance, as seen in Fig. 5.13, which is our only observable here. This method however gives the position itself only up to the noise therm, which is still several order of magnitudes smaller than the α term.

5.4.3 Experimental results

Here, we use the above approach to study out-of-equilibrium evolutions with a time-dependent stiffness $\kappa(t)$. The simplest possible out-of-equilibrium process is the transient occurring when the stiffness $\kappa(t)$ is suddenly changed from an initial value κ_i to a final value κ_f (step-like protocol). The system is at thermal equilibrium at the initial and final times. The transient evolution of the variance can be computed using Eq. (5.47), allowing us to construct the modified stiffness $\bar{\kappa}(t)$, which evolves from $\bar{\kappa}_i$ to $\bar{\kappa}_f$ in a non-trivial way due to the influence of $S(t)$. One can argue that, since different values of ϵ lead to different values of $\bar{\kappa}$ for the initial and final equilibria, the classical ($\epsilon = 0$) and quantum (here, $\epsilon = 1$, 1.4 and 1.8) transients are difficult to compare, as they do not begin and end with the same values of the stiffness. With this in mind, we also implemented an equivalent classical protocol $\bar{\kappa}_{\rm cl}(t)$ that goes from $\bar{\kappa}_i$ to $\bar{\kappa}_f$ in a step-like way, i.e. without the dynamical influence of the Bohm force. These two protocols, represented in the inset of Fig. 5.13, connect the same initial and final equilibria, and are thus well-suited to compare the classical and quantum dynamics out-of-equilibrium.

Finally, in order to obtain ensemble averages out of our single trajectory, we rely on the ergodic hypothesis and use a time-series of trajectories instead of a statistical ensemble. We send the same $\kappa(t)$ protocol at a low enough repetition rate so that equilibrium is reached between two consecutive events, and then reconstruct a synchronized ensemble from this time series. The result is an ensemble of over $\mathcal{N} = 2\times10^4$ trajectories experiencing a given protocol, either $\bar{\kappa}(t)$ in the quantum case or $\bar{\kappa}_{\rm cl}(t)$ in the classical case.

The main observable of interest here is the time evolution of the ensemble variance, represented in Fig. 5.13 for both the quantum and classical cases. Our measurements clearly reveal the influence of the Bohm force on $S(t)$. Strikingly, the addition of an effective quantum force accelerates its relaxation, and this for all selected values of ϵ. Looking at $\bar{\kappa}(t)$ in the McKean-Vlasov process (Fig. 5.13, (d) inset), the acceleration appears as the result of a strong and sudden reduction of the optical trapping volume under the influence of the quantum Bohm force field. On each curve, we also represent the result of numerical simulations, where the evaluation of the Bohm term is not performed through the solution of Eq. (5.47), but by actually computing the ensemble variance of $\mathcal{N} = 2\times10^4$ distinct trajectories at each time-step. The agreement of both the experimental and numerical results with the analytical solution of Eq. (5.47) is quite remarkable.

The error on the experimental variance essentially comes from three main sources. One is the error on the experimental parameters such as the temperature or the radius of the trapped bead, through the viscous drag coefficient γ. It is dominated by the 2.8% uncertainties on the beads radius R that result in a similar error on $\gamma = 6\pi\eta R$ where η is the water viscosity. Other sources of errors (temperature) are also taken into account but their final influence is not significant. The temperature, in particular, is controlled with a precision better than 1 K. The error on the radius is simply taken into account by carrying the whole analysis with the two "worst-case" values of radius, yielding an error $\delta_{param} \approx 3\%$ between the two extreme results. The second source of errors is the statistical reliability of an estimator of the variance on an ensemble of finite size. It is obtained following the χ^2 test on $N-1$ degrees of freedom, where N is the size of the ensemble. We carry the test with $3\sigma = 99.7\%$ confidence interval giving δ_{χ^2}. The third source is the error arising from the fitting procedure in the calibration of the decay to obtain the stiffness and to calibrate the variance from V to m^2 giving δ_{fit}. The obtained variance is then defined up to:

$$S_{exp} = \langle x^2(t)\rangle \pm (\delta_{\chi^2}(t) + \delta_{param}(t) + \delta_{fit}(t))\,. \tag{5.52}$$

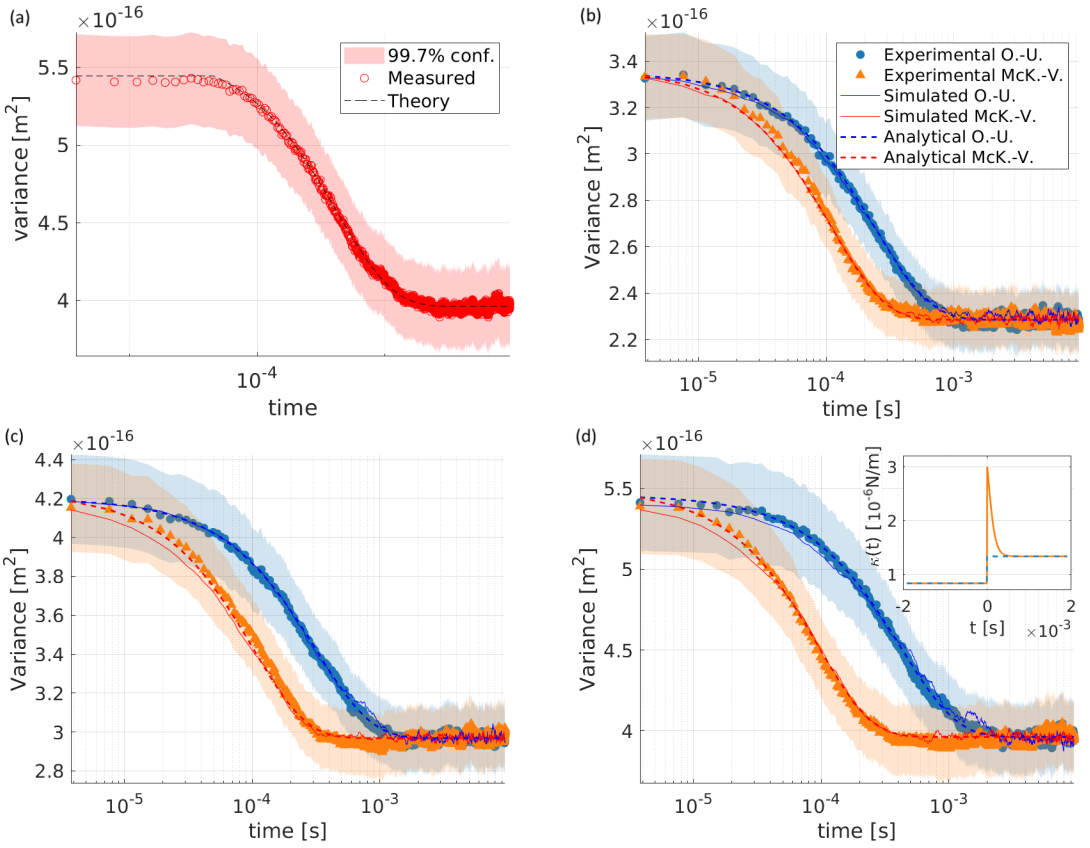

Figure 5.13: Experimental results: we show the evolution of the variance of the ensemble of over 2×10^4 trajectories during an out-of-equilibrium process, between two harmonic confinements of different stiffnesses. The corresponding values of the ϵ parameter governing the strength of the Bohm force are $\epsilon = 0$ (a); $\epsilon = 1.0558$ (b); $\epsilon = 1.4089$ (c); and $\epsilon = 1.801$ (d). For all cases, we show the result of McKean-Vlasov dynamics (orange triangles) as well as a classical equivalent Ornstein-Uhlenbeck dynamic (blue circles) experiencing a transition between the same initial and final distributions. The colored patches corresponds to a 99.7% confidence interval, taking into account both experimental and statistical errors. On each curve, we superimpose the result of a numerical simulation performed by measuring at each time-step the ensemble variance of $N = 2 \times 10^4$ simultaneous trajectories and reinjecting it in the next time-step (respectively red and blue thin solid lines). We also show the result of the variance differential equation (respectively red and blue thick dashed lines). The inset in figure (d) shows the evolution of the stiffness $\bar{\kappa}(t)$ (orange line) as well as the equivalent classical step $\bar{\kappa}_{cl}(t)$ (blue dashed line).

These different sources of error give the colored patch shown on each experimental plot.

5.5 Conclusion

In this chapter, we highlighted an analogy between an open quantum system immersed in a thermal bath and a classical nonlinear stochastic process (McKean-Vlasov process). This correspondence opened up the possibility to build a classical analog of the quantum model, by evolving many stochastic trajectories in parallel and using their distribution to reconstruct the quantum Bohm potential. With a numerical study, we explored this analogy for an anharmonic potential, unveiling effects like longer-lasting correlations and the tunnelling through a potential barrier. We explored the special case of harmonic external potential and Gaussian process, which corresponds to our experimental optical trap. In this case, Bohm's potential takes a simple form that can be integrated in our optical potential. Our ability to control the stiffness through time allowed to probe out-of-equilibrium dynamic.

The present work is a first step in the experimental implementation of classical analogs of quantum systems using optically trapped Brownian particles. Of course, the QDD equation used here is a highly specific model, whose validity is constrained by several conditions. But the approach outlined in this work should pave the way to the classical realization of fully quantum evolutions, described in their most general case by the time-dependent Schrödinger equation.

Chapter 6

Conclusion

Brownian motion in an optical trap is a paradigmatic implementation of a well controlled stochastic process. The capacity to tune the potential energy and additional external forces that act on the trapped object makes it a versatile platform to explore the properties of microscopic systems subjected to fluctuations, ranging from microelectronics [117, 198] to biological process at small scales [54]. In this thesis we studied the Brownian motion of a polystyrene micrometric sphere diffusing in water at ambiant temperature and confined in an optical trap. We explored fundamental properties of the trajectory of the microsphere, such as the nature of the diffusion, or the ergodic character of the stochastic process. Taking advantage of the flexibility of our optical trapping experiment and the universality of fluctuations at small scales, we designed and implemented two analogues, that extended the range of applicability of optically trapped Brownian motion. In a first analogue work, with a flexible external radiation pressure force, we built a secondary artificial bath, mimicking the behaviour of a large class of biological processes at the microscopic scale. The second analogue is based on the formal similarity between the dynamical evolution of the position probability density of a Brownian object and fluid models of quantum mechanics. By controlling the potential energy in which the microsphere diffuses, we built a classical stochastic analogue of a quantum process.

Those two developments extend the range of application of optical traps, taking advantage both of the simplicity and generality of the process at play, as well as the experimental control on the parameters. It also allows to draw conclusions in domains a priori disconnected from optical trapping, as when we unveiled a connection between the informative content of an environment and the thermodynamics of an objet immersed in it. Such a result can have implications in the understanding of biological intracellular processes, such as the action of micro-motors. In the following, we review the main results discussed in this thesis.

Brownian motion in an optical trap

The scope of the first chapter was to introduce the experimental methods used to optically trap a microparticle and record its time-dependent position. The electronic signal processing and associated data analysis where also detailed. We introduced the numerical method used to run simulations of Brownian trajectories, similar to the one observed experimentally and care was taken on convergence tests of such stochastic simulations. The connection between the stochastic Langevin process and the associated deterministic Fokker-Planck equation was made explicit. In our case of harmonic confinement, a Gaussian distribution is an exact solution and Fokker-Planck equation simplifies to an ordinary differential equation for the motional variance. The time-dependent variance analysis of the process goes with the notion of statistical ensemble, built by cutting and reassembling a long time-series of positions. It was illustrated with the response of the trapped microsphere to a quench in optical potential: by applying the same quench sequentially we built an ensemble of sub-trajectories on which deterministic quantities, such as the position probability distribution and its moments where derived. The main observables of Brownian motion: Power Spectral Density (PSD) position autocorrelation function and Mean-Square-Displacement (MSD) where derived analytically in our case of Ornstein-Uhlenbeck process and probed on experimental trajectories. The PSD is used to calibrate our optical setup and recover the trajectory of the microsphere from the recorded signal. The MSD was also exploited to assess the normality of the diffusion, by probing the short-time linear increase of squared displacements.

Noise properties of an optically trapped Brownian object, ergodicity, stability

Ergodic and stationary processes are an important sub-class among stochastic processes. Their nature allows easy manipulation that makes them central in many experimental applications. Ergodicity allows the construction of large ensembles of sub-trajectories out of single long time-series of positions, as it is routinely done to study statistical observables such as motional variance. The ergodic or non-ergodic nature of a trajectory is also deeply connected to other fundamental properties, such as the possibility to process memory effects, paving the way to information thermodynamics. The long-time stability of a stochastic process is again an important experimental parameter to allow high-resolution measurement, needed in particular in the context of weak force sensing.

In this chapter we experimentally demonstrated the ergodic nature of standard

Brownian motion in our optical trap, detailing the application of an operative criteria of ergodicity. By applying the same criteria on a more complex process, known as stochastic resetting, we unveiled its non-ergodic nature, that was theoretically predicted. Since non-ergodicity is a necessary condition for memory processing [125], experimentally probing the non-ergodic nature of a process is a key aspect in its potential applications in information thermodynamics. With an Allan-variance based test, we also carefully checked the long-time stability of the noise properties. Those two tests of course justificatify the methodology used throughout the thesis, using long time-series of positions to build ensembles and study averaged quantities. But they also reveal fundamental properties of the trajectories, as the difference, visible on all observables, between short-time free-like diffusion regime and long-time trapped regime. These regimes induce different characteristic trends for the ergodic criteria and the Allan variance.

Theoretical and numerical work on stochastic resetting are numerous [134], but most of them rely on an idealized resetting: the diffusing particle is instantaneously sent to a reference position x_0, with no energetic cost. Yet an experimental realization of stochastic resetting is very different: each resetting event is a physical process that moves the particle to x_0. They are only two experimental platform exploring such issues [199, 200] and they rely on two different experimental methods to implement resetting. Understanding the connection between the specific physical process through which resetting is implemented and associated ergodic, informational or energetic features is an open challenge.

Bath engineering, active matter and information harnessing

By using a secondary laser beam, passing through an acousto-optic modulator piloted numerically, we were able to send a time dependent external radiation pressure force on the trapped microsphere. This non-conservative external driving is an additional contribution in the Langevin equation governing the motion of the Brownian object. If the force is chosen to be a stochastic process, then its effect on the microsphere will look alike an additional bath. Since the properties of the external stochastic drive are chosen with a large flexibility, various baths can be engineered. In this work, we focused on the case of exponentially correlated noise, as it is theoretically and numerically used as a minimal model for *active* matter. A system is said to be active if it is able to convert an energy from its environment -a fuel- into a thermodynamic energy, as work, through directed motion, or heat, dissipated in the surrounding. Many different examples of active matter have been studied, some of them being reviewed in the introduction of the chapter. These systems span from microscopic biological processes

[52] to large ensemble of living systems, as flocks of birds [166]. Despite this diversity, the key aspects of active matter can be studied with minimal models as self-propelled micro-swimmers (e.g. bacteria), displaying paradigmatic effects, mostly due to their intrinsically out-of-equilibrium thermodynamics [49, 63, 58, 56]. In this chapter, we explored how adding an exponentially correlated stochastic force in the dynamics of the trapped microsphere makes it an operative analogue of a self-propelled object, or equivalently, of a passive object immersed in an active bath, such as water crowded with self-propelled bacteria.

Our experimental implementation of the active matter analogue allowed us to show superdiffusion in the mean-square-displacement of the microsphere, typical of a self-propelled system and in sharp contrast with the diffusive nature of Brownian motion in a standard fluid bath. The out-of-equilibrium nature of the trajectories, even in stationary states (genuine non-equilibrium steady-states -NESS) was probed using different observables, and the breaking of some central laws of equilibrium statistical mechanics. We demonstrated the violation of the law of equipartition of energy, with a stationary motional variance that depends explicitly on the correlation time of the bath, indicating the impossibility to describe the system with a simple constant temperature, as in equilibrium thermodynamics. We further explored the non-equilibrium state via the breaking of the fluctuation-dissipation theorem, with rheological measurements of the response of the microsphere in the trap.

By noting that the amplitude of the motional variance of the microsphere depends on the correlation time (i.e. the color) of the noise, we used it as a time-dependent parameter to perform protocols connecting one NESS to another. Such color-driven NESS-to-NESS transitions appears as a novel way to interact with the Brownian object, changing the correlation time of the bath allows to change the steady-state of the process. An important difference with other methods (such as potential engineering as in the last chapter of the thesis) is the absence of experimental cost (as laser power): the energy input needed is constant when only the color of the noise is modified. This apparent paradox was studied within the framework of stochastic thermodynamics, where we derived the first law of our process and unveiled non-trivial behaviour for the heat production rate as a function of the bath correlations. The paradox is resolved with an information thermodynamics perspective, where the heat produced by the sphere during the transient with no energy input was shown to be coinciding with the input of spectral information in the bath. This intriguing connection was explored at the end of the chapter.

The analogue of active matter proposed in this chapter had a very general character. The bath properties can be tuned by the experimentalist with a remarkable flexibility, and eventually combined with potential engineering, paving the way to full thermodynamics engine in non-trivial environments. The intrinsic difficulty to work with genuine biological matter makes these kinds of analogue systems very appealing to answer understand active systems.

Combining our ability to engineer non-trivial baths as done in Chap. 4 and potential control as done in Chap. 5 opens many perspectives. Indeed, as explained in Sec. 4.2.3, by changing the amplitude of the noise, we effectively change the kinetic temperature. In addition, a change of potential stiffness is effectively changing the volume available to the diffusing microsphere. Combining temperature and volume control gives ways to set up Brownian thermodynamics engines [100, **?**, 101]. The inclusion of non-trivial baths in Brownian engines [201] is raising many questions, such as the relation between the efficiency of an engine and the properties of the surrounding non-thermal bath. These issues are highly relevant in the context of biological micro-motors. The analogue proposed in this thesis could allow to explore this field of active engines with a good level of control on all dynamic and thermal parameters.

Classical stochastic analogues of a quantum process

The hydrodynamical formulation of quantum dynamics has been a rich source of original ideas to build classical analogues, such as in Yves Couder's famous walking-droplets experiments [174, 175]. Within this context, we proposed an analogue of another kind, where the probabilistic nature of the Brownian trajectories is used to build statistically a quantum densities in a specific limit of the quantum fluid model. This quantum fluid equation, known as quantum drift diffusion model has the same form as a Fokker-Planck equation where the quantum nature of the object is contained in an additional potential, the Bohm potential. We derived the associated stochastic process which is a Langevin equation with two conservative forces: one deriving from the external potential as in the classical case, and one deriving from the quantum Bohm potential. The specificity of this stochastic process stems from the fact that Bohm's potential depends on the position probability distribution. Such stochastic differential equation where the random variable's dynamics depends on its own probability distribution is known as McKean-Vlasov processes.

In this last chapter, we implemented both numerically and experimentally a McKean-Vlasov process with Bohm's quantum potential and studied its properties on three illustrative cases.

We first studied numerically the behaviour of such trajectories in an anharmonic single-well quartic potential. An ensemble of trajectories obeying to the quantum process was launched in this potential, with a classical probability distribution as initial condition. At each time-step, the dependency of Bohm's potential on the probability density was computed with an ensemble-estimation of the position distribution. After some relaxation time, the probability density of position is converging to the solution of the quantum drift diffusion model. The autocorrelation function of the trajectories is showing a longer correlation time with the quantum potential than in the classical case and these longer-lasting correlations were interpreted as stemming from the non-local interaction encapsulated in Bohm's potential. In a second study, we focused on trajectories evolving in a bistable Duffing potential. In this energy landscape, the particles were diffusing in one of both wells for some time, before crossing the potential barrier under thermal activation and fall in the second well. The statistics of residency times are following an exponential distribution both for classical Langevin trajectories and quantum McKean-Vlasov trajectories. The average residency time is however significantly smaller in the case of quantum trajectories. Such improvement of the ability of barrier-crossing was interpreted as a first approximation of tunnelling and was described by an effective lowering of the potential barrier.

Finally, we focused on the special case of harmonic potential, where a Gaussian Ansatz was shown to be an exact solution of the McKean-Vlasov process and where Bohm's potential can be explicitly computed. The analytical simplicity of this case allowed us to derive a unique modified potential that took into account the quantum effects without relying on an explicit evaluation of the density at each time-step. This allowed an experimental implementation in which we realized potential protocols, to study the out-of-equilibrium relaxation of the quantum process from one equilibrium state to another. We observed that Bohm potential induces a sharp and short quench of the potential, inducing a faster thermalization for a quantum object than for an equivalent classical Langevin trajectory.

The analogue proposed here is emulating a specific limit of a quantum process but we are currently exploring how one could set up a more general Schrödinger's equation analogue. This generalization is based on Nelson's formalism of quantum mechanics as a stochastic process [202] which draws an analytical connection between Schrödinger equation and standard Brownian motion. In this framework, the temperature-driven fluctuations are playing the role of quantum uncertainties. Experimental implementation of Nelson's mechanics is a natural extension of the analogue studied in this thesis.

From there, one could test how relaxation engineering techniques, well controlled in Brownian dynamics, could be applied to quantum state-to-state transitions, offering a new handle in the context of shortcut to adiabaticity [203].

Chapter 7

Résumé de la thèse

7.1 Introduction

Les fluctuations jouent un rôle important dans de nombreux processus naturels, à différentes échelles, qui peuvent être illustrés par de nombreux exemples. À l'intérieur des cellules de notre corps, un ensemble de filaments constitue un réseau qui en soutient la structure. Sur certains d'entre eux -les microtubules- se déplacent de microscopiques bipèdes : les kinésines. Ces moteurs moléculaires qui transportent du materiel biologique à travers la cellule. Si la kinésine ressemble à une funambule marchant sur un fil, il existe une différence fondamentale. Un.e funambule n'est pas déstabilisé par les chocs avec les molécules qui constituent l'air environnant alors que le monde à l'échelle d'une kinésine est agité, par ces collisions moléculaires, de forces aussi grandes que celles qui lui servent à se déplacer. À cette échelle, un fluide n'est pas lisse comme l'air que l'on sent autour de nous, mais agité de larges fluctuations et les mouvements de la kinésine sont déterminées par ces fluctuations [50, 27]. Il ne s'agit pas une petite perturbation sur le chemin rectiligne de la protéine, mais d'un environnement déterminant sa structure et sa stratégie de déplacement. La compréhension de la nature de ces fluctuation et de leur effet sur un moteur moléculaire est nécessaire pour appréhender la nature des processus biophysique ayant lieu dans les cellules.

L'importance des fluctuations dans la dynamique de la kinésine vient de la proximité d'échelle entre la protéine et les molécules qui l'entourent. Plus précisément, de la proximité entre l'énergie que la kinésine peut mettre en jeu dans son mouvement et l'énergie de l'agitation du fluide environnant à une température donnée. Si nous y sommes insensibles, c'est parce que nous sommes trop grands et lourds.

Néanmoins, il existe de nombreux autres exemples de fluctuations et de leur effet,

à de plus grandes échelles. On peut penser aux turbulences d'un fluide déplacé, que l'on sent lorsqu'on tend la main par la fenêtre d'une voiture à grande vitesse [204], ou encore au caractère aléatoire de la météo [205]. Ces phénomènes sont de nature très variées, et résultent de cause diverse -turbulences, chaos du climat- très différentes de l'agitation moléculaire à l'origine des fluctuations de la kinésine. Leur point commun est leur caractère stochastique : la position de la kinésine à un instant donné, tout comme la position de la main tendue par la fenêtre ou la température dans un lieu donné, gardent une part aléatoire.

Dans l'étude des processus stochastiques en physique un exemple historique contient, malgré sa simplicité, toute la richesse phénoménologique des processus aléatoires. Il s'agit du mouvement erratique d'un objet micrométrique inerte, suspendu dans un fluide à température ambiante. Un tel objet, grand d'un millième de millimètre est petit par rapport aux échelles de la vie quotidienne, mais reste dix milles fois plus grand qu'un atome. Comme la kinésine, il est assez léger pour être sensible à l'agitation moléculaire du fluide, mais assez grand pour être observé avec un simple microscope. La trajectoire suivie par cet objet est appelé *mouvement Brownian*, en référence au biologiste Robert Brown, qui en a fait une étude systématique au début du dix-neuvième siècle. Le lien entre son mouvement et la nature moléculaire du liquide environnant à été rendue quantitative par Albert Einstein en 1905 [1] et a permis la première mesure du nombre d'Avogadro, par Jean Perrin en 1909 [6], donnant un argument décisif pour l'acceptation de la nature atomique du monde.

Le mouvement brownien est un modèle minimal pour comprendre les effets de l'agitation thermique. En ce sens, il a servi de base mécanique pour comprendre de nombreux phénomènes de physique statistique ou de thermodynamique jusqu'alors connus empiriquement. Un premier exemple est la démonstration du principe de réciprocité par Lars Onsager en 1931 [206, 207], qui relie la réponse d'un objet brownien à une petite perturbation extérieur à ses fluctuations dues à l'agitation thermique. Formulé en ses termes historiques de thermodynamique hors-d'équilibre, ce principe relie le flux des variables extensives (par exemple un flux de chaleur) qui caractérisent un système, aux affinités thermodynamiques correspondantes (un gradient de température). Ce principe à permis de comprendre que deux effets thermoélectriques bien connus, d'un côté l'effet Peltier (un flux de chaleur dû à une différence de potential électrique) et de l'autre l'effet Seebeck (un courant électrique dû à une différence de température) étaient deux manifestations réciproques du même lien flux-affinité. Ici les équations mécaniques simples de la diffusion à l'échelle microscopique (le mouvement brownien) ont donné une explication précise à ces effets macroscopiques empiriques.

La formulation du principe de réciprocité en terme de réponse à une perturbation et de fluctuations spontanées est une forme théorème de fluctuation-dissipation qui à ensuite été développé par Callen et Welton en 1951 [162] puis Kubo dans les années soixante [169].

Un autre effet thermodynamique connu empiriquement depuis la fin du dix-neuvième siècle est la loi d'Arrhenius, qui relie la vitesse d'une réaction chimique la température ambiante par une loi exponentielle. La description par Henrik A. Kramers de la diffusion d'un objet Brownien dans un état métastable [38], minimum local d'un potentiel à donné une description mécanique plus fine du phénomène. Dans ces deux exemples, le mouvement brownien permet de donner une description plus satisfaisante mais aussi plus unificatrice de divers phénomènes de près ou de loin liés à la température. Le mouvement brownien étant le rôle de la physique statistique qui explique les lois empiriques de la thermodynamique aux cas hors-d'équilibre.

Les développements expérimentaux du vingtième siècle ont amené un regain d'intérêt pour le mouvement Brownien. Avec les lasers apparaît la capacité de manipuler des objects microscopiques avec des forces du même ordre de grandeurs que celles en jeu dans leur mouvement naturel et ainsi, d'interagir avec ces objets. Les pièges -ou pinces- optiques qui permettent ces manipulations ont été développés dans les années quatre-vingt par Arthur Ashkin [2] et leur application au mouvement brownien a été décisive. Les études historiques du mouvement Brownien étaient uniquement de observations, il est désormais possible de sonder la réponse d'une trajectoire brownienne à des forces choisies de façon précise et contrôlable.

Parmi les test expérimentaux majeurs permis par le mouvement brownien en piège optique, on peut citer deux exemples. Le premier est la mesure expérimentale de de la théorie de Kramers, mentionnée plus haut. En 1999, en combinant deux faisceaux lasers, l'équipe de Brage Golding [43] a réalisé un piège optique bistable où deux minima sont séparés par une barrière de potentiel. Une bille microscopique placée dans ce champ optique est piégée dans l'un des minima. L'agitation du fluide environnant lui fournit une énergie suffisante pour sauter d'un minimum à l'autre. En étudiant la trajectoire d'une microparticule, ils mesurent la relation exponentielle entre le taux d'activation (taux de saut d'un puit à l'autre) et la température du fluide environnant. En 2017, l'équipe de Lukas Novotny [44] généralisent ce résultat en réalisant une expérience similaire dans le vide au lieu d'un liquide comme dans le cas précédent. Ils accèdent ainsi à un régime permettant de tester l'hypothèse de Kramers selon laquelle, pour une certaine combinaision de hauteur de la barrière de potentiel et d'amplitude

de la force thermique, un taux d'activation maximal peut être atteint. Cet exemple montre comment, au cours des dernières dizaines d'années, le contrôle croissant sur la dynamique brownienne dans un piège optique permet de tester expérimentalement des théories majeures du vingtième siècle.

Un second exemple important obtenu dans le cadre du mouvement brownien en piège optique est l'accélération de la relaxation d'un système vers son état d'équilibre, par l'ingénierie du potentiel. Lorsqu'un paramètre définissant l'état d'équilibre d'un système statistique ou thermodynamique (température, pression, volume etc.) est modifié, le système évolue spontanément vers un nouvel état d'équilibre, défini par la nouvelle valeur du paramètre. Cette évolution prend un temps qui est défini par des caractéristiques intrinsèques au couple système-environnement (masse de l'objet, viscosité de l'environnement etc.). Ce temps de relaxation d'un état d'équilibre à un autre est a priori une limite fondamentale. En 2016, l'équipe de Sergio Ciliberto [33] a proposé une méthode pour outrepasser cette limite. Ce travail se concentre sur la relaxation d'un objet brownien dans un piège optique lorsque la raideur du piège (analogue à l'inverse d'un volume) est modifiée. Plutôt que de modifier brutalement la raideur d'une valeur initiale à une valeur finale et laisser le système hors-d'équilibre relaxer spontanément, ils dérivent un protocol plus subtil qui accompagne la relaxation de la distribution des positions de l'objet brownien. Ainsi, ils obtiennent des temps de relaxation jusqu'à cent fois plus courts que le temps naturel. Un tel résultat peut s'appliquer dans deux nombreux contextes et à différentes échelles, mais la simplicité du formalisme du mouvement brownien a permis sa dérivation tandis que le contrôle expérimental des pièges optique a permis sa réalisation.

Les deux exemples cités étudient la dynamique d'un objet brownien dans un bain thermique à l'équilibre, à une température définie. Un tel bain, qui résulte des nombreuses collisions avec les molécules du liquide ou du gaz environnant n'a pas de corrélation temporelle, il agit à toutes les fréquences et est appelé un bruit blanc (dans le blanc, toutes les couleurs -fréquences- sont représentées également). Néanmoins, le cas de la kinésine mentionnée plus haut souligne l'importance des fluctuations en biologie, hors le bain qu'expérience un moteur moléculaire micrométrique n'est pas un simple fluide. Le cytoplasme dans lequel évolue la kinésine est saturé de nombreux agents, filaments, protéines, molécules de tailles diverses. Un tel bain n'est pas bien décrit par un bruit blanc et la diffusion d'un objet dans ce milieu n'est pas brownienne au sens d'Einstein. La compréhension de la dynamique d'objets biologiques ou immergé dans un materiel biologique appartient au domaine de la matière active. Une première approche consiste en l'étude de la rhéologie et la diffusion de particules sondes, injectées

par exemple dans le cytoplasme d'une cellule. Une autre approche est la réalisation d'analogues, qui reproduisent, par des moyens électroniques ou optiques, certaines caractéristiques d'un environnement biologique. Ces deux approches reposent à nouveau sur la capacité du mouvement brownien à capturer la physique de nombreux systèmes où les fluctuations sont importantes.

Cette thèse s'inscrit dans ce contexte varié de l'étude de la dynamique brownienne d'un objet micrométrique optiquement piégé, sous l'influence d'un bain thermique ainsi que de forces bien contrôlées. Dans ce travail, débuté en octobre 2019 nous étudions les propriété statistiques et thermodynamiques hors-d'équilibre d'un objet unique. Plus généralement, ces recherches s'inscrivent dans une collaboration entre une équipe théorique (QDyno, Institut de Physique et Chimie des Matériaux de Strasbourg), sous la direction de Giovanni Manfredi et Paul-Antoine Hervieux, et une équipe expérimentale (LiMaCS, Centre Européen de Sciences Quantiques) sous la direction de Cyriaque Genet. Le dialogue constant entre un aspect expérimental sur une plateforme de piégeage optique et un travail théorique (à la fois analytique et numérique) nous a permis de développer plusieurs projets originaux qui permettent d'observer la dynamique brownienne sous des aspects appartenants à des domaines variées, de la matière active biologique aux objets quantiques. Cette thèse est constituée de trois projet trans-disciplinaires, focalisés sur des thématiques différentes, mais liés par le même cadre de physique statistique hors-d'équilibre mésoscopique.

7.2 Résultats et discussion

Le manuscrit débute par une introduction générale qui inscrit ce travail dans le contexte de la recherche contemporaine sur les sujets abordés, suivie de quatre chapitres qui détaillent le travail réalisé.

7.2.1 Mouvement Brownien dans un piège optique

La dynamique stochastique d'une microparticule soumises aux forces thermiques est décrite par l'équation de Langevin. Sa distribution de probabilité de position quant à elle, obéit à l'équation déterministe de Fokker-Planck. Le premier chapitre de ce manuscrit décrit les méthodes qui permettent l'étude exhaustive du mouvement brownien d'une sphère de polystyrène micrométrique suspendue dans de l'eau à température ambiante. Cette microsphère est suffisamment légère pour que les collisions avec les

molécules d'eau qui l'entourent la mettent en mouvement et cette agitation aléatoire (ce bruit) est un mouvement brownien. Lorsque de plus, on focalise une faisceau laser à profile transverse gaussien sur la sphère, le fort gradient d'intensité lumineuse autour du point focal permet de créer un potentiel localement harmonique qui piège mécaniquement la sphère, limitant l'étendue de son mouvement brownien. La dynamique de la sphère sous l'effet combiné du bruit thermique et du piège optique est correctement décrite par une équation de Langevin sur-amortie

$$\dot{x}_t = -\omega_0 x_t + \sqrt{2D}\xi_t \tag{7.1}$$

où ω_0 est l'inverse du temps de relaxation de la bille dans le potentiel et D le coefficient de diffusion, ratio entre l'énergie thermique $k_B T$ et le coefficient de friction γ de la bille dans le fluide. Le terme ξ_t est un bruit blanc qui émule l'action du fluide. C'est une variable aléatoire sans corrélation temporelle : $\langle \xi_t \xi_s \rangle = \delta(t-s)$ où $\langle . \rangle$ dénote la moyenne sur de nombreuses réalisations du bruit.

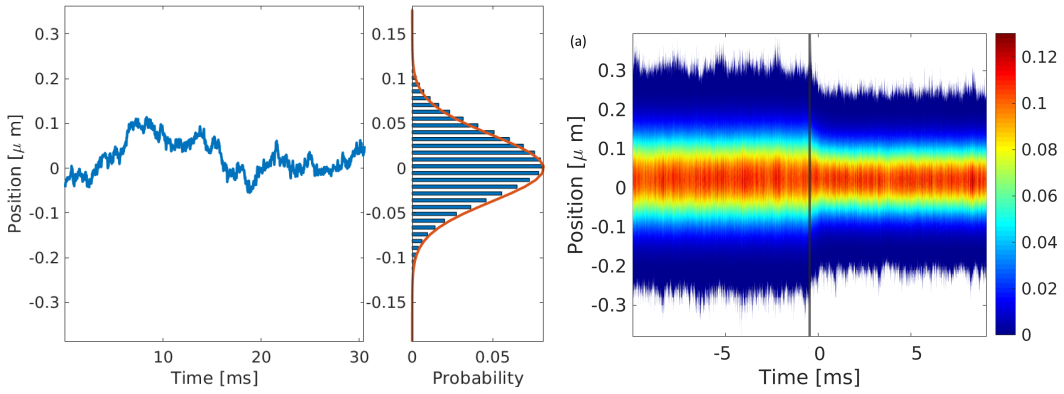

Figure 7.1: (gauche) Trajectoire x_t d'une microparticule dans le piège optique expérimental. La trajectoire obéit à l'équation de Langevin suramortie. (centre) distribution des position à l'équilibre dans un piège, en bleue l'histogramme mesuré sur une trajectoire brownienne et en rouge la distribution gaussienne théorique d'un état d'équilibre thermique dans ce potentiel. (droite) densité de probabilité évoluant au cours du temps lorsque le système subit une modification de la raideur du potentiel optique. La densité, gaussienne en tout temps, obéit à l'équation déterministe de Fokker-Planck.

L'objet du premier chapitre est d'introduire les outils nécessaires pour étudier les propriétés des trajectoires x_t de la microsphère dans le piège optique. Une trajectoire unique mesurée dans notre piège, telle que montrée Fig. 7.1 (gauche) est une réalisation de l'équation de Langevin. La distribution de probabilité de position, montrée

dans Fig. 7.1 (centre) est déterministe, c'est la solution stationnaire de l'équation de Fokker-Planck. Il s'agit d'une gaussienne dont la variance est proportionnelle à la température du fluide. Dans ce chapitre, nous expliquons la méthode de piégeage, de mesure de la position de la sphère en temps réel, ainsi que la calibration de l'expérience [95]. L'exemple d'une modification abrupte de la raideur du piège, implémentée expérimentalement en modifiant l'intensité du faisceau laser permet d'étudier la dynamique hors-d'équilibre du système. Dans ce contexte est introduite la notion d'ensemble statistique qui permet d'étudier les propriétés statistiques du système au cours du temps. Sur la figure 7.1 (droite) est représentée la distribution de probabilité de position évoluant au cours du temps lorsque la raideur est modifiée. La distribution obéit à l'équation de Fokker-Planck.

De plus ce premier chapitre introduit les observables stationnaires majeures du mouvement brownien. Son étude spectrale, qui permet la calibration du dispositif expérimental, est liée à la fonction de corrélation par le théorème de Wiener-Khinchine. Le déplacement carré moyen de la microsphère dans le piège est utile pour caractériser la nature de la diffusion, c'est une mesure locale dans le temps, de la manière dont l'objet brownien explore l'espace disponible à son mouvement. Ces quantités sont dérivées analytiquement et appliquées à des trajectoires mesurées expérimentalement. Nous introduisons dans ce chapitre les méthodes numériques nécessaires pour simuler des trajectoires dans des conditions similaires à une expérience physique, ces simulations constituent un outil qui alimente et vérifie les résultats expérimentaux. Pour finir, une section plus théorique introduit le formalisme de la thermodynamique stochastique, tel qu'il à été proposé dans les années 1990 par Ken Sekimoto [46], ces notions seront utilisées plus loin dans le manuscrit pour caracteriser la thermodynamique d'un système actif.

Ce chapitre introduit des outils, mais permet également de placer nos méthodes et notre expérience dans le paysage scientifique contemporain du mouvement brownien en piège optique. Les chapitres suivants décrivent les développements plus originaux que nous proposons.

7.2.2 Propriétés du bruit pour un objet Brownien en piège optique, ergodicité, stabilité

L'utilisation des trajectoires browniennes pour l'étude de problèmes de physique statistique, de thermodynamique ou pour construire des simulateurs analogiques comme

nous le ferons dans les chapitres suivants repose sur plusieurs hypothèses. Il est nécessaire de construire de grands ensembles statistiques pour étudier, par exemple la réponse moyenne du système à une perturbation ou sa relaxation d'un état à un autre. Dans notre cas, notre dispositif expérimental n'est constitué que d'un objet brownien unique. Un ensemble statistique peut être obtenu en appliquant la même perturbation de façon cyclique et en enregistrant la longue trajectoire répondant à cette série de perturbation avant de la réarranger en un ensemble de sous-trajectoires indépendantes.

Cette réorganisation de la trajectoire repose sur l'hypothèse que chacune des sous-trajectoires est équivalente à toutes les autres, signifiant aussi que, dans le cas stationnaire, une observable calculée comme une moyenne temporelle sur cette sous-trajectoire est égale à la même observable calculée comme une moyenne d'ensemble sur toutes les trajectoires à un instant donné. Cette hypothèse est appelée ergodicité de l'ensemble et doit être vérifiée avant d'utiliser les trajectoires expérimentales dans ce contexte. De plus, que ce soit pour réaliser un grand ensemble statistique pour étudier des états non-stationnaires ou simplement pour étudier un état stationnaire avec une grande précision, de très longues trajectoires sont nécessaires, typiquement plusieurs minutes. Cela repose à nouveau sur une hypothèse, qui est la stabilité de l'ensemble du dispositif expérimental.

Le deuxième chapitre présente un ensemble cohérent d'observables qui permettent de tester l'ergodicité et la stabilité dans le contexte des expériences de piège optique, travail publié en 2021 [105]. La méthode utilisée pour construire un ensemble à partir d'une trajectoires unique est présentée Fig. 7.2. Comme nous l'avons souligné, l'ergodicité d'un ensemble de trajectoire signifie qu'une observable stationnaire calculée sur cette trajectoire donnera le même résultat que si elle est calculée sur une autre trajectoire, ou sur l'ensemble. Nous proposons l'implémentation d'un test d'ergodicité, qui est dérivé de la définition formelle de l'ergodicité mais qui peut être appliqué expérimentalement. Ce test [97] est basée sur l'étude précise de la dépendance temporelle des moments du ratio de déplacements carrés moyens calculés sur l'ensemble et sur le temps. Le paramètre ergodique obtenu est montré Fig. 7.2 et valide l'hypothèse ergodique par l'accord entre son expression analytique et ses mesures expérimentale et numérique.

De plus nous adaptons un test basé sur la variance d'Allan, initialement utilisé pour vérifier la stabilité temporelle des horloges atomiques [140] pour s'assurer de la stabilité de notre plateforme expérimentale. L'ensemble de ce travail constitue une étude expérimentale, théorique et numérique de propriétés statistiques subtiles des

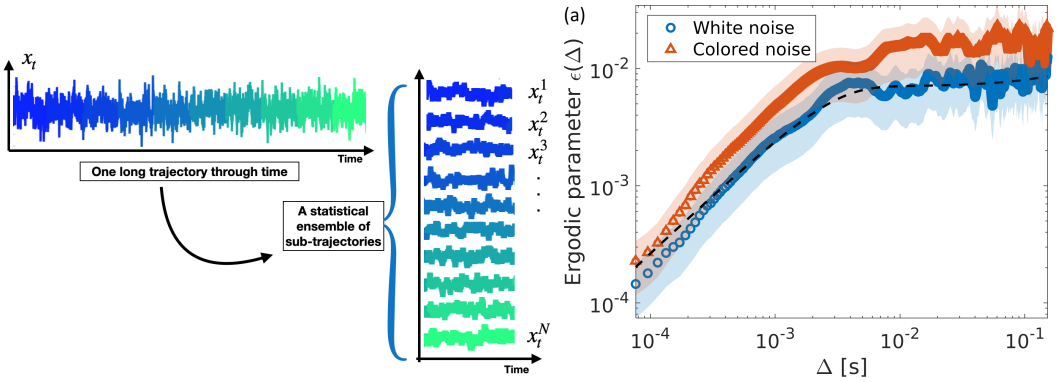

Figure 7.2: (gauche) Explication schématisée de la méthode pour construire un ensemble statistique à partir d'une longue trajectoire unique. (droite) Paramètre ergodique. Construit à partir de déplacements carrés moyens, ce paramètre est un moyen d'évaluer l'ergodicité d'un ensemble fini sur des temps fini. Pour un ensemble de sous-trajectoires de durée $\mathcal{T}$, la décroissance du paramètre $\epsilon(\Delta)$ dans la limite $\mathcal{T}/\Delta \to \infty$ valide l'hypothèse ergodique de l'ensemble construit. Le résultat expérimental est représenté en bleu, comparé à un résultat numérique en rouge et analytique en noir.

trajectoires browniennes mais sert également de justification méthodologique pour la suite de notre travail.

7.2.3 Ingénierie de bain, matière active et information

Comme nous l'avons introduit au début de ce résumé, les fluctuations jouent un rôle important dans les systèmes biologiques à l'échelle micrométrique comme dans l'exemple proposée de la kinésine. Le mouvement brownien en piège optique, par son caractère flexible est bien contrôlé, est un candidat intéressant pour étudier ces systèmes. Néanmoins, les trajectoires browniennes telles qu'elles sont présentées dans les chapitres précédents différent des systèmes biologiques sur plusieurs points. La matière vivante transforme constamment de l'énergie, d'uns source généralement chimique (glucides ou ATP) en quantités thermodynamiques comme le travail et la chaleur. Cette consommation contante d'énergie les maintient hors de l'équilibre thermodynamique avec le bain thermique environnant [143, 58]. À l'échelle microscopique, les fluctuations sont importante et les techniques de conversion d'énergie doivent prendre en compte un environnement fortement stochastique. La combinaison du non-équilibre thermodynamique et de la présence des fluctuations permet une grande richesse de phénomènes physiques, comme par exemple la rectification des fluctuations lors du transport axonal de la kinésine [27] ou la dynamique complexe d'une bactérie propulsée par ses flagelles

dans l'agitation thermique d'un fluide [63]. De ce point de vue thermodynamique, les systèmes vivants appartiennent à la classe plus large de la matière active, qui contient également des systèmes non-biologiques, comme des assemblées d'objets mécaniques autopropulsés. Le cas de l'autopropulsion, biologique ou mécanique, est un example paradigmatique de la matière active, où une énergie disponible est utilisée pour modifier la dynamique d'un objet. L'utilisation du mouvement brownien en piège optique pour implémenter un simulateur analogique d'un système autopropulsé permet alors d'étudier les propriétés thermodynamique d'un modèle paradigmatique de la matière active, sans pour autant manipuler de véritables systèmes biologiques.

Ainsi, le troisième chapitre décrit l'utilisation de notre système expérimental pour sonder les lois régissant une grande classe de systèmes biologiques a l'échelle microscopique, travail soumis à la publication et disponible sur ArXiv [208]. Dans ce chapitre nous proposons d'utiliser une force optique pour émuler l'effet d'un système d'autopropulsion stochastique sur la microsphère optiquement piégée. Cette dernière possède alors les même caractéristiques dynamique et thermodynamique d'une bactérie dans un fluide, ou de manière équivalente d'une colloïde inerte plongé dans un bain saturé de bactéries [98].

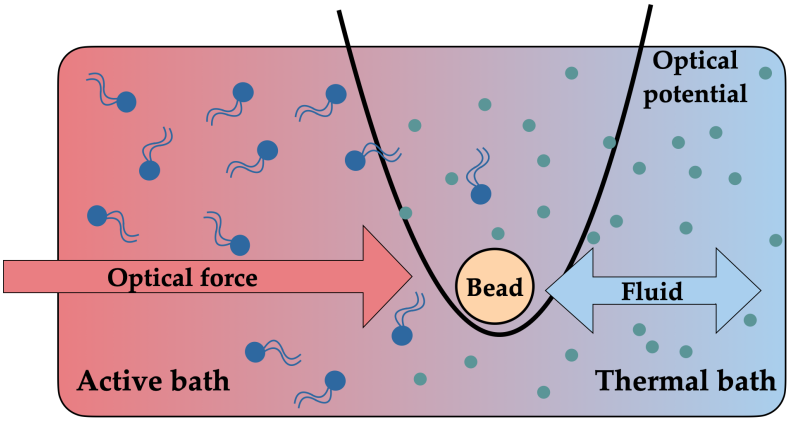

Figure 7.3: Schéma de l'analogie optomécanique-matière active proposée : la force optique est un bruit coloré (signal stochastique avec une fonction d'autocorrelation exponentielle) joue le même rôle sur la microsphère qu'un bain actif hors-d'équilibre tel qu'un fluide saturé de bactéries. La microsphère est alors connectée à deux bains : un bain thermique à température ambiante, par l'interaction avec le fluide environnant et un bain non-thermique par la force externe. Elle n'est plus à l'équilibre thermodynamique et sa trajectoires montre des effets typiques de l'autopropulsion, comme la superdiffusion à temps courts.

La force externe est appliquée à l'aide de la pression de radiation (voir schéma Fig. 7.3) exercée par un laser additionnel piloté par un modulateur accousto-optique, lui-même controlé par ordinateur. Cet important développement expérimental permet d'appliquer une force mécanique sur la microsphère, avec une dépendance temporelle arbitraire. Ici nous appliquons à la sphère une force stochastique, un bruit η_t qui, contrairement au bruit thermique dû au fluide, n'est pas blanc mais coloré par une mémoire exponentielle $\langle \eta_t \eta_s \rangle = \alpha e^{-\omega_c |t-s|}$, où ω_c est l'inverse du temps de corrélation de ce bruit. En effet, il à été montré sur des systèmes biophysiques [98] qu'une telle force décrit correctement la dynamique du modèle de bain actif utilisé ici, une microsphère dans un fluide saturé de bactéries.

Cette force appliquée à la sphère permet non-seulement de retrouver les résultats connus pour la matière biologique mais aussi d'étendre significativement les régimes sondés jusqu'ici par des expériences de biophysique. Le caractère hors-d'équilibre des trajectoires se manifeste par la difficulté à définir une température dans le système, ce qui a pour conséquence la brisure du théorème d'équipartition de l'énergie qui relie simplement la variance de position de la particule brownienne à la température du fluide. De façon plus subtile, la notion de température apparaît à nouveau lors d'un test expérimental du théorème de fluctuation-dissipation, qui, dans sa forme simple est également brisé par les trajectoires hors-d'équilibre observées. Ce théorème peut être rétablit si l'on s'en sert pour définir une température effective. Celle-ci est alors une fonction de la fréquence à laquelle le système est observé, ce qui complique son sens physique. De façon intéressante, une température dépendant de la fréquence est également une mesure la répartition spectrale de l'énergie injectée, sous la forme de l'énergie thermique $k_B T_{eff}[f]$, qui donne une compréhension intuitive de la relation entre la couleur du bruit et la réponse du système. Le fait de réaliser un analogue au lieu de travailler avec du matériel biologique permet d'éviter de nombreuses contraintes et de ce fait de simplifier l'étude de certains régimes loin de l'équilibre thermodynamique.

La thermodynamique des trajectoires est étudiées avec le formalisme introduit dans le premier chapitre et met en valeur des quantités de chaleur dissipée dans le fluide du même ordre que celles en jeux dans des système biologiques micrométriques. Un résultat important de ce travail à été la découverte d'une relation expérimentale simple et robuste entre une quantité thermodynamique -l'énergie rejetée par la microsphère sous forme de chaleur dans le fluide- et une quantité informative -l'entropie spectrale qui mesure la quantité d'information contenue dans le bain actif que constitue la pression de radiation. Cette relation est exposée Fig. 7.4 pour différentes intensités de bruit coloré. Sa mise en perspective avec les phénomène informatif dans les systèmes

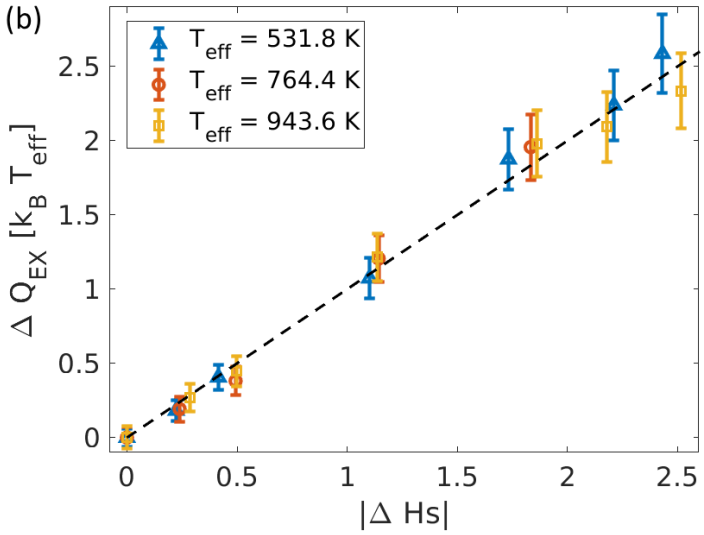

Figure 7.4: Mesure de l'égalité expérimentale entre la chaleur rejetée dans le bain normalisée par la température effective et l'information spectrale contenue dans le bain actif, suggérant une conversion information-énergie opérée par le système mécanique.

biologique est assurément une question fertile.

7.2.4 Analogue classique stochastique d'un processus quantique

La dynamique d'un objet quantique est connue pour être différente des objets classiques qui constituent notre quotidien. De nombreux effets quantiques apparaissent à l'échelle nanométrique -effet tunnel, superposition, diffraction d'un objet massif etc.- et n'ont pas d'équivalent classiques, ce qui les rends souvent plus difficile à appréhender. Ces effets fondamentaux de la matière sont, de plus, parfois difficiles à mettre en oeuvre expérimentalement, car ils apparaissent à très petite échelle, à très basse température, ou parce qu'ils sont facilement dominés par d'autre effets. Cette double barrière : éloignement avec les objets classiques et difficulté à manipuler rend intéressante la réalisation d'analogues. Si un objet classique bien contrôlé peut reproduire certaines caractéristiques d'un système quantique, il peut être utiliser pour explorer les caractéristiques de ce dernier tout en restant dans le monde classique, doublement accessible.

Dans ce contexte, une expérience importante a été la réalisation en 2005 par Yves Couder [174, 175] d'un analogue hydrodynamique d'une dynamique quantique, à l'aide de gouttes d'huile millimétriques. Les gouttes sont maintenues en suspension au dessus

d'une surface liquide par une oscillation rapide de cette dernière, empêchant la coalescence. L'interaction entre la goutte et le liquide oscillant crée une onde qui va entraîner la goutte sur une trajectoire erratique sur la surface. Ce phénomène peut être décrit avec d'autres mots : une particule, possédant une masse et une position bien définie, crée une onde qui guide sa trajectoire. Cette formulation est en adéquation avec la théorie de l'onde-pilote, formulée par Louis de Broglie au début du vingtième siècle pour une particule quantique et reprise par David Bohm dans les années cinquante [177]. À partir de cette analogie, l'équipe de Yves Couder à pu montrer plusieurs effets typiquement quantiques avec ce dispositif expérimental simple, tel que la diffraction par d'une goutte unique par une fente.

Dans ce contexte, le dernier chapitre de la thèse présente un travail publié en 2021 [**?**] et met en avant une seconde approche analogique pour appliquer notre dispositif expérimental hors de son cadre actuel. Dans ce travail nous nous servons d'une famille d'équation stochastiques appelés processus de McKean-Vlasov [181] pour émuler la dynamique d'un objet quantique dans un bain thermique. Un processus de McKean-Vlasov est une équation différentielle stochastique pour une variable aléatoire comme la position x_t où apparait explicitement la distribution de probabilité de cette variable. Cette dépendance non-triviale permet de construire des forces non-locales où la position instantanée d'un objet brownien dépend de la position d'un ensemble d'autres objets similaire, quelque soit leur distance. Un cas particulier de force non-locale est celle qui dérive du potentiel quantique $Q[n(x,t)] = -\frac{\hbar^2}{2m}\frac{\Delta\sqrt{n(x,t)}}{\sqrt{n(x,t)}}$ où $\hbar$ est la constante de Planck, m la masse de la particule et $n(x,t)$ la distribution de probabilité de la position x_t. Ce potentiel, bien connu en hydrodynamique quantique est, comme nous le montrons dans ce chapitre, la première correction à ajouter à une équation classique pour prendre en compte des effets quantiques dans la dynamique de la distribution $n(x,t)$ [180]. En ajoutant la force $F_Q = \nabla Q$ à l'équation gouvernant le mouvement de la microsphère dans le piège Eq. (7.1), nous obtenons un processus stochastique dont la distribution de probabilité obéit à une dynamique quantique - mais où $\hbar$ est arbitraire. Nous appliquons ce formalisme à différents potentiels, d'abord numériquement, puis expérimentalement dans cas d'un potentiel parabolique.

La réalisation de notre analogue nécessite de mesurer en temps réel la distribution $n(x,t)$. Pour cela nous proposons dans un cas général d'utiliser un ensemble de $\mathcal{N}$ pièges optiques -voir schéma Fig. 7.5- sur lesquels il est possible de mesurer instantanément la distribution, calculer le potentiel quantique $Q[n]$ et l'injecter au pas de temps suivant.

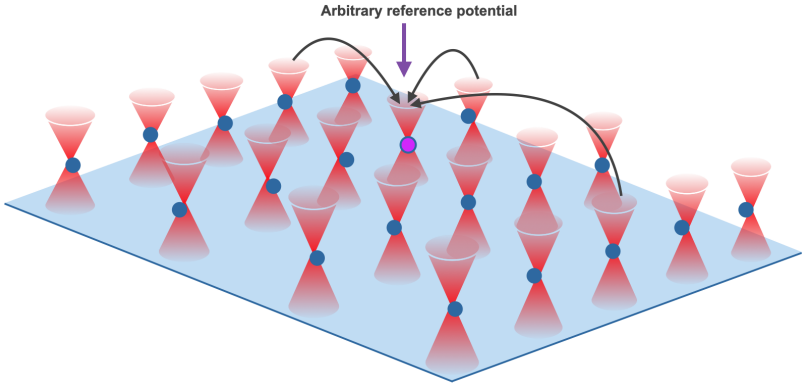

Figure 7.5: Représentation schématique de la réalisation expérimentale possible dans le cas général : un ensemble de pièges optiques agissent en parallèle. Dans chacun se trouve un objet brownien indépendant, à chaque instant du temps, l'ensemble est utilisé pour mesurer la distribution de probabilité instantanée. De cette dernière est calculé le potentiel de Bohm et la force qui en dérive qui est appliquée à l'ensemble des puits pour l'instant suivant. Chacune des trajectoires obéit alors à une dynamique de McKean-Valsov et la densité de l'ensemble, au modèle de drift-diffusion quantique.

Cette méthode est implémentée numériquement pour observer la dynamique d'un objet quantique dans un double puit de potentiel (potentiel de Duffing) à deux paramètres positifs a et b : $V(x) = -ax^2 + bx^4$. Sur la Fig. 7.6 (gauche) nous représentons deux trajectoires stochastiques dans le piège bistable. En bleu est représentée une trajectoire classique, qui réside dans un minimum pendant un temps aléatoire τ avant de sauter par activation thermique dans l'autre minimum. En rouge est représenté une trajectoire obéissant au processus de McKean-Vlasov, qui prend en compte la correction quantique. On observe un plus grand nombre de passage de la barrière de potential, ce qui amène à une distribution moins piquée sur les deux minima. Ce changement est visible dans la modification de la statistique des temps de résidence Fig. 7.6 (droite) où l'on observe la distribution exponentielle dans les deux cas, mais avec un temps moyen $\langle\tau\rangle$ plus faible dans le cas du processus de McKean-Vlasov. Nous interprétons cette modification comme la première approximation de l'effet tunnel : un abaissement effectif de la barrière de potentiel dû à la nature quantique de l'objet. Un deuxième exemple étudié numériquement est le cas d'un potentiel mono-stable, avec une non-linéarité quartique $V(x) = ax^2 + bx^4$. Dans ce cas, les propriétés stationnaires de la trajectoires sont étudiées : sa distribution de probabilité converge vers la solution du modèle de drift-diffusion quantique et sa fonction d'autocorrelation décroit plus lentement que l'équivalent classique.

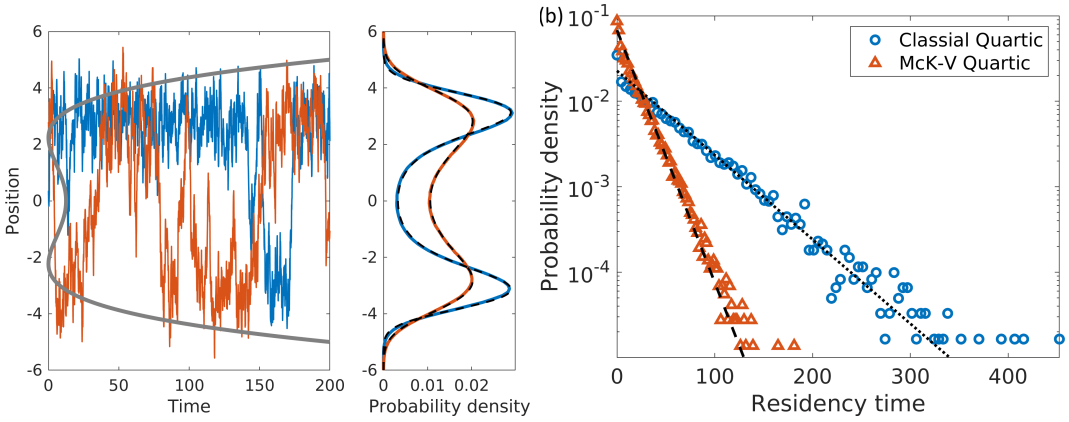

Figure 7.6: (gauche) Trajectoire brownienne classique (ligne bleu) et McKean-Vlasov quantique (ligne rouge) dans un double-puit V. Le potentiel quantique Q a pour effet d'abaisser la barrière de potentiel séparant les deux minima, comme on peut le voir par les deux distribution de probabilité. (droite) Mesure expérimentale de la distribution exponentiel des temps de résidence de la particule dans un puit. Le temps moyen est plus court pour la trajectoire quantique, signature au premier ordre de l'effet tunnel.

Ce processus a également pu être implémenté expérimentalement en se basant sur la simplicité analytique du potentiel harmonique. Dans ce cas, le potentiel quantique peut être explicitement dérivé et ses effets incorporés dans une variation temporelle de la raideur du piège optique. Cette réalisation a permis d'étudier la dynamique hors-d'équilibre d'un objet quantique en contact avec un bain thermique, dans système expérimental purement classique.

Le travail présenté dans ce chapitre propose un analogue original d'un processus quantique, il est dérivé à partir du formalisme hydrodynamique et implémenté dans différents cas numériques et expérimentaux. La nature probabiliste à la fois de la mécanique quantique et de processus stochastique peut amener à des généralisations de cette analogie, tel que le formalisme de Nelson [202] de la mécanique quantique.

7.3 Conclusion

Dans cette thèse nous avons utilisé une approche à la fois expérimentale et théorique pour développer autour d'un même système physique un ensemble d'applications originales qui étendent le champ d'étude accessible au mouvement brownien en piège optique. Un premier travail formel sur le propriétés statistiques des trajectoires nous

a permis de développer et d'implémenter expérimentalement un ensemble de test validant à la fois l'ergodicité et la stabilité des trajectoires. Si ces tests sont des vérifications nécessaires pour l'application de nos méthodes expérimentales par la suite, il s'agit également d'un accès expérimental à des propriétés fondamentales des processus stochastiques en jeux. La distinction des processus stochastiques ergodiques et non-ergodiques implique de nombreuses conséquences, à titre d'exemple, la non-ergodicité est le point de départ de la manipulation d'information. En effet, l'utilisation d'un système stochastique comme une mémoire demande avant tout que différents sous-ensembles de l'espace de configuration du système soient distinguables. Cela ne peut-être le cas d'un processus ergodique, où chaque trajectoires explore la totalité de l'espace accessible, sans pouvoir être discriminée. La non-ergodicité, au moins locale dans le temps ou l'espace est donc une propriété importante, que nous explorons dans ce chapitre avec un exemple expérimental.

Dans les deux chapitres suivants, nous proposons deux développement connectant notre système optomécanique classique respectivement aux systèmes biologiques microscopique et aux objets quantiques. Ces deux applications proposent de nouveaux chemins aux expériences optomécaniques mais apportent également des résultats inédits dans les deux domaines concernés. Ces travaux suggèrent de nombreuses perspectives. Tout d'abord, la réalisation d'un bain additionnel, aux propriétés contrôlées, apporte de nombreuses possibilités. Dans ce travail, nous avons exploré en détail le cas d'un bruit gaussien exponentiellement corrélé pour sa capacité à simuler l'effet d'un bain actif constitué d'objet autopropulsés, mais la méthode développée est plus générale : d'autres bruits peuvent êtres explorés, avec des distributions et des fonctions de correlations différentes. Un autre exemple paradigmatique de matière active vivante, les fluides dits encombrés, comme le cytoplasme, sont saturés non pas d'objets autopropulsés mais de filaments de diverses natures, et représentent des bains différents [94, 52]. Ils sont connus pour induire des trajectoires sous-diffusives qui pourraient également être explorées avec les méthodes proposées ici. D'autres familles de bruits naturels sont souvent étudiés numériquement, les bruits de Levy par exemples et pourraient également être appliqués expérimentalement ici. On peut également se demander, en lien avec le dernier chapitre et les analogues quantiques, quel serait l'effet d'un bruit doté d'un spectre quantique (statistique des photons) tel qu'ils apparaissent en optomécanique métrologique (détecteurs d'onde gravitationnelles).

D'un autre point de vue, l'ingénierie de bain par pression de radiation pourrait être transposées également sur des expériences de biophysiques manipulant de la matière biologique. Il a été montré récemment que le déplacement d'une kinsine sur un brin

de microtubule in vitro est accélérée en présence de bruit artificiel [27] ; de plus cette dernière possède une réponse mécanique non-triviale en fonction de la fréquence. Est-ce que l'application sur une kinésine en mouvement, d'un bruit imitant les caractéristiques du milieu intracellulaire maximise son efficacité ? Un tel résultat serait en accord avec un point de vue évolutionniste : ce moteur moléculaire doit être optimisé à son environnement naturel.

Pour finir, la manipulation du bain proposée ici peut être combinée avec le savoir-faire mieux connu de manipulation du potentiel. D'un côté, cela permettrait d'explorer l'effet d'un bain actif hors-d'équilibre sur les propriétés thermodynamiques de transformations connues : la compression ou décompression du volume accessible à l'objet brownien. La manipulation de la température effective (simple dans le cas d'un bruit blanc, plus complexe sinon) adjointe à la modification du volume amène au concept de moteur cyclique, pour lesquels la généralisation à des bains actifs est questionnées de nos jours [201]. D'un autre côté, comme nous l'avons exploré dans ce chapitre, la couleur du bruit appliqué est elle-même un paramètre qui permet des transformations thermodynamiques. Ce paramètre peut servir pour construire des cycles, avec des propriétés fondamentalement différentes d'un changement de température.

On voit ainsi les nombreuses perspectives suggérées par ce travail, tant en lien avec les concepts hérités de la biophysique, qu'avec des questions plus fondamentalement thermodynamiques.

Le dernier chapitre, qui présente un analogue classique stochastique d'un processus quantique peut suggérer, lui aussi, plusieurs développements. Premièrement, l'implémentation du processus de McKean-Vlasov dans un dispositif expérimental possédant un ensemble de pièges optiques simultanés permettrait de réaliser expérimentalement le processus de McKean-Vlasov dans des potentiels arbitraires. Comme le montre l'exemple du potentiel de duffing, des profils plus complexes mettent en valeur des effets non-triviaux, comme ici l'effet tunnel, la généralisation expérimental du potentiel permettrait d'injecter ces nouveaux phénomènes dans le cadre de mouvement brownien classique. Il faut souligner que, si la force de Bohm dans le cas du potentiel harmonique induit uniquement une modification de la raideur, et donc ne modifie pas fondamentalement la dynamique dans le cas stationnaire, ce n'est pas le cas en général, ou le potentiel de Bohm prends une forme complexe, dépendant de la densité au cours du temps.

Si le cas étudié ici correspond à un processus quantique particulier, le modèle de

drift-diffusion quantique, qui n'est valide que dans une certaine limite visqueuse, il est intéressant de chercher à généraliser l'analogie brownienne de la mécanique quantique à des modèles plus généraux. La théorie de Nelson de la mécanique quantique est une généralisation possible. Dans ce formalisme, Edward Nelson démontre en 1966 [202] que l'équation de Schrödinger peut être exactement dérivée à partir d'un processus de Ornstein-Uhlenbeck, c'est-à-dire une équation de Langevin dans la limite suramortie. Pour cela, le coefficient de diffusion est fixé à $\hbar/2m$, le terme de drift est une fonction de l'amplitude et de la phase de la fonction d'onde. Un tel formalisme est effectivement directement réalisable avec un système classique, au prix bien sûr d'un facteur d'échelle sur les paramètres. L'application de ce formalisme dans un piège optique permettrait de simuler des effets quantiques généraux à l'aide d'un dispositif expérimental classique. Ainsi, l'analogie proposée dans ce chapitre et illustrée sur certains exemples choisis peut être étendue à d'autres potentiels, ou à d'autres formalisme, gardant comme pivot l'analogie entre l'aléatoire statistique et quantique.

Chapter 8

Appendix

8.1 Optical trapping force

Here we give a brief summary of optical forces in the Rayleigh (dipolar) regime. Strictly speaking, the dipolar approximation is valid only for an object with a radius very small with respect to the wavelength of the trapping beam. This is not our case, since our micron-sized spheres have radius of the same order that the 0.785 micron wavelength of the trapping laser beam. Yet, as shown in [102], the dipolar approximation still gives satisfactory results with respect to gradient forces for objects with size of the same order than the beam waist radius. With this in mind, the Rayleigh approximation can be a suited model to describe physically the process at play in the optical trap, while keeping in mind that it is not an exact quantitative description, in contrast with a Mie calculation.

In the dipolar approximation [209], the fields can be considered as homogeneous on the scale of the particle. The dipolar moment writes $\mathbf{p} = \mathbf{p_0} e^{-i\omega t}$ is related to the field $\mathbf{E_0}$ by $\mathbf{p_0} = n^2\alpha^2\mathbf{E_0}$ where n is the refractive index and α the polarisability.

For monochromatic fields, with $\mathcal{E} = \mathrm{Re}\{\mathbf{E_0}e^{-i\omega t}\}$, $\mathcal{H} = \mathrm{Re}\{\mathbf{H_0}e^{-i\omega t}\}$ and $\mathcal{P} = \mathrm{Re}\{\mathbf{p}\}$, we can write Lorentz force

$$\mathbf{F} = (\mathcal{P}\cdot\nabla)\,\mathcal{E} + \mu_0\dot{\mathcal{P}}\times\mathcal{H}. \tag{8.1}$$

If we furthermore introduce the quantity $\mathbf{f_0} = (\mathbf{E_0}\cdot\nabla)\mathbf{E_0}^* - i\mu_0\omega\mathbf{E_0}\times\mathbf{H_0^*} = \rho\nabla\rho - i\rho^2\nabla\phi$ in the case of linear polarisation $\mathbf{E_0} = \rho e^{i\phi\mathbf{y}}$, we can write the time-averaged Lorentz force

$$\langle\mathbf{F}\rangle_{time} = \frac{n^2}{2}\mathrm{Re}\{\alpha\mathbf{f_0}\}. \tag{8.2}$$

This expression can be decomposed into

$$\langle \mathbf{F} \rangle_{time} = \frac{n^2}{2} \mathrm{Re}\left\{\alpha\right\} \mathrm{Re}\left\{\mathbf{f_0}\right\} - \frac{n^2}{2} \mathrm{Im}\left\{\alpha\right\} \mathrm{Im}\left\{\mathbf{f_0}\right\} \tag{8.3}$$

where the first term is reactive, and can be expressed with intensity gradient $\nabla\rho$ while the second is dissipative and can be expressed as phase gradient $\nabla\phi$, leading to

$$\langle \mathbf{F} \rangle_{time} = \frac{n^2}{2} \mathrm{Re}\left\{\alpha\right\} \rho\nabla\rho + \frac{n^2}{2} \mathrm{Im}\left\{\alpha\right\} \rho^2\nabla\phi. \tag{8.4}$$

The first term is the gradient conservative force, responsible for trapping. The second term is the non-conservative radiation pressure force.

8.2 Stationary solution by Laplace transform

We recall some useful Laplace transformations

$$\begin{aligned} &\mathcal{L}[x(t)] = x[s] \\ &\mathcal{L}[\dot{x}(t)] = sx[s] - \tilde{x}_0 \\ &\mathcal{L}[a] = a/s \end{aligned} \tag{8.5}$$

Eq. (4.5) can then be written in the s Laplace-domain

$$x[s] = \frac{1}{(s+\omega_0)} \left(x_0 + \sqrt{2D}\xi[s] \right). \tag{8.6}$$

We now recall useful inverse Laplace transformations

$$\begin{aligned} &\mathcal{L}^{-1}[\frac{1}{s}] = 1 \\ &\mathcal{L}^{-1}[\frac{1}{s+\omega_0}] = e^{-\omega_0 t} \\ &\mathcal{L}^{-1}[\frac{1}{s(s+\omega_0)}] = \frac{1}{\omega_0}\left(1 - e^{-\omega_0 t}\right) \\ &\mathcal{L}^{-1}[\frac{1}{s+\omega_0} * f[s]] = \int_0^t e^{-\omega_0(t-t')} f(t') dt' \end{aligned} \tag{8.7}$$

the last transformation being a consequence of convolution theorem. We can now transform back into the time-domain

$$x(t) = x_0 e^{-\omega_0 t} + \sqrt{2D} \int_0^t \xi_{t'} e^{-\omega_0(t-t')} dt' \tag{8.8}$$

Obtaining the solution of the Ornstein-Uhlenbeck process.

8.3 Calculation of the covariance of the displacement dx_t

We will compute the autocorrelation function (or covariance, since the process has zero mean) of displacements dX_t defined by the Ornstein-Uhlenbeck process $dX_t = -aX_t dt + bdW_t$ (adopting simple notations $\kappa/\gamma \equiv a$ and $\sqrt{2k_BT/\gamma} \equiv b$) as:

$$\begin{aligned}\langle dX_t dX_s\rangle &= \langle (-aX_t dt + bdW_t)\,(-aX_s ds + bdW_s)\rangle \\ &= \underbrace{a^2\langle X_t X_s\rangle dt^2}_{(1)} - \underbrace{ab\langle X_t dt dW_s\rangle}_{(2)} \\ &- \underbrace{ab\langle X_s ds dW_t\rangle}_{(3)} + \underbrace{b^2\langle dW_t dW_s\rangle}_{(4)}.\end{aligned} \tag{8.9}$$

Using the solution of the Ornstein-Uhlenbeck process

$$X_t = X_0 e^{-at} + be^{-at}\int_0^t e^{at'} dW_{t'}, \tag{8.10}$$

and assuming that all time increments are equal ($\forall t, s : dt = ds$), we can compute the different terms in (8.9) one by one:

$$(1) = \frac{ab^2}{2} e^{-a|t-s|} dt^2 \tag{8.11}$$

since at equilibrium $\langle X_0^2\rangle = k_BT/\kappa = b^2/2a$ (see below Eq. (**??**)).

$$\begin{aligned}(2) &= -ab\langle X_t dt dW_s\rangle \\ &= -ab\langle X_0 dW_s\rangle e^{-at} dt - ab^2 dt\int_0^t e^{a(t_1-s)}\langle dW_{t_1} dW_s\rangle \\ &= -ab\delta(s-0)dt^2 e^{-at} - ab^2 dt\int_0^t e^{a(t_1-s)}\delta(t_1-s)ds\end{aligned}$$

If we consider non-zero times, we can ignore the first term. For the second, we have two cases :

$$(2) = \begin{cases} -ab^2 dt^2 e^{-a(t-s)} & \text{if } t \geq s \\ 0 & \text{if } t < s \end{cases} \tag{8.12}$$

Similarly:

$$(3) = \begin{cases} 0 & \text{if } t > s \\ -ab^2 dt^2 e^{-a(s-t)} & \text{if } t \leq s \end{cases} \tag{8.13}$$

We can therefore combine them into $(2) + (3) = -ab^2 dt^2 e^{-a(\max(t,s)-\min(t,s))}$ giving:

$$(2) + (3) = -ab^2 e^{-a|t-s|} dt^2 \tag{8.14}$$

For the forth term, we have simply:

$$(4) = b^2\delta(t-s)dt \tag{8.15}$$

that vanishes if $t \neq s$. These 4 terms added together lead to the simple expression of the autocorrelation of displacements:

$$\langle dX_t dX_s \rangle = -\frac{ab^2}{2} e^{-a|t-s|} dt^2 + b^2\delta(t-s)dt. \tag{8.16}$$

Putting back physical dimensions with $ab^2dt^2 = \frac{2\kappa k_B T}{\gamma^2}dt^2$ and $\beta^2 dt = \frac{2k_BT}{\gamma}dt$ (both in [m^2]), we get

$$\langle dX_t dX_s \rangle = -\frac{2\kappa k_B T}{\gamma^2} e^{-\kappa|t-s|/\gamma} dt^2 + 2D\delta(t-s)dt. \tag{8.17}$$

Since $\langle dW_t dW_s \rangle = \overline{dW_t dW_s}$ for a Wiener process [110], we can identify the ensemble average $\langle dX_t dX_s \rangle$ with a time averaged covariance $\overline{dX_t dX_s}$ that is experimentally measured -see Eq.(**??**) in the main text- and displayed in Fig. **??** in the main text and in Fig. 8.1 here.

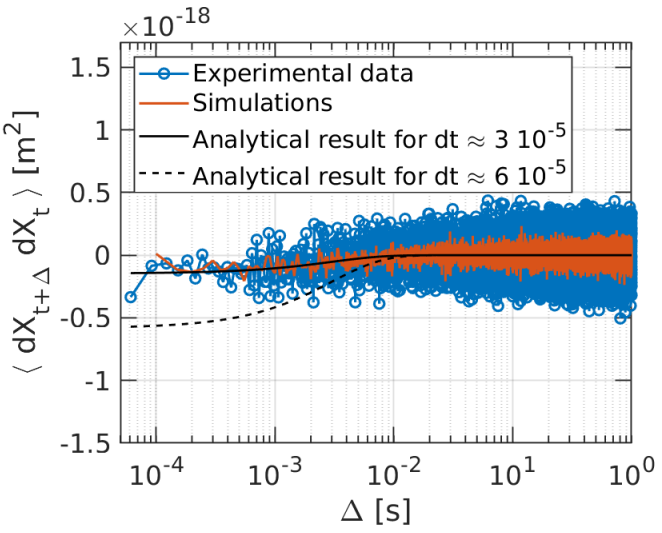

Figure 8.1: Covariance of displacements for the Ornstein-Uhlenbeck process. We plot the experimental result (blue open circles), calculated with $dt = 3.0518 \cdot 10^{-5}s$ along with simulation result (orange continuous line) and analytical solution (8.17) (black continuous line). We plot (black dashed and continuous lines) the analytical result for two different values of the time-step dt in order to highlight the fact that the deviation from zero of the Ornstein-Uhlenbeck displacements is strongly dependent on the value of dt, converging rapidly to zero with increasing acquisition frequency.

Fig. 8.1 reveals a good agreement between the experimental results, the simulations and the theoretical result (8.17). The covariance converges towards zero (which is the covariance of the Wiener increment) for decreasing dt. However, the non-differentiability of the stochastic process prevent us from taking the limit of vanishingly small dt and from observing the convergence of the short-time Ornstein-Uhlenbeck process towards a Wiener process.

8.4 Stochastic algorithms

This appendix complement Sec. 2.3. It gives details on the derivation of first and second-order discretization scheme for an Ornstein-Uhlenbeck process as well as PYTHON code extract that implement these algorithms.

The generic method to build a stochastic truncation is based on the Itô's lemma that is simply an extension of the chain rule to take into account the second term $b(x_t)dW_t$ Then the Itô-Taylor expansion, generalises to stochastic differential equations the standard Taylor expansion procedures [107]. We define two operators $\mathcal{L}^0 = a_t\frac{\partial}{\partial x} + \frac{1}{2}b_t^2\frac{\partial^2}{\partial x^2}$ and $\mathcal{L}^1 = b_t\frac{\partial}{\partial x}$ and apply Itô lemma to a function f of the stochastic process leading to

$$f(x_t) = f(x_0) + \int_0^t \mathcal{L}^0 f(x_s)ds + \int_0^t \mathcal{L}^1 f(x_s)dW_s. \tag{8.18}$$

We can apply this to x_t itself before iteratively applying it to the quantities $a(x_t)$ and $b(x_t)$ inside the integrals. Doing so, we obtain successive approximations of the process $f(x_t)$ up to a specified order.

Now in the case of numerical simulations of trajectories x_t, the function of interest is x_t itself. The algorithm that we want to obtain is an approximation of the change is x_t over a small time interval Δt.

Hence for the process x_t on a time interval Δt, an approximation can be given by:

$$x_{t+\Delta t} = X_t + a(x_t)\int_t^{t+\Delta t} ds + b(x_t)\int_t^{t+\Delta t} dW_s + R \tag{8.19}$$

where R is the reminder, containing higher order terms. This first order truncation of the expansion gives rise to the Euler-Maruyama scheme for Y_i found in the main text of the manuscript

$$Y_{i+1} = Y_i + a(x_t)\Delta t + b(x_t)\Delta W_i, \tag{8.20}$$

where $\Delta t = \int_t^{t+\Delta t} ds$ and the Wiener increment $\Delta W = \int_t^{t+\Delta t} dW$ can be simulated by $\Delta W = \xi\sqrt{\Delta t} \equiv \mathcal{N}(0,1)\sqrt{\Delta t}$. Here, the normally distributed random number can be

produced by various means, often using built-in functions for random number generation. In our case, the function used is based on the Box-Muller algorithm.

As in the case of ordinary differential equation the difference between the approximation Y_i and the process x_t decreases with Δt. However, for a given time-step, the error of the algorithm depends on the order at which it has been truncated. Higher order algorithms are therefore more efficient, since they does not demands as small time increments to give good results. As detailed in the main text of the manuscript, we focus here on the weak convergence criteria for variance. To perform the convergence test, we run the algorithm several time with the same pre-generated time series of random numbers. We run one simulation with a very small Δt and use it as a reference trajectory, it represents x_t; then by performing numerical simulations with increasing Δt, we observe how the error increases.

The Euler-Maruyama algorithm is known to converge with weak order $n = 1$. We show in Fig. 2.4 the results of the weak convergence test, giving an exponent $n_{meas.} = 1.1748$.

By iterating the same procedure up to higher orders, we obtain algorithms with better precision for a given time increment Δt. A second order algorithm can be built by keeping the following terms. This gives the following scheme (derived in [107], where we use the notation $a_i = a[Y_i]$ and $b_i = b[Y_i]$):

$$\begin{aligned} Y_{i+1} = Y_i + a_i\Delta t + b_i\Delta W_i + \frac{1}{2}b_i b_i'\left(\Delta W_i^2 - \Delta t\right) \\ a_i' b_i \Delta Z + \frac{1}{2}\left(a_i a_i' + \frac{1}{2}b_i^2 a_i^{(2)}\right)\Delta t^2 \\ + \left(a_i b_i' + \frac{1}{2}b_i^2 b_i^{(2)}\right)\left(\Delta W \Delta t - \Delta Z\right) \\ + \frac{1}{2}b_i\left(b_i b_i^{(2)} + (b_i')^2\right)\left(\frac{1}{3}\Delta W^2 - \Delta t\right). \end{aligned} \tag{8.21}$$

where $\Delta Z = \int_t^{t+\Delta t}\left[\int_t^S dW\right] dS$. To simplify this expression, we can now use the fact that the physical process Eq. (2.6) which will be simulated is defined by $a[x_t] = \kappa x_t/\gamma$ and $b[x_t] = \sqrt{2D}$ which brings all first derivatives of $b[x_t]$ and second derivatives of $a[x_]t$ to zero. With this simplification, we obtain:

$$Y_{i+1} = Y_i + a_i\Delta t + b_i\Delta W_i + b_i a_i'\Delta Z_i + a_i a_i'\Delta t^2. \tag{8.22}$$

As ΔW_i is simulated with a random number η, it is shown in [107] that ΔZ can be

simulated using two independent random numbers η and θ, and accordingly:

$$\begin{aligned} Y_{i+1} = Y_i + a_i\Delta t + b_i\sqrt{\Delta t}\eta \\ + b_i a_i' \frac{1}{2}\left(\eta + \frac{1}{\sqrt{3}}\theta\right)\Delta t^{3/2} + a_i a_i' \Delta t^2 \end{aligned} \tag{8.23}$$

This is the weak-$\mathcal{O}(2)$ scheme that we have implemented in a PYTHON code to simulate the Brownian trajectories used in this chapter and the following. This efficient algorithm reduces numerical errors while keeping a reasonable computing cost.

Below, we display minimal examples of PYTHON implementation of the stochastic algorithm derived above. In the next box is a function that implement a first order Euler-Maruyama code. In input are the number of time-step of the trajectory nt, the size of the time-step dt and an array of random number of zero mean and unit variance, to feed the Wiener increment. The output is a stochastic trajectory.

```
def overdamped1(nt, dt, rand): # Order one overdamped dynamics
    algorithm
    position = np.zeros(nt) # Position array
    S0 = kb * T / kappa # initial variance by equipartition
    r0 = np.sqrt(S0) * rand[0] # initial random position
    position[0] = r0 # store in array
    for i in range(1,nt): # time-loop
        noise = rand[i] # random number
        gradU = kappa * r0 # linear force
        a = - gradU/gamma\
        + (1/np.sqrt(dt)) * np.sqrt(2*kb*T/gamma)*noise # force/gamma
        r_new = r0 + a * dt # x(t+\Delta t)
        position[i] = r_new # store in array
        r0 = r_new # update initial position
    return position # output
```

In the next box is a function that implement a second-order code as Eq. (8.23) In input are the number of time-step of the trajectory nt, the size of the time-step dt and two arrays of random number of zero mean and unit variance, to feed dW and dZ. The output is a stochastic trajectory.

```
def overdamped2(nt, dt, rand1, rand2): # Order two overdamped
    dynamics algorithm
    position = np.zeros(nt) # Position array
    S0 = kb * T / kappa # initial variance by equipartition
    r0 = np.sqrt(S0) * rand1[0] # initial random position
    position[0] = r0 # store in array
    for i in range(1,nt): # time-loop
        noise1 = rand1[i] # first random number
        noise2 = rand2[i] # second random number
```

```
        dW = np.sqrt(dt) * noise1 # Wiener increment
        dZ = dt**(3/2) * (noise1 + noise2/np.sqrt(3))/2 # second-order increment
        r_new = r0  - kappa/gamma * r0 * dt\
        + np.sqrt(2*D) * dW - np.sqrt(2*D) * kappa/gamma * dZ\
        + 0.5 * kappa**2/gamma**2 * r0 * dt**2 # x(t+\Delta t)
        position[i] = r_new # store in array
        r0 = r_new # update initial position
    return position # output x(t)
```

Below an example of simple code to generate NTraj trajectories of NTime time-steps with a step $\Delta t = 10^{-4}$ s

```
import numpy as np
from numpy.random import RandomState

kb = 1.3806e-23 # Boltzmann's constant in J/K
T = 298 # temperature in K
gamma = 8.7e-9 # viscous drag in kg/s^2
kappa = 2.9e-6 # stiffness in N/m

NTime = int(1e6) # number of time-steps
Ntraj = 500 # number of trajectories in the ensemble to simulate
dt = 1e-4 # time-step

TrajectoryOrder1 = np.zeros([NTime, NTraj])
for j in trange(Ntraj): # loop over the trajectories
  random_num0 = np.random.standard_normal(Nt) # generate random numbers
        TrajectoryOrder1[Ntime, j] = overdamped1(Nt, dt, random_num0) # compute trajectory

  random_num1 = np.random.standard_normal(Nt) # generate random numbers
        random_num2 = np.random.standard_normal(Nt) # generate random numbers
        TrajectoryOrder1[Ntime, j] = overdamped1(Nt, dt, random_num1) # compute trajectory
        TrajectoryOrder2[Ntime, j] = overdamped2(Nt, dt, random_num1, random_num2) # compute trajectory
```

8.5 Analytical expression of the ergodic parameter

Under the condition of stationarity, the position correlation function depends only on the time lag Δ with:

$$C_x(\Delta) = \langle x(\Delta + t)x(t)\rangle = \frac{2k_BT}{\kappa}e^{-\frac{\kappa}{\gamma}\Delta}. \tag{8.24}$$

We remind the definition of the ergodic parameter $\epsilon(\Delta)$ [97]:

$$\epsilon(\Delta) = \frac{\sigma^2\left(\overline{\delta x_i^2(\Delta)}\right)}{\left\langle\overline{\delta x_i^2(\Delta)}\right\rangle^2}, \tag{8.25}$$

where $\sigma^2\left(\overline{\delta x_i^2(\Delta)}\right)$ stands for the variance of a single trajectory time average MSD

$$\overline{\delta x_i^2(\Delta)} = \frac{1}{\mathcal{T}-\Delta}\int_0^{\mathcal{T}-\Delta}\left[x_i(t'+\Delta) - x_i(t')\right]^2 dt', \tag{8.26}$$

and $\left\langle\overline{\delta x_i^2(\Delta)}\right\rangle$ stands for the mean of time average MSD taken over the available ensemble $\{i\}$ of trajectories

$$\left\langle\overline{\delta x_i^2(\Delta)}\right\rangle = \frac{1}{\mathcal{T}-\Delta}\int_0^{\mathcal{T}-\Delta}\left\langle\left[x_i(t'+\Delta) - x_i(t')\right]^2\right\rangle dt'. \tag{8.27}$$

Under the ergodic hypothesis, the time ensemble average MSD is:

$$\left\langle\overline{\delta x_i^2(\Delta)}\right\rangle = \frac{2k_BT}{\kappa}\left(1 - e^{-\frac{\kappa}{\gamma}\Delta}\right), \tag{8.28}$$

and the variance is defined as:

$$\sigma^2\left(\overline{\delta x_i^2(\Delta)}\right) = \left\langle\overline{\delta x_i^2(\Delta)}^2\right\rangle - \left\langle\overline{\delta x_i^2(\Delta)}\right\rangle^2. \tag{8.29}$$

The first term can be written as

$$\begin{aligned}\left\langle\overline{\delta x_i^2(\Delta)}^2\right\rangle = \frac{1}{(\mathcal{T}-\Delta)^2}\int_0^{\mathcal{T}-\Delta}dt_1\int_0^{\mathcal{T}-\Delta}dt_2 \\ \left\langle(x(t_1+\Delta)-x(t_1))^2(x(t_2+\Delta)-x(t_2))^2\right\rangle\end{aligned} \tag{8.30}$$

for which the Wick's relation yields 4 terms:

$$\begin{aligned}\langle x(t_1)x(t_2)x(t_3)x(t_4)\rangle = &\langle x(t_1)x(t_2)\rangle\langle x(t_3)x(t_4)\rangle \\ &+ \langle x(t_1)x(t_3)\rangle\langle x(t_2)x(t_4)\rangle \\ &+ \langle x(t_1)x(t_4)\rangle\langle x(t_2)x(t_3)\rangle.\end{aligned} \tag{8.31}$$

The integrand in Eq. (8.30) then becomes:

$$\begin{aligned}&\left\langle (x(t_1+\Delta)-x(t_1))^2 (x(t_2+\Delta)-x(t_2))^2 \right\rangle \\ &= [\left\langle (x(t_1+\Delta)-x(t_1))^2 \right\rangle \left\langle (x(t_2+\Delta)-x(t_2))^2 \right\rangle \\ &+ 2\left\langle (x(t_1+\Delta)-x(t_1))(x(t_2+\Delta)-x(t_2)) \right\rangle^2].\end{aligned} \tag{8.32}$$

With the first term in the LHS of Eq. (8.32) identified as the square of the time-ensemble average MSD $\left\langle \overline{\delta x_i^2(\Delta)} \right\rangle^2$, the variance of time average MSD can finally be written as:

$$\begin{aligned}\sigma^2(\overline{\delta x_i^2(\Delta)}) &= \frac{2}{(\mathcal{T}-\Delta)^2}\int_0^{\mathcal{T}-\Delta} dt_1 \int_0^{\mathcal{T}-\Delta} dt_2 \\ &\quad \left\langle (x(t_1+\Delta)-x(t_1))(x(t_2+\Delta)-x(t_2)) \right\rangle^2 \\ &= \frac{2k_B^2T^2}{(\mathcal{T}-\Delta)^2\kappa^2}\int_0^{\mathcal{T}-\Delta} dt_1 \int_0^{\mathcal{T}-\Delta} dt_2 \\ &\quad \left(2e^{-\frac{\kappa}{\gamma}|t_1-t_2|} - e^{-\frac{\kappa}{\gamma}|t_1-t_2+\Delta|} - e^{-\frac{\kappa}{\gamma}|t_2-t_1+\Delta|}\right)^2,\end{aligned} \tag{8.33}$$

using Eq.(8.24).

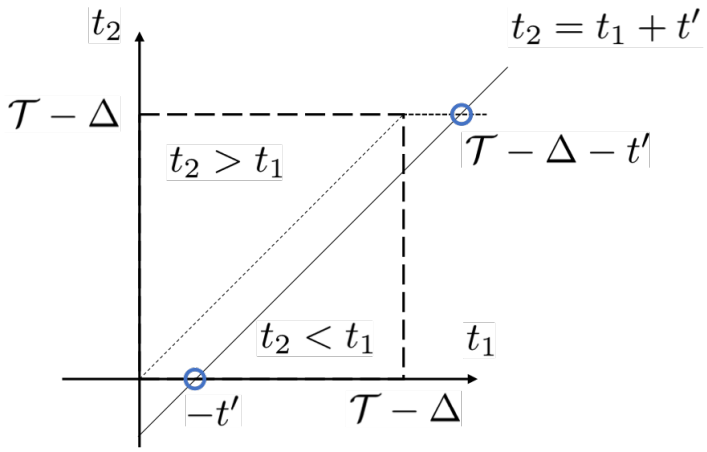

Figure 8.2: Integration surface for Eq. (8.34) on which the two sectors $[t_2 > t_1]$ and $[t_2 < t_1]$ are distinguished. This defines the appropriate change of variables $(t_1, t_2) \leftrightarrow (t_1, t')$, with the line $t_2 = t_1 + t'$ crossing the $t_2 = 0$ axis at $-t'$ and the $t_2 = \mathcal{T} - \Delta$ axis at $\mathcal{T} - \Delta - t'$.

The integral is calculated through a standard change of variables $t_1 = t_1, t' = t_2 - t_1$ described in Fig. 8.2 and possible since the integrand only depends on the $|t_1 - t_2|$ difference. One can formally write:

$$\sigma^2(\overline{\delta x_i^2(\Delta)}) = \frac{2k_B^2T^2}{(\mathcal{T}-\Delta)^2\kappa^2}\int_0^{\mathcal{T}-\Delta} dt_1 \int_0^{\mathcal{T}-\Delta} dt_2 \cdot \alpha^2(t'), \tag{8.34}$$

with t' varying from negative to positive values in the (t_1, t_2) plane. For the $t' > 0$ sector:

$$\int_0^{\mathcal{T}-\Delta} dt' \int_0^{\mathcal{T}-\Delta-t'} dt_1 \cdot \alpha^2(t') = \int_0^{\mathcal{T}-\Delta} dt'(\mathcal{T}-\Delta-t') \cdot \alpha^2(t'), \tag{8.35}$$

and for the $t' < 0$ sector:

$$\int_{-(\mathcal{T}-\Delta)}^{0} dt' \int_{-t'}^{\mathcal{T}-\Delta} dt_1 \cdot \alpha^2(t') = \int_{-(\mathcal{T}-\Delta)}^{0} dt'(\mathcal{T}-\Delta+t') \cdot \alpha^2(t'). \tag{8.36}$$

By combining the two 2 sectors, on gets:

$$\begin{aligned} &\int_{-(\mathcal{T}-\Delta)}^{\mathcal{T}-\Delta)} dt'(\mathcal{T}-\Delta-|t'|) \cdot \alpha^2(t') \\ &= 2\int_0^{\mathcal{T}-\Delta} dt'(\mathcal{T}-\Delta-|t'|) \cdot \alpha^2(t') \\ &= 2\int_0^{\mathcal{T}-\Delta} dt'(\mathcal{T}-\Delta-t') \cdot \alpha^2(t') \end{aligned} \tag{8.37}$$

leading to express the ergodic parameter ϵ as:

$$\begin{aligned} \epsilon(\Delta) = &\frac{4k_B^2T^2}{\kappa^2(\mathcal{T}-\Delta)^2\left\langle\overline{\delta x_i^2(\Delta)}\right\rangle^2} \\ &\int_0^{\mathcal{T}-\Delta} dt'(\mathcal{T}-\Delta-t')\left(2e^{-\frac{\kappa t'}{\gamma}} - e^{-\frac{\kappa}{\gamma}(t'+\Delta)} - e^{-\frac{\kappa}{\gamma}|\Delta-t'|}\right)^2 \end{aligned} \tag{8.38}$$

In order to simplify the notations, we define $K = \frac{k_BT}{\kappa}$ and write the time ensemble average MSD as $\left\langle\overline{\delta x_i^2(\Delta)}\right\rangle = 2K(1-e^{-\frac{\kappa}{\gamma}\Delta})$. The ergodic parameter is then written as $\epsilon(\Delta) = I/4K^2(1-e^{-\frac{\kappa}{\gamma}\Delta})^2$ where the variance of the MSD I is calculated as:

$$\begin{aligned} I = &\frac{4K^2}{(\mathcal{T}-\Delta)^2}\int_0^{\mathcal{T}-\Delta} dt'(\mathcal{T}-\Delta-t') \\ &\left(2e^{-\frac{\kappa t'}{\gamma}} - e^{-\frac{\kappa}{\gamma}(t'+\Delta)} - e^{-\frac{\kappa}{\gamma}|\Delta-t'|}\right)^2, \end{aligned}$$

splitted in three terms depending on the sign of the absolute value

$$\begin{aligned} I = &\frac{4K^2}{(\mathcal{T}-\Delta)^2}\mathcal{T}\int_0^{\Delta}\left(2e^{-\frac{\kappa t'}{\gamma}} - e^{-\frac{\kappa}{\gamma}(t'+\Delta)} - e^{-\frac{\kappa}{\gamma}(\Delta-t')}\right)^2 dt' \\ &- \frac{4K^2}{(\mathcal{T}-\Delta)^2}\int_0^{\Delta}(t'+\Delta)\left(2e^{-\frac{\kappa t'}{\gamma}} - e^{-\frac{\kappa}{\gamma}(t'+\Delta)} - e^{-\frac{\kappa}{\gamma}(\Delta-t')}\right)^2 dt' \\ &+ \frac{4K^2}{(\mathcal{T}-\Delta)^2}\int_{\Delta}^{\mathcal{T}-\Delta}(\mathcal{T}-\Delta-t')\left(2e^{-\frac{\kappa t'}{\gamma}} - e^{-\frac{\kappa}{\gamma}(t'+\Delta)} - e^{\frac{\kappa}{\gamma}(\Delta-t')}\right)^2 dt' \\ &= V_1 + V_2 + V_3. \end{aligned} \tag{8.39}$$

Each term is calculated as:

$$
\begin{aligned}
V_1 =& \frac{4K^2}{(\mathcal{T}-\Delta)^2}\cdot\frac{\gamma t}{2\kappa}\left[5+\frac{4\kappa}{\gamma}\left(e^{-\frac{2\kappa}{\gamma}\Delta}-2e^{-\frac{\kappa}{\gamma}\Delta}\right)-4e^{-\frac{2\kappa}{\gamma}\Delta}+4e^{-\frac{3\kappa}{\gamma}\Delta}-4e^{-\frac{\kappa}{\gamma}\Delta}-e^{-\frac{4\kappa}{\gamma}\Delta}\right],\\
V_2 =& \frac{K^2}{(\mathcal{T}-\Delta)^2}\cdot\frac{\gamma^2}{\kappa^2}\Bigg[\left(4\frac{\kappa}{\gamma}\Delta-1\right)\\
&+12\frac{\kappa^2}{\gamma^2}\Delta^2 e^{-2\frac{\kappa}{\gamma}\Delta}\left(1-2e^{\frac{\kappa}{\gamma}\Delta}\right)+\frac{2\kappa}{\gamma}e^{-\frac{4\kappa}{\gamma}\Delta}\Delta\left(-4e^{2\frac{\kappa}{\gamma}\Delta}+4e^{\frac{\kappa}{\gamma}\Delta}-1\right),\\
&+\left(\frac{2\kappa}{\gamma}\Delta+1\right)\left(-4e^{-2\frac{\kappa}{\gamma}\Delta}+4e^{-3\frac{\kappa}{\gamma}\Delta}-4e^{-\frac{\kappa}{\gamma}\Delta}-e^{-4\frac{\kappa}{\gamma}\Delta}+4\right)+2e^{-2\frac{\kappa}{\gamma}\Delta}\Bigg]\\
V_3 =& \frac{16K^2}{(\mathcal{T}-\Delta)^2}\left(\cosh\left(\frac{\kappa}{\gamma}\Delta\right)-1\right)^2\Bigg\{\frac{\gamma}{2\kappa}(\mathcal{T}-\Delta)\left(e^{-2\frac{\kappa}{\gamma}\Delta}-e^{-2\frac{\kappa}{\gamma}(\mathcal{T}-\Delta)}\right)\\
&+\frac{\gamma^2}{4\kappa^2}\Bigg[\left(\frac{2\kappa}{\gamma}(\mathcal{T}-\Delta)+1\right)e^{-2\frac{\kappa}{\gamma}(\mathcal{T}-\Delta)}\\
&-\left(\frac{2\kappa}{\gamma}\Delta+1\right)e^{-2\frac{\kappa}{\gamma}\Delta}\Bigg]\Bigg\},
\end{aligned}
$$

whose analytical expression is drawn as the theory curve in Fig. 3.5 in the main text.

8.6 Analytical expression of the Allan variance

For the Ornstein-Uhlenbeck process, we have the following power spectral density (PSD) –with $\omega = 2\pi f$:

$$S(\omega) = \frac{2D}{\omega^2+\omega_0^2}, \tag{8.40}$$

where $D = k_B T/\gamma$ is the diffusion coefficient and $\omega_0 = \kappa/\gamma$ corresponds to the trap roll-off frequency. The Allan variance $\sigma^2(\tau)$ is linked to the PSD through a $\sin^4$ transformation, as we discussed previously in [132]:

$$\sigma^2(\tau) = \frac{4}{\pi\tau^2}\int_{-\infty}^{+\infty} S(\omega)\sin^4\left(\frac{\omega\tau}{2}\right)d\omega. \tag{8.41}$$

With $\sin^4(x) = \left(e^{4ix}-4e^{2ix}+6-4e^{-2ix}+e^{4ix}\right)/16$ and $\int_{-\infty}^{+\infty}\left(e^{ix}+e^{-ix}\right)dx = 2\int_{-\infty}^{+\infty}e^{ix}dx$ by parity, we write:

$$\sigma^2(\tau) = \frac{4}{\pi\tau^2}\int_{-\infty}^{+\infty}\frac{2D}{\omega^2+\omega_0^2}\left(2e^{2i\omega\tau}-8e^{i\omega\tau}+6\right)d\omega, \tag{8.42}$$

giving three complex integrals to compute with a simple pole in $\omega = \pm i\omega_0$

$$\begin{aligned}
\int_{-\infty}^{+\infty} \frac{2e^{2i\omega\tau}}{\omega^2+\omega_0^2} d\omega &= 2i\pi \mathrm{Res}\left(\frac{2e^{2i\omega\tau}}{\omega^2+\omega_0^2}, i\omega_0\right) = \frac{2\pi}{\omega_0} e^{-2\omega_0\tau}, \\
\int_{-\infty}^{+\infty} \frac{8e^{i\omega\tau}}{\omega^2+\omega_0^2} d\omega &= 2i\pi \mathrm{Res}\left(\frac{8e^{i\omega\tau}}{\omega^2+\omega_0^2}, i\omega_0\right) = \frac{8\pi}{\omega_0} e^{-\omega_0\tau}, \\
\int_{-\infty}^{+\infty} \frac{6}{\omega^2+\omega_0^2} d\omega &= 2i\pi \mathrm{Res}\left(\frac{6}{\omega^2+\omega_0^2} i\omega_0\right) = \frac{6\pi}{\omega_0}.
\end{aligned}$$

This done, we obtain

$$\begin{aligned}
\sigma^2(\tau) &= \frac{8D}{\pi\tau^2}\frac{1}{16}\left(\frac{2\pi}{\omega_0}e^{-2\omega_0\tau} - \frac{8\pi}{\omega_0}e^{-\omega_0\tau} + \frac{6\pi}{\omega_0}\right) \\
&= \frac{k_B T}{\kappa\tau^2}\left(4\left[1-e^{-\kappa\tau/\gamma}\right] - \left[1-e^{-2\kappa\tau/\gamma}\right]\right)
\end{aligned} \tag{8.43}$$

that corresponds to Eq. 3.15 in the main text. Two limits are important to draw:
(i) the short-time limit $\tau \ll \gamma/\kappa$ where we get $\sigma^2(\tau) \approx 2D/\tau$ corresponding to free Brownian motion [132, 114]
(ii) the long-time limit $\tau \gg \gamma/\kappa$ where we get a different behavior $\sigma^2(\tau) \approx 3k_B T/\kappa\tau^2$.

8.7 Tracking error analysis

8.7.1 Tracking error on position

In all our experiments, the trajectories are recorded by a photodiode and the positions are interpreted from the photodiode signal. The error on the localization of the particle are originated in our experiments from multiple noise sources dominated by the laser fluctuation and the diode electronic noise. A white noise can be a good starting approximation to estimate and describe the localization error. Therefore, each measured position $x_i(t_k)$ for a trajectory i at time t_k can be related to the real position $x_i^0(t_k)$ as [132, 88]:

$$x_i(t_k) = x_i^0(t_k) + \mu_i(t_k), \tag{8.44}$$

where $\mu_i(t_k)$ is a random uncorrelated tracking error with $\langle \mu_i(t_k) \rangle = 0$ and $\langle \mu_i(t_k)\mu_j(t_l) \rangle = \delta_{ij}\delta_{kl}\sigma_0^2$.

8.7.2 Tracking error on time ensemble average MSD

We now propagate the position tracking error described by Eq.(8.44) into the measured MSD. We write:

$$\begin{aligned}
&\left\langle \overline{(x_i(t+\Delta)-x_i(t))^2} \right\rangle \\
&= \left\langle \overline{(x_i^0(t+\Delta)+\mu_i(t+\Delta)-x_i^0(t)-\mu_i(t+\Delta))^2} \right\rangle \\
&= \left\langle \overline{[(x_i^0(t+\Delta)-x_i^0(t))+(\mu_i(t+\Delta)-\mu_i(t))]^2} \right\rangle \\
&= \left\langle \overline{(x_i^0(t+\Delta)-x_i^0(t))^2} \right\rangle + \left\langle \overline{(\mu_i(t+\Delta)-\mu_i(t))^2} \right\rangle \\
&= \left\langle \overline{(x_i^0(t+\Delta)-x_i^0(t))^2} \right\rangle + 2\sigma_0^2,
\end{aligned} \tag{8.45}$$

showing how the measured MSD can be related to the theoretical one as:

$$\left\langle \delta x^2(\Delta) \right\rangle_{\text{exp}} = \left\langle \delta x^2(\Delta) \right\rangle_{\text{th}} + 2\sigma_0^2. \tag{8.46}$$

Since $\sigma_0^2 > 0$, the MSD is always overdetermined experimentally, in agreement with our observations -in the log-log representation of Fig. 3.3 (a), this error can mainly be seen at short time lags.

8.7.3 Tracking error on Allan variance

From the definition of Allan variance, we can also relate the experimental Allan variance that includes the tracking errors to the theoretical Allan variance with

$$\begin{aligned}
\sigma^2_{\text{exp}}(\Delta) &= \frac{1}{2\Delta^2}\left\langle \big(x((n+2)\Delta)-2x((n+1)\Delta)+x(\Delta)\big)^2 \right\rangle \\
&= \frac{1}{2\Delta^2}\left\langle \big(x^0((n+2)\Delta)-2x^0((n+1)\Delta)+x^0(\Delta) \right. \\
&\quad \left. +\mu_1-2\mu_2+\mu_3\big)^2 \right\rangle \\
&= \sigma^2_{\text{th}}(\Delta) + \frac{1}{2\Delta^2}\left\langle \big(\mu_1-2\mu_2+\mu_3\big)^2 \right\rangle \\
&= \sigma^2_{\text{th}}(\Delta) + \frac{3\sigma_0^2}{\Delta^2}.
\end{aligned} \tag{8.47}$$

The difference $3\sigma_0^2/\Delta^2$ between experimental and theoretical Allan variances is always positive and decays with Δ^2, again a feature perfectly consistent with our observations –see Fig. 3.5 in the main text.

8.7.4 Tracking error on the ergodic estimator

In order to account for the error on the ergodic estimator $\epsilon(\Delta)$, we first consider Eq.(8.46) for the MSD error analysis. For the single trajectory time averaged MSD,

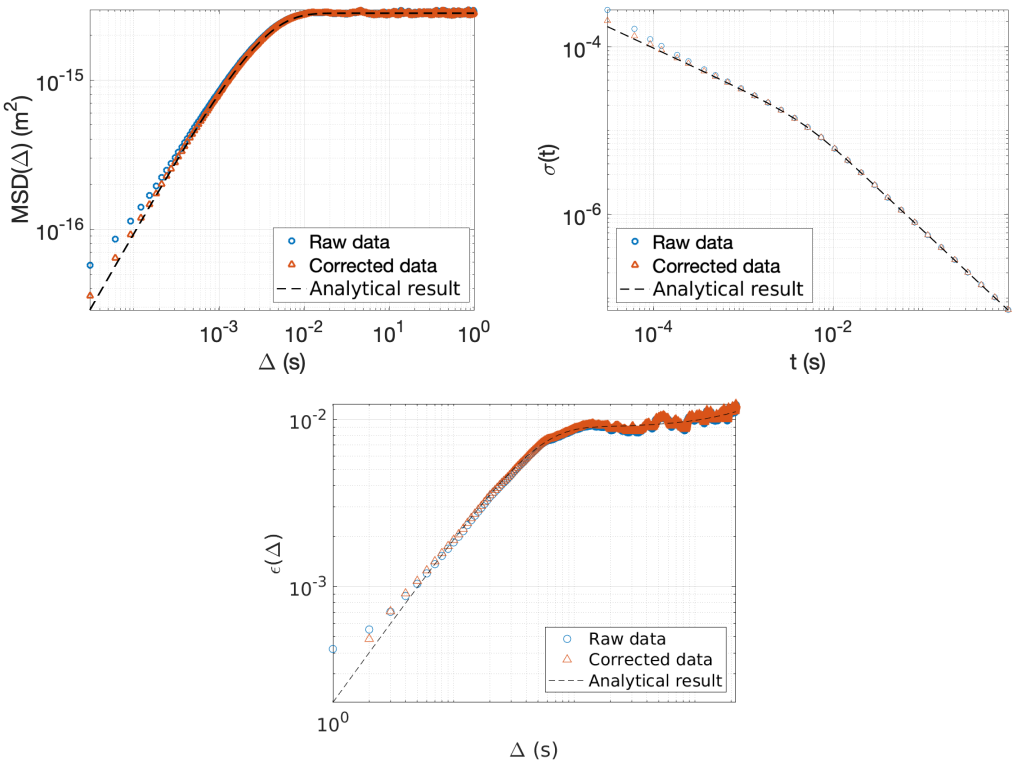

Figure 8.3: Raw experimental and corrected data (top) for the MSD, (middle) for the Allan variance and (bottom) for the ergodic estimator. We see the correction mostly for short time-lags. The correction works well for the MSD and Allan variance, but a deviation remains on the ergodic estimator. This difference could actually point to a slight deviation of the localization noise from the white Gaussian noise we have assumed in our modeling of the localization error.

one has

$$\overline{\delta x_i^2(\Delta)}_{\text{exp}} = \overline{\delta x_i^2(\Delta)}_{\text{th}} + \mu_i \tag{8.48}$$

where μ_i is a random constant with $\langle \mu_i \rangle^2 = 2\sigma_0^2$. The experimental ergodic estimator can thus be written as:

$$\epsilon(\Delta)_{\text{exp}} = \frac{\left\langle \left(\overline{\delta x_i^2(\Delta)}_{\text{exp}} \right)^2 \right\rangle}{\left\langle \overline{\delta x_i^2(\Delta)} \right\rangle_{\text{exp}}^2} - 1 = \frac{\left\langle \left(\overline{\delta x_i^2(\Delta)}_{\text{th}} + \mu_i \right)^2 \right\rangle}{\left\langle \overline{\delta x_i^2(\Delta)} \right\rangle_{\text{exp}}^2} - 1. \tag{8.49}$$

We define the ratio

$$\phi(\Delta) = \frac{\left\langle \overline{\delta x_i^2(\Delta)} \right\rangle_{\text{th}}}{\left\langle \overline{\delta x_i^2(\Delta)} \right\rangle_{\text{exp}}} \tag{8.50}$$

as the ratio between the theoretical and experimental MSD variance value. With this ratio, the experimental ergodic estimator $\epsilon(\Delta)$ can be written as:

$$\begin{aligned}\epsilon(\Delta)_{\text{exp}} &= \phi^2(\Delta)\epsilon(\Delta)_{\text{th}} \\ &+ \phi^2(\Delta)\left(\frac{2\left\langle \mu_i \overline{\delta x_i^2(\Delta)}_{\text{th}}\right\rangle + \langle \mu_i^2\rangle}{\left\langle \overline{\delta x_i^2(\Delta)}\right\rangle_{\text{th}}^2} + 1\right) - 1.\end{aligned} \tag{8.51}$$

Assuming that the error μ_i is uncorrelated with the single trajectory time ensemble MSD, $\langle \epsilon_i \delta x_i(\bar{\Delta})_{th}\rangle = \langle \epsilon_i\rangle\langle \delta x_i(\bar{\Delta})_{th}\rangle$. Taking this into account additionally leads to $\langle \mu_i^2\rangle = \langle \mu_i\rangle^2 + \sigma^2(\mu_i) = 2\sigma_0^2 + \sigma^2(\mu_i)$ and therefore to:

$$\epsilon(\Delta)_{\text{exp}} = \phi^2(\Delta)\left[\epsilon(\Delta)_{\text{th}} + \frac{\sigma^2(\mu_i)}{\left\langle \overline{\delta x_i^2(\Delta)}\right\rangle_{\text{th}}^2}\right]. \tag{8.52}$$

The ratio

$$\phi(\Delta) = \frac{1}{1 + \frac{\kappa\sigma_0^2}{k_B T(1-e^{-\kappa\Delta/\gamma})}} \tag{8.53}$$

can be estimated once the value of the localization error σ_0^2 is known. As for the variance of μ, Eq. (8.48) gives:

$$\sigma^2(\mu_i) = \sigma^2(\overline{\delta x_i^2(\Delta)}_{\text{exp}}) - \sigma^2(\overline{\delta x_i^2(\Delta)}_{\text{th}}). \tag{8.54}$$

Since $\sigma^2(\overline{\delta x_i^2(\Delta)}_{\text{th}})$ goes to zero when $\Delta \to 0$, one is left, at small Δ with $\sigma^2(\epsilon) \sim \sigma^2(\overline{\delta x_i^2(\Delta)}_{\text{exp}})$. Taking the experimental variance measured on the time average MSD for the smallest time lag Δ is therefore a good estimation for $\sigma^2(\mu)$. This analysis leads us to approaching the real value of the tracking error on the estimator $\epsilon(\Delta)$ and this way explaining the difference between the experimental data and the theoretical curve in Fig. 3.5 and 8.3 (c).

8.8 Stationary solution by Laplace transform

We recall some useful Laplace transformations

$$\begin{aligned}\mathcal{L}[x(t)] &= \tilde{x}[s] \\ \mathcal{L}[\dot{x}(t)] &= s\tilde{x}[s] - \tilde{x}_0 \\ \mathcal{L}[a] &= a/s\end{aligned} \tag{8.55}$$

Eq. 4.5 can then be written in the s Laplace-domain

$$\tilde{x}[s] = \frac{1}{(s+\omega_0)}\left(\tilde{x}_0 + \frac{F_0}{\gamma s} + \sqrt{2D}\tilde{\xi}[s] + \sqrt{2D_A}\tilde{\eta}[s])\right). \tag{8.56}$$

We now recall useful inverse Laplace transformations

$$\begin{aligned}
&\mathcal{L}^{-1}[\frac{1}{s}] = 1 \\
&\mathcal{L}^{-1}[\frac{1}{s+\omega_0}] = e^{-\omega_0 t} \\
&\mathcal{L}^{-1}[\frac{1}{s(s+\omega_0)}] = \frac{1}{\omega_0}\left(1 - e^{-\omega_0 t}\right) \\
&\mathcal{L}^{-1}[\frac{1}{s+\omega_0} * \tilde{f}[s]] = \int_0^t e^{-\omega_0 (t-t')} f(t') dt'
\end{aligned} \tag{8.57}$$

the last transformation being a consequence of convolution theorem. We can now transform back into the time-domain

$$\boxed{x(t) = x_0 e^{-\omega_0 t} + \frac{F_0}{\kappa}\left(1 - e^{-\omega_0 t}\right) + \int_0^t \left(\sqrt{2D}\xi_{t'} + \sqrt{2D_A}\eta_{t'}\right) e^{-\omega_0 (t-t')} dt'.} \tag{8.58}$$

We can note here that the average position is $\langle x(t)\rangle = \frac{F_0}{\kappa}\left(1 - e^{-\omega_0 t}\right)$ hence the effect of the DC component of the radiation pressure can be trivially discarded by looking at the centred process $x(t) - \langle x\rangle$.

8.9 PSD autocorrelation and MSD of a bead under colored noise

Our system, consisting of an optically trapped bead thermally diffusing within active fluctuations, is described by a couple of stochastic differential equations that determine the evolution of the position of the bead within the trap according to:

$$\dot{x}_t = -\omega_0 x_t + \sqrt{2D}\xi_t + \sqrt{2D_a}\eta_t \tag{8.59}$$

where the active noise η_t, solution of the Ornstein-Uhlenbeck process

$$d\eta_t = -\omega_c \eta_t dt + \sqrt{2\alpha\omega_c} dW_t, \tag{8.60}$$

is an exponentially correlated Gaussian variable.

We can derive the noise power spectrum density by Fourier transforming Eq. (8.60)

$$-i\omega\eta[\omega] = -\omega_c \eta[\omega] + \sqrt{\alpha\omega_c}\xi[\omega] \tag{8.61}$$

where ω_c is the correlation pulsation. Taking the squared norm leads to the active noise power spectral density (PSD)

$$\eta[\omega]\eta^*[\omega] = |\eta[\omega]|^2 = \frac{\alpha\omega_c}{\omega_c^2 + \omega^2}. \tag{8.62}$$

On Fig. 4.4, we plot the PSD directly measured from the laser output signal used to induce the noisy radiation pressure, both in the case of a white noise and colored noise. As expected, the spectrum of the white noise is flat on all the studied bandwidth, whereas the spectrum of the colored noise is following a Lorentzian profile, well captured by a fit following Eq. (8.62). The PSD of the motion x_t is evaluated from Eq. (8.59) as:

$$x[\omega]x^*[\omega] = \frac{1}{\omega_0^2+\omega^2}\left(2D\xi[\omega]\xi^*[\omega] + 2D_a\eta[\omega]\eta^*[\omega]\right), \tag{8.63}$$

noting that the implicit averaging performed in this square cancels the two cross-product of the uncorrelated noises $\eta[\omega]\xi^*[\omega]$ and the complex conjugate. In Eq. (8.63), $\omega_0 = \kappa/\gamma$ is the inverse of the characteristic relaxation time of the system, and $\eta[\omega]\eta^*[\omega]$ is given by Eq. (8.62) and $\xi[\omega]\xi^*[\omega] = 1$. Hence

$$x[\omega]x^*[\omega] = |x[\omega]|^2 = \frac{1}{\omega_0^2+\omega^2}\left(2D + \frac{2D_a\alpha\omega_c}{\omega_c^2+\omega^2}\right) \tag{8.64}$$

On Fig. 2.7 (b), we plot the measured spectra of x_t both for a white and colored external drive, with the analytical result of Eq. (8.64) using the value of D_a obtained from the fit of the MSD for the colored noise (see Fig. 4.9 above) and using the $D_a \to 0$ limit for the white noise case. A very good agreement between the theory and the experimental data is clearly seen, confirming that our model captures well the real diffusive dynamics of the trapped bead.

We can also compute the correlation function of the colored noise driven process from the Wiener-Khintchine theorem as:

$$\begin{aligned} C_{xx}(\Delta) &= \frac{1}{2\pi}\int_{-\infty}^{+\infty} |x[\omega]|^2 e^{-i\omega\Delta}d\omega \\ &= \frac{1}{2\pi}\int_{-\infty}^{+\infty} \frac{2De^{-i\omega\Delta}d\omega}{\omega_0^2+\omega^2} \\ &+ \frac{1}{2\pi}\int_{-\infty}^{+\infty} \frac{2D_a\alpha\omega_c e^{-i\omega\Delta}d\omega}{(\omega_0^2+\omega^2)(\omega_c^2+\omega^2)}, \end{aligned} \tag{8.65}$$

where both integrals can be computed via contour integration. For the first one, $f[\omega] = \frac{D}{\pi}\frac{e^{-i\omega\Delta}}{\omega_0^2+\omega^2}$ has one simple pole in the upper-half complex plane in $i\omega_0$, leading to compute one residue

$$\begin{aligned} \int_{-\infty}^{+\infty} f[\omega]d\omega &= 2i\pi Res\{f[\omega], i\omega_0\} \\ &= \lim_{\omega\to\omega_0} \frac{2De^{-i\omega\Delta}}{\omega+i\omega_0} \\ &= \frac{D}{\omega_0}e^{-\omega_0\Delta}. \end{aligned} \tag{8.66}$$

Similarly, the second integral with $g[\omega] = \frac{D_a\alpha\omega_c e^{-i\omega\Delta}}{\pi\left(\omega_0^2+\omega^2\right)(\omega_c^2+\omega^2)}$ is evaluated by separating it through partial fraction decomposition in $g[\omega] = \frac{D_a\alpha\omega_c e^{-i\omega\Delta}}{\pi(\omega_c^2-\omega_0^2)}\left(\frac{1}{\omega_0^2+\omega^2} - \frac{1}{\omega_c^2+\omega^2}\right) \equiv g_1[\omega] + g_2[\omega]$ leading to two integrals with simple poles in $i\omega_0$ and $i\omega_c$

$$\begin{aligned}\int_{-\infty}^{+\infty} g[\omega]d\omega &= 2i\pi Res\{g_1[\omega], i\omega_0\} + 2i\pi Res\{g_1[\omega], i\omega_c\} \\ &= D_a\alpha\omega_c^2\left(\frac{e^{-\omega_0\Delta}}{\omega_0\left(\omega_c^2-\omega_0^2\right)} - \frac{e^{-\omega_c\Delta}}{\omega_c\left(\omega_c^2-\omega_0^2\right)}\right) \\ &= \frac{D_a\alpha\omega_c}{\omega_0(\omega_c^2-\omega_0^2)}\left(e^{-\omega_0\Delta} - \frac{\omega_0}{\omega_c}e^{-\omega_c\Delta}\right).\end{aligned} \tag{8.67}$$

These evaluations are combined to provide the expression for the correlation function of the diffusion process:

$$C_{xx}(\Delta) = \frac{D}{\omega_0}e^{-\omega_0\Delta} + \frac{D_a\alpha\omega_c}{\omega_0(\omega_c^2-\omega_0^2)}\left(e^{-\omega_0\Delta} - \frac{\omega_0}{\omega_c}e^{-\omega_c\Delta}\right) \tag{8.68}$$

On Fig. 2.10 we represent the normalised correlation function C_{xx} for both white and colored noise drives where we superimpose the analytical result, using the value of D_a obtained, as indicated above, from the fit of the MSD for the colored noise. Here too, we use the $D_a \to 0$ limit for the white noise. Again, the good agreement between the exponential decays and the analytical models is observed.

The MSD of a colloid diffusing in a thermal environment obeys an Ornstein-Uhlenbeck process and is thus characterised by the white noise MSD:

$$\langle\delta x^2(\Delta)\rangle \equiv \langle(x(t+\Delta)-x(t))^2\rangle = \frac{2D}{\omega_0}\left(1-e^{-\omega_0\Delta}\right) \tag{8.69}$$

where D is the diffusion coefficient in the thermal bath, expressed in m^2/s, and $\omega_0 = \kappa/\gamma$ is the inverse of the characteristic relaxation time of the bead in the trap.

In contrast, the MSD of an active particle obeys Eq. (4.5) and can be computed as $\langle\delta x^2(\Delta)\rangle = 2\langle x_t^2\rangle - 2C_{xx}(\Delta)$ where the variance is the stationary variance of the process and $\langle x_t^2\rangle$ is taken as the limit $\lim_{t\to\infty}[\langle x_t^2\rangle] = \frac{D}{\omega_0} + \frac{D_a\alpha\omega_c}{\omega_0(\omega_c+\omega_0)})$. This leads us to calculate directly:

$$\begin{aligned}\langle\delta x^2(\Delta)\rangle =& \frac{2D}{\omega_0} + \frac{2D_a\alpha}{\omega_0(\omega_c+\omega_0)} + \frac{2D}{\omega_0}e^{-\omega_0\Delta} \\ &+ \frac{2D_a\alpha\omega_c}{\omega_0(\omega_c^2-\omega_0^2)}\left(e^{-\omega_0\Delta} - \frac{\omega_0}{\omega_c}e^{-\omega_c\Delta}\right) \\ &= \frac{2D}{\omega_0}\left(1-e^{-\omega_0\Delta}\right) \\ &+ \frac{2D_a\alpha\omega_c}{\omega_0(\omega_c^2-\omega_0^2)}\left(1 - e^{-\omega_0\Delta} - \frac{\omega_0}{\omega_c}(1-e^{-\omega_c\Delta})\right)\end{aligned} \tag{8.70}$$

that constitutes the result used in the main text.

The long-time limit can be easily derived as:

$$\lim_{\Delta\to\infty}[\langle\delta x^2(\Delta)\rangle] = \frac{2D}{\omega_0} + \frac{2D_a\alpha}{\omega_0(\omega_c+\omega_0)}. \tag{8.71}$$

8.10 Derivation of the heat expression

The ensemble average heat, is expressed in terms of variance and cross-correlations

$$\begin{aligned} Q(t) \equiv \langle q(t)\rangle &= \int_0^t \kappa\frac{d\langle x_s^2\rangle}{ds}ds - \gamma\int_0^t \sqrt{2D_a}\langle\eta_s\dot{x}_s\rangle ds \\ &\equiv Q_{EX}(t) + Q_{HK}(t), \end{aligned} \tag{8.72}$$

The first term is connected to the evolution of the variance. It vanishes in the steady-state and only accounts for the heat released during a transient evolution of the distribution. Here we will focus on the case of a steady-state, where Q_{EX} is zero, to derive the housekeeping heat. Q_{HK} can be computed analytically by injecting the differential equation Eq. (4.5) for $\dot{x}_t$: $\langle\dot{x}_t\eta_t\rangle = -\omega_0\langle x_t\eta_t\rangle + \sqrt{2D_a}\alpha$. First, the $\langle x_t\eta_t\rangle$ term can be computed

$$\begin{aligned} \langle x_t\eta_t\rangle &= \int_0^t \sqrt{2D_a}\langle\eta_t\eta_s\rangle e^{-\omega_0(t-s)}ds \\ &= \alpha\int_0^t \sqrt{2D_a}e^{-\omega_c|t-s|-\omega_0(t-s)}ds \\ &= \frac{\sqrt{2D_a}\alpha}{\omega_0+\omega_c}\left(1-e^{-t(\omega_0+\omega_c)}\right), \end{aligned} \tag{8.73}$$

leading for the steady-state Q_{HK}, to

$$\begin{aligned} &-\gamma\int_0^t \sqrt{2D_a}\langle\eta_s\dot{x}_s\rangle ds \\ &= -\gamma\int_0^t \sqrt{2D_a}\left(-\omega_0\langle x_s\eta_s\rangle + \sqrt{2D_a}\alpha\right)ds \\ &= 2\gamma D_a\alpha\left(\int_0^t \frac{\omega_0}{\omega_0+\omega_c}\left[1-e^{-s(\omega_0+\omega_c)}\right]ds - t\right) \\ &= 2\gamma D_a\alpha\left(\frac{\omega_0}{\omega_0+\omega_c}-1\right)t + \frac{2\gamma D_a\omega_0}{(\omega_0+\omega_c)^2}(1-e^{-t(\omega_0+\omega_c)}). \end{aligned} \tag{8.74}$$

This gives, after an exponential decorrelation at short times (just after the noise is turned on, a short-time regime that is never probed in our experiments), a linear heat expenditure with negative (since $\omega_0 > 0$) slope $2\gamma D_a\alpha\left(\frac{\omega_0}{\omega_0+\omega_c}-1\right)$ that account for the heat needed to maintain the system in its NESS.

Therefore, if we discard the decorrelation after the noise is turned on, we obtain the following expression for the cumulative housekeeping heat:

$$Q_{HK}(t) = 2\gamma D_a \alpha \left(\frac{\omega_0}{\omega_0 + \omega_c} - 1 \right) t \tag{8.75}$$

8.11 Color protocol: differential equation and solution by Laplace transform

We subject the process to a *color protocol* which is a sudden change (STEP) in correlation time. We model this by applying two different noises with two Heaviside functions to model the STEP. We consider that at time $t = 0^-$ the system is at thermal equilibrium with no additional noise ; at time $t = 0^+$ a first colored noise η_1 is turned on ; at time $t = t_0$ η_1 is turned off and η_2 is turned on. The differential equation for the centred process $(x - \langle x \rangle)$ writes

$$\begin{aligned} \dot{x} &= -\omega_0 x + \theta(t_0 - t)\sqrt{2D_1}\eta_1(t) + \theta(t - t_0)\sqrt{2D_2}\eta_2(t) + \sqrt{2D}\xi(t) \\ &= -\omega_0 x + \theta(t - t_0)\left(\sqrt{2D_2}\eta_2(t) - \sqrt{2D_1}\eta_1(t)\right) + \sqrt{2D_2}\eta_2(t) + \sqrt{2D}\xi(t) \end{aligned} \tag{8.76}$$

we define

$$f(t) = \theta(t - t_0)\left(\sqrt{2D_2}\eta_2(t) - \sqrt{2D_1}\eta_1(t)\right) \tag{8.77}$$

with Laplace transform $\mathcal{L}[f(t)] = F[s]$. The differential equation transforms to

$$\tilde{x}[s] = \frac{1}{\omega_0 + s}\left\{x(0) + F[s] + \sqrt{2D_1}\tilde{\eta_1}[s] + \sqrt{2D}\tilde{\xi}[s]\right\} \tag{8.78}$$

we compute the inverse Laplace transform of the different terms by convolution. We explicite the calculation

$$\begin{aligned} \mathcal{L}^{-1}\left[\frac{1}{\omega_0 + s}F[s]\right] &= \int_0^t e^{-\omega_0(t-\tau)}\left(\sqrt{2D_2}\eta_2(\tau) - \sqrt{2D_1}\eta_1(\tau)\right)\theta(\tau - t_0)d\tau \\ &= \int_{t_0}^t e^{-\omega_0(t-\tau)}\left(\sqrt{2D_2}\eta_2(\tau) - \sqrt{2D_1}\eta_1(\tau)\right)d\tau \end{aligned} \tag{8.79}$$

$$\mathcal{L}^{-1}\left[\frac{1}{\omega_0 + s}\sqrt{2D_1}\tilde{\eta_1}[s]\right] = \int_0^t e^{-\omega_0(t-\tau)}\sqrt{2D_1}\eta_1(\tau)d\tau \tag{8.80}$$

by combining the two integrals on η_1 these two terms give together

$$\sqrt{2D_2}\int_{t_0}^t e^{-\omega_0(t-\tau)}\eta_2(\tau)d\tau + \sqrt{2D_1}\int_0^{min(t_0,t)} e^{-\omega_0(t-\tau)}\eta_1(\tau)d\tau \tag{8.81}$$

therefore, the solution for the position, experiencing a STEP-like change of correlation time writes

$$\boxed{x(t) = x_0 e^{-\omega_0 t} + e^{-\omega_0 t}\left[\sqrt{2D_2}\int_{t_0}^{t} e^{\omega_0\tau}\eta_2(\tau)d\tau + \sqrt{2D_1}\int_{0}^{min(t_0,t)} e^{\omega_0\tau}\eta_1(\tau)d\tau + \sqrt{2D}\int_{0}^{t} e^{\omega_0\tau}\xi(\tau)d\tau\right]} \tag{8.82}$$

the result obtained make sense : the first noise η_1 stops at t_0 so the integral stops either at t if $t < t_0$ or at t_0 otherwise. The second noise η_2 starts at t_0 so does its integral. The thermal noise is always present, hence the integral goes from 0 to t. Note that even if the integral of the first noise stops at t_0, we will see on variance that it still has an influence on the process for a certain time.

Calculation of the variance:

We compute the variance

$$\begin{aligned}
\sigma_x^2(t) &= \langle x_0^2\rangle e^{-2\omega_0 t} + 2De^{-2\omega_0 t}\int_0^t dt_1\int_0^t dt_2\langle\xi(t_1)\xi(t_2)\rangle e^{\omega_0(t_1+t_2)} \\
&+ 2D_1 e^{-2\omega_0 t}\int_0^{min(t_0,t)} dt_1\int_0^{min(t_0,t)} dt_2\langle\eta_1(t_1)\eta_1(t_2)\rangle e^{\omega_0(t_1+t_2)} \\
&+ 2D_2 e^{-2\omega_0 t}\int_0^t dt_1\int_0^t dt_2\langle\eta_2(t_1)\eta_2(t_2)\rangle e^{\omega_0(t_1+t_2)} \\
&\equiv \langle x_0^2\rangle e^{-2\omega_0 t} + \mathcal{J}_1 + \mathcal{J}_2 + \mathcal{J}_3
\end{aligned} \tag{8.83}$$

$\mathcal{J}_1$ can be easily computed using $\langle\xi(t_1)\xi(t_2)\rangle = \delta(t_1 - t_2)$

$$\mathcal{J}_1 = e^{-2\omega_0 t}2D\int_0^t e^{2\omega_0 t}dt_1 = \frac{D}{\omega_0}\left(1 - 2e^{-2\omega_0 t}\right) \tag{8.84}$$

To compute $\mathcal{J}_2$ we use the correlation $\langle\eta_1(t_1)\eta_1(t_2)\rangle = \alpha e^{-\omega_1|t_1-t_2|} = \alpha e^{-\omega_1(t_1+t_2-2min(t_1,t_2))}$. We also define $m \equiv min(t_0, t)$ the upper bound of the integral.

$$\mathcal{J}_2 = 2D_1\alpha e^{-2\omega_0 t}\int_0^m\int_0^m e^{\omega_0(t_1+t_2)-\omega_1(t_1+t_2-2min(t_1,t_2))} \tag{8.85}$$

we split the inside integral in two, depending of $min(t_1, t_2)$

$$\begin{aligned}
\mathcal{J}_2 &= 2D_1\alpha e^{-2\omega_0 t}\int_0^m\left[\int_0^{t_1} e^{\omega_0(t_1+t_2)-\omega_1(t_1-t_2)} + \int_{t_1}^m e^{\omega_0(t_1+t_2)-\omega_1(t_2-t_1)}\right] \\
&= 2D_1\alpha e^{-2\omega_0 t}\int_0^m\left[\int_0^{t_1} e^{t_1(\omega_0-\omega_1)+t_2(\omega_0+\omega_1)} + \int_{t_1}^m e^{t_1(\omega_0+\omega_1)+t_2(\omega_0-\omega_1)}\right] \\
&= 2D_1\alpha e^{-2\omega_0 t}\int_0^m\left[\frac{e^{t_1(\omega_0-\omega_1)}}{\omega_0+\omega_1}\left(e^{t_1(\omega_0+\omega_1)}-1\right) + \frac{e^{t_1(\omega_0+\omega_1)}}{\omega_0-\omega_1}\left(e^{m(\omega_0+\omega_1)} - e^{t_1(\omega_0-\omega_1)}\right)\right]
\end{aligned} \tag{8.86}$$

and we obtain, after some calculations the result

$$\mathcal{J}_2 = \frac{2D_1\alpha e^{-2\omega_0 t}}{\omega_0^2 - \omega_1^2}\left[1 - 2e^{m(\omega_0-\omega_1)} + e^{2\omega_0 m} - \frac{\omega_1}{\omega_0}\left(e^{2\omega_0 m} - 1\right)\right] \tag{8.87}$$

that still depends on m. We finally compute $\mathcal{J}_3$ using $\langle \eta_2(t_1)\eta_2(t_2)\rangle = \alpha e^{-\omega_2|t_1-t_2|}$, same amplitude α than for $\mathcal{J}_2$ because we study protocols with constant noise variance.

$$\begin{aligned}
\mathcal{J}_3 &= 2D_2\alpha e^{-2\omega_0 t}\int_{t_0}^{t} dt_1 \int_{t_0}^{t} dt_2 e^{\omega_0(t_1+t_2)-\omega_2(t_1+t_2-2min(t_1,t_2))} \\
&= 2D_2\alpha e^{-2\omega_0 t}\int_{t_0}^{t} dt_1 \left[\int_{t_0}^{t_1} dt_2 e^{\omega_0(t_1+t_2)-\omega_2(t_1-t_2)} + \int_{t_1}^{t} dt_2 e^{\omega_0(t_1+t_2)-\omega_2(t_2-t_2)}\right] \\
&= 2D_2\alpha e^{-2\omega_0 t}\int_{t_0}^{t} dt_1 \left[\frac{e^{t_1(\omega_0-\omega_2)}}{\omega_0+\omega_2}\left(e^{t_1(\omega_0+\omega_2)} - e^{t_0(\omega_0+\omega_2)}\right) + \frac{e^{t_1(\omega_0+\omega_2)}}{\omega_0-\omega_2}\left(e^{t(\omega_0-\omega_2)} - e^{t_1(\omega_0-\omega_2)}\right)\right]
\end{aligned} \tag{8.88}$$

which gives, after some calculations

$$\mathcal{J}_3 = \frac{2D_2\alpha}{\omega_0^2 - \omega_2^2}\left[1 - 2e^{(t_0-t)(\omega_0+\omega_2)} + e^{2(t_0-t)\omega_0} - \frac{\omega_2}{\omega_0}\left(1 - e^{2(t_0-t)\omega_0}\right)\right] \tag{8.89}$$

We will now study two cases : before and after the STEP. Before the STEP $t < t_0$, hence $m = t$ and we can rewrite $\mathcal{J}_2$ as

$$\mathcal{J}_2 = \frac{2D_1\alpha}{\omega_0^2 - \omega_1^2}\left[1 - 2e^{-t(\omega_0+\omega_1)} + e^{-2\omega_0 t} - \frac{\omega_1}{\omega_0}\left(1 - e^{-2\omega_0 t}\right)\right] \tag{8.90}$$

we furthermore note that in this case $\mathcal{J}_3 = 0$ (its integration domain is null), and we can write the variance

$$\begin{aligned}
\sigma_x^2(t) &= \langle x_0^2\rangle e^{-2\omega_0 t} + \frac{2D_1\alpha}{\omega_0^2 - \omega_1^2}\left[1 - 2e^{-t(\omega_0+\omega_1)} + e^{-2\omega_0 t} - \frac{\omega_1}{\omega_0}\left(1 - e^{-2\omega_0 t}\right)\right] + \frac{D}{\omega_0}\left[1 - e^{-2\omega_0 t}\right] \\
&= \left[\frac{D}{\omega_0} + \frac{2D_1\alpha}{\omega_0^2 - \omega_1^2}(1 - \omega_1/\omega_0)\right] + \left[\langle x_0^2\rangle - \frac{D}{\omega_0} - \frac{2D_1\alpha}{\omega_0^2 - \omega_1^2}(1 + \omega_1/\omega_0)\right] e^{-2\omega_0 t} - \frac{4D_1\alpha}{\omega_0^2 - \omega_1^2} e^{-t(\omega_0-\omega_1}
\end{aligned} \tag{8.91}$$

and we note the limit

$$\lim_{t\to\infty}[\sigma_x^2(t)] = \frac{D}{\omega_0} + \frac{2D_1\alpha}{\omega_0^2 - \omega_1^2}(1 - \omega_1/\omega_0) \tag{8.92}$$

where $D/\omega_0 = k_B T/\kappa$ is equipartition, and the second term is the correction due to the colored noise. hence we can rewrite simply the variance as

$$\sigma_x^2(t) = \sigma_x^2(\infty) + (\langle x_0^2\rangle - \sigma_x^2(\infty))e^{-2\omega_0 t} - \frac{4D_1\alpha}{\omega_0^2 - \omega_1^2} e^{-t(\omega_0-\omega_1)} \tag{8.93}$$

which is a relaxation from an initial thermal equilibrium towards a final non-equilibrium steady-state.

After the STEP, $t > t_0$ hence $m = t_0$ and we can rewrite

$$\mathcal{J}_2 = \frac{2D_1\alpha}{\omega_0^2 - \omega_1^2}\left[e^{-2\omega_0 t} - 2e^{(t_0-t)\omega_0 - t_0\omega_1} + e^{-2\omega_0(t_0-t)} - \frac{\omega_1}{\omega_0}\left(e^{2\omega_0(t_0-t)} - e^{-2\omega_0 t}\right)\right] \quad (8.94)$$

what we wan to study, is the variance at a finite time after the STEP, while the time of the STEP itself, t_0 is far from 0, hence the system is in steady-state before the change of correlation. With this in mind, we define $\Delta = t - t_0$ and write

$$\begin{aligned}
\mathcal{J}_1 &= \frac{D}{\omega_0}\left[1 - e^{-2\omega_0(t_0+\Delta)}\right] \\
\mathcal{J}_2 &= \frac{2D_1\alpha}{\omega_0^2 - \omega_1^2}\left[e^{-2\omega_0(t_0+\Delta)} - 2e^{\Delta\omega_0 - (t-\Delta)\omega_1} + e^{-2\omega_0\Delta} - \frac{\omega_1}{\omega_0}\left(e^{2\omega_0\Delta} - e^{-2\omega_0(t_0+\Delta)}\right)\right] \\
\mathcal{J}_3 &= \frac{2D_2\alpha}{\omega_0^2 - \omega_2^2}\left[1 - 2e^{\Delta(\omega_0+\omega_2)} + e^{2\Delta\omega_0} - \frac{\omega_2}{\omega_0}\left(1 - e^{2\Delta\omega_0}\right)\right]
\end{aligned} \quad (8.95)$$

we finally take the limit of $t_0 \gg \frac{1}{\omega_0}, \frac{1}{\omega_1}, \frac{1}{\omega_2}$ hence all terms $\sim e^{-t_0}$ vanishes. We obtain

$$\begin{aligned}
\mathcal{J}_1 &= \frac{D}{\omega_0} \\
\mathcal{J}_2 &= \frac{2D_1\alpha}{\omega_0^2 - \omega_1^2}\left[e^{-2\omega_0\Delta} - \frac{\omega_1}{\omega_0}e^{-2\omega_0\Delta}\right] \\
\mathcal{J}_3 &= \frac{2D_2\alpha}{\omega_0^2 - \omega_2^2}\left[1 - 2e^{\Delta(\omega_0+\omega_2)} + e^{2\Delta\omega_0} - \frac{\omega_2}{\omega_0}\left(1 - e^{2\Delta\omega_0}\right)\right]
\end{aligned} \quad (8.96)$$

that gives for the variance after the STEP

$$\boxed{\sigma_x^2(\Delta) = \frac{D}{\omega_0} + \frac{2D_1\alpha(\omega_0 - \omega_1)}{\omega_0^2 - \omega_1^2}e^{-2\omega_0\Delta} + \frac{2D_2\alpha}{\omega_0^2 - \omega_2^2}\left[1 - 2e^{-\Delta(\omega_0+\omega_2)} + e^{-2\omega_0\Delta} - \frac{\omega_2}{\omega_0}(1 - 2e^{-2\omega_0\Delta})\right]} \quad (8.97)$$

while we recall the variance before the STEP when t_0 is very large

$$\boxed{\sigma_x^2 = \frac{D}{\omega_0} + \frac{2D_1\alpha}{\omega_0^2 - \omega_1^2}(1 - \omega_1/\omega_0).} \quad (8.98)$$

We can note on Eq. 8.97 that the influence of the first noise η_1 decreases exponentially with the characteristic time $1/\omega_0$ while the second noise appears with a more complicated exponential relaxation. The overall variance evolution is non-monotonic.

8.12 Two dimensional process

The (x, η) joint-process obeys to

$$\begin{aligned}
\dot{x} &= -\omega_0 x + \sqrt{2D_a}\eta + \sqrt{2D}\xi \\
\dot{\eta} &= -\omega_c\eta + \sqrt{2\alpha\omega_c^2}\theta
\end{aligned} \quad (8.99)$$

where θ_t is a hidden white noise variable, hence the system behaves like an asymmetrically coupled pair of systems x and η immersed in two different δ-correlated baths. See Fig. 4.7 for a schematic view. This couple of equation, reminiscent of the the unified colored-noise approach [158, 159] is said markovian [66, 210] because both process are driven by Markovian (white) noises. The system of Eq. 8.99 can be written more concisely as a vectorial process [67, 69] of $\boldsymbol{X} = (x_t, \eta_t)$, obeys to the following matrix equation

$$\frac{d\mathbf{X}}{dt} = -\mathcal{A}\mathbf{X} + \boldsymbol{\mathcal{N}} \tag{8.100}$$

where the coupling matrix

$$\mathcal{A} = \begin{pmatrix} \omega_0 & -\sqrt{2D_a} \\ 0 & \omega_c \end{pmatrix} \tag{8.101}$$

and $\langle N_i(t)N_j(s)\rangle) = 2D_{ij}\delta(t-s)$ where the D_{ij} are the elements of a diffusion matrix

$$\mathcal{D} = \begin{pmatrix} D & 0 \\ 0 & \alpha\omega_c \end{pmatrix} \tag{8.102}$$

The system is linear in $\mathbf{X}$ and the can reach steady-state because trace and determinant of $\mathcal{A}$ are positive. Such stationary state is characterised by a bivariate Gaussian distribution (see [69] for details)

$$P_S(\mathbf{X}) = Ne^{-\mathbf{X}\sigma^{-1}\mathbf{X}/2} \tag{8.103}$$

where N is a normalisation coefficient and the matrix σ obeys to

$$\mathcal{D} = \frac{\mathcal{A}\sigma + \sigma\mathcal{A}^T}{2} \tag{8.104}$$

and as show in [69] we obtain a steady-state distribution

$$P_S(\mathbf{X}) \sim e^{-Ax^2 - B\eta^2 - Cx\eta} \tag{8.105}$$

where A, B and C can be explicitly compute. The C term, leading to an elliptic distribution is $\sim 1/\omega_c$ and therefore grows with increasing correlation time of the noise. In the white noise limit $\omega_c \gg \omega_0$ we get

$$\lim_{\omega_c \gg \omega_0} [P_S(x,\eta)] = Nexp\left(\frac{-\omega_0}{D + 2D_A\alpha/\omega_c}x^2 - \frac{1}{\alpha}\eta^2 - \frac{2\sqrt{2D_A}\omega_0}{\omega_c}x\eta\right). \tag{8.106}$$

We can compute the marginal distribution for position x in this limit as

$$\lim_{\omega_c \gg \omega_0} [\rho_S(x)] = \sqrt{\pi\alpha}Nexp\left(\frac{-\omega_0}{D + 2D_A\alpha/\omega_c}x^2 - \mathcal{O}(\omega_c^{-2})\right) \tag{8.107}$$

where we find again as variance of position D_{eff}/ω_0 in agreement with the result on $\langle x^2 \rangle$.

Taking the "strong" limit of $\omega_c \to \infty$ gives the bivariate distribution of two uncoupled processes $P \sim exp(-\omega_0 x^2/D - \eta^2/\alpha)$ where effective temperature converges to room temperature.

Steady-state distribution of the bivariate process:

The system is linear in $\mathbf{X}$ and the can reach steady-state because trace and determinant of $\mathcal{A}$ are positive. Such stationary state is characterised by a bivariate Gaussian distribution (see [69] for details)

$$P_S(\mathbf{X}) = Ne^{-\mathbf{X}\sigma^{-1}\mathbf{X}/2} \tag{8.108}$$

where N is a normalisation coefficient and the matrix σ obeys to

$$\mathcal{D} = \frac{\mathcal{A}\sigma + \sigma\mathcal{A}^T}{2} \tag{8.109}$$

In our case we obtain

$$\sigma = \begin{pmatrix} \frac{2D_A C\omega_c + D(\omega_0+\omega_c)}{\omega_0(\omega_0+\omega_c)} & -\frac{\sqrt{2D_a}C\omega_c}{\omega_0+\omega_c} \\ -\frac{\sqrt{2D_a}C\omega_c}{\omega_0+\omega_c} & C\omega_c \end{pmatrix} \tag{8.110}$$

and therefore for the distribution

$$P_S(x_t, \eta_t) = Nexp\left(\frac{1}{2\phi}\left[-C\omega_c x^2 - \frac{2D_A C\omega_c + D(\omega_0+\omega_c)}{\omega_0(\omega_0+\omega_C)}\eta^2 + \frac{-2\sqrt{2D_a}C\omega_c}{\omega_0+\omega_c}x\eta\right]\right) \tag{8.111}$$

with $\phi = 1/(\sigma_{11}\sigma_{22} - \sigma_{12}\sigma_{21})$. We can explicit

$$\begin{aligned} P_S(x_t, \eta_t) = Nexp\Bigg(& -\frac{\omega_0(\omega_0+\omega_c)^2}{2D_A C\omega_c(\omega_0+\omega_c) + D(\omega_0+\omega_c)^2 - 2D_A\omega_0 C\omega_c}x^2 \\ & - \frac{2D_A C\omega_c + D(\omega_0+\omega_c)}{2D_A C^2\omega_c^2(\omega_0+\omega_c) + DC\omega_c(\omega_0+\omega_c)^2 - 2D_A\omega_0 C^2\omega_c^2}\eta^2 \\ & - \frac{2\sqrt{2D_a}\omega_0 C\omega_c(\omega_0+\omega_c)}{2D_A C^2\omega_c^2(\omega_0+\omega_c) + DC\omega_c(\omega_0+\omega_c)^2 - 2D_A\omega_0 C^2\omega_c^2}x\eta\Bigg) \end{aligned} \tag{8.112}$$

We can note mostly that the third term in the exponential, leading to an elliptic distribution is $\sim 1/\omega_c$ and therefore grows with increasing correlation time of the noise.

Bibliography

[1] A. Einstein *Annalen der Physik*, vol. 322, no. 8, pp. 549–560, 1905.

[2] A. Ashkin, J. M. Dziedzic, J. E. Bjorkholm, and S. Chu, "Observation of a single-beam gradient force optical trap for dielectric particles," *Optics letters*, vol. 11, no. 5, pp. 288–290, 1986.

[3] A. Ashkin, "History of optical trapping and manipulation of small-neutral particle, atoms, and molecules," *IEEE Journal of Selected Topics in Quantum Electronics*, vol. 6, no. 6, pp. 841–856, 2000.

[4] G. Volpe and al., "Roadmap to optical tweezes," *ArXiv*, vol. 2206.13789, June 2022.

[5] P. H. Jones, O. M. Maragò, and G. Volpe, *Optical Tweezers: Principles and Applications*. Cambridge University Press, 2015.

[6] C. Bigg, "A visual history of jean perrin's brownian motion curves," in *Histories of Scientific Observation* (L. Daston and E. Lunbeck, eds.), University of Chicago Press, 2011.

[7] A. Einstein, *Investigations on the Theory of the Brownian Movement*. Courier Corporation, 1956.

[8] E. Kappler, "Versuche zur messung der avogadro-loschmidtschen zahl aus der brownschen bewegung einer drehwaage," *Annalen der Physik*, vol. 403, no. 2, pp. 233–256, 1931.

[9] J. Gieseler, B. Deutsch, R. Quidant, and L. Novotny, "Subkelvin parametric feedback cooling of a laser-trapped nanoparticle," *Phys. Rev. Lett.*, vol. 109, p. 103603, Sep 2012.

[10] P. Langevin, "Sur la théorie du mouvement brownien," *Compte rendu des seances de l'academie des sciences*, vol. 146, pp. 530–533, 1908.

[11] P. Wu, R. Huang, C. Tischer, A. Jonas, and E.-L. Florin, "Direct measurement of the nonconservative force field generated by optical tweezers," *Phys. Rev. Lett.*, vol. 103, p. 108101, Sep 2009.

[12] Y. Amarouchene, M. Mangeat, B. V. Montes, L. Ondic, T. Guérin, D. S. Dean, and Y. Louyer, "Nonequilibrium dynamics induced by scattering forces for optically trapped nanoparticles in strongly inertial regimes," *Phys. Rev. Lett.*, vol. 122, p. 183901, May 2019.

[13] Y. F. Barooji, K. G. Hvid, I. I. Petitjean, J. M. Brickman, L. B. Oddershede, and P. M. Bendix, "Changes in cell morphology and actin organization in embryonic stem cells cultured under different conditions," *Cells*, vol. 10, no. 11, 2021.

[14] C. Selhuber-Unkel, P. Yde, K. Berg-Sørensen, and L. B. Oddershede, "Variety in intracellular diffusion during the cell cycle.," *Physical biology*, vol. 6 2, p. 025015, 2009.

[15] A. V. Taubenberger, B. Baum, and H. K. Matthews, "The mechanics of mitotic cell rounding," *Frontiers in Cell and Developmental Biology*, vol. 8, p. 687, 2020.

[16] S. Hurst, B. E. Vos, M. Brandt, and T. Betz, "Intracellular softening and increased viscoelastic fluidity during division," *Nature Physics*, Oct 2021.

[17] M. Levin, R. Sorkin, D. Pine, R. Granek, A. Bernheim-Groswasser, and Y. Roichman, "Kinetics of actin networks formation measured by time resolved particle-tracking microrheology," *Soft Matter*, vol. 16, pp. 7869–7876, 2020.

[18] M. Levin, G. Bel, and Y. Roichman, "Different anomalous diffusion regimes measured in the dynamics of tracer particles in actin networks," *ArXiv*, vol. 2011.00539, 2020.

[19] C. Gonzalez-Ballestero, M. Aspelmeyer, L. Novotny, R. Quidant, and O. Romero-Isart, "Levitodynamics: Levitation and control of microscopic objects in vacuum," *Science*, vol. 374, no. 6564, p. eabg3027, 2021.

[20] U. Delic, M. Reisenbauer, D. Grass, N. Kiesel, V. Vuletić, and M. Aspelmeyer, "Cavity cooling of a levitated nanosphere by coherent scattering," *Phys. Rev. Lett.*, vol. 122, p. 123602, Mar 2019.

[21] D. Windey, C. Gonzalez-Ballestero, P. Maurer, L. Novotny, O. Romero-Isart, and R. Reimann, "Cavity-based 3d cooling of a levitated nanoparticle via coherent scattering," *Phys. Rev. Lett.*, vol. 122, p. 123601, Mar 2019.

[22] T. Li, S. Kheifets, and M. G. Raizen, "Millikelvin cooling of an optically trapped microsphere in vacuum," *Nature Physics*, vol. 7, pp. 527–530, Jul 2011.

[23] T. Li, "Nanoparticles get cool by light scattering," *Viewpoints in Physics*, vol. 12, March 2019.

[24] U. Delić, M. Reisenbauer, K. Dare, D. Grass, V. Vuletić, N. Kiesel, and M. Aspelmeyer, "Cooling of a levitated nanoparticle to the motional quantum ground state," *Science*, vol. 367, no. 6480, pp. 892–895, 2020.

[25] Q. Wu, L. Mancino, M. Carlesso, M. A. Ciampini, L. Magrini, N. Kiesel, and M. Paternostro, "Nonequilibrium quantum thermodynamics of a particle trapped in a controllable time-varying potential," *PRX Quantum*, vol. 3, p. 010322, Feb 2022.

[26] T. Ariga, M. Tomishige, and D. Mizuno, "Nonequilibrium energetics of molecular motor kinesin," *Phys. Rev. Lett.*, vol. 121, p. 218101, Nov 2018.

[27] T. Ariga, K. Tateishi, M. Tomishige, and D. Mizuno, "Noise-induced acceleration of single molecule kinesin-1," *Phys. Rev. Lett.*, vol. 127, p. 178101, Oct 2021.

[28] D. V. Averin and J. P. Pekola, "Statistics of the dissipated energy in driven single-electron transitions," *EPL (Europhysics Letters)*, vol. 96, p. 67004, dec 2011.

[29] J. P. Pekola, A. Kutvonen, and T. Ala-Nissila, "Dissipated work and fluctuation relations for non-equilibrium single-electron transitions," *Journal of Statistical Mechanics: Theory and Experiment*, vol. 2013, p. P02033, feb 2013.

[30] J. P. Pekola, "Towards quantum thermodynamics in electronic circuits," *Nature Physics*, vol. 11, pp. 118–123, Feb 2015.

[31] E. Dieterich, J. Camunas-Soler, M. Ribezzi-Crivellari, U. Seifert, and F. Ritort, "Single-molecule measurement of the effective temperature in non-equilibrium steady states," *Nature Physics*, vol. 11, pp. 971–977, Nov 2015.

[32] S. Ciliberto, "Experiments in stochastic thermodynamics: Short history and perspectives," *Phys. Rev. X*, vol. 7, p. 021051, Jun 2017.

[33] I. A. Martínez, A. Petrosyan, D. Guéry-Odelin, E. Trizac, and S. Ciliberto, "Engineered swift equilibration of a brownian particle," *Nature Physics*, vol. 12, no. 9, pp. 843–846, 2016.

[34] D. Guéry-Odelin, C. Jarzynski, C. A. Plata, A. Prados, and E. Trizac, "Driving rapidly while remaining in control: classical shortcuts from hamiltonian to stochastic dynamics," *arXiv preprint arXiv:2204.11102*, 2022.

[35] Y. Jun, M. c. v. Gavrilov, and J. Bechhoefer, "High-precision test of landauer's principle in a feedback trap," *Phys. Rev. Lett.*, vol. 113, p. 190601, Nov 2014.

[36] A. Bérut, A. Arakelyan, A. Petrosyan, S. Ciliberto, R. Dillenschneider, and E. Lutz, "Experimental verification of landauer's principle linking information and thermodynamics," *Nature*, vol. 483, pp. 187–189, Mar 2012.

[37] T. Admon, S. Rahav, and Y. Roichman, "Experimental realization of an information machine with tunable temporal correlations," *Phys. Rev. Lett.*, vol. 121, p. 180601, Nov 2018.

[38] H. Kramers, "Brownian motion in a field of force and the diffusion model of chemical reactions," *Physica*, vol. 7, no. 4, pp. 284–304, 1940.

[39] P. Hänggi, P. Talkner, and M. Borkovec, "Reaction-rate theory: fifty years after kramers," *Rev. Mod. Phys.*, vol. 62, pp. 251–341, Apr 1990.

[40] P. L. García-Müller, F. Borondo, R. Hernandez, and R. M. Benito, "Solvent-induced acceleration of the rate of activation of a molecular reaction," *Phys. Rev. Lett.*, vol. 101, p. 178302, Oct 2008.

[41] A. Sali, E. Shakhnovich, and M. Karplus, "How does a protein fold?," *Nature*, vol. 369, pp. 248–251, May 1994.

[42] R. B. Best and G. Hummer, "Diffusive model of protein folding dynamics with kramers turnover in rate," *Phys. Rev. Lett.*, vol. 96, p. 228104, Jun 2006.

[43] L. I. McCann, M. Dykman, and B. Golding, "Thermally activated transitions in a bistable three-dimensional optical trap," *Nature*, vol. 402, pp. 785–787, Dec 1999.

[44] L. Rondin, J. Gieseler, F. Ricci, R. Quidant, C. Dellago, and L. Novotny, "Direct measurement of kramers turnover with a levitated nanoparticle," *Nature Nanotechnology*, vol. 12, pp. 1130–1133, Dec 2017.

[45] K. Sekimoto, *Stochastic energetics*. Springer-Verlag, Berlin Heidelberg, 2010.

[46] K. Sekimoto, "Langevin Equation and Thermodynamics," *Progress of Theoretical Physics Supplement*, vol. 130, pp. 17–27, 01 1998.

[47] U. Seifert, "Stochastic thermodynamics, fluctuation theorems and molecular machines," *Reports on Progress in Physics*, vol. 75, p. 126001, nov 2012.

[48] J. Bechhoefer, S. Ciliberto, S. Pigolotti, and E. Roldán, "Stochastic thermodynamics: experiment and theory," *J. Stat. Mech.*, vol. 2020, p. 064001, jun 2020.

[49] H. C. BERG and D. A. BROWN, "Chemotaxis in escherichia coli analysed by three-dimensional tracking," *Nature*, vol. 239, pp. 500–504, Oct 1972.

[50] A. Yildiz, M. Tomishige, R. D. Vale, and P. R. Selvin, "Kinesin walks hand-over-hand," *Science*, vol. 303, no. 5658, pp. 676–678, 2004.

[51] G. Woehlke and M. Schliwa, "Walking on two heads: the many talents of kinesin," *Nature Reviews Molecular Cell Biology*, vol. 1, pp. 50–58, Oct 2000.

[52] F. Jülicher, K. Kruse, J. Prost, and J.-F. Joanny, "Active behavior of the cytoskeleton," *Physics Reports*, vol. 449, no. 1, pp. 3–28, 2007. Nonequilibrium physics: From complex fluids to biological systems III. Living systems.

[53] P. A. Pullarkat, P. A. Fernández, and A. Ott, "Rheological properties of the eukaryotic cell cytoskeleton," *Physics Reports*, vol. 449, no. 1, pp. 29–53, 2007. Nonequilibrium physics: From complex fluids to biological systems III. Living systems.

[54] C. Bustamante, J. Liphardt, and F. Ritort, "The nonequilibrium thermodynamics of small systems," *Physics Today*, vol. 58, no. 7, pp. 43–48, 2005.

[55] Z. Wang, H.-Y. Chen, Y.-J. Sheng, and H.-K. Tsao, "Diffusion, sedimentation equilibrium, and harmonic trapping of run-and-tumble nanoswimmers," *Soft Matter*, vol. 10, pp. 3209–3217, 2014.

[56] E. Fodor, C. Nardini, M. E. Cates, J. Tailleur, P. Visco, and F. van Wijland, "How far from equilibrium is active matter?," *Phys. Rev. Lett.*, vol. 117, p. 038103, Jul 2016.

[57] A. Argun, A.-R. Moradi, E. m. c. c. v. Pinçe, G. B. Bagci, A. Imparato, and G. Volpe, "Non-boltzmann stationary distributions and nonequilibrium relations in active baths," *Phys. Rev. E*, vol. 94, p. 062150, Dec 2016.

[58] E. Flenner and G. Szamel, "Active matter: Quantifying the departure from equilibrium," *Phys. Rev. E*, vol. 102, p. 022607, Aug 2020.

[59] H. Turlier, D. A. Fedosov, B. Audoly, T. Auth, N. S. Gov, C. Sykes, J.-F. Joanny, G. Gompper, and T. Betz, "Equilibrium physics breakdown reveals the active nature of red blood cell flickering," *Nature Physics*, vol. 12, pp. 513–519, May 2016.

[60] D. Martin, J. O'Byrne, M. E. Cates, E. Fodor, C. Nardini, J. Tailleur, and F. van Wijland, "Statistical mechanics of active ornstein-uhlenbeck particles," *Phys. Rev. E*, vol. 103, p. 032607, Mar 2021.

[61] C. Nardini, E. Fodor, E. Tjhung, F. van Wijland, J. Tailleur, and M. E. Cates, "Entropy production in field theories without time-reversal symmetry: Quantifying the non-equilibrium character of active matter," *Phys. Rev. X*, vol. 7, p. 021007, Apr 2017.

[62] C. Bechinger, R. Di Leonardo, H. Löwen, C. Reichhardt, G. Volpe, and G. Volpe, "Active particles in complex and crowded environments," *Rev. Mod. Phys.*, vol. 88, p. 045006, Nov 2016.

[63] E. Lauga and R. E. Goldstein, "Dance of the microswimmers," *Physics Today*, vol. 65, no. 9, pp. 30–35, 2012.

[64] T. Sanchez, D. T. N. Chen, S. J. DeCamp, M. Heymann, and Z. Dogic, "Spontaneous motion in hierarchically assembled active matter," *Nature*, vol. 491, pp. 431–434, Nov 2012.

[65] L. Dabelow, S. Bo, and R. Eichhorn, "Irreversibility in active matter systems: Fluctuation theorem and mutual information," *Phys. Rev. X*, vol. 9, p. 021009, Apr 2019.

[66] C. Sandford, A. Y. Grosberg, and J.-F. m. c. Joanny, "Pressure and flow of exponentially self-correlated active particles," *Phys. Rev. E*, vol. 96, p. 052605, Nov 2017.

[67] S. A. M. Loos and S. H. L. Klapp, "Irreversibility, heat and information flows induced by non-reciprocal interactions," *New Journal of Physics*, vol. 22, p. 123051, dec 2020.

[68] D. Hartich, A. C. Barato, and U. Seifert, "Sensory capacity: An information theoretical measure of the performance of a sensor," *Phys. Rev. E*, vol. 93, p. 022116, Feb 2016.

[69] A. Crisanti, A. Puglisi, and D. Villamaina, "Nonequilibrium and information: The role of cross correlations," *Phys. Rev. E*, vol. 85, p. 061127, Jun 2012.

[70] C. Battle, C. P. Broedersz, N. Fakhri, V. F. Geyer, J. Howard, C. F. Schmidt, and F. C. MacKintosh, "Broken detailed balance at mesoscopic scales in active biological systems," *Science*, vol. 352, no. 6285, pp. 604–607, 2016.

[71] L. Mercier de Lépinay, B. Pigeau, B. Besga, and O. Arcizet, "Eigenmode orthogonality breaking and anomalous dynamics in multimode nano-optomechanical systems under non-reciprocal coupling," *Nature Communications*, vol. 9, p. 1401, Apr 2018.

[72] J. C. Maxwell, "On physical lines of force," *Philosophical Magazine*, vol. 90.

[73] J. C. Maxwell, "Essay for the apostles on "analogies in nature"," *From Campbell and Garnet, Life of Maxwell*, p. 376, Feb 1856.

[74] F. Nappo, "The double nature of maxwell's physical analogies," *Studies in History and Philosophy of Science Part A*, vol. 89, pp. 212–225, 2021.

[75] C. Barceló, S. Liberati, and M. Visser, "Analogue gravity," *Living Reviews in Relativity*, vol. 14, p. 3, 05 2011.

[76] D. Dragoman and M. Dragoman, *Quantum-Classical Analogies*. Springer, 2004.

[77] D. Bouwmeester, N. Dekker, F. Dorsselaer, C. Schrama, P. Visser, and J. Woerdman, "Observation of landau-zener dynamics in classical optical systems," *Physical Review A*, vol. 51, pp. 646–654, 02 1995.

[78] C. Sheng, H. Liu, Y. Wang, S. N. Zhu, and D. A. Genov, "Trapping light by mimicking gravitational lensing," *Nature Photonics*, vol. 7, pp. 902–906, Nov 2013.

[79] NASA, ESA, CSA, and STScI, "Nasa webb delivers deepest infrared image of universe yet,"

[80] M. R. Evans and S. N. Majumdar, "Diffusion with stochastic resetting," *Phys. Rev. Lett.*, vol. 106, p. 160601, Apr 2011.

[81] V. Stojkoski, T. Sandev, L. Kocarev, and A. Pal, "Autocorrelation functions and ergodicity in diffusion with stochastic resetting," *Arxiv*, Jul 2021.

[82] D. G. Grier, "A revolution in optical manipulation," *Nature*, vol. 424, pp. 810–816, Aug 2003.

[83] P. Wu, R. Huang, C. Tischer, A. Jonas, and E.-L. Florin, "Direct measurement of the nonconservative force field generated by optical tweezers," *Phys. Rev. Lett.*, vol. 103, p. 108101, Sep 2009.

[84] L. Liu, S. Kheifets, V. Ginis, and F. Capasso, "Subfemtonewton force spectroscopy at the thermal limit in liquids," *Phys. Rev. Lett.*, vol. 116, p. 228001, Jun 2016.

[85] L. P. Ghislain, N. A. Switz, and W. W. Webb, "Measurement of small forces using an optical trap," *Review of Scientific Instruments*, vol. 65, no. 9, pp. 2762–2768, 1994.

[86] G. Schnoering, Y. Rosales-Cabara, H. Wendehenne, A. Canaguier-Durand, and C. Genet, "Thermally limited force microscopy on optically trapped single metallic nanoparticles," *Phys. Rev. Applied*, vol. 11, p. 034023, Mar 2019.

[87] D. S. Ether, L. B. Pires, S. Umrath, D. Martinez, Y. Ayala, B. Pontes, G. R. de S. Araújo, S. Frases, G.-L. Ingold, F. S. S. Rosa, N. B. Viana, H. M. Nussenzveig, and P. A. M. Neto, "Probing the casimir force with optical tweezers," *Europhys. Lett.*, vol. 112, p. 44001, nov 2015.

[88] X. Michalet and A. J. Berglund, "Optimal diffusion coefficient estimation in single-particle tracking," *Phys. Rev. E*, vol. 85, no. 6, p. 061916, 2012.

[89] F. Ricci, R. A. Rica, M. Spasenović, J. Gieseler, L. Rondin, L. Novotny, and R. Quidant, "Optically levitated nanoparticle as a model system for stochastic bistable dynamics," *Nature Commun.*, vol. 8, no. 1, pp. 1–7, 2017.

[90] B. Lukić, S. Jeney, C. Tischer, A. J. Kulik, L. Forró, and E.-L. Florin, "Direct observation of nondiffusive motion of a brownian particle," *Phys. Rev. Lett.*, vol. 95, p. 160601, Oct 2005.

[91] T. Li, S. Kheifets, D. Medellin, and M. G. Raizen, "Measurement of the instantaneous velocity of a brownian particle," *Science*, vol. 328, no. 5986, pp. 1673–1675, 2010.

[92] I. M. Toli ć Nørrelykke, E.-L. Munteanu, G. Thon, L. Oddershede, and K. Berg-Sørensen, "Anomalous diffusion in living yeast cells," *Phys. Rev. Lett.*, vol. 93, p. 078102, Aug 2004.

[93] S. Chattopadhyay, R. Moldovan, C. Yeung, and X. L. Wu, "Swimming efficiency of bacterium escherichia coli," *Proceedings of the National Academy of Sciences*, vol. 103, no. 37, pp. 13712–13717, 2006.

[94] C. Bechinger, R. Di Leonardo, H. Löwen, C. Reichhardt, G. Volpe, and G. Volpe, "Active particles in complex and crowded environments," *Rev. Mod. Phys.*, vol. 88, p. 045006, Nov 2016.

[95] K. Berg-Sorensen and H. Flyvbjerg, "Power spectrum analysis for optical tweezers," *Review of Scientific Instruments*, vol. 75, no. 3, pp. 594–612, 2004.

[96] R. Metzler and J. Klafter, "The random walk's guide to anomalous diffusion: a fractional dynamics approach," *Physics Reports*, vol. 339, no. 1, pp. 1–77, 2000.

[97] R. Metzler, J.-H. Jeon, A. G. Cherstvy, and E. Barkai, "Anomalous diffusion models and their properties: non-stationarity, non- ergodicity, and ageing at the centenary of single particle tracking," *Phys. Chem. Chem. Phys.*, vol. 16, pp. 24128–24164, 2014.

[98] C. Maggi, M. Paoluzzi, N. Pellicciotta, A. Lepore, L. Angelani, and R. Di Leonardo, "Generalized energy equipartition in harmonic oscillators driven by active baths," *Phys. Rev. Lett.*, vol. 113, p. 238303, Dec 2014.

[99] I. A. Martínez, E. Roldán, L. Dinis, D. Petrov, and R. A. Rica, "Adiabatic processes realized with a trapped brownian particle," *Phys. Rev. Lett.*, vol. 114, p. 120601, Mar 2015.

[100] V. Blickle and C. Bechinger, "Realization of a micrometre-sized stochastic heat engine," *Nature Physics*, vol. 8, pp. 143–146, Feb 2012.

[101] I. A. Martinez, E. Roldán, L. Dinis, and R. Rica, "Colloidal heat engines: a review," *Soft Matter*, vol. 13, pp. 22–36, 2017.

[102] A. Rohrbach, "Stiffness of optical traps: Quantitative agreement between experiment and electromagnetic theory," *Phys. Rev. Lett.*, vol. 95, p. 168102, Oct 2005.

[103] Y. Harada and T. Asakura, "Radiation forces on a dielectric sphere in the rayleigh scattering regime," *Optics Communications*, vol. 124, no. 5, pp. 529–541, 1996.

[104] T. Franosch, M. Grimm, M. Belushkin, F. M. Mor, G. Foffi, L. Forró, and S. Jeney, "Resonances arising from hydrodynamic memory in brownian motion," *Nature*, vol. 478, pp. 85–88, Oct 2011.

[105] R. Goerlich, M. Li, S. Albert, G. Manfredi, P.-A. Hervieux, and C. Genet, "Noise and ergodic properties of brownian motion in an optical tweezer: Looking at regime crossovers in an ornstein-uhlenbeck process," *Phys. Rev. E*, vol. 103, p. 032132, Mar 2021.

[106] G. Volpe and G. Volpe, "Simulation of a brownian particle in an optical trap," *Am. J. Phys.*, vol. 81, no. 3, pp. 224–230, 2013.

[107] P. E. Kloeden and E. Platen, *Numerical Solutions of stochastic differential equations*, vol. 23. Springer-Verlag Berlin Heidelberg, 1 ed., 1992.

[108] D. J. Higham., "An algorithmic introduction to numerical simulation of stochastic differential equations," *SIAM Review*, vol. 43, no. 3, pp. 525–546, 2001.

[109] E. Vanden-Eijnden and G. Ciccotti, "Second-order integrators for langevin equations with holonomic constraints," *Chem. Phys. Lett.*, vol. 429, no. 1, pp. 310 – 316, 2006.

[110] C. Gardiner, *Stochastic Methods A Handbook for the Natural and Social Sciences*, vol. 13 of *10*. Springer-Verlag Berlin Heidelberg, 4 ed., 2009.

[111] F. Douarche, S. Ciliberto, and A. Petrosyan, "Estimate of the free energy difference in mechanical systems from work fluctuations: experiments and models," *Journal of Statistical Mechanics: Theory and Experiment*, vol. 2005, pp. P09011–P09011, sep 2005.

[112] U. Seifert, "Entropy production along a stochastic trajectory and an integral fluctuation theorem," *Phys. Rev. Lett.*, vol. 95, p. 040602, Jul 2005.

[113] R. Goerlich, G. Manfredi, P.-A. Hervieux, L. Mertz, and C. Genet, "Probing quantum effects with classical stochastic analogs," *Phys. Rev. Research*, vol. 3, p. 033203, Sep 2021.

[114] F. Czerwinski, A. C. Richardson, and L. B. Oddershede, "Quantifying noise in optical tweezers by allan variance," *Opt. Express*, vol. 17, pp. 13255–13269, Jul 2009.

[115] N. M. Mutothya, Y. Xu, Y. Li, and R. Metzler, "Characterising stochastic motion in heterogeneous media driven by coloured non-gaussian noise," *Journal of Physics A: Mathematical and Theoretical*, 2021.

[116] F. Douarche, S. Joubaud, N. B. Garnier, A. Petrosyan, and S. Ciliberto, "Work fluctuation theorems for harmonic oscillators," *Phys. Rev. Lett.*, vol. 97, p. 140603, Oct 2006.

[117] M. Baiesi, S. Ciliberto, G. Falasco, and C. Yolcu, "Thermal response of nonequilibrium rc circuits," *Phys. Rev. E*, vol. 94, p. 022144, Aug 2016.

[118] T. Harada and S.-i. Sasa, "Equality connecting energy dissipation with a violation of the fluctuation-response relation," *Phys. Rev. Lett.*, vol. 95, p. 130602, Sep 2005.

[119] T. Speck, "Stochastic thermodynamics for active matter," *EPL (Europhysics Letters)*, vol. 114, p. 30006, may 2016.

[120] G. Gallavotti and E. G. D. Cohen, "Dynamical ensembles in nonequilibrium statistical mechanics," *Phys. Rev. Lett.*, vol. 74, pp. 2694–2697, Apr 1995.

[121] C. Jarzynski, "Nonequilibrium equality for free energy differences," *Phys. Rev. Lett.*, vol. 78, pp. 2690–2693, Apr 1997.

[122] D. J. Evans and D. J. Searles, "The fluctuation theorem," *Advances in Physics*, vol. 51, no. 7, pp. 1529–1585, 2002.

[123] G. E. Crooks, "Nonequilibrium measurements of free energy differences for microscopically reversible markovian systems," *Journal of Statistical Physics*, vol. 90, pp. 1481–1487, Mar 1998.

[124] G. E. Crooks, "Entropy production fluctuation theorem and the nonequilibrium work relation for free energy differences," *Phys. Rev. E*, vol. 60, pp. 2721–2726, Sep 1999.

[125] E. Lutz and S. Ciliberto, "Information: From maxwell's demon to landauer's eraser," *Physics Today*, vol. 68, no. 9, pp. 30–35, 2015.

[126] S. Ciliberto and E. Lutz, *The Physics of Information: From Maxwell to Landauer*, pp. 155–175. Cham: Springer International Publishing, 2019.

[127] M. Esposito and C. V. den Broeck, "Second law and landauer principle far from equilibrium," *EPL (Europhysics Letters)*, vol. 95, p. 40004, aug 2011.

[128] Y. Rosales-Cabara, G. Manfredi, G. Schnoering, P.-A. Hervieux, L. Mertz, and C. Genet, "Optimal protocols and universal time-energy bound in brownian thermodynamics," *Phys. Rev. Research*, vol. 2, p. 012012, Jan 2020.

[129] A. G. Cherstvy and R. Metzler, "Ergodicity breaking, ageing, and confinement in generalized diffusion processes with position and time dependent diffusivity," *J. Stat. Mech.*, vol. 2015, p. P05010, may 2015.

[130] B. M. Lansdorp and O. A. Saleh, "Power spectrum and allan variance methods for calibrating single-molecule video-tracking instruments," *Rev. Sci. Instrum.*, vol. 83, p. 025115, 2012.

[131] I. L. Morgan and O. A. Saleh, "Tweezepy: A python package for calibrating forces in single-molecule video-tracking experiments," *PLoS One*, vol. 16, p. e0262028, Dec. 2021.

[132] M. Li, O. Sentissi, S. Azzini, G. Schnoering, A. Canaguier-Durand, and C. Genet, "Subfemtonewton force fields measured with ergodic brownian ensembles," *Phys. Rev. A*, vol. 100, p. 063816, Dec 2019.

[133] S. C. Manrubia and D. H. Zanette, "Stochastic multiplicative processes with reset events," *Phys. Rev. E*, vol. 59, pp. 4945–4948, May 1999.

[134] M. R. Evans, S. N. Majumdar, and G. Schehr, "Stochastic resetting and applications," *Journal of Physics A: Mathematical and Theoretical*, vol. 53, p. 193001, apr 2020.

[135] M. Montero, A. Masó-Puigdellosas, and J. Villarroel, "Continuous-time random walks with reset events," *The European Physical Journal B*, vol. 90, p. 176, Sep 2017.

[136] J. Fuchs, S. Goldt, and U. Seifert, "Stochastic thermodynamics of resetting," *EPL (Europhysics Letters)*, vol. 113, p. 60009, mar 2016.

[137] V. Stojkoski, T. Sandev, L. Kocarev, and A. Pal, "Geometric brownian motion under stochastic resetting: A stationary yet nonergodic process," *Phys. Rev. E*, vol. 104, p. 014121, Jul 2021.

[138] W. Wang, A. G. Cherstvy, H. Kantz, R. Metzler, and I. M. Sokolov, "Time averaging and emerging nonergodicity upon resetting of fractional brownian motion and heterogeneous diffusion processes," *Phys. Rev. E*, vol. 104, p. 024105, Aug 2021.

[139] D. W. Allan, "Statistics of atomic frequency standards," *Proceedings of the IEEE*, vol. 54, no. 2, pp. 221–230, 1966.

[140] J. A. Barnes, A. R. Chi, L. S. Cutler, D. J. Healey, D. B. Leeson, T. E. McGunigal, J. A. Mullen, W. L. Smith, R. L. Sydnor, R. F. Vessot, and G. M. R. Winckler, "Characterization of frequency stability," *IEEE Transactions on Instrumentation and Measurement*, vol. 20, no. 2, p. 105, 1971.

[141] E. Hebestreit, M. Frimmer, R. Reimann, C. Dellago, F. Ricci, and L. Novotny, "Calibration and energy measurement of optically levitated nanoparticle sensors," *Review of Scientific Instruments*, vol. 89, no. 3, p. 033111, 2018.

[142] C. Bechinger, R. Di Leonardo, H. Löwen, C. Reichhardt, G. Volpe, and G. Volpe, "Active particles in complex and crowded environments," *Rev. Mod. Phys.*, vol. 88, p. 045006, Nov 2016.

[143] S. Ramaswamy, "Active matter," *Journal of Statistical Mechanics: Theory and Experiment*, vol. 2017, p. 054002, may 2017.

[144] M. C. Marchetti, J. F. Joanny, S. Ramaswamy, T. B. Liverpool, J. Prost, M. Rao, and R. A. Simha, "Hydrodynamics of soft active matter," *Rev. Mod. Phys.*, vol. 85, pp. 1143–1189, Jul 2013.

[145] M. E. Cates, "Diffusive transport without detailed balance in motile bacteria: does microbiology need statistical physics?," *Reports on Progress in Physics*, vol. 75, p. 042601, mar 2012.

[146] U. M. B. Marconi, A. Puglisi, and C. Maggi, "Heat, temperature and clausius inequality in a model for active brownian particles," *Scientific Reports*, vol. 7, p. 46496, Apr 2017.

[147] S. Chaki and R. Chakrabarti, "Entropy production and work fluctuation relations for a single particle in active bath," *Physica A: Statistical Mechanics and its Applications*, vol. 511, pp. 302–315, 2018.

[148] S. Chaki and R. Chakrabarti, "Effects of active fluctuations on energetics of a colloidal particle: Superdiffusion, dissipation and entropy production," *Physica A: Statistical Mechanics and its Applications*, vol. 530, p. 121574, 2019.

[149] E. Fodor, J. L. Robert, and M. E. Cates, "Irreversibility and biased ensembles in active matter: Insights from stochastic thermodynamics," *ArXiv*, Apr 2021.

[150] L. Dabelow and R. Eichhorn, "Irreversibility in active matter: General framework for active ornstein-uhlenbeck particles," *Frontiers in Physics*, vol. 8, p. 516, 2021.

[151] X.-L. Wu and A. Libchaber, "Particle diffusion in a quasi-two-dimensional bacterial bath," *Phys. Rev. Lett.*, vol. 84, pp. 3017–3020, Mar 2000.

[152] C. Maggi, M. Paoluzzi, L. Angelani, and R. Di Leonardo, "Memory-less response and violation of the fluctuation-dissipation theorem in colloids suspended in an active bath," *Scientific Reports*, vol. 7, p. 17588, Dec 2017.

[153] I. A. Martínez, E. Roldán, J. M. R. Parrondo, and D. Petrov, "Effective heating to several thousand kelvins of an optically trapped sphere in a liquid," *Phys. Rev. E*, vol. 87, p. 032159, Mar 2013.

[154] P. Mestres, I. A. Martinez, A. Ortiz-Ambriz, R. A. Rica, and E. Roldan, "Realization of nonequilibrium thermodynamic processes using external colored noise," *Phys. Rev. E*, vol. 90, p. 032116, Sep 2014.

[155] J. T. Park, G. Paneru, C. Kwon, S. Granick, and H. K. Pak, "Rapid-prototyping a brownian particle in an active bath," *Soft Matter*, vol. 16, pp. 8122–8127, 2020.

[156] A. Militaru, M. Innerbichler, M. Frimmer, F. Tebbenjohanns, L. Novotny, and C. Dellago, "Escape dynamics of active particles in multistable potentials," *Nature Communications*, vol. 12, p. 2446, Apr 2021.

[157] G. Paneru, J. T. Park, and H. K. Pak, "Transport and diffusion enhancement in experimentally realized non-gaussian correlated ratchets," *The Journal of Physical Chemistry Letters*, vol. 12, pp. 11078–11084, Nov 2021.

[158] M. S. Miguel and J. M. Sancho, "A colored-noise approach to brownian motion in position space. corrections to the smolucski equation," *Journal of Statistical Physics*, vol. 22, pp. 605–624, May 1980.

[159] P. Jung and P. Hänggi, "Dynamical systems: A unified colored-noise approximation," *Phys. Rev. A*, vol. 35, pp. 4464–4466, May 1987.

[160] G. Szamel, "Self-propelled particle in an external potential: Existence of an effective temperature," *Phys. Rev. E*, vol. 90, p. 012111, Jul 2014.

[161] M. C. Wang and G. E. Uhlenbeck, "On the theory of the brownian motion ii," *Rev. Mod. Phys.*, vol. 17, pp. 323–342, Apr 1945.

[162] H. B. Callen and T. A. Welton, "Irreversibility and generalized noise," *Physical Review*, vol. 83, no. 1, p. 34, 1951.

[163] E. Ben-Isaac, Y. Park, G. Popescu, F. L. H. Brown, N. S. Gov, and Y. Shokef, "Effective temperature of red-blood-cell membrane fluctuations," *Phys. Rev. Lett.*, vol. 106, p. 238103, Jun 2011.

[164] M. Li, O. Sentissi, S. Azzini, G. Schnoering, A. Canaguier-Durand, and C. Genet, "Subfemtonewton force fields measured with ergodic brownian ensembles," *Phys. Rev. A*, vol. 100, p. 063816, Dec 2019.

[165] F. J. Schwarzendahl and H. Lowen, "Anomalous cooling and overcooling of active systems," *ArXiv*, 2021.

[166] M. Nagy, Z. Ákos, D. Biro, and T. Vicsek, "Hierarchical group dynamics in pigeon flocks," *Nature*, vol. 464, pp. 890–893, Apr 2010.

[167] T. Vicsek and A. Zafeiris, "Collective motion," *Physics Reports*, vol. 517, no. 3, pp. 71–140, 2012. Collective motion.

[168] L. Balasubramaniam, R.-M. Mège, and B. Ladoux, "Active nematics across scales from cytoskeleton organization to tissue morphogenesis," *Current Opinion in Genetics and Development*, vol. 73, p. 101897, 2022.

[169] R. Kubo, "The fluctuation-dissipation theorem," *Reports on Progress in Physics*, vol. 29, pp. 255–284, jan 1966.

[170] N. Zaccarelli, B.-L. Li, I. Petrosillo, and G. Zurlini, "Order and disorder in ecological time-series: Introducing normalized spectral entropy," *Ecological Indicators*, vol. 28, pp. 22–30, 2013. 10 years Ecological Indicators.

[171] O. Vasicek, "A test for normality based on sample entropy," *Journal of the Royal Statistical Society: Series B (Methodological)*, vol. 38, no. 1, pp. 54–59, 1976.

[172] S. Y. Park and A. K. Bera, "Maximum entropy autoregressive conditional heteroskedasticity model," *Journal of Econometrics*, vol. 150, no. 2, pp. 219–230, 2009. Recent Development in Financial Econometrics.

[173] T. Roger, C. Maitland, K. Wilson, N. Westerberg, D. Vocke, E. M. Wright, and D. Faccio, "Optical analogues of the Newton-Schrödinger equation and boson star evolution," *Nature Commun.*, vol. 7, p. 13492, 2016.

[174] Y. Couder, S. Protière, E. Fort, and A. Boudaoud, "Walking and orbiting droplets," *Nature*, vol. 437, no. 7056, pp. 208–208, 2005.

[175] G. Pucci, D. M. Harris, L. M. Faria, and J. W. M. Bush, "Walking droplets interacting with single and double slits," *Journal of Fluid Mechanics*, vol. 835, pp. 1136–1156, 2018.

[176] E. Madelung, "Quantum theory in hydrodynamical form," *Zeit. f. Phys.*, vol. 40, p. 322, 1927.

[177] D. Bohm, "A suggested interpretation of the quantum theory in terms of hidden variables," *Physical Review*, vol. 85, no. 2, pp. 166–179, 1952.

[178] T. Takabayasi, "The Formulation of Quantum Mechanics in terms of Ensemble in Phase Space," *Progress of Theoretical Physics*, vol. 11, pp. 341–373, 04 1954.

[179] P. Degond, F. Méhats, and C. Ringhofer, "Quantum energy-transport and drift-diffusion models," *Journal of Statistical Physics*, vol. 118, pp. 625–667, Feb. 2005.

[180] R. Pinneau, "A review on the quantum drift diffusion model," *Transport Theory and Statistical Physics*, vol. 31, pp. 367–395, 2002.

[181] H. P. McKean, "A class of markov processes associated with nonlinear parabolic equations," *Proc. Natl. Acad. Sci.*, vol. 56, pp. 1907–1911, 1966.

[182] V. N. Kolokoltsov, *Nonlinear Markov Processes and Kinetic Equations*. Cambridge Tracts in Mathematics, Cambridge University Press, 2010.

[183] Y. Rosales-Cabara, G. Manfredi, G. Schnoering, P.-A. Hervieux, L. Mertz, and C. Genet, "Optimal protocols and universal time-energy bound in brownian thermodynamics," *Phys. Rev. Research*, vol. 2, p. 012012, Jan 2020.

[184] W. S. Bakr, J. I. Gillen, A. Peng, S. Fölling, and M. Greiner, "A quantum gas microscope for detecting single atoms in a hubbard-regime optical lattice," *Nature*, vol. 462, pp. 74–77, Nov 2009.

[185] Y. Wang, S. Shevate, T. M. Wintermantel, M. Morgado, G. Lochead, and S. Whitlock, "Preparation of hundreds of microscopic atomic ensembles in optical tweezer arrays," *npj Quantum Information*, vol. 6, no. 1, pp. 1–5, 2020.

[186] R. E. Wyatt, *Quantum Dynamics with Trajectories*, vol. 28. Springer Publishing, nov 2005.

[187] G. Manfredi, P.-A. Hervieux, and J. Hurst, "Phase-space modeling of solid-state plasmas," *Rev. Mod. Plasma Phys.*, vol. 3, p. 13, 2019.

[188] C. L. Gardner, "The quantum hydrodynamic model for semiconductor devices," *J. Appl. Math.*, vol. 54, no. 2, 1994.

[189] G. Manfredi, "How to model quantum plasmas," *Fields Institute Communications Series*, vol. 46, pp. 263–287, may 2005.

[190] G. Manfredi, P.-A. Hervieux, and J. Hurst, "Fluid descriptions of quantum plasmas," *Reviews of Modern Plasma Physics*, vol. 5, p. 7, Oct 2021.

[191] I. Burghardt and K. Moller, "Quantum dynamics for dissipative systems: A hydrodynamical perspective," *Journal of Chemical Physics*, vol. 117, 2002.

[192] M. H. R. F. O. M. O. S. E. P. Wigner, "Distribution functions in physics: fundamentals," *Physics Reports*, vol. 106, no. 3, 1984.

[193] W. H. Zurek, "Decoherence and the transition from quantum to classical - revisited," *Los Alamos Science*, vol. 27, pp. 11–12, 2002.

[194] P. E. Kloeden and E. Platen, *Numerical Solutions of stochastic differential equations*, vol. 23. Springer-Verlag Berlin Heidelberg, 1 ed., 1992.

[195] D. S. Grebenkov, "First exit times of harmonically trapped particles: a didactic review," *Journal of Physics A: Mathematical and Theoretical*, vol. 48, p. 013001, dec 2014.

[196] L. Mandel, "Sub-poissonian photon statistics in resonance fluorescence," *Opt. Lett.*, vol. 4, pp. 205–207, Jul 1979.

[197] A. Simon and A. Libchaber, "Escape and synchronization of a brownian particle," *Phys. Rev. Lett.*, vol. 68, pp. 3375–3378, Jun 1992.

[198] N. Freitas, J.-C. Delvenne, and M. Esposito, "Stochastic and quantum thermodynamics of driven rlc networks," *Phys. Rev. X*, vol. 10, p. 031005, Jul 2020.

[199] B. Besga, A. Bovon, A. Petrosyan, S. N. Majumdar, and S. Ciliberto, "Optimal mean first-passage time for a brownian searcher subjected to resetting: Experimental and theoretical results," *Phys. Rev. Research*, vol. 2, p. 032029, Jul 2020.

[200] O. Tal-Friedman, A. Pal, A. Sekhon, S. Reuveni, and Y. Roichman, "Experimental realization of diffusion with stochastic resetting," *The Journal of Physical Chemistry Letters*, vol. 11, pp. 7350–7355, Sep 2020.

[201] S. Krishnamurthy, S. Ghosh, D. Chatterji, R. Ganapathy, and A. K. Sood, "A micrometre-sized heat engine operating between bacterial reservoirs," *Nature Physics*, vol. 12, pp. 1134–1138, Dec 2016.

[202] E. Nelson, "Derivation of the schrödinger equation from newtonian mechanics," *Phys. Rev.*, vol. 150, pp. 1079–1085, Oct 1966.

[203] D. Guéry-Odelin, A. Ruschhaupt, A. Kiely, E. Torrontegui, S. Martínez-Garaot, and J. G. Muga, "Shortcuts to adiabaticity: Concepts, methods, and applications," *Rev. Mod. Phys.*, vol. 91, p. 045001, Oct 2019.

[204] J. P. Arenas-López and M. Badaoui, "Stochastic modelling of wind speeds based on turbulence intensity," *Renewable Energy*, vol. 155, pp. 10–22, 2020.

[205] K. Hasselmann, "Stochastic climate models part i. theory," *Tellus*, vol. 28, no. 6, pp. 473–485, 1976.

[206] L. Onsager, "Reciprocal relations in irreversible processes. i.," *Phys. Rev.*, vol. 37, pp. 405–426, Feb 1931.

[207] L. Onsager, "Reciprocal relations in irreversible processes. ii.," *Phys. Rev.*, vol. 38, pp. 2265–2279, Dec 1931.

[208] R. Goerlich, L. Pires, G. Manfredi, P.-A. Hervieux, and C. Genet, "Harvesting information to control non-equilibrium states of active matter," *ArXiv*, Dec 2021.

[209] L. Novotny and B. Hecht, *Principles of nano-optics*. Cambridge university press, 2012.

[210] C. Sandford and A. Y. Grosberg, "Memory effects in active particles with exponentially correlated propulsion," *Phys. Rev. E*, vol. 97, p. 012602, Jan 2018.

Rémi GOERLICH

Optical control of Brownian diffusion: from bath engineering to quantum analogues

Résumé

Cette thèse explore les propriétés de différents processus stochastiques dans un piège optique. La manipulation des trajectoires browniennes issues d'un piège optique expérimental repose sur des hypothèses fortes quant à l'ergodicité et la stabilité du processus, qui sont ici démontrées expérimentalement. En ajoutant une force de pression de radiation aléatoire, pilotée numériquement, le système est connecté à un bain auxiliaire qui permet d'implémenter un analogue de matière active. Nous explorons les trajectoires non-browniennes qui en résultent ainsi que leur propriétés thermodynamiques hors-d'équilibre. Enfin, nous utilisons la formulation hydrodynamique de la mécanique quantique pour dériver un analogue classique stochastique d'un système quantique ouvert. Ce dernier est implémenté numériquement et expérimentalement, nous permettant de retrouver l'évolution de la densité d'un objet quantique en contact avec un bain thermique. Cet analogue permet d'accéder à des effets quantiques, tel que l'effet tunnel, à l'aide d'un système classique.

Mots-clés : piège optique, ergodicité, ingénierie de bain, matière active, analogues, hydrodynamique quantique.

Résumé en anglais

This thesis explores the properties of different stochastic processes within an optical trapping setup. The manipulation of Brownian trajectories in experimental optical traps relies on strong hypotheses regarding ergodicity and stability of the process, which are here experimentally demonstrated. By adding a numerically generated random radiation pressure force, the system is connected to an auxiliary engineered bath which allows to implement an analogue of active matter. We explore the resulting non-Brownian trajectories and non-equilibrium thermodynamic features. Finally, we use the hydrodynamic model of quantum mechanics, to derive a classical stochastic analogue of an open quantum system. Implementing it numerically and experimentally, we recover the evolution of the density of a quantum object in a thermal bath. This analogue allows to access quantum effects, such as tunnelling, through a classical system.

Keywords: Optical trapping, ergodicity, bath engineering, active matter, analogues, quantum hydrodynamics.